

**Computer simulation of residual stress and distortion  
of thick plates  
in multi-electrode submerged arc welding.  
Their mitigation techniques**

**by**

**Artem Pilipenko**

Department of Machine Design and Materials Technology  
Norwegian University of Science and Technology  
N-7491 Trondheim, Norway

This thesis has been submitted to the Norwegian University of Science and Technology (NTNU), Department of Machine Design and Materials Technology in partial fulfillment of the requirements for the Norwegian academic degree of Doktor Ingeniør.

Trondheim July 2001



## ACKNOWLEDGEMENTS

More than four years have passed since I started the work for this thesis. There are many people who helped and supported me along the way and to whom I feel grateful.

My deep gratitude goes to Professor Einar Halmøy and Professor Viktor Karkhin for their initiation and supervision of this study and for their continuous support and engagement in the project. I am very grateful to Professor E. Halmøy for his inspiration and guidance. I am also very grateful to Professor V.A. Karkhin for sharing his knowledge with me, for his valuable criticisms, fruitful discussions and continuous guidance.

I greatly appreciate the discussions on metallurgical aspects of welding with Professor Øystein Grong, and I am grateful for his advises concerning the thesis.

Very fruitful for the thesis were two weeks that I spent at Lehrstuhl für Metallische Werkstoffe, Fakultät für Angewandte Naturwissenschaften, Universität Bayreuth (Germany). And I would like to thank the simulation group and especially Dr. Vassili Plochikhine for valuable discussion and interesting ideas.

I am grateful to Dr. Zhiliang Zhang for his advises and help with ABAQUS. I am also grateful to the laboratory staff for their assistance. Special thanks go to Halvard Støwer for his help with the hardware and software.

Many thanks to Bjørn Uno Kolstad and Ragnhild Brakstad, the officers of the International Office (NTNU), for their help.

Finally, I thank Vera R. Brosset for her encouragement, kind support and involvement in my scientific career.

Last but most importantly I thank my family and friends for their support and patience during my studies.

This thesis is dedicated to my wife and son, whose love, guidance, sacrifice, and encouragement is boundless.

July 2001

Artem Pilipenko



## **ABSTRACT**

Welding is the main joining method used in shipbuilding. A multi-electrode submerged arc welding is usually applied to long joints of massive components since the early 1950s.

The problem of welding stresses and deformations arose almost simultaneously with the introduction of welding as a joining method. In 1892 Slavianov, in his works, mentioned about "harmful stresses in metal" appearing during welding. Despite tremendous development in welding technology since that time, this problem is still present.

This dissertation presents the development of an experimental, numerical and analytical approach to the analysis of weldability. Focus is placed on the investigation of transient and residual welding stresses and distortions in thick-walled ship hull structures. The investigation mostly relies on the finite element analysis. Some recommendations about mitigation techniques for reducing their negative influence on welded structure efficiency are given.

A number of simulation systems for the sequentially coupled thermo-mechanical analysis of welding process, taking into account the welding conditions during the butt welding of thick-walled steel panels, are developed. Two welding techniques are investigated. The three-electrode one-pass welding process and the one-electrode multi-pass process are compared in terms of the joint characteristics and transient stresses and deformations.

The accuracy of each finite element models is evaluated based on experimental results and the results of the analytical solution.

Several techniques allowing to reduce residual stresses and deformations are investigated. Both, obtained results and governing phenomena, are studied and explained based on physical principles.

The first part of the thesis is a significant part of the work. Its purpose is a deep analysis of the thermo-mechanics of welding allowing better understanding of the complicated phenomena.



## Contents at a glance

<b>CHAPTER I INTRODUCTION .....</b>	<b>10</b>
1. EVOLUTION OF SHIPBUILDING .....	10
2. WELDING PROCESS AND WELDABILITY .....	10
3. USE OF SUBMERGED ARC WELDING (SAW) IN SHIPBUILDING .....	11
4. AIM OF STUDY .....	11
<b>CHAPTER II STATE OF THE ART .....</b>	<b>15</b>
1. THERMAL FIELDS .....	15
2. WELDING STRESS FIELDS AND STRUCTURE DISTORTION ANALYSIS .....	21
<b>CHAPTER III THEORETICAL BACKGROUND .....</b>	<b>61</b>
1. PROCESS UNDER INVESTIGATION .....	61
2. HEAT TRANSFER ANALYSIS METHODS .....	70
3. STRESS AND STRAIN FIELDS ANALYSIS MODEL .....	90
<b>CHAPTER IV EXAMINATION OF MODELS AND DISCUSSION OF RESULTS.....</b>	<b>109</b>
1. HEAT FLOW ANALYSIS .....	109
2. STRESS FIELDS .....	120
3. OVERALL DEFORMATION OF WELDED STRUCTURES.....	132
4. OUT-OF-PLANE DEFORMATION.....	143
<b>CHAPTER V MITIGATION TECHNIQUES.....</b>	<b>157</b>
1. MECHANICAL STRAIGHTENING .....	158
2. THERMAL TENSIONING.....	162
3. TECHNIQUES FOR MITIGATION OF ANGULAR DEFORMATIONS.....	170
4. CONCLUSIONS.....	174
<b>CHAPTER VI CONCLUSIONS .....</b>	<b>177</b>
<b>APPENDIX A .....</b>	<b>181</b>
<b>APPENDIX B .....</b>	<b>203</b>
<b>APPENDIX C .....</b>	<b>207</b>
<b>APPENDIX D .....</b>	<b>209</b>
<b>APPENDIX E .....</b>	<b>213</b>
<b>APPENDIX F .....</b>	<b>219</b>
<b>APPENDIX G .....</b>	<b>221</b>

## Contents

<b>CHAPTER I INTRODUCTION .....</b>	<b>10</b>
1. EVOLUTION OF SHIPBUILDING .....	10
2. WELDING PROCESS AND WELDABILITY .....	10
3. USE OF SUBMERGED ARC WELDING (SAW) IN SHIPBUILDING .....	11
4. AIM OF STUDY.....	11
 <b>CHAPTER II STATE OF THE ART.....</b>	 <b>15</b>
1. THERMAL FIELDS .....	15
1.1. <i>Basics of the heat transfer analysis</i> .....	16
1.1.1. Heat sources- and geometry schematisation .....	16
1.2. <i>Basic equations</i> .....	17
1.3. <i>Initial and boundary conditions</i> .....	18
1.4. <i>Conclusions</i> .....	20
2. WELDING STRESS FIELDS AND STRUCTURE DISTORTION ANALYSIS .....	21
2.1. <i>Theory of plasticity, main conventional principles</i> .....	21
2.1.1. Stress-strain behaviour of the metallic materials .....	21
2.1.2. Prerequisites of the deformation theory .....	22
2.1.3. Elastic deformation .....	24
2.1.4. Plastic deformation. The criterion of yielding .....	24
2.1.5. Strain hardening .....	26
2.1.6. Conclusions.....	28
2.2. <i>Welding stresses and deformations</i> .....	29
2.2.1. Classification of welding stresses and deformations .....	29
2.2.2. Causes of welding stresses and deformations.....	31
2.2.3. Transient stress field .....	33
2.2.3.1 Longitudinal stress development during the welding process .....	33
2.2.3.2 Transverse stress development during welding process .....	37
2.2.4. Residual stress field .....	38
2.2.4.1 Residual longitudinal stress formed due to welding process .....	38
2.2.4.2 Residual transverse stress formed due to welding process .....	42
2.2.5. Conclusions.....	45
2.3. <i>Deformations of the welded structure</i> .....	46
2.3.1. Mechanism of transverse shrinkage in butt welds .....	46
2.3.2. Longitudinal and transverse shrinkage in butt welds.....	47
2.3.3. Kinetics of metal movement during welding process.....	48
2.3.4. Rotational distortion of butt joints .....	49
2.3.5. Angular shrinkage.....	50
2.3.5.1 Variety of local deformations .....	50
2.3.5.2 Kinetics of angular distortion developing.....	52
2.3.5.3 Angular distortion .....	53
2.3.6. Conclusions.....	56

---

<b>CHAPTER III THEORETICAL BACKGROUND .....</b>	<b>61</b>
1. PROCESS UNDER INVESTIGATION .....	61
1.1. <i>Description of the structure under investigation</i> .....	61
1.2. <i>Material description</i> .....	62
1.2.1. Steels for shipbuilding .....	62
1.2.2. Thermal and mechanical properties of the investigated steel .....	63
1.3. <i>Description of the welding process. Multi-electrode and multi-pass techniques</i> .....	66
1.4. <i>Conclusions</i> .....	69
2. HEAT TRANSFER ANALYSIS METHODS .....	70
2.1. <i>Analytical solutions</i> .....	70
2.1.1. Variety of analytical solutions .....	70
2.1.2. Model of the temperature distribution during multi-electrode SAW.....	71
2.1.2.1 Selection of the appropriate model .....	71
2.1.2.2 Mathematical modelling .....	72
2.2. <i>Finite element analysis</i> .....	75
2.2.1. Variety of finite element solutions.....	75
2.2.2. "Element birth" technique.....	76
2.2.3. 2D YZ-plane model for temperature distribution in the cross-section of the plate.....	76
2.2.3.1 Meshes for 2D heat flow analysis.....	77
2.2.3.2 Applied initial and boundary conditions.....	77
2.2.3.3 Calculation procedure .....	78
2.2.4. 2D shell-elements model for temperature distribution in the plane of the plate.....	79
2.2.4.1 2D solid elements versus 2D shell-elements .....	79
2.2.4.2 Mesh for 2D heat flow analysis with shell-elements .....	80
2.2.4.3 Applied boundary and initial conditions, and calculation procedure .....	80
2.2.5. 3D heat flow model for butt welding of plates .....	81
2.2.5.1 Finite element mesh and applied initial and boundary conditions.....	81
2.2.5.2 Calculation procedure .....	82
2.2.6. Methodical example of heat flow analysis.....	83
2.2.6.1 Purpose of the example.....	83
2.2.6.2 Method .....	83
2.2.6.3 Exact solution .....	83
2.2.6.4 3D FEA heat flow model .....	84
2.2.6.5 2D FEA heat flow model .....	86
2.2.6.6 Discussion of results .....	86
2.3. <i>Conclusions</i> .....	89
3. STRESS AND STRAIN FIELDS ANALYSIS MODEL .....	90
3.1. <i>Variety of models for stress and strain fields analysis</i> .....	90
3.2. <i>Metal plasticity in ABAQUS</i> .....	90
3.3. <i>2D sequentially coupled thermal-stress model (plane strain and generalized plane strain)</i> .....	91
3.3.1. Meshes for 2D plane strain and generalised plane strain analysis.....	91
3.3.2. Applied boundary conditions.....	92
3.3.3. Utilisation of the "element birth" technique .....	93
3.3.4. Elements used in 2D models.....	94
3.3.5. Contact analysis implementation.....	95
3.4. <i>3D sequentially coupled thermal-stress model</i> .....	96

---

## CONTENTS

---

3.4.1. Meshes for 3D thermal-stress analysis .....	96
3.4.2. Applied boundary conditions .....	98
3.4.3. Elements used in 3D models .....	98
3.4.4. Different sources of non-linearity in the models .....	99
3.4.5. Mesh accuracy .....	100
3.4.5.1 Purpose of the evaluation .....	100
3.4.5.2 Method .....	100
3.4.5.3 Discussion of the results .....	100
3.4. Conclusions.....	105
<b>CHAPTER IV EXAMINATION OF MODELS AND DISCUSSION OF RESULTS.....</b>	<b>109</b>
1. HEAT FLOW ANALYSIS .....	109
1.1. Results of the analytical model of the temperature distribution during ME SAW assuming the case of infinitely wide and long medium-thick plates and moving heat source.....	109
1.2. Results of the 2D model for temperature distribution in the cross-section of the weld assuming simultaneous seam completion.....	111
1.3. Results of the 2D model involving “element birth” technique for temperature distribution in the cross-section of the weld (comparison of the multi-electrode- and the multi-pass welding procedures) .....	113
1.4. Results of the complete 3D heat flow model for butt welding of the plates ..	115
1.5. Solid phase transformations due to three-electrode welding procedure and multi-pass welding procedure.....	116
1.6. Conclusions.....	119
2. STRESS FIELDS .....	120
2.1. Overall stress fields description .....	120
2.2. Characteristic features of two welding procedures under investigation.....	126
2.2.1. Stress development .....	126
2.2.2. Residual stresses .....	129
2.3. Conclusions.....	131
3. OVERALL DEFORMATION OF WELDED STRUCTURES.....	132
3.1. In-plane deformation .....	132
3.1.1. Transverse shrinkage .....	132
3.1.2. Longitudinal shrinkage .....	134
3.2. Inherent strain as a source for elastic finite element analysis.....	135
3.3. Plastic strain evolution .....	139
3.4. Conclusions.....	142
4. OUT-OF-PLANE DEFORMATION.....	143
4.1. Variation of the data reported in literature.....	143
4.2. Comparison of the 3D FEA results with different experimental data .....	144
4.3. Overall shape of the plates deformed due to welding.....	148
4.4. The effect of heat source distribution on the angular deformation .....	149
4.5. Evolution of the out-of-plane distortion.....	151
4.6. Angular deformation caused by multi-electrode and multi-pass welding ....	153
4.7. Conclusions.....	154
<b>CHAPTER V MITIGATION TECHNIQUES.....</b>	<b>157</b>
1. MECHANICAL STRAIGHTENING .....	158
1.1. Model of post-welding mechanical stretching.....	158

---

## CONTENTS

---

1.2. <i>3D model of mechanical stretching</i> .....	160
2. THERMAL TENSIONING.....	162
2.1. <i>Factors affecting selection of the thermal load</i> .....	162
2.2. <i>Implementation of the stationary heating blankets and the moving heating sources</i> .....	165
2.3. <i>Mechanism of thermal tensioning</i> .....	168
3. TECHNIQUES FOR MITIGATION OF ANGULAR DEFORMATIONS.....	170
4. CONCLUSIONS.....	174
<b>CHAPTER VI CONCLUSIONS</b> .....	<b>177</b>
RECOMMENDATIONS FOR FURTHER WORK .....	179
<b>APPENDIX A</b> .....	<b>181</b>
<b>APPENDIX B</b> .....	<b>203</b>
<b>APPENDIX C</b> .....	<b>207</b>
<b>APPENDIX D</b> .....	<b>209</b>
<b>APPENDIX E</b> .....	<b>213</b>
<b>APPENDIX F</b> .....	<b>219</b>
<b>APPENDIX G</b> .....	<b>221</b>



LIST OF SYMBOLS

---

**NOMENCLATURE**

$3\varepsilon$	[-], [%]	volumetric expansion
$a$	[m <sup>2</sup> ·s]	thermal diffusivity
$A$	[m <sup>2</sup> ]	cross-section area
$ALPHA_{ij}$		kinematic hardening shift tensor components (i,j=1÷3)
$B$	[m]	seam width
$c$	[J·kg <sup>-1</sup> ·K <sup>-1</sup> ]	specific heat capacity
$C$	[J·m <sup>-2</sup> ·s <sup>-1</sup> ·K <sup>-4</sup> ]	Stefan-Boltzmann's coefficient ( $C=5.67\times 10^{-8}$ W/m <sup>2</sup> ·K <sup>4</sup> )
$CCT$		continuous cooling transformation
$CL$		center line
$CPE4$		4-node bilinear plane strain element
$CPU$		central processing units
$DC2D4$		4-node linear diffusive heat transfer element
$d_{el}$	[m]	electrode diameter
$D_f$	[m]	weld size
$dx, dy, dz$	[m]	spatial step in x-, y- and z-direction
$dz$	[m]	displacement in z-direction
$E$	[N·m <sup>-2</sup> ]	elastic modulus
$EE_{ij}$	[-], [%]	elastic strain components (i,j=1÷3)
$E_i$	[J·m <sup>-1</sup> ]	gross heat input per unit length of weld
$E_{ij}$	[-], [%]	strain components (i,j=1÷3)
$e_{ij}$	[-], [%]	deviatoric components of the strain tensor
$EP_n$	[-], [%]	minimum, intermediate and maximum principal strains ( $EP1\leq EP2\leq EP3$ )
$ER_{ij}$	[-], [%]	mechanical strain rate components (i,j=1÷3)
$f$	[m]	deflection
$f$		yield function
$F$	[-]	function responsible for the heat source distribution effect on the steady state temperature field
$FCB$		flux copper backing
$FDM$		finite difference method
$FEA$		finite element analysis
$G$	[N·m <sup>-2</sup> ]	shear modulus
$g$		flow potential
$G_L$	[K·m <sup>-1</sup> ]	temperature gradient in weld pool
$h$	[m]	plate thickness
$H$	[m]	seam depth
$HAZ$		heat affected zone
$H_{iso}$		isotropic hardening parameter
$h_x, h_y, h_z$	[m]	step in x-, y- and z-directions
$I$	[A]	current
$I$	[m <sup>4</sup> ]	moment of inertia
$i$	[-]	sequence of numbers, $i=1, 2, 3$
$IE_{ij}$	[-], [%]	inelastic strain components (i,j=1÷3)
$I_{im}$	[-]	function of the trough-thickness power distribution expanded in the Fourier cosine series
$j$	[-]	sequence of numbers, $j=1, 2, 3$
$K_0$	[-]	modified Bessel function of second kind and zero order

---

LIST OF SYMBOLS

$l$	[m]	length
$l_1$	[m]	distance between leading and first trailed electrodes
$l_2$	[m]	distance between first and second trailed electrodes
$L_w$	[m]	weld length
$ME$		multi-electrode
$MISES$		Mises equivalent stress
$M_n$	[-]	number of simple sections in which the $n^{\text{th}}$ heat source distribution is divided
$MP$		multi-pass
$n$	[-]	normal vector
$NLGEOM$		parameter assigning analysis to be large-displacement analysis
$n_s$	[-]	number of integration points used through shell section
$NT$	[K]	temperature value at a node
$P$	[N]	force, gravitational force
$PE$	[-], [%]	plastic strain in ABAQUS specification
$Q$	[J]	net heat input
$q_0$	[J·s <sup>-1</sup> ]	source net power
$q_1(z), q_2(z), q_3(z)$	[J·s <sup>-1</sup> ·m <sup>-1</sup> ]	leading and two trailed heat sources distribution through the plate thickness
$q_2$	[J·m <sup>-2</sup> ·s <sup>-1</sup> ]	density of the heat flow
$q_3$	[J·m <sup>-3</sup> ·s <sup>-1</sup> ]	volumetric density of the heat source
$q_n$	[J·s <sup>-1</sup> ]	total net power of the $n^{\text{th}}$ heat source
$q_{nm}$	[J·s <sup>-1</sup> ·m <sup>-1</sup> ]	heat source distribution through the plate thickness
$q_w$	[J·m <sup>-1</sup> ]	heat input per unit length of weld
$r$	[m]	distance from the source
$R^2$	[-]	average standard deviation
$RF_n, RM_n$	[N], [N·m]	components of reaction forces, including reaction moments
$R_i$	[m]	distance from real and imaginary heat source
$R_L$	[m·s <sup>-1</sup> ]	local crystal growth rate
$r_n$	[m]	distance to $n^{\text{th}}$ heat source
$S$		surface
$s_1, s_2, s_3$	[N·m <sup>-2</sup> ]	components of the deviatoric stress tensor
$SAW$		submerged arc welding
$S_{ij}$	[N·m <sup>-2</sup> ]	stress components (i,j=1÷3)
$S_{ij}$	[N·m <sup>-2</sup> ]	deviatoric components of the stress tensor
$SP_n$	[N·m <sup>-2</sup> ]	minimum, intermediate and maximum principal stress (SP1≤SP2≤SP3)
$T$	[K]	temperature
$T_h^{max}$	[K]	maximum heating temperature for avoiding plastic deformation during thermal tensioning
$T^*$	[K]	temperature of material softening (for mild steel $T^* \approx 600^{\circ}\text{C}$ )
$T^{*0}$	[K]	isotherm corresponding to metal softening temperature on a top surface
$T^{*h}$	[K]	isotherm corresponding to metal softening temperature on a bottom surface
$T_0$	[K]	ambient and initial temperature
$TEP$		thermo-elasto-plastic
$THE_{ij}$	[-], [%]	thermal strain components (i,j=1÷3)
$T_{max}$	[K]	maximum reached temperature

## LIST OF SYMBOLS

---

$TRESC$	$[N \cdot m^{-2}]$	Tresca equivalent stress
$T_s$	$[K]$	surface temperature
$T_{tl}$	$[K]$	temperature of the end of microstructure transformation
$T_{tu}$	$[K]$	temperature of the beginning of microstructure transformation
$U$	$[V]$	voltage of the arc
$u_1, u_2, u_3$	$[m]$	translations in the $x$ -, $y$ - and $z$ -directions
$U_n, UR_n$	$[m], [rad]$	displacement components, including rotations at nodes
$u_x, u_y, u_z$	$[m]$	translational degrees of freedom
$v$	$[m \cdot s^{-1}]$	welding speed
$w$	$[kg \cdot m^{-1}]$	weight of the electrode consumed
$X$	$[m]$	$x$ -axis/welding direction
$x_n, y_n$	$[m]$	coordinates of the $n^{\text{th}}$ heat source
$Y$	$[m]$	$y$ -axis/transverse direction
$Z$	$[m]$	$z$ -axis/through thickness direction
$z'_m, z''_m$	$[m]$	coordinates of the beginning and the end of the $m^{\text{th}}$ section of the line heat source
$\Delta l$	$[m]$	length difference
$\Delta l$	$[m]$	shortening in a longitudinal direction
$\Delta T$	$[K]$	temperature difference
$\Delta t_{8/5}$	$[s]$	cooling time from 800 to 500 <sup>0</sup> C
$\Delta T_{max}$	$[K]$	largest temperature change per integration
$\Delta t_{max}$	$[s]$	maximum allowed time step
$\Delta t_r$	$[m]$	shortening in a transverse direction
$\Delta u_x, \Delta u_y, \Delta u_z$	$[m]$	expansion in $x$ -, $y$ - and $z$ -directions
$\Delta \phi_x, \Delta \phi_y$	$[rad]$	rotation of the plane around $x$ - and $y$ -axis
$EE$	$[-], [ \% ]$	elastic strain in ABAQUS specification
$IE$	$[-], [ \% ]$	inelastic strain in ABAQUS specification
$THE$	$[-], [ \% ]$	thermal strain in ABAQUS specification
$\alpha$	$[1/K]$	thermal expansion coefficient
$\alpha_1, \alpha_2$	$[J/m^2 \cdot s^{-1} \cdot K^{-1}]$	coefficient of convective heat transfer from the two surfaces
$\alpha_c$	$[J/m^2 \cdot s^{-1} \cdot K^{-1}]$	coefficient of convective heat transfer
$\alpha_m$	$[1/K]$	mean value of the thermal expansion coefficient
$\alpha_r$	$[J/m^2 \cdot s^{-1} \cdot K^{-1}]$	coefficient of radiation heat transfer
$\beta$	$[rad]$	angular shrinkage
$\varepsilon$	$[-], [ \% ]$	strain
$\dot{\varepsilon}$	$[s^{-1}]$	mechanical strain rate
$\varepsilon_1, \varepsilon_2, \varepsilon_3$	$[-], [ \% ]$	principal elongations
$\varepsilon^c$	$[-], [ \% ]$	creep strain in ABAQUS specification
$\varepsilon^e$	$[-], [ \% ]$	elastic strain
$\dot{\varepsilon}^{el}$	$[s^{-1}]$	elastic strain rate
$\varepsilon^{ep}$	$[-], [ \% ]$	elasto-plastic strain
$\varepsilon^i$	$[-], [ \% ]$	inelastic strain
$\varepsilon_i$	$[-], [ \% ]$	strain intensity
$\varepsilon_{ij} (i, j = 1 \div 3)$	$[-], [ \% ]$	components of the strain tensor
$\varepsilon^p$	$[-], [ \% ]$	plastic strain
$\dot{\varepsilon}^{pl}$	$[s^{-1}]$	plastic strain rate
$\varepsilon^p_x, \varepsilon^p_y, \varepsilon^p_z$	$[-], [ \% ]$	components of the plastic strain

---

## LIST OF SYMBOLS

---

$\varepsilon^T$	[-], [%]	thermal strain
$\varepsilon_{tr}$	[-], [%]	transformation strain
$\varepsilon_x, \varepsilon_y, \varepsilon_z$	[-], [%]	strain in $x$ -, $y$ - and $z$ -direction
$\eta$	[-]	arc efficiency coefficient
$\lambda$	$[\text{J}\cdot\text{m}^{-1}\cdot\text{s}^{-1}\cdot\text{K}^{-1}]$	thermal conductivity
$\mu$	[-]	friction coefficient
$\nu$	[-]	Poisson's ratio
$\pi$	[-]	Archimedes constant ( $\pi=3.14159$ )
$\theta$	[rad]	is groove angle
$\rho$	$[\text{kg}\cdot\text{m}^{-3}]$	density
$\sigma$	$[\text{N}\cdot\text{m}^{-2}]$	average pressure
$\sigma_1, \sigma_2, \sigma_3$	$[\text{N}\cdot\text{m}^{-2}]$	principal stresses
$\sigma_c$	$[\text{N}\cdot\text{m}^{-2}]$	compressive stress
$\sigma_c^*$	$[\text{N}\cdot\text{m}^{-2}]$	residual compressive stress after mechanical straightening
$\sigma_{contr}$	$[\text{N}\cdot\text{m}^{-2}]$	contraction stress
$\sigma_{contr}$	$[\text{N}\cdot\text{m}^{-2}]$	contraction stress
$\sigma_{cr}$	$[\text{N}\cdot\text{m}^{-2}]$	stress corresponding to a critical load for buckling initiation
$\sigma_{cr}$	$[\text{N}\cdot\text{m}^{-2}]$	critical load
$\sigma_h$	$[\text{N}\cdot\text{m}^{-2}]$	hydrostatic pressure
$\sigma_i$	$[\text{N}\cdot\text{m}^{-2}]$	stress intensity
$\sigma^I, \sigma^{II}, \sigma^{III}$	$[\text{N}\cdot\text{m}^{-2}]$	residual stress of first, second and third order
$\sigma_{ij} (i,j=1\div 3)$	$[\text{N}\cdot\text{m}^{-2}]$	components of the stress tensor
$\sigma_l$	$[\text{N}\cdot\text{m}^{-2}]$	weld-longitudinal stress
$\sigma_t$	$[\text{N}\cdot\text{m}^{-2}]$	tensile stress
$\sigma_t^*$	$[\text{N}\cdot\text{m}^{-2}]$	residual tensile stress after mechanical straightening
$\sigma_{tr}$	$[\text{N}\cdot\text{m}^{-2}]$	weld-transverse stress
$\sigma_x$	$[\text{N}\cdot\text{m}^{-2}]$	normal stress in $x$ -direction
$\sigma_x, \sigma_y, \sigma_z$	$[\text{N}\cdot\text{m}^{-2}]$	stress in $x$ -, $y$ - and $z$ -direction
$\sigma_Y$	$[\text{N}\cdot\text{m}^{-2}]$	yield stress
$\sigma_{Yw}$	$[\text{N}\cdot\text{m}^{-2}]$	yield stress of the seam

## CHAPTER I INTRODUCTION

### 1. EVOLUTION OF SHIPBUILDING

For hundreds and thousands years shipping has been established as one of the main methods of transportation. Shipping and shipbuilding has developed tremendously over these years. In place of small wooden cogs came almost a thousand meters long vessels made of high-strength steels.

Methods of fabrication change all the time. During the past century construction time for each ship has decreased from four years down to eight weeks. This tremendous progress became possible owing to the introduction of several important innovations. First of all, from the middle 1930s welding was introduced as a new method of joining in shipbuilding. It displaced poorer quality riveted joints. Together with the introduction of prefabrication techniques, it is accelerating ship production by approximately three times.

From the beginning, new techniques and materials introduce new problems as well. One of the most dramatic examples of it is a series of ships of the “Liberty” class. These all-welded vessels were produced in the 1940s in USA. Totally 2580 units were put to sea. Building of the first ship took 250 days. One of the following crafts was made in record-breaking time of 7 days, 14 hours and 23 minutes.<sup>1</sup>

But, unfortunately, these ships become famous not only because of their short production time. Several ships of the “Liberty” class broke in two pieces during service and sank, taking to the bottom their crew. Their problem was lack of experience in the new joining technique.

### 2. WELDING PROCESS AND WELDABILITY

A series of careful investigations concerning the nature of the welding process in shipbuilding have been conducted since that time.

The welding process causes a highly nonuniform heating of the parts being joined. Areas of the workpiece close to the welding arc are heated up to several thousand degree Celsius (depending on the welding process), and then subsequently cooled down, conducting the heat further to the bulk of the body. The local heating and subsequent cooling induce volumetric changes producing transient and residual stresses and deformation.

Welding stresses and deformations are closely related phenomena. During heating and cooling, thermal strains occur in the weld and adjacent areas. The strains produced during the heating stage of welding are always accompanied by plastic deformation of the metal. The stresses resulting from these strains combine and react to produce internal forces that cause a variety of welding distortions.

Residual deformations introduce severe problems in assembling of the welded structure and reduce its quality. Distorted shape and dimensions reduce the usefulness of the structure.

The above mentioned allows us to see the importance of stress and strain development modeling on the design and manufacturing stages. It is important for the estimation of the reliability of the structure, and development of suitable methods for improving the dimensional accuracy of the welded structure.

### **3. USE OF SUBMERGED ARC WELDING (SAW) IN SHIPBUILDING**

Welding in each shipyard is a key factor and it is directly related to production cost and quality. It represents 20-30% of production hours and approximately 10% of total cost.

Although the consumption of electrodes for submerged arc welding has decreased in the world from 10% in 1975 down to approximately 7% in 1996<sup>2</sup>, this process still plays an important role in shipbuilding.

Most of the small, and some medium-size shipyards, weld their flat panels on both sides, using conventional single-electrode SAW. The larger shipyards, producing larger flat panels, have developed the one-sided welding process. This process involves the use of several heat sources. Multi-electrode SAW first time was reported in the literature in the early 1950s.<sup>3,4</sup> This technique avoids the use of panel-turning devices. Furthermore, it gives a productivity increase of up to 50%.<sup>5,6</sup>

The main aim of the present dissertation is an investigation of the submerged arc welding procedures applied in the ship building industry. These processes are:

- one-sided three-electrode SAW with flux and copper backing (FCB);
- one-sided single-electrode SAW with multi-pass weld completion.

These welding process are used for butt welding of long plates. In such operations welding shrinkage is too large to be ignored. And, extra length should be considered in advance according to the prediction. This makes welding deformation and its prediction important factors.

### **4. AIM OF STUDY**

The aim of this study is to investigate transient and residual welding stresses and distortions in thick-walled ship hull structures, and give recommendations about mitigation techniques for reducing their negative influence on the welded structure efficiency.

To reach this aim we need to solve the following problems:

1. Based on analytical and numerical methods develop a simulation system for temperature fields during welding.

2. Develop a simulation system for thermo-mechanical welding processes taking into account the welding conditions during butt welding of thick-walled steel panels (three-electrode one-pass welding process and one-electrode multi-pass process).
3. Investigate the influence of the geometrical parameters on the transient and residual stress fields and deformation.
4. Investigate the influence of the welding technique (three-electrode one-pass welding process and one-electrode multi-pass process) parameters on the transient and residual stress fields and deformation.
5. Investigate the possibility to reduce residual stresses and distortions by means of thermal tensioning and mechanical straightening techniques.

**References**

- 
- 1 V. B. Zjinkin: "Theory and design of the ship", Sudostroenie, St-Petersburg, 1995, *Rus.*;
  - 2 L. Svensson, J. Elvander: "Challenges for welding consumables for the new millennium", Svetsaren, Vol. 54, No. 1-2, 1999, pp. 3-11;
  - 3 B. I. Medovar: "Two-arc automatic welding at high speeds", Avtogennoe Delo, 1950, Vol.11, pp. 20-23, *Rus.*;
  - 4 D. E. Knight: "Multiple electrode welding by "unionmelt" process", The Weld. J., Apr. 1954, pp. 303-312;
  - 5 R. Boekholt: "Welding mechanization and automation in shipbuilding worldwide", Abington Publishing, Cambridge, England, 1996;
  - 6 V. F. Sokolov: "Basics of shipbuilding engineering", Sudostroenie, St-Petersburg, 1995, *Rus.*;

## CHAPTER II STATE OF THE ART

### 1. THERMAL FIELDS

Most of the welding processes are based on a local heating of manufactured parts up to melting temperature and then cooling them down. The temperature distribution is highly nonuniform both in spatial co-ordinates and in time. This nonuniform heating is a reason causing a welded structure deformation.

A very important step towards resolving of any kind of deformation and stress problem in welding applications is to find the most appropriate resolution of the temperature distribution. Over the years many different scientific approaches to the solution of this problem were developed. Among those:

- a whole series of analytical models, from the simplest 1D solutions to complicated 3D models taking into account 3D heat source distribution and heat losses from work piece surfaces;
- finite differences analysis;
- finite element analysis (FEA).

Over the time the main techniques for solving heat transfer problems were changing with growing computer capacity. In the list introduced above the solutions are ranged in "chronological" order. The analytical solutions were introduced over 60 years ago.<sup>1,2,3,4,5,6,7</sup> Then about 30 years ago numerical methods (finite difference- and finite element analysis) were introduced as solutions for the heat transfer problems.<sup>8,9,10</sup> To be more precise, FDM was introduced to the welding applications in the early 60s. And the first published materials concerning FEA in welding made its appearance ten years later.<sup>11,12,13,14</sup> The part of the doctoral thesis of professor Ola Westby was the first publication concerning the use of FE method for mechanical problems in welding applications.<sup>15</sup> But FEA methods gained a wide acceptance only over the last decade.<sup>16,17,18,19</sup>

Analytic methods are capable of computing with reasonable accuracy temperature distributions in geometrically simple weldments.<sup>55</sup> The accuracy of the analysis is reasonably high in dealing with temperature changes in areas not so close to the welding arc. An advantage of this method is that it allows us to analyse the effect of the main factors: welding parameters, main dimensions of the work piece and material properties; and the computing time for solving the analytical models usually has range  $10^0 \div 10^2$  seconds. One of the main drawbacks of the analytical solution is that it does not give possibility to solve non-linear problems.

The use of finite difference methods is more a transition between analytical and finite element methods. The main advantage of the FD method is that it is rather simple and easily understandable physically (the variables are: temperature, time, and spatial co-ordinates; in contrast to some mathematical functional, involved in FEA solution).<sup>20</sup> But with this method approximation of curvilinear areas is quite complicated. In addition, the FD methods use uniform steps over the space co-ordinates (it is possible to avoid this but it also severely complicates the task).

Over the past 10 years the FE method has become the most popular and powerful technique of solving the heat transfer problems.<sup>21,22,23,24,25</sup> During these years, together with the powerful super computers, many different commercial programs based on FEA showed up on the market.<sup>26,27,28</sup> Now to create a very complicated model we do not have to write the long tangled programs manually. There are several commercial packages with user-friendly programming environment, with understandable graphical interfaces that are able to help the user to create the program just by some mouse clicks. But, of course, in order to obtain reliable results the user has to know what he is doing and understand the main principles and algorithms the program is based on. In FEM a structure is represented as an assembly of the finite elements. In the earliest developments of finite element methods all the attention was drawn to the development of effective finite elements for the solution of specific problems.<sup>29</sup> However, more general techniques were developed as soon as the great potential of the method was discovered.

**1.1. Basics of the heat transfer analysis**

**1.1.1. Heat sources- and geometry schematisation**

It is safe to assume that all electric energy of the arc converts into heat energy. But not all the energy is used for the heating of the electrode and base metal. A part of this energy goes to heat dissipation (losses to the surroundings, gas or flux heating, etc.). So, the effective energy of the welding arc can be expressed in this way:

$$Q = \eta UI \tag{eq. II-1}$$

where  $Q$  is the net heat input, [W];  $\eta$  is the arc efficiency coefficient;  $U$  is the voltage of the arc, [V];  $I$  is the current, [A].

The values of the arc efficiency coefficient for different welding processes are presented in *Table II-1*.

*Table II-1. Recommended arc efficiency factors for different welding processes.*<sup>30</sup>

Welding process	SAW, steel	SMAW, steel	GMAW, CO <sub>2</sub> -steel	GMAW, Ar-steel	GTAW, Ar-steel	GTAW, He-Al	GTAW, Ar-Al
$\eta$	0,91÷0,99	0,66÷0,85	0,75÷0,93	0,66÷0,70	0,25÷0,75	0,55÷0,80	0,22÷0,46

The heat source power density is also an important characteristic of the welding process. *Fig. II-1* illustrates how significantly different can be the action of the welding heat source. The curve for the flame is wide and low. In contrasted to it, the curve for the arc is narrow and high, and the curve for plasma, electron and laser beam welding is even higher and narrower. These facts form the basis for the heat source approximation principles. It helps us to choose what kind of model for the source we should take: the line, the point, or the arbitrary distributed heat source. It concerns both analytical and numerical solutions.

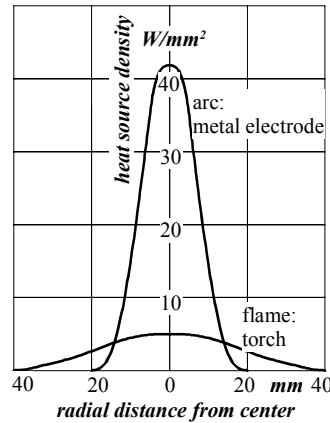


Fig. II-1. Heat source density for arc and flame welding with equal net heat output  $q=9.7kW$ .<sup>46</sup>

## 1.2. Basic equations

One of the basic equations of the heat transfer analysis is Fourier's law of heat conduction. It represents the heat flow density  $q_2$  [ $J \cdot m^{-2} \cdot s^{-1}$ ] in dependence on the temperature gradient  $\frac{\partial T}{\partial n}$  [ $K \cdot m^{-1}$ ]. In other words, it maps the fact that the heat propagates in a solid from the hot to the colder areas:

$$q_2 = -\lambda \frac{\partial T}{\partial n} \quad \text{eq. II-2}$$

where  $\lambda$  is the coefficient of thermal conductivity, [ $J \cdot m^{-1} \cdot s^{-1} \cdot K^{-1}$ ]. It should be mentioned that in reality this coefficient depends on the chemical composition, microstructural state and the temperature.

The next equation that should be mentioned as a main principle of heat transfer analysis is the field equation of heat conduction. Physically it associates the spatial and time dependent temperature distribution.

$$c\rho \frac{\partial T}{\partial t} = \frac{\partial}{\partial x} \left( \lambda_x \frac{\partial T}{\partial x} \right) + \frac{\partial}{\partial y} \left( \lambda_y \frac{\partial T}{\partial y} \right) + \frac{\partial}{\partial z} \left( \lambda_z \frac{\partial T}{\partial z} \right) + q_3 \quad \text{eq. II-3}$$

where  $c$  is the mass-specific heat capacity, [ $J \cdot kg^{-1} \cdot K^{-1}$ ];  $\rho$  is the material density, [ $kg \cdot m^{-3}$ ] and  $q_3$  is the volumetric density of the heat source, [ $W \cdot m^{-3}$ ].

This equation can be easily derived based on Fourier's law of heat conduction and the law of energy conservation.

Because in the general case the  $c\rho$ ,  $\lambda_x$ ,  $\lambda_y$  and  $\lambda_z$  characteristics depend on temperature, eq. II-3 itself is non-linear. The method of analytical solution forces us to ignore the temperature dependence of the above listed factors (the heat flow problems for welding applications are accessible to linearizations and simplifications without significant loss of accuracy). This assumption leads to a simpler linearized form of the field equation of heat conduction:

$$\frac{\partial T}{\partial t} = \frac{\lambda}{c\rho} \left( \frac{\partial^2 T}{\partial x^2} + \frac{\partial^2 T}{\partial y^2} + \frac{\partial^2 T}{\partial z^2} \right) + \frac{q_3}{c\rho} = a \nabla^2 T + \frac{q_3}{c\rho} \quad \text{eq. II-4}$$

where  $a = \lambda/c\rho$  is the thermal diffusivity, [m<sup>2</sup>·s].

### 1.3. Initial and boundary conditions

In order to formulate correctly the problem of heat conduction in a solid body we need to specify the initial- and boundary conditions. The initial condition for our type of problem consists of specifying the initial ( $t=0$ s) temperature distribution as function of spatial co-ordinates:  $T(x,y,z,0)$ . In the case of the welding applications the initial condition is usually isothermal:  $T(x,y,z,0)=T_0=const$ .

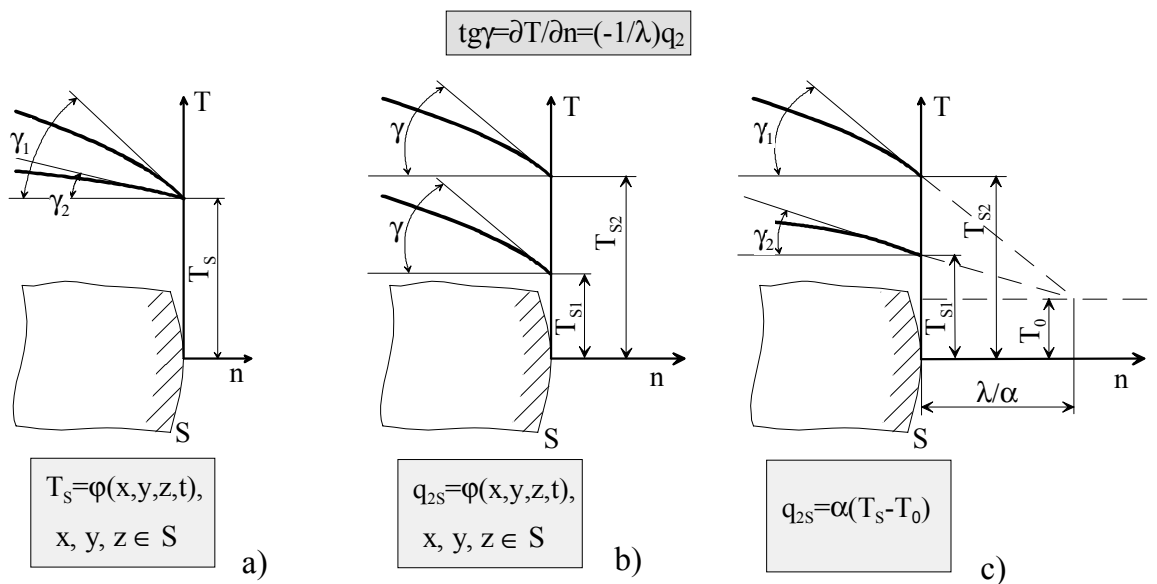


Fig. II-2. Three different types of boundary conditions employed in welding related heat transfer tasks; (a) "prescribed surface temperature" condition; (b) "prescribed heat source density" condition; (c) Newton's law of heat interaction.

The boundary condition represents the law of the interaction of the work piece surfaces with the surroundings. In the problems concerning welding the three types of boundary conditions are usually involved:<sup>31</sup>

- prescribed temperature of the surface;
- prescribed density of the heat source distributed over the surface as a function of time;
- prescribed density of the heat source distributed over the surface as a function of the surface- and ambient temperature.

The first type of the boundary condition is graphically represented by *Fig. II-2.a*. It illustrates that no matter what kind of temperature distribution is inside of the body, the nodes belonging to the surfaces are forced to have temperature  $T_S$ . In practice a specific case can be the process of underwater welding, when the most of the work piece surface has the temperature of the surrounding water.

The prescribed heat flow through the surface is illustrated in *Fig. II-2.b*. This condition forces the tangents to the temperature distribution at the surface to have a certain value. This value is invariant with the temperature distribution inside the body. With this condition, for example, a heat source distributed over some part of the surface can be introduced into the model. A special case of this type of the condition is the adiabatic boundary condition. The adiabatic boundary is widely used especially in simplified analytical approaches. The use of this kind of condition is a fair approximation if the isotherms are more or less perpendicular to the surface considered ( $(\partial T/\partial n)_S=0$ ).

The third type of the boundary condition is also called heating/cooling by Newton's law. The graphical representation of this law is shown in *Fig. II-2.c*. The tangents to the temperature distribution at the surface are forced to cross each other at a certain distance from the surface. This fact can be explaining using Fourier's law of heat conduction. The mathematical formulation in *Fig. II-2.c* can be rewritten in this way:

$$-\lambda \left( \frac{\partial T}{\partial n} \right)_S = \alpha (T_S - T_0) \quad \text{eq. II-5}$$

Newton's law assumes the heat source/sink density over the body surface to be proportional to the difference between surface temperature  $T_S$  and the ambient temperature  $T_0$  through the heat transfer coefficient  $\alpha$ . This coefficient can be presented as a sum of the convective,  $\alpha_c$ , and the radiation,  $\alpha_r$ , heat transfer coefficients. The values of  $\alpha_c$  for various heat exchange conditions and materials can be found in the reference literature. Meanwhile, the radiation heat transfer coefficient is usually not listed. But it can be calculated as  $\alpha_r=C(T_S+T_0)(T_S^2+T_0^2)$ , where  $C$  is Stefan-Boltzmann's coefficient. This coefficient in its turn is available in the most of the reference books on the heat transfer subjects.

#### **1.4. Conclusions**

In this section the development of heat flow analysis in welding applications is evaluated. The main principles and simplifications are introduced. The following conclusions can be drawn:

1. Together with growing computer capacity the heat flow simulation methods have developed over the past 60 years from simple analytical solutions to highly non-linear three dimensional finite element models.
2. The heat flow problems for welding applications are accessible to linearization and simplifications without significant loss of accuracy.

## 2. WELDING STRESS FIELDS AND STRUCTURE DISTORTION ANALYSIS

### 2.1. Theory of plasticity, main conventional principles

#### 2.1.1. Stress-strain behaviour of the metallic materials

A simple tension or compression test reveals the so-called true stress-strain curve (true stress  $\sigma$  is plotted against natural strain  $\epsilon$ ). True stress, defined as a load divided by the current cross-sectional area of a specimen, can be substantially different from the nominal stress (load per unit initial area of cross-section). If we assign  $l$  to be the current specimen length and  $dl$  the increase of the length produced by small increment of stress, then the true strain gets an increment  $d\epsilon=dl/l$ . If the initial length is  $l_0$ , the total strain  $\epsilon=\ln(l/l_0)$  is called the true or natural strain. Another quantity is the engineering strain  $e$ . It is the amount of extension or contraction per unit original length. The natural strain can be expressed in terms of engineering strain as  $\epsilon=\ln(1+e)$  for the case of tension, and  $\epsilon=-\ln(1-e)$  for the case of compression. Thus,  $\epsilon$  becomes progressively lower than  $e$  in tension and higher than  $e$  in compression, as the plastic deformation develops.

Fig. II-3 represents a typical true stress-strain curve for steel for the case of simple tensioning. While the stress is relatively small, the material behaves elastically. The initial part of the stress-strain curve is a straight line with a slope  $E$  (Young's modulus). After stretching the specimen further than point A, representing the limit of proportionality, plastic deformation occurs.

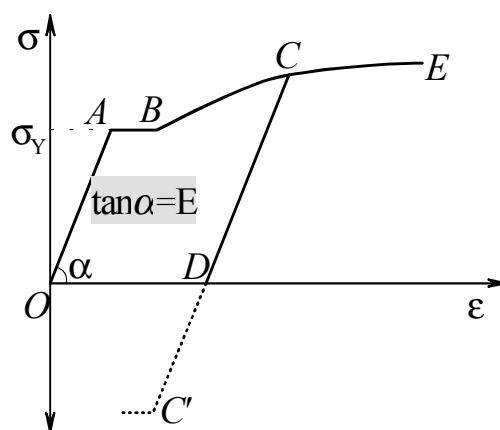


Fig. II-3. True stress-strain curve.<sup>32,33</sup>

The segment AB represents the condition of the metal when dislocations start to move freely until they reach the grain boundary.<sup>34,35,36</sup> It is typical for ductile materials. This stage of material “flowing” is quite insignificant and often omitted by authors. Beyond the yield point, the stress continuously increases with further plastic strain. The slope of the stress-strain curve steadily decreases with increasing stress. If the loading is released

at the point C, there is an elastic recovery CD with a slope quite close to E. At that point the specimen has accumulated a plastic strain equal to OD.

If the specimen is being stretched further from the point D, the deformation follows the path DCE (at least very close to this trajectory). It is evident that in this case the material has an extended area of elastic deformation (higher value of  $\sigma_Y^C > \sigma_Y$ ). This phenomenon is called "work hardening".

If, from the point D, the specimen is being reloaded in simple compression along the path DC', then the new yield point C' corresponds to a stress that is significantly smaller than at point C ( $\sigma_Y^C > \sigma_Y^{C'}$ ). This phenomenon is known as Bauschinger effect. The lowering of the yield stress during reversed loading is caused mainly by residual stress left on a microscopic level (different stress states in the different grains). This Bauschinger effect can play an important part in the case of cyclic alternating loading with high amplitude of the load.

### 2.1.2. Prerequisites of the deformation theory

The main characteristics of the stress-strained condition of a body under loading are:<sup>37</sup>

- stress tensor;
- strain tensor;
- offset vector.

The stress tensor  $\sigma_{ij}$  is a matrix of nine components:

$$\sigma_{ij} = \begin{vmatrix} \sigma_{xx} & \sigma_{xy} & \sigma_{xz} \\ \sigma_{yx} & \sigma_{yy} & \sigma_{yz} \\ \sigma_{zx} & \sigma_{zy} & \sigma_{zz} \end{vmatrix}$$

where  $i=x, y, z$  determines the perpendicular to the plane of the elementary volume around the point under consideration;  $j=x, y, z$  – the direction of the stress application at the plane  $i$ .

The assumption about stress tensor symmetry is used. In terms of stress tensor components it can be written as  $\sigma_{xy} = \sigma_{yx}$ ,  $\sigma_{xz} = \sigma_{zx}$ , etc. By this means, the stressed condition of the body can generally be characterised by six components of the stress tensor  $\sigma_{ij}$ . The components that have indexes  $i=j$  ( $\sigma_{xx}$ ,  $\sigma_{yy}$ ,  $\sigma_{zz}$ ) are called normal stresses. The components with  $i \neq j$  ( $\sigma_{xy}$ ,  $\sigma_{xz}$ ,  $\sigma_{yz}$ ) are called shearing stresses.

It is possible to decompose the stress tensor down to a spherical tensor  $\delta_{ij} \cdot \sigma$  and a deviator  $S_{ij}$ :

$$\delta_{ij} \cdot \sigma = \begin{vmatrix} \sigma & 0 & 0 \\ 0 & \sigma & 0 \\ 0 & 0 & \sigma \end{vmatrix}$$

where  $\sigma = 1/3(\sigma_{xx} + \sigma_{yy} + \sigma_{zz})$  is the average pressure at the point considered;

$$S_{ij} = \sigma_{ij} - \delta_{ij} \cdot \sigma = \begin{vmatrix} \sigma_{xx} - \sigma & \sigma_{xy} & \sigma_{xz} \\ \sigma_{yx} & \sigma_{yy} - \sigma & \sigma_{yz} \\ \sigma_{zx} & \sigma_{zy} & \sigma_{zz} - \sigma \end{vmatrix}$$

The strain tensor by analogy is given by:

$$\epsilon_{ij} = \begin{vmatrix} \epsilon_{xx} & \epsilon_{xy} & \epsilon_{xz} \\ \epsilon_{yx} & \epsilon_{yy} & \epsilon_{yz} \\ \epsilon_{zx} & \epsilon_{zy} & \epsilon_{zz} \end{vmatrix}$$

The assumption about strain tensor symmetry is also used and the spherical tensor  $\delta_{ij} \cdot \epsilon$  and deviator  $e_{ij}$  is introduced by analogy.

For any point of the body under consideration, the components of the tensors  $\sigma_{ij}$  and  $\epsilon_{ij}$  introduced above depend on a chosen co-ordinate system. Still, the tensors  $\sigma_{ij}$ ,  $\epsilon_{ij}$  and  $S_{ij}$ ,  $e_{ij}$  have characteristics (invariant) that do not change with a new co-ordinate system. The most useful characteristics are:

1. average pressure  $\sigma$ ;
2. volumetric expansion  $3\epsilon = \epsilon_{xx} + \epsilon_{yy} + \epsilon_{zz}$ ;
3. equivalent stress  $\sigma_i = \frac{1}{\sqrt{2}} \sqrt{(\sigma_{xx} - \sigma_{yy})^2 + (\sigma_{xx} - \sigma_{zz})^2 + (\sigma_{yy} - \sigma_{zz})^2 + 6(\sigma_{xy}^2 + \sigma_{xz}^2 + \sigma_{yz}^2)}$
4. strain intensity

$$\epsilon_i = \frac{\sqrt{2}}{3} \sqrt{(\epsilon_{xx} - \epsilon_{yy})^2 + (\epsilon_{xx} - \epsilon_{zz})^2 + (\epsilon_{yy} - \epsilon_{zz})^2 + 6(\epsilon_{xy}^2 + \epsilon_{xz}^2 + \epsilon_{yz}^2)}$$

For any point in the body there exist three mutually perpendicular planes at which the tangential strains and stresses equal to zero. The directions of the normals to these planes generate the main directions of the stress- and strain tensors. These directions do not depend on the selection of the initial co-ordinate system. It means that any stressed state can be represented as a combination of a simple compression (stretching) in three mutually perpendicular directions. The corresponding stresses  $\sigma_1$ ,  $\sigma_2$ ,  $\sigma_3$  are called the principal stresses, and the strains  $\epsilon_1$ ,  $\epsilon_2$ ,  $\epsilon_3$  are called the principal elongations.

To create a complete phenomenological model of the deformation process it is not enough to know the concepts introduced above. A theory about stress-strain interaction is needed. The introduction of such theory in a general form is a very complicated task. The use of several simplifications and assumptions is widely accepted. One approach is based on the assumption that the deformation at any point of the body can be represented by the sum:

$$\epsilon_{ij} = \epsilon_{ij}^e + \epsilon_{ij}^p + \epsilon_{ij}^c, \quad (\text{thermal stress is excluded})$$

where indexes  $e$ ,  $p$  and  $c$  mark the elastic-, plastic- and diffusive plastic deformation components. Subdivision of the deformation into the three components agrees with the modern concepts of microscopic conceptions on the deformation mechanism of the polycrystalline material. By these notions, the elastic deformation of the metallic specimen is a result of *recoverable* distortion of the lattice. It can be caused by the temperature or the stress change.

*Irrecoverable* (plastic) deformation occurs only in the case of certain combinations of the time, temperature and the stress patterns. In most cases, the deformation of the metals is caused by a shear mechanism, i.e. determined by the shear stress values.

### 2.1.3. Elastic deformation

Linkage between the stress- and deformation tensors can be based on a classical understanding of the linearly elastic material. The law determining the dependence between stress and deformation in a linearly elastic material was formulated by Robert Hooke in 1678: the elongation is proportional to the force.

The modern formulation of this law is slightly more extended: for any point of the deformed body, the components of the elastic strain tensor linearly depend on the components of the stress tensor. In a general case, the matrix of elastic properties contains of 36 components. At the same time, from the elastic properties point of view, the majority of the materials can be considered as practically isotropic materials. This fact allows reducing the number of coefficients down to two. These are: module of normal elasticity  $E$  and shear modulus  $G$ . They are related to each other this way:  $E/G=2(1+\nu)$ , where  $\nu$  is the Poisson's coefficient.

### 2.1.4. Plastic deformation. The criterion of yielding

Let us consider the situation when the body is subjected to a load. The initial deformation of the body is entirely elastic (after load removal the body returns to its initial undeformed shape). For a certain critical combination of the applied stresses plastic deformation first appears in the body. A law defining the limit of elastic behaviour is called a yield criterion.<sup>38</sup> In developing a mathematical theory of the yielding criterion, it is necessary to introduce several idealisations:

- the influence of the strain rate and thermal effects is negligible;
- the Bauschinger effect and hysteresis loop are disregarded;
- the material is isotropic.

The experimental facts show that yielding is unaffected by uniform hydrostatic tension or compression. This phenomenon allows us to introduce important simplifications into the yielding criterion definition.

Let us consider a system of three mutually perpendicular axes with the principal stress along each co-ordinate direction (see Fig. II-4). A vector going from the origin may represent the state of the stress of any point of the body. The line  $OP$  is equally inclined to the three axes. Let us consider a vector  $OA$  that represents some stressed condition. This vector can be subdivided into two components. Component  $OH$  going along  $OP$  represents the *hydrostatic stress* with equal components  $(\sigma, \sigma, \sigma)$ . Component  $OD$  going perpendicular to the direction  $OP$  represents the *deviatoric stress* with components  $(s_1, s_2, s_3)$ . For any given state of stress, the deviatoric stress vector will lie in the plane passing through  $O$  and perpendicular to  $OP$ . This plane called the *deviatoric plane*. As stated above, the hydrostatic stress has no affect on yielding. So, yielding can depend only on the characteristics of the deviatoric stress vector  $OP$ . The yield surface is therefore a cylinder with generators perpendicular to the deviatoric plane. Any stress state in which the stress point lies on the surface of this cylinder, corresponds to the state of yielding. Any stress point that lies inside of this cylinder corresponds to the elastic state of stress. The curve  $L$  along which the yielding surface is intersected by the deviatoric plane represents the yielding criterion.

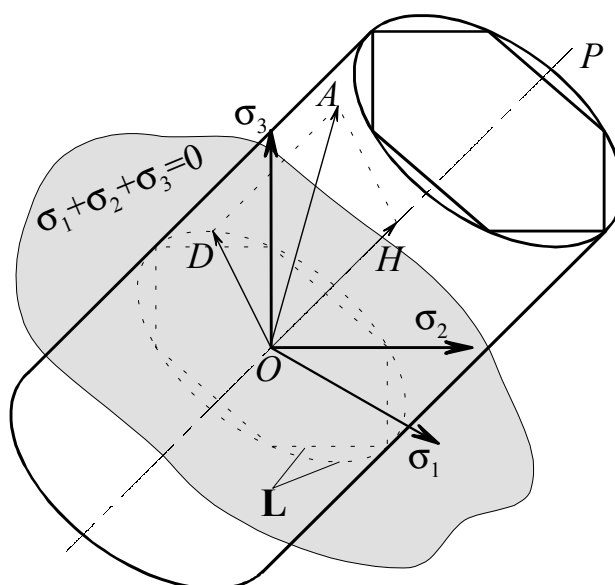


Fig. II-4. Geometrical representation of the yield criterion in the principal stress space.<sup>36,39,40</sup>

Yielding in isotropic materials depends only on the values of the principal stresses and not on their directions. Thus, if the stress  $(\sigma_1, \sigma_2, \sigma_3)$  cause yielding, so will the stress  $(\sigma_1, \sigma_3, \sigma_2)$ . It means that the yield locus is symmetrical about the projected  $\sigma_1$  axis. Similarly, the yield locus is symmetrical about the projected  $\sigma_2$  and  $\sigma_3$  axes.

It was mentioned above that we neglect the Bauschinger effect. Thus if  $(\sigma_1, \sigma_2, \sigma_3)$  is a plastic state,  $(-\sigma_1, -\sigma_2, -\sigma_3)$  is a plastic state as well.

The two above-mentioned facts allow us to conclude that the yield locus is repeated over the twelve  $30^\circ$  segments as shown in Fig. II-5.

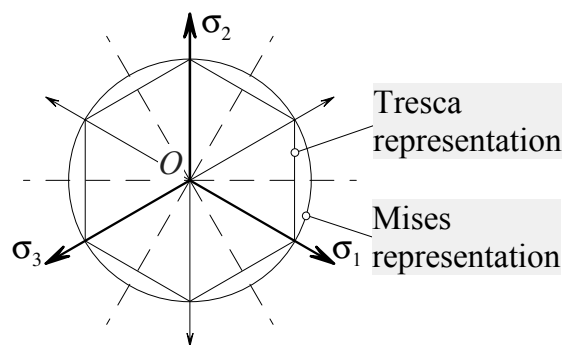


Fig. II-5. Deviatoric yield locus having six axes of symmetry.

A great number of different yielding criteria have been suggested over the years.<sup>41,42,43</sup> At present, the yielding criteria of Tresca and von Mises are the most widely used. In Fig. II-5 a graphical representation of these two criteria is shown.

### 2.1.5. Strain hardening

It has been demonstrated that a material starts to yield as soon as the deviatoric stress vector reaches the yield locus. If the material is non-hardening, the stress point always lies on a constant yield locus. For a strain-hardening material, the size and shape of the yield locus depends on the total history of deformation. For simplification, two approaches to describe the way a material yields are:<sup>36</sup>

- isotropic hardening;
- kinematic (anisotropic) hardening.

Isotropic hardening theory is based on these assumptions: the material is isotropic and the Bauschinger effect is neglected. Later on it is assumed that the yield surface expands without change in shape.

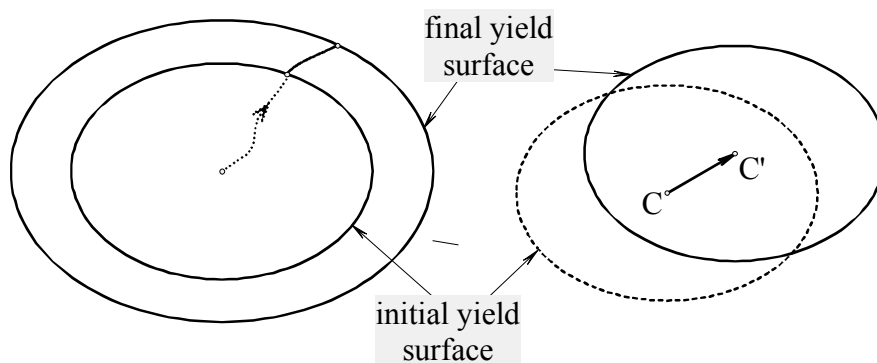


Fig. II-6. Schematic representation of the isotropic and kinematic hardening rules.<sup>39</sup>

Kinematic hardening theory takes into account the Bauschinger effect and considers the material as a nonisotropic continuum. The yield surface is assumed to undergo translation in nine-dimensional stress space. In reality the hardening process involves simultaneous translation and expansion of the yield surface, combining the approaches described above .

### 2.1.6. Conclusions

In this section the main principles of the theory of plasticity relevant to welding applications are reviewed. The metallic material behaviour under loading is specified. The following conclusions can be drawn:

1. The behaviour of the metallic material during deformation is highly non-linear.
2. In mechanical models the number of variables and governing equations is significantly higher than heat flow analysis.
3. Even a highly advanced 3D model is only an approximation to the very complicated nature of the deformation process.
4. At present there exist several non-related theories concerning the stress-strain behaviour of the deforming body.

## 2.2. Welding stresses and deformations

### 2.2.1. Classification of welding stresses and deformations

Stresses arising during the welding process are referred to as internal or locked-in stresses.<sup>44,45</sup> Internal stresses are those which exist in a body without external forces applied. This kind of stresses usually arise in details or structures during processing. For example, these stresses develop in details subjected to cutting, grinding, bending or many other types of metal-working. A bolted joint, where the bolt body is stretched and the joined pieces are compressed, is also an example of internal stresses equilibrium.

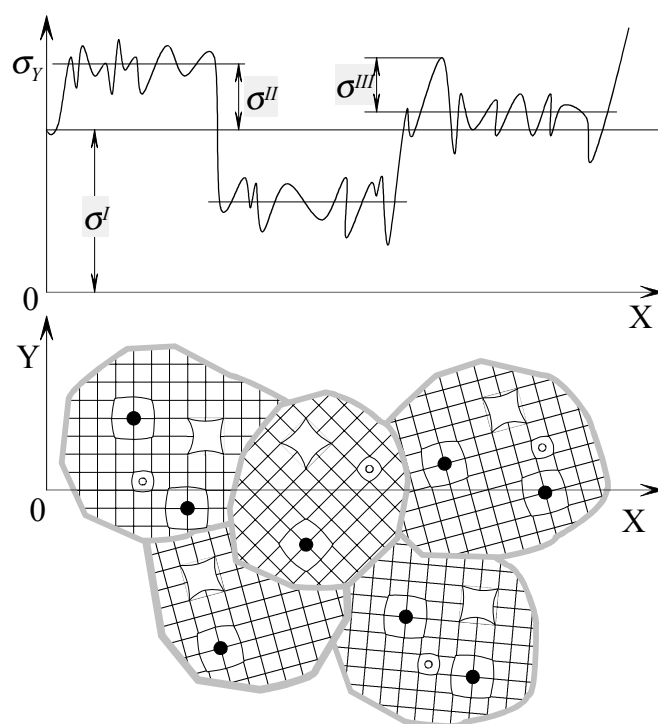


Fig. II-7. First, second and third order residual stresses ( $\sigma^I$ ,  $\sigma^{II}$ ,  $\sigma^{III}$ ) acting in  $y$ -direction (defects – foreign substitutional atom; Frenkel defect (vacancy and interstitial atom)). Adopted from Radaj.<sup>44</sup>

Internal stresses also subdivide into macro- and micro-stresses (first, second, and third order, see Fig. II-7). First order residual stress,  $\sigma^I$ , extend over macroscopic areas and is the averaged stress over a volume with several material grains. Second order residual stress,  $\sigma^{II}$ , acts between adjacent grains. It is averaged within each grain. Third order residual stress,  $\sigma^{III}$ , acts on the interatomic level. It is a kind of deviation from the averaged  $\sigma^I$ , caused by different impurities of the atomic lattice (examples shown in Fig. II-7 are: foreign substitutional atom; Frenkel defect (vacancy and interstitial atom)).

First order residual stresses are in equilibrium with themselves within the limits of the structure or structural element, and an isotropic material formulation is usually suitable for the determination of such stresses. Micro-stresses do change significantly over the grain. They depend on crystal anisotropy.

In evaluating the influence of the internal stresses on a deformation process, attention should be paid to the macro-stresses. The usual stresses caused by an external force are macro-stresses. And welding stresses are also rank among those.

As mentioned before, internal stresses are in a self-equilibrium state. Hence, independently of the stress distribution in the body, the stresses in any cross-section should be balanced by the sum of the forces and the sum of the moments of forces. In particular, in any plane perpendicular to the  $x$ -axis, should be:

$$\int_A \sigma_x \cdot dA = 0; \quad \int_A \sigma_x \cdot y \cdot dA = 0; \quad \int_A \sigma_x \cdot z \cdot dA = 0, \quad \text{eq. II-6}$$

where  $\sigma_x$  is the normal stress in the point with co-ordinates  $(y, z)$  in the cross-section area  $A$ .

Welding stresses can be classified by these characteristics:

1. *lifetime*;
2. *direction*;
3. *origin of*.

According to the first characteristic, welding stresses can be temporary or residual. The temporary stresses do exist only in a specific moment of the non-stationary process of heating and cooling the detail. The residual stresses can be found after the whole process of welding is completed and structure is cooled down to the room temperature.

Directionally the welding stresses subdivide into longitudinal (parallel to the welding direction) and transversal (perpendicular to the weld seam).

By origins the welding stresses are subdivided into:<sup>46</sup>

- thermal stress (caused by nonuniform temperature distribution);
- stresses caused by the plastic deformation of the metal;
- stresses caused by phase transformations.

Thermal stresses vanish after temperature equalisation. Phase-transformation stresses may appear during welding of some alloyed steels. In processing low-alloyed structural steels, phase transformation occurs at elevated temperatures. The material, being soft, accommodates volume change caused by phase transformation without significant change in the stress development process. Stresses caused by plastic deformation almost always exist in the areas close to the weld and weld seam itself.

In classifying *welding deformations*, it should be mentioned that this term covers not only the strain at various points, but also the integral characteristics, such as deflection, angular displacement and change in linear dimensions.

As in the case of stresses, welding deformations can be temporary or residual. Three fundamental dimensional changes of the welded plate are:

- transverse shrinkage;
- longitudinal shrinkage;
- angular distortion (rotation around the weld line).

From a more detailed point of view, the welding deformations (in other terms – "shrinkage", "distortion" or "warpage") can be classified as:

- transverse shrinkage – shrinkage perpendicular to the weld centreline;
- longitudinal shrinkage – shrinkage in the direction of the weld line;
- angular distortion – distortion caused by nonuniform temperature distribution in the through-thickness direction;
- rotational distortion – angular distortion in the plane of the plate due to thermal expansion or contraction;
- bending distortion – distortion in a plane through the weld line and perpendicular to the plate;
- buckling – distortion caused by compressive stresses inducing instability when the plates are thin.

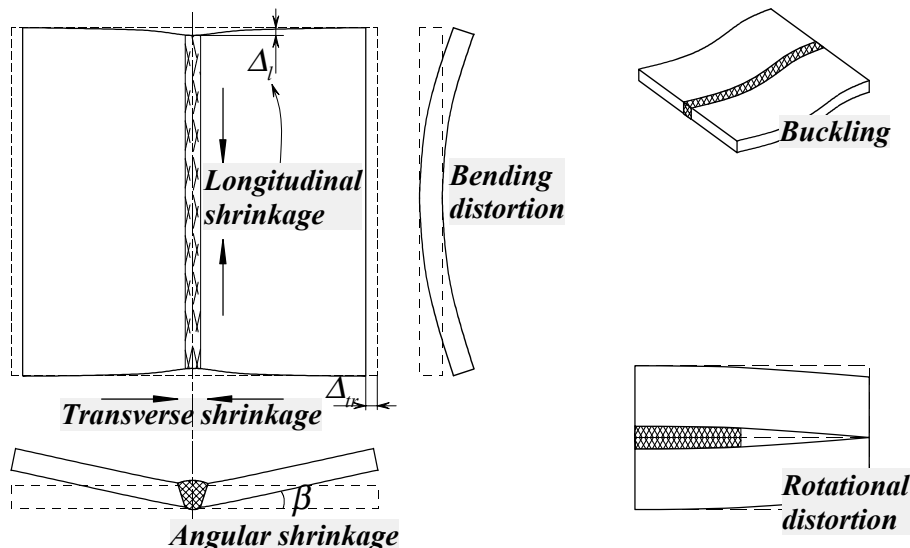


Fig. II-8 Various types of welding distortion.

### 2.2.2. Causes of welding stresses and deformations

The welding process causes a highly nonuniform heating of the parts being joined. Areas close to the weld arc are heated up to several thousands degrees Celsius, and then cooled down, the heat being conducted to the bulk of the body. The local heating and subsequent cooling induces volumetric changes producing temporary and residual stresses and deformation.

Let us consider the body to be composed of many equal small cubic elements. The process of heating these elements evenly will lead all the elements to uniform expansion in all spatial directions. Hence, all the elements will have the same size. It is possible to join these cubes and get a solid body, and no stresses will be induced in the body. But, if the heating is nonuniform, then each element tries to expand proportionally to the temperature rise  $\Delta T$  in this element. In this situation the elements have different size, and it is not possible to join such cubes into one solid body. At the same time, the body is continuous and each element restrains the free expansion of the neighbouring elements. As a result stress is build up. The neighbours expanding differently act on the element in a different way. As a result of this, the lengths of the element edges change to a different degree, and angles at the vertices vary as well.

In other words, we get complex stresses both in the element and in the body. If, during heating, all the elements were stressed elastically, then, after cooling, the body will return to its initial stress-free condition.

If, during heating, the element was deformed plastically, then, after cooling, it tends to change dimensions proportionally to the amount of the plastic deformation. All the elements now have different size and cannot be reassembled into a solid body without some changes in their stress- and deformation state. As a result, residual stresses and deformation form in the body.

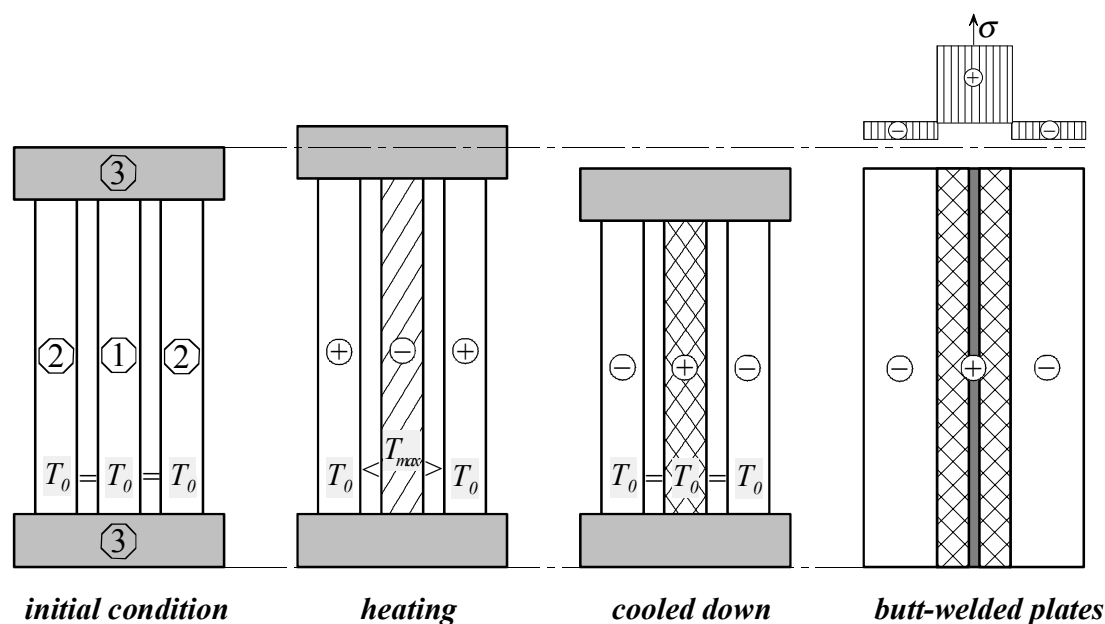


Fig. II-9. Three-rods system constrained by rigid bases, and a butt-welded plate simulated by the three-rod system.

In general, the non-uniformity of the temperature distribution during welding of a real structure causes a complex three-axial stress. In other words, the cubes expand differently in all three directions. But, in most cases some components of the stress are negligible, and it is possible to consider 2D or even 1D stressed states.

A simple model that can help to understand the process of 1D-stress formation is presented in *Fig. II-9*. The model consists of one central rod 1 and two limiting rods 2, joined with each other by the rigid plates 3.<sup>47</sup> At any instant of time the rods have the same length. The central rod being exposed to a high temperature simulates the zone close to the weld. The limiting rods are kept at a constant temperature, representing the rest of the joining plates.

Heating the central rod up to some temperature  $T_{max}$  will try to expand it by  $\Delta l = \alpha \cdot T_{max} \cdot l$  (where  $l$  is the initial length of the rod). The limiting rods do not allow a free expansion of the central one, causing rising compression stresses in it. If the central rod has been compressed elastically, then, after cooling, the system comes to its initial stress- and deformation-free state. But, if during heating the central rod was compressed plastically, then a plastic compressive strain is introduced into the rod. During the cooling stage the central rod tends to contract while the limiting rods are trying to keep their initial length. Hence, in the central rod (the zone close to the weld) tensile stress arises, whereas the limiting rods (the rest of the plate) are being subjected to compressive stress.

### 2.2.3. Transient stress field

During welding the process of stress-strain field development is characterised by the elastic-plastic behaviour of the metal, non-stationary temperature conditions with a high temperature limit (up to several thousands °C), and very high temperature gradients (locally of the order of  $10^3$  °C/mm). The transient and residual stress development is based on volumetric change of the structure elements. With the heat propagating through the body and the temperature equalisation, the metal redistribution continues.

Kinetics of the stress field during welding is a process of stress development lasting the whole period of welding and subsequent cooling. The stress kinetics investigation is quite a complicated task because of the huge amount of variables affecting the process. At the same time, the physical nature of the stress development process can be evaluated by means of quite simple examples.

#### 2.2.3.1 Longitudinal stress development during the welding process

As a starting point a typical thermal cycle can be taken (*Fig. II-10*, low right corner). To monitor the stress development at a point, an elementary volume element should be chosen.

Let us consider the case of thin plate welding (the through-thickness temperature gradient is negligible). The elementary element can be chosen as shown in *Fig. II-10*. The temperature inside of the prism can be considered to be constant because the volume of the element is small.

Usually, a welded structure is stiff enough to keep the total deformation along the welding direction (in our case -  $\epsilon_x$ ) significantly smaller than the unrestrained thermal

deformation  $\epsilon^T$ . This state is true for the elements situated close to the weld seam. That is why it is normal to assume that the prism does not change its dimensions in the  $x$ -direction (as shown in Fig. II-10). At the same time, during the heating and cooling stages, longitudinal stresses  $\sigma_x$  develop in the elements.

For simplification let us consider the 1D-stressed case, and assume  $\sigma_y$  to be equal to zero (in the  $y$ -direction the element can be deformed stress-free). Summarising, in the longitudinal direction  $\sigma_x \neq 0$ ,  $\epsilon_x = 0$ , but in the transverse direction  $\sigma_y = 0$ ,  $\epsilon_y \neq 0$ .

To analyse the stress-cycles in the elements, data about the metal volume expansion due to the elevated temperatures (the dilatometric curve) and curves of material deformation (the stress-strain curves) are needed. Neglecting the structural changes in the material, the dilatometric curve can be approximated as a straight line (the thermal expansion coefficient  $\alpha$  is constant).

The set of stress-strain curves can, as a first approximation, be substituted by an idealised stress-strain curve (as shown in the upper left corner in Fig. II-10). To systematise the analysis, the curve is scaled so that the elastic part of the curve would form  $45^\circ$  to the  $\epsilon^{ep}$ -axis (the elastic deformation and the corresponding stress are presented by the same length on the diagram).

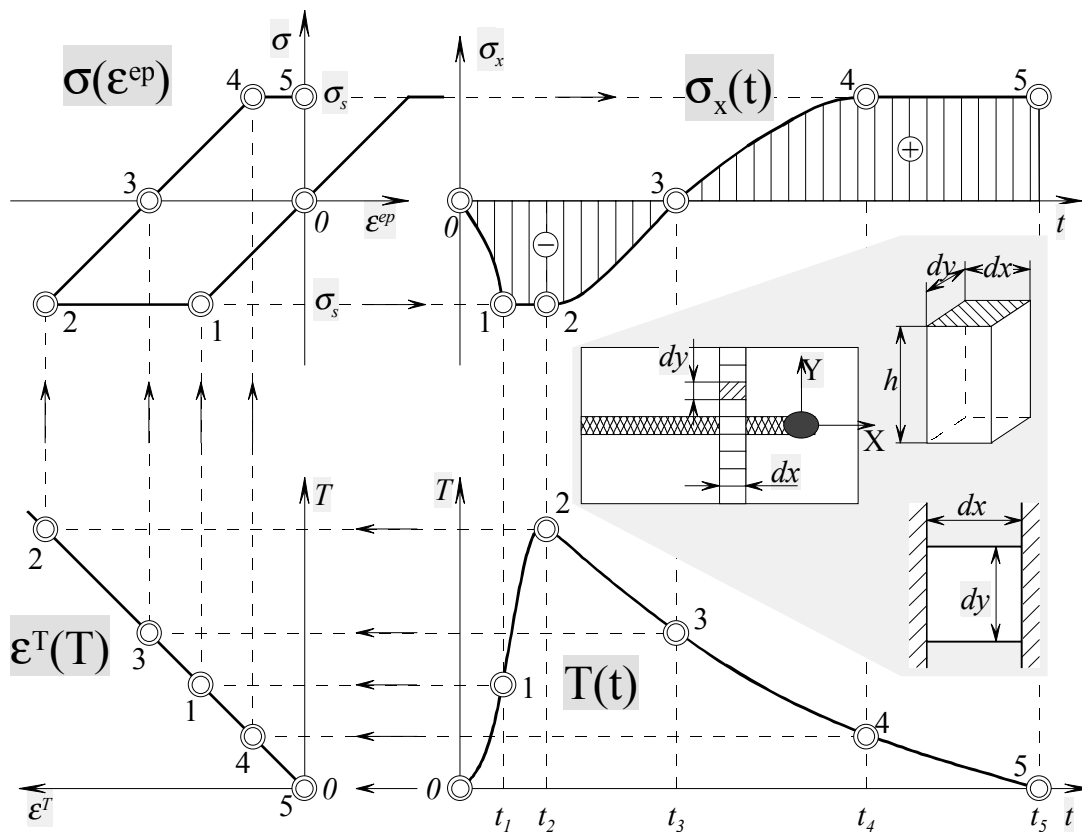


Fig. II-10. Kinetics of the stress in a prismatic solid.

The dilatometric curve  $\varepsilon^T(T)$  is placed under the stress-strain diagram  $\sigma(\varepsilon^{ep})$ . The thermal cycle  $T(t)$  is placed to the right of the  $\varepsilon^T(T)$ . All the scales are kept co-ordinated. Now, the stress-cycle  $\sigma_x(t)$  can be plotted following the tracings in *Fig. II-10* shown by the arrows.

For example, at the time  $t_1$  the temperature  $T_1$  is characterised by the point *I*. From this point a horizontal line, characterising the thermal expansion corresponding to  $T_1$ , will determine the point *I* on the dilatometric curve. For the case of a rigid prism in the  $x$ -direction, the  $\varepsilon^T_1$  will determine the free (confined) thermal expansion. Extending vertically up onto the  $\sigma(\varepsilon^{ep})$  diagram, another point *I* is obtained. This point is characterised by  $\sigma_x$  and  $\varepsilon^e_x$  at  $t_1$  and coincident with the moment in time when the  $\sigma_x$  reaches the yielding limit  $\sigma_y$ .

Now the required point *I* on the stress-curve can be found by the intersection of the perpendiculars from the thermal cycle and the stress-strain curve. In the same manner the rest of the points characterising the stress-cycle can be found. The point 2 corresponds to the maximum temperature on the thermal cycle and the maximum of the plastic compressive strain.

After  $t_2$  the cooling process and, hence, the unloading start and last until  $t_3$ . At  $t_3$  the elastic stress and strain are both equal to zero. From  $t_3$  until  $t_4$  the elastic tensile strain is growing. At  $t_4$  the second plastic (but of the opposite sign) deformation begins. The time  $t_5$  corresponds to the completely cooled down state.

*Fig. II-11* gives a schematic representation of the temperature and the resulting longitudinal stress distributions that occur during welding. In this example a simple bead-on-plate case is analysed (see *Fig. II-11.a*). The welding arc, which is moving along the  $x$ -axis with a speed  $v$ , is indicated by the arrow.

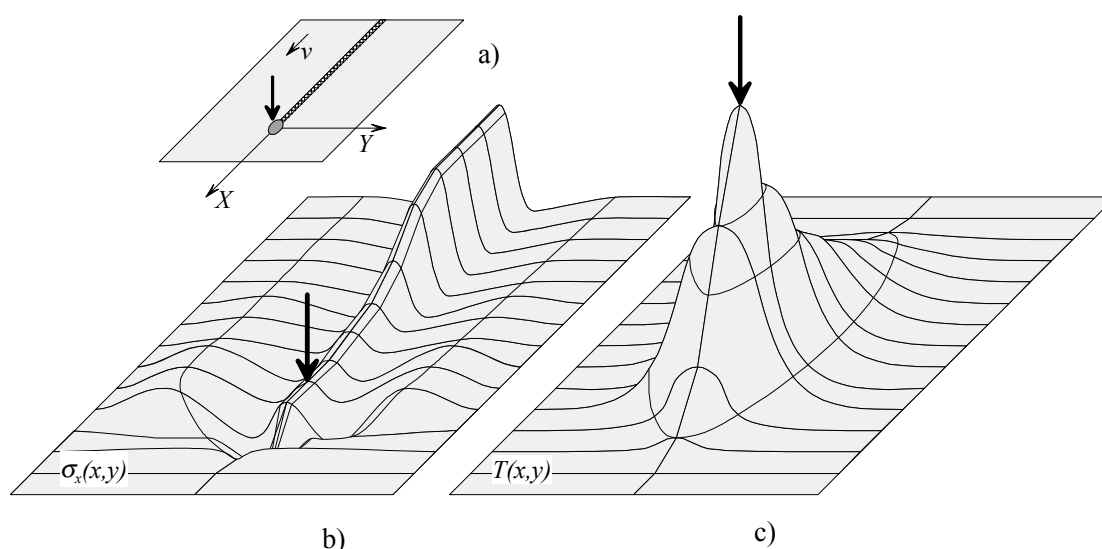


*Fig. II-11. Schematic representation of changes of temperature and stress during welding; (a) scheme of the welding process; (b) longitudinal stress distribution over the plate; (c) temperature distribution over the plate.*

Far ahead from the heat source the temperature is constant and the stress is equal to zero in all the points. Moving in the negative direction of the  $x$ -axis, we reach the point where the temperature starts to rise. The points close to the weld line start to experience compression in the longitudinal direction. This deep fall changes to a fast rise of the longitudinal stress.

The rate of stress change is proportional to the temperature gradient ahead of the source. It is caused by the yielding point  $\sigma_Y$  changing with temperature. As known, at elevated temperatures the material begins to soften. After some temperature (for mild steel the softening temperature  $T_s \approx 600^\circ\text{C}$ ) the material reaches the stage when  $\sigma_Y$  is almost zero. And so, the points situated close to the centreline reach the softening temperature, and climb up to a zero value of the longitudinal stress.

Stresses in the regions a short distance from the arc are compressive, because the expansion of these areas is restrained by the surrounding metal where the temperature is lower. However, stresses in the areas further away from the weld arc are tensile and balanced by compressive stresses in the areas near the weld.

Going further, at some distance behind the welding arc, the temperature drops sufficiently for the material to be stiff enough to resist the deformation caused by the temperature change. Due to cooling the areas close to the weld contract and cause tensile stresses.

After a certain time, the temperature change due to welding diminishes. High tensile longitudinal stresses (usually up to the yielding stress) are produced near the weld. In the regions further away from the weld, compressive stresses do exist.

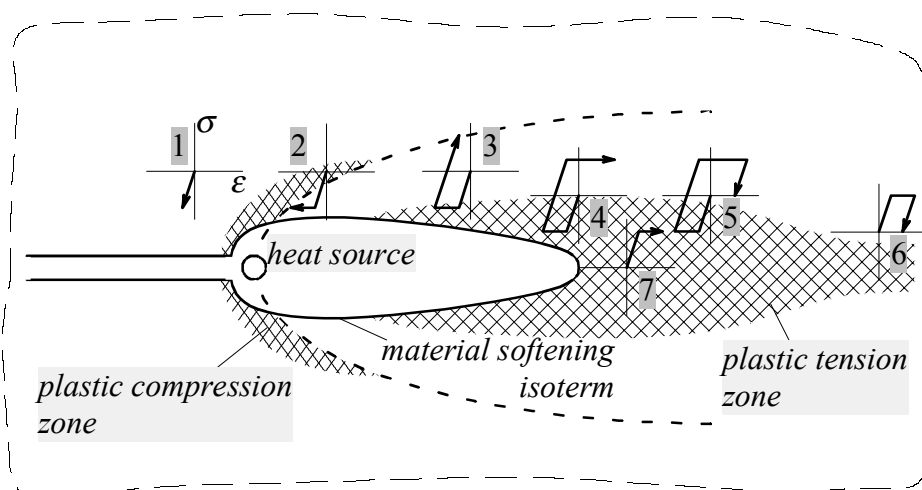


Fig. II-12. Plastic compression and tension zones; local stress-strain cycles in quasi-stationary temperature field of the moving heat source (adopted from Radaj<sup>44</sup>).

In Fig. II-12 the scheme of plastic zone distribution for a case of quasi-stationary temperature field caused by a moving line heat source is presented. As mentioned

above, the material reaching some temperature loses its strength. Beyond this temperature limit the material is almost free of stress because of the reduced yield limit at elevated temperatures. Furthermore, if the material has been subjected to some deformation or stress, after passing through this region the material becomes stress-free.

As an example the point **6** in *Fig. II-12* may be suggested. At first sight the schematic stress-strain cycle in point **6** should have looked like in point **5**. But the difference is that material in point **6**, after reaching some elastic and plastic compression, was "annealed" inside of the material softening isotherm.

The parabola-like curve drawn as a broken line indicates the local temperature maximum. This line serves as a boundary between the area ahead of it, subjected to elastic or elasto-plastic compression, and area behind it, exposed to tensioning. The elastic unloading zone, corresponding to the segment **2-3** in *Fig. II-10*, separates these areas.

Points **1**, **2** and **3** are situated along one horizontal line. Therefore, they represent the consecutive stress development at a point lying at some distance from the weld centreline. First, the material is being exposed to elastic compression (point **1**), and then, reaching the yield limit, the material undergoes plastic deformation (point **2**), followed by elastic unloading (point **3**).

Point **7** has a peculiar position. It lies on the weld centreline and the material in this point has been subjected only to elastic and then plastic tensioning. It is true because before the welding arc has passed over this point, the material in it did not exist, there was a groove.

#### 2.2.3.2 Transverse stress development during the welding process

To demonstrate welding transverse stress development in a free plate, the results from a 3D FEM model are presented in *Fig. II-13.b*. The evolution of stress was traced along the line transverse to the welding direction marked in *Fig. II-13.a*.

At first sight, the behaviour of the transverse stress is somewhat similar to the longitudinal stress behaviour, at least during the beginning of the cooling.

Far ahead of the heat source, the stress is equal to zero because there is no disturbance factor, i.e. no temperature change. Approaching the heat source, we first meet a tensile stress hump, while the temperature is still equal to zero. Then follows an abrupt fall down to compression, reaching the yield limit at slightly elevated temperatures. Then, with rising temperature and, hence, lower yield limit, the transverse stresses climb up to near zero values.

This highly compressed region right ahead of heat source explains the existence of the tensile hump. According to *eq. II-6* on *page 30*, the transverse stresses have to be in a self-equilibrium state in the longitudinal section. So, the tension region has the function of sustaining the equilibrium against the unavoidable compression area around the hot elements of the structure trying to expand.

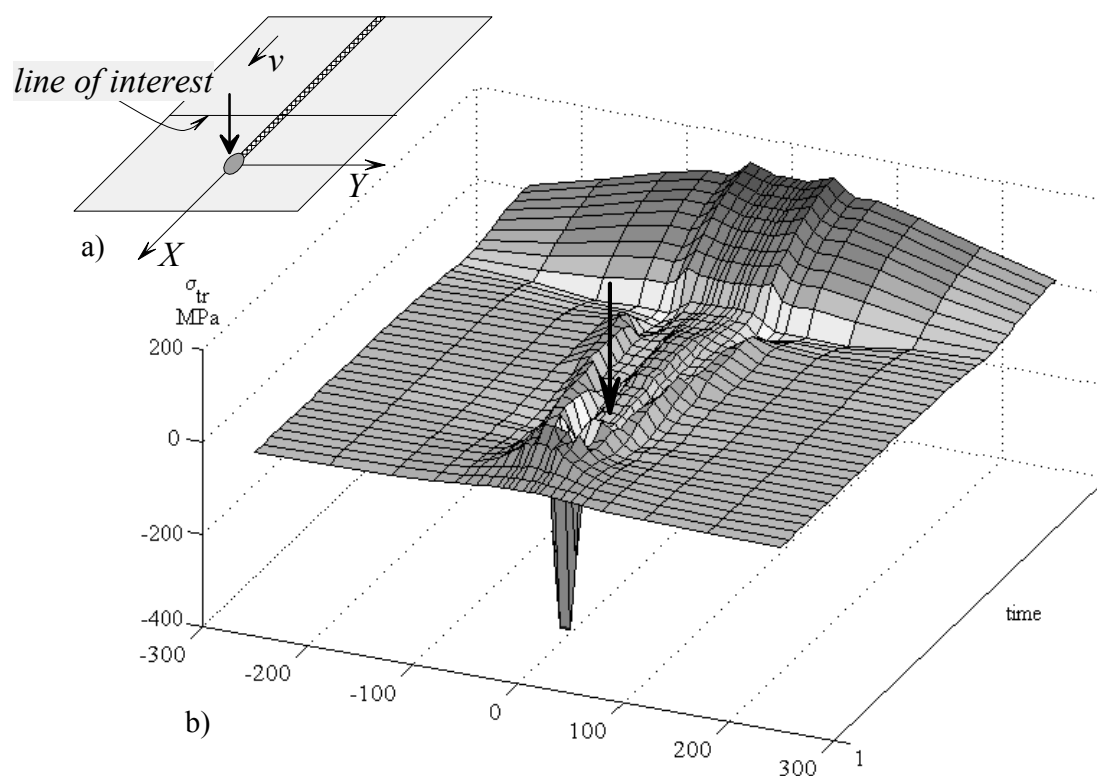


Fig. II-13. Transverse stress evolution; (a) scheme of the welding process; (b) evolution of the transverse stress in a cross-section of the weld.

Further along the time axis, at some distance behind the welding arc, the temperature drops sufficiently for the material to be stiff enough to resist the deformation caused by the temperature change. Due to cooling the areas close to the weld contract and cause gradually growing tensile stresses.

## 2.2.4. Residual stress field

### 2.2.4.1 Residual longitudinal stress formed due to the welding process

Maximum longitudinal residual stresses  $\sigma_x$  in welds are usually close to the yielding limit  $\sigma_Y$ . Gradually decreasing away from the weld axis in the plastic deformation zone, the longitudinal tensioning stresses then relax down to compression values in the adjacent areas. The residual stress distribution in a weld can differ from the one shown in Fig. II-14.a. Depending on alloying level of the weld- and base metal, the picture may change significantly. The cooling rate during welding process and the initial state of the steel can have a serious effect on the stress distribution.

Austenitic steels have thermal expansion coefficients  $\alpha$  greater than low-carbon steels. For these steels the softening happens at higher temperatures, compared to the low-carbon steels. These facts evidence that austenitic steels undergo higher thermal stresses. They do not have yielding plateau on the stress-strain diagram (see Fig. II-3 on page 21). This fact and the high level of plastic deformation cause metal strain

hardening and, hence, generation of the longitudinal stresses higher than yielding limit for the non-deformed state of the material.

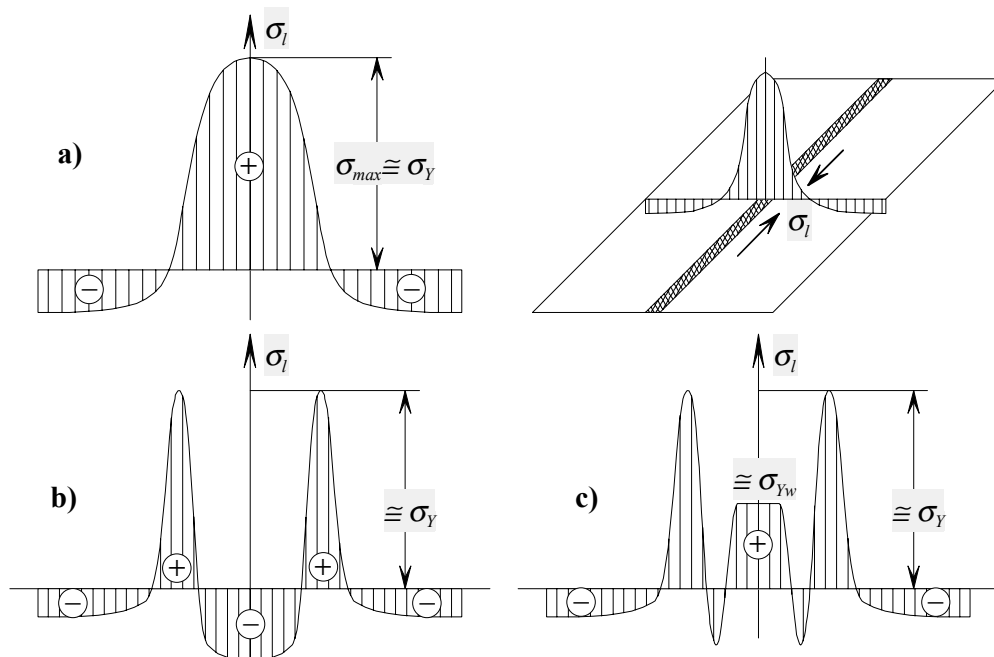


Fig. II-14. Examples of weld-longitudinal stresses; (a) – for mild steel; (b) – for high-alloy steel with martensitic filler metal; (c) – for high-alloy steel with austenitic filler metal.

The behaviour of the longitudinal stresses in the cross-section of the weld is similar for austenitic and low-carbon steels (Fig. II-14.a).

The micro-structural changes in the materials during welding may modify the residual stress distribution radically. In Fig. II-15.b the dilatometric curve for a material with structural changes is presented.

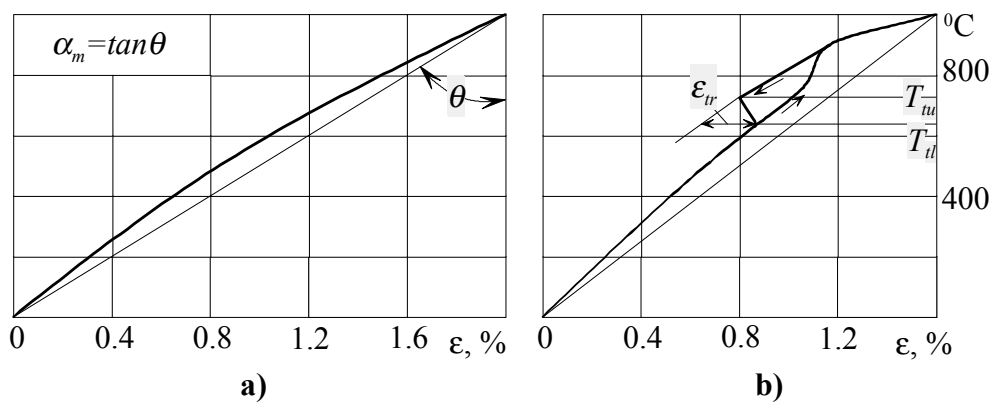
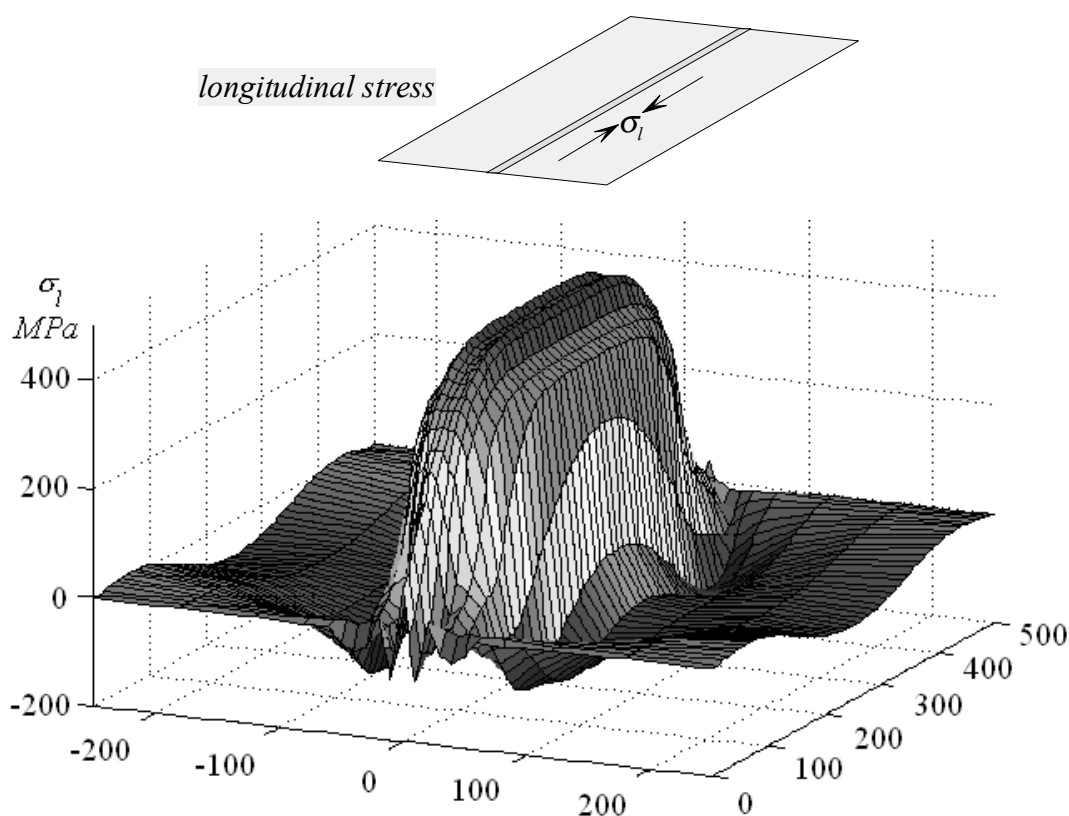


Fig. II-15. Characteristic dilatometer curves; (a) – for austenitic steel; (b) – for steel with perlite microstructure.<sup>52</sup>

If structural changes during cooling happen at low temperatures, then the gradual contraction changes to a quick expansion. And the formed tensile stresses are reduced and turn into compression. Subsequent cooling produces further elongation of the material close to the weld seam and may give rise to tensile stresses. The residual stress distribution depends on the transformation strain  $\varepsilon_{tr}$  and the lower transformation temperature  $T_{tl}$ . If the cooling rate is high enough to result in formation of martensite, then the areas close to the weld are in a compressed state (see *Fig. II-14.b.*).

The width of the plastic deformation zone depends on the welding parameters, the material properties and the stiffness of the structure. For this parameter the most important material properties are: the yield stress  $\sigma_Y$ , the elastic modulus  $E$  and the thermal expansion coefficient  $\alpha$ . The greater the  $\sigma_Y$  of the material, the narrower the plastic deformation zone. The greater  $E$  and  $\alpha$ , the wider the plastic deformation zone.<sup>48,49</sup>



*Fig. II-16 3D representation of weld-longitudinal stress distribution.*

The main welding parameters are the heat input per unit length  $q_w$  and the welding speed  $v$ . During welding of wide plates the higher value of  $q_w$ , the wider the plastic deformation zone. Increasing the welding speed with constant  $q_w$  and insignificant heat loss from the free surfaces leads to proportional growth of the isotherms. Increasing the welding speed with constant  $q_w$  results in reduction of the width of the plastic deformation zone.<sup>48</sup>

In *Fig. II-16* an example of 3D representation of longitudinal stress distribution is shown. It helps to create an overall notion about the complexity of the stress-state caused by the welding procedure. This distribution corresponds to the case when the material does not undergo a phase transformation at low temperature. In the middle of the plate it corresponds to *Fig. II-14.a*.

The influence of the specimen length is depicted in *Fig. II-17*. These data were acquired for welding of 25mm thick plates by two-pass SAW by DeGarmo et al.<sup>50</sup> These data can not be taken as reference values for any welding parameters. It should be mentioned that the distance from the beginning or end of the weld, at which the longitudinal stress along the weld CL reaches its maximum value is close to the width of the plastic deformation zone.

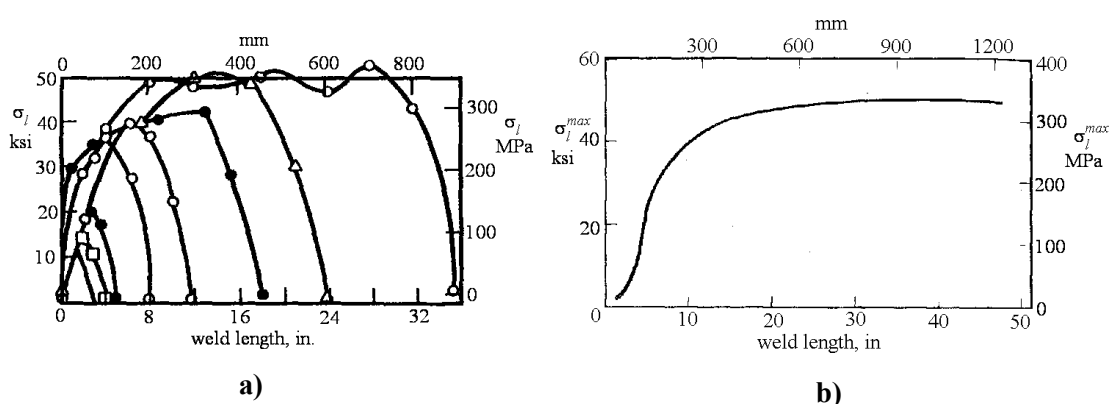


*Fig. II-17. Effect of length of weld on: (a) – longitudinal residual stress distribution; (b) – maximum longitudinal stress distribution.*<sup>50</sup>

The reduction of end effects to acceptable levels relies on Saint-Venant's principle. For bodies extended in two or three dimensions the stress or strain due to loading on a small part of the body may be expected to diminish with distance on account of "geometrical divergence" whether or not the resultant is zero.<sup>51</sup> This is also evident from *Fig. II-16*. In summary it can be concluded that the shape of the graph in *Fig. II-17.b* depends on the welding parameters, the material properties and the stiffness of the structure.

Longitudinal residual stresses start to grow at a distance from both ends of the weld. High tensile stresses exist in the central region of the welds. From *Fig. II-17.a* can be clearly seen that the peak stress in the central region increases with increasing weld length. It is evident that for the experiment under consideration, a weld longer than 450mm is needed to produce maximum residual tensile stresses in the longitudinal direction. Longitudinal residual stresses become uniform in the central region for welds longer than 450mm.

### 2.2.4.2 *Residual transverse stress formed due to welding process*

After the welded plates were cooled down, due to the transverse and longitudinal material shortening, residual transverse stresses arise in the structure. If the plates were welded in a free condition (without tack welds and additional clamps), then the transverse stresses are not too large. The greatest values are reached near the ends of the weld. Stresses there can be both compressive and tensile.

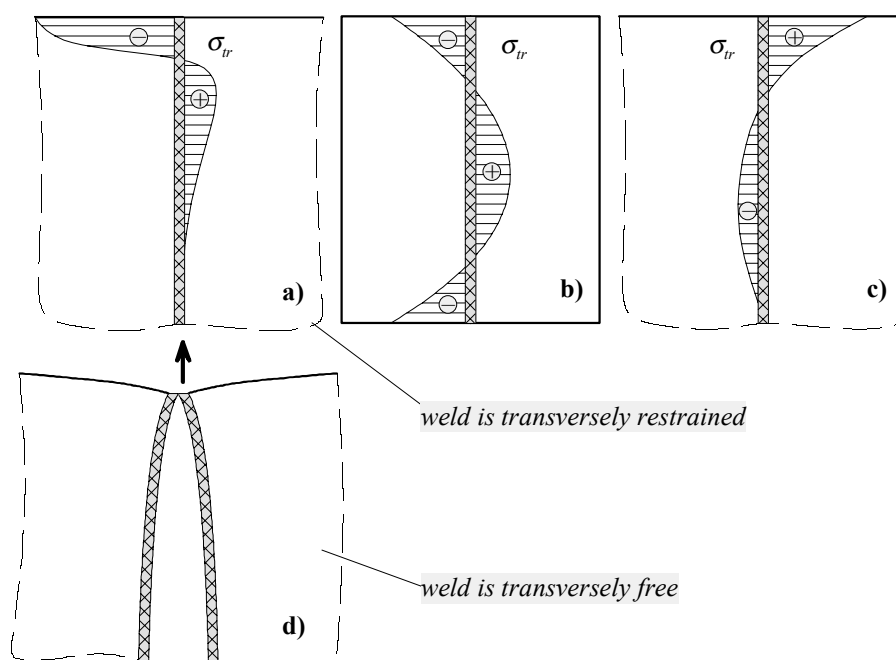


Fig. II-18. Transverse residual stresses due to one-pass butt welding in: (a) – rapidly deposited weld in long plate; (b) – rapidly deposited weld in short plate; (c) – slowly deposited weld in long plate (Adopted from Radaj<sup>44</sup>).

A weld deposited instantaneously between two plates produces a gaping section in the middle of the weld length if the weld cools down without transverse restraint. The compressive stresses are initiated due to longitudinal shortening of the plastic deformation zone, and the plate edge tends to bend the way shown in Fig. II-18.d. Transverse compression arises at the weld ends with a change to transverse tension when approaching the middle section of the weld length.

During welding of short and narrow plates with a high welding speed, the plate edges move towards each other during cooling. The longitudinal shortening tries to bend plates in the plane. As a result, the residual stresses illustrated in Fig. II-18.b are formed along the weld centreline.

If the welding speed is low enough for the weld metal to cool down to the temperature when the material is able to withstand loading (for mild steel the softening temperature  $T^* \approx 600^\circ\text{C}$ ), and it happens not so far behind the welding arc, then the end of the weld

seam experiences tensile stresses as shown in *Fig. II-18.c*. The additional clamping has a serious effect on the residual transverse stress distribution in welds.

An example of 3D residual transverse stress distribution is given in *Fig. II-19*. This distribution corresponds to the case of welding in small plates (see *Fig. II-18.b*). At the same time each plate is 250mm wide and 500mm long. So, the term “small” should be considered as complex term, combining not only geometrical dimensions but also welding parameters and even material properties.

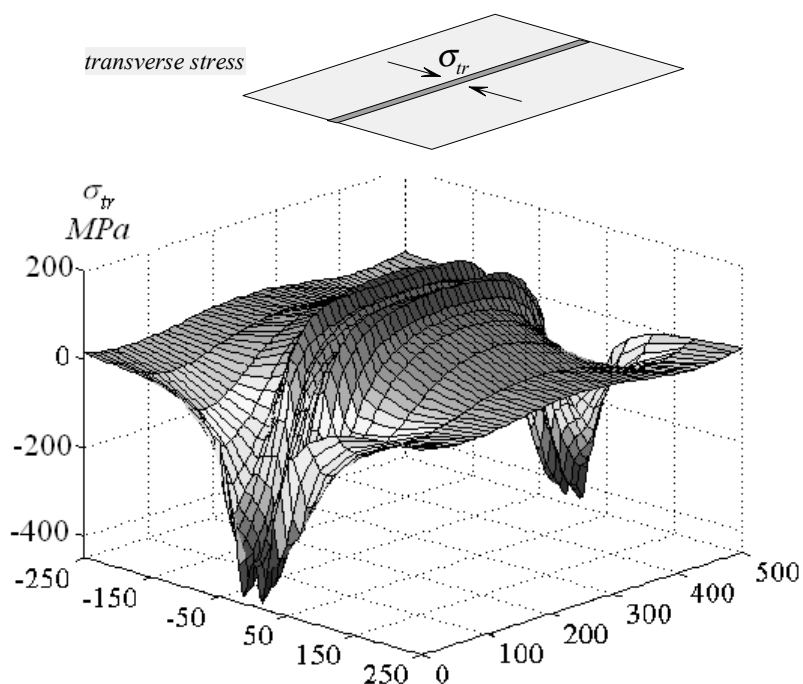


*Fig. II-19. 3D representation of weld-transverse stress distribution.*

From *Fig. II-19* can be seen that the main peaks of the residual transversal stresses are concentrated near the weld ends.

It should be mentioned that transverse stresses in the through-thickness direction also exist in weldments. Their level is high enough in some cases of welding to pay serious attention to them.

This dissertation is concentrated on the problems concerning welding methods employed in the shipbuilding industry (mostly on submerged arc welding of relatively thick plates). For such cases, the residual transverse stresses in the through-thickness direction are negligible because of the configuration of the plastically deformed zone. This fact is schematically illustrated in *Fig. II-20*. Stress and deformation are largely opposed. High stresses occur where the deformation is restrained (i.e. low), low stresses where the deformation is unrestrained (i.e. high).

An example for the case in *Fig. II-20.a* can be a one-pass SAW used for joining two medium-thick plates or any kind of welding in thin plates. Such processes are usually

characterised by a relatively wide plastically deformed zone. The material in the area close to the welding line is able to “breathe” in the through-thickness direction more or less freely. Hence, transverse stresses are low.

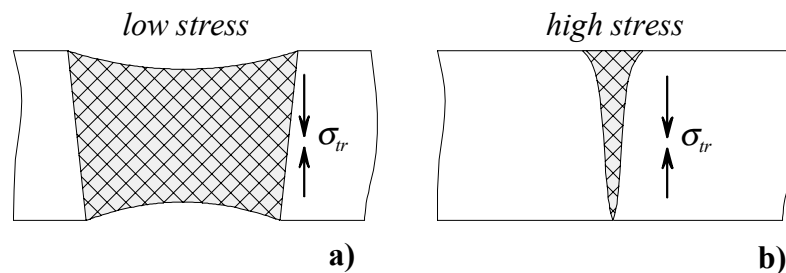


Fig. II-20. Transverse weld stress in through-thickness direction; (a) – with relatively wide plastically deformed zone; (b) – with narrow plastically deformed zone.

To Fig. II-20.b corresponds the case of highly concentrated electron-beam welding in thick and middle-thick plates. The metal of the narrow area close to the welding line is restricted in a through-thickness movement. And, in such a way, high residual stresses in the through-thickness direction are initiated.

### 2.2.5. Conclusions

In this section the stress distribution analysis in welding applications is introduced. The main principles of the analysis and the stress classifications are reviewed. The following conclusions can be drawn:

1. Deformation and stresses arising during welding process are caused by non-uniform heating of the parts being joined.
2. A variety of the distinct types of welding deformations exists. Any particular case of welding usually lead to deformed shape combining several types of distortions.
3. The welding residual stresses and deformation are formed due to plastic deformation during the heating stage and subsequent cooling.
4. Initially stressed material being heated up to the material softening temperature (for mild steel  $T^*=600^{\circ}\text{C}$ ) loses its stress history.
5. As result of welding, residual stresses are formed in the workpiece. The longitudinal stress usually prevail over the transverse ones, usually reaching the yielding point along most of the weld.
6. Low temperature microstructural transformations in the weld metal and the HAZ can change the residual stress distribution significantly, whereas transformations achieved at elevated temperatures may have no significant effect.
7. Close to the ends of the weld the residual transverse stress is substantial, in some cases reaching the yielding point.
8. High-heat input SAW, characterised by a wide plastically deformed zone, has low residual stress in the through-thickness direction.

### 2.3. Deformations of the welded structure

#### 2.3.1. Mechanism of transverse shrinkage in butt welds

One of the most widely used weld joint types is butt weld of plates completed in one pass. The mechanism of deformation for this case is quite characteristic for the whole spectrum of welding deformations.

To understand better the causes of the weld deformation, let us study the formation process of the transverse deformations. Taking a closer look at the cross-section  $dx$ , we can see that it consists of three characteristic zones:

- zone (number 1) of softened metal (inside the  $T^*$  isotherm);
- zone (number 2) between  $T^*$  and  $\approx T_0$ , where we have a smooth temperature fall down to the initial temperature  $T_0$ ;
- cold zone (number 3) where the temperature does not change significantly; this zone embraces the heated zone, not allowing it to expand.

Let us subdivide the cold cross-section into several equal rectangles, and control how the shape of these rectangles is changing during welding process. The first stage considered in *Fig. II-21* corresponds to the moment in time soon after the source has passed the cross-section.

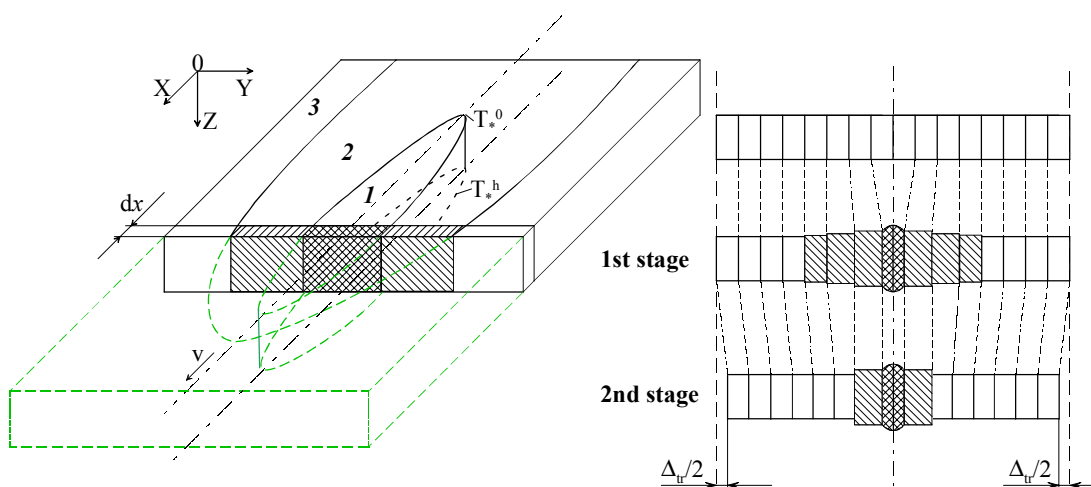


*Fig. II-21. Weld-transverse shrinkage formation.*

Cross-section  $dx$  passes each of three zones mentioned above. The cold zones are rigidly bounded with each other, not allowing the cross-section considered to expand. In this case the heated metal (zones 1 and 2) tends to expand closer to the centreline, causing compression of the zone 1, including its residual plastic deformation. At the same time, the elements of the cold zone remain unchanged, while the metal in the first and second zone is moving towards the centreline of the weld. The softened elements of the first zone are getting plastically deformed by an amount  $\Delta_{tr}$  in the  $y$ -direction. In other

words, the elements of the second zone expand in the  $y$ -direction owing to elastic and plastic contraction of the soft elements in the first zone.

### 2.3.2. Longitudinal and transverse shrinkage in butt welds

During cooling the elements of the plate gradually return to their initial geometrical state, except the elements close to the weld centreline (not only the elements of the soft zone). Some elements of the intermediate zone during the heating period could also achieve plastic deformation. As a result in the cooled down state, the outer edges of the plate come closer to the weld centreline.

Gatovskii in his works, based on several simplifications, introduces a physical model for residual transverse and longitudinal shrinkage. According to him, the residual longitudinal and transverse shrinkage can be expressed in similar terms.<sup>45</sup>

$$\Delta_{tr} = \mu_{tr} \frac{\alpha}{c\rho} \cdot \frac{q_w}{h} = -1.25 \frac{\alpha}{c\rho} \cdot \frac{q_w}{h} \quad \text{eq. II-7}$$

$$\Delta_l = \mu_l \frac{\alpha}{c\rho} \cdot \frac{q_w}{h} = -0.335 \frac{\alpha}{c\rho} \cdot \frac{q_w}{A} \cdot L_w \quad \text{eq. II-8}$$

where  $\mu_{tr}$  and  $\mu_l$  are coefficients of transverse and longitudinal shrinkage;  $q_w$  is net heat input per unit length of weld [ $\text{J}\cdot\text{s}^{-1}\cdot\text{m}^{-1}$ ];  $A$  – cross-section area [ $\text{m}^2$ ];  $L_w$  – weld length [m].

Vinokurov in his works assign the value of the  $\mu_{tr}$  to be in the interval between 1.0 and 1.4 ( $\mu_{tr}=1.0\div 1.4$ ). He also postulates that *eq. II-7* works for low-carbon-, low-alloy- and austenitic steels for the thickness up to 16mm.

The equations introduced above are approximate, but for the most cases they work quite well. As exceptions should be mentioned cases with:

- significant effect of the heat loss from the surfaces (welding of thin plates or process with high values of convective heat transfer coefficient  $\alpha_c$ ). In this case longitudinal and transverse shrinkage can be noticeably reduced;
- welding of pre-stressed parts. Initial tension reduces the deformation in the corresponding direction. Initial compression stresses give the opposite effect;
- welding with incomplete penetration. The presence of the cold metal beneath the weld gives additional stiffness to the structure, significantly reducing the longitudinal and transverse deformation.

Of course, these equations give only estimates because according to them, the plates are just shrunk proportionally. But, the real shape of the deformed plates is more complicated than a simple rectangle. In *Fig. II-22* an example of the real shape of deformation is shown.

It is evident that the longitudinal shrinkage is concentrated mostly close to the weld. Over the rest of the plate width it is close to zero if the plates are wide and, hence, stiff enough to withstand the longitudinal load applied along the weld centreline. The transverse shrinkage is larger in the middle section of the plate compared to that at both

ends. This gives the U-shaped distribution along the length of the plate. This uneven character of the distribution smoothes out with increasing plate width.

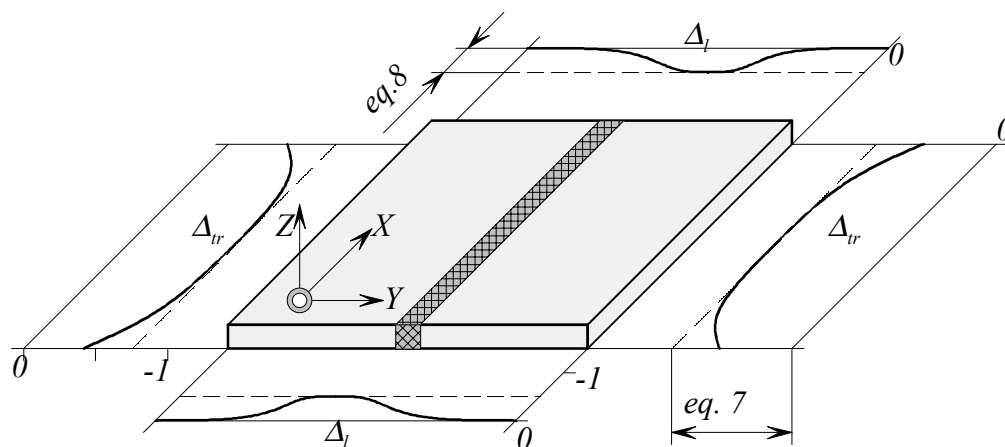


Fig. II-22. Distribution of in-plane deformations; ---- - distribution according to equations above.

The U-shaped transverse shrinkage distribution can be explained by the reduced stiffness of the plates close to the edges. And, hence, the cross-section  $dx$  from Fig. II-21, being situated close to the beginning or end of the weld, is less restricted during the first hot stage. It leads to reduced transverse shrinkage close to the plate ends.

At the same time, such a U-shape is not uniquely defined. In some instances (for example, small specimens) a barrel-like distortion can be achieved.

### 2.3.3. Kinetics of metal movement during welding process

In-plane deformation of the welded plates becomes noticeable only after the plates are cooled down completely. It happens in spite of the fact that plastic deformation, causing shrinkage, is achieved during the welding process itself.

While the source passes over the plate, only a limited part of metal is moving. That is why additional clamps do not have a significant effect on shrinkage during welding. During cooling the picture changes. If the clamps are strong enough, then plastic deformation, reducing residual transverse or longitudinal shrinkage, may take place.

In Fig. II-23 the actual transversal metal movement for the points situated close to the weld is shown. Because of the rising temperature ahead of the source, the metal starts to expand.

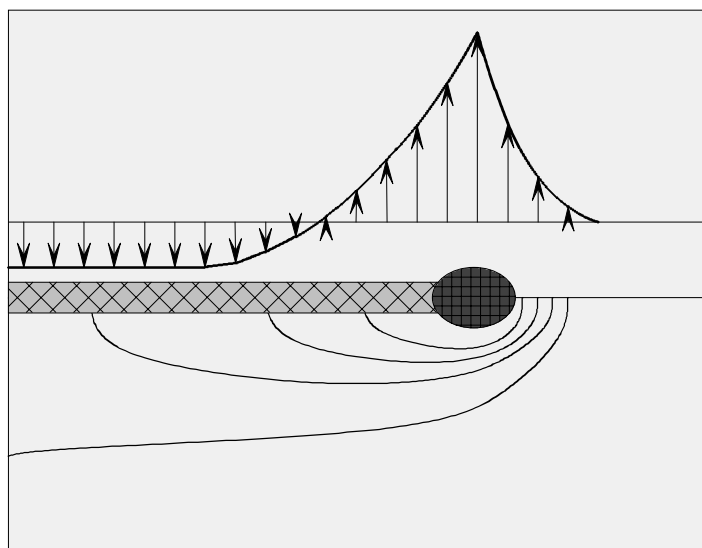


Fig. II-23. Weld-transverse displacement of points situated along the parallel to the weld CL line, situated close to the weld.

#### 2.3.4. Rotational distortion of butt joints

Rotational distortion of butt joints during welding is affected by ratio of the plate length to the length of the metal-softening isotherm (for mild steel  $T^*=600^{\circ}\text{C}$ ). In the case when the  $T^*$  isotherm expands over a big part of the plate length (see Fig. II-24.c), the plate edges along the weld seam have a chance to expand in both longitudinal directions.

A gap forms because the hot part situated close to the weld is expanding, but the cold part of the plate is struggling against it. It leads to the plate shape shown in Fig. II-24.d. This kind of rotational distortion is characteristic for the SAW processes, combining a high welding speed and a powerful heat source.

For the case with relatively short and rounded  $T^*$  isotherm (see Fig. II-24.a), the hot area tries to expand more or less evenly in all directions. The metal behind the heat source is already solidified and cooled down to the temperatures where it is able to withstand loads.

The gap closes because the hot part situated near the arc is expanding, but the cold part of the plate is struggling against it. The plate edges behind the source do not have a chance to expand freely in all directions. The only way for metal to move is to travel forward, closing the gap ahead of the source as marked by arrows in Fig. II-24.b. This kind of rotational distortion is reported to be characteristic for flux covered electrode processes, combining a low welding speed and a less powerful heat source.

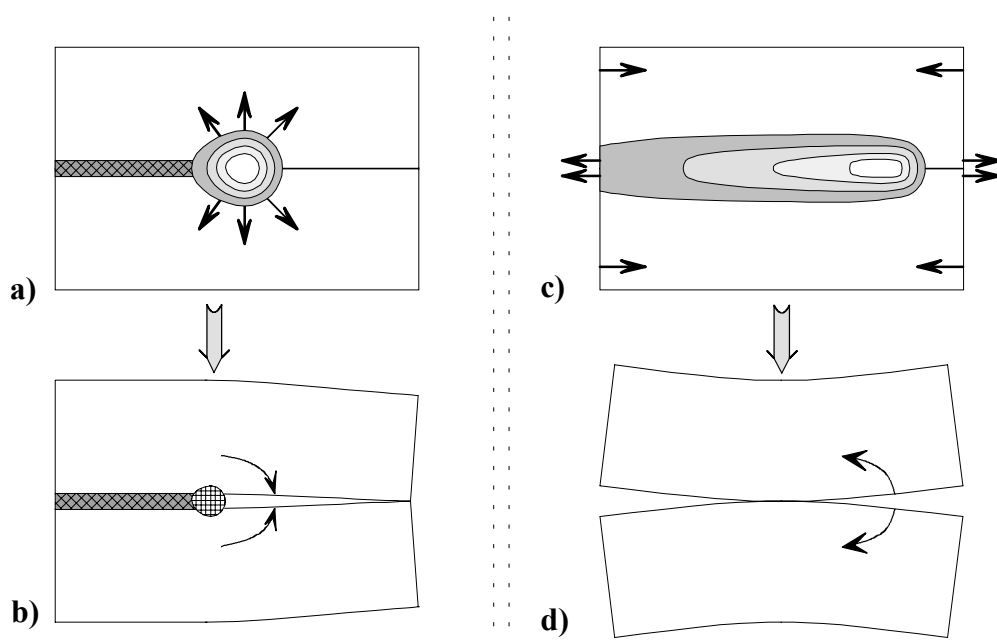


Fig. II-24. Scheme of "closing" and "opening" (rotational distortion) formation in butt joints; (a) and (c) – temperature distribution and forces formation with relatively short and long metal-softening isotherm respectively; (b) – closing formation; (c) – opening formation.

### 2.3.5. Angular shrinkage

#### 2.3.5.1 Variety of local deformations

During fabrication of the welded structures local deformations arise ("warpage" and "buckling") in addition to the total one (*longitudinal* and *transverse* shrinkage). The sources of the local deformations are:

- two joining plates rotate relative to each other in a plane perpendicular to the welding direction (so called "angular" deformation). It happens because of through-thickness non-uniform heating;
- plate stability loss due to a longitudinal shrinkage force (buckling). It usually happens in thin plates.

Angular deformation appears under any kind of welding procedure. Fig. II-25 shows qualitatively the angular deformation as a function of plate thickness and heat input.

For small thicknesses, angular deformation is not significant because of the high homogeneity of the temperature field through the plate thickness. The insignificant angular distortion in the region of great thickness is caused by the greater plate stiffness. The region of intermediate plate thickness corresponds to the greatest angular distortion. An increase of a *net heat input* per unit length of weld, assigned as  $q_w$ , shifts the whole curve to the right.

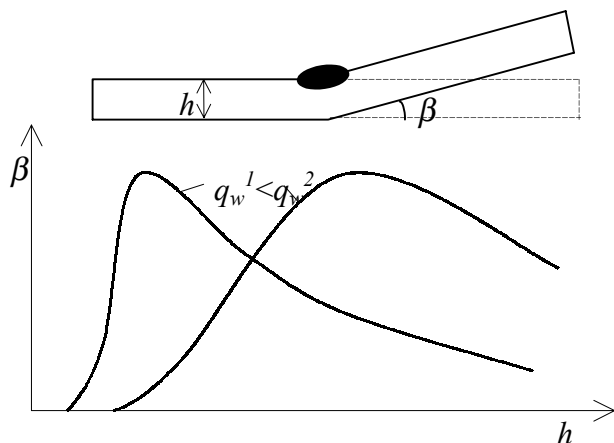


Fig. II-25. Scheme of plate thickness - angular deformation relation.<sup>55</sup>

As mentioned, buckling may occur only in the case of thin-plate welding. In this case the longitudinal contraction stress  $\sigma_{contr}$  reaches the value of a stress corresponding to a critical load for buckling initiation  $\sigma_{cr}$ :

$$\sigma_{contr} \approx \sigma_{cr}$$

eq. II-9

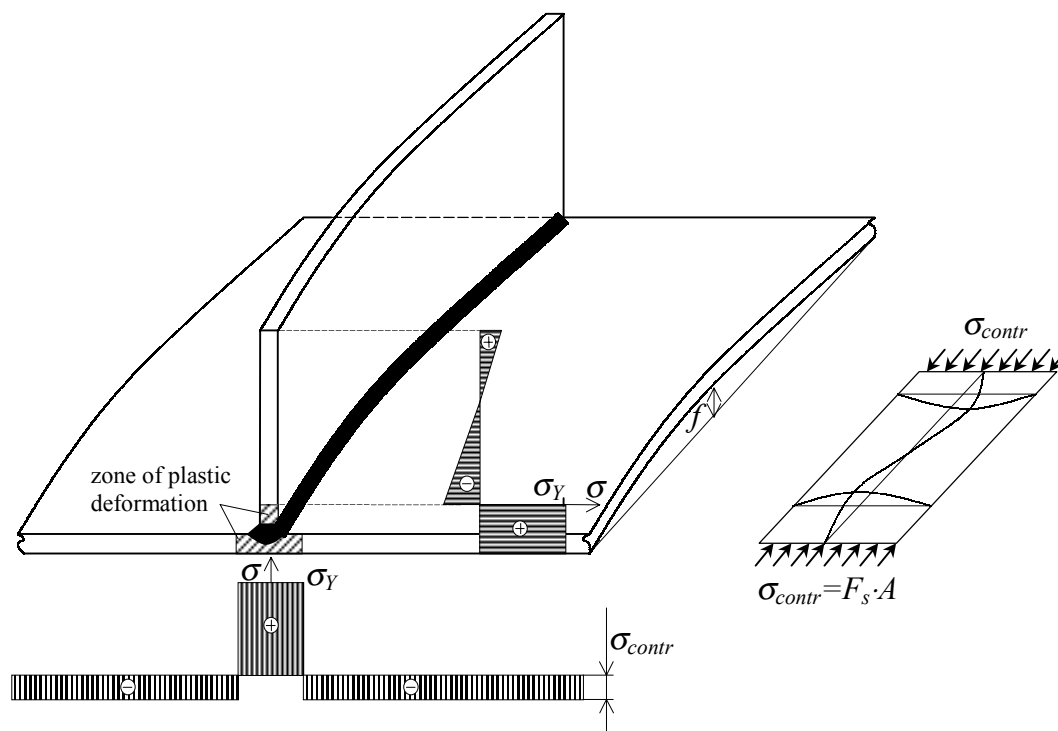


Fig. II-26. Out of plane distortion due to loss of the plate stability (buckling).

In *Fig. II-26* the longitudinal residual stress distribution in a transverse section of a T-joint is shown. Excluding the narrow region near the weld, the longitudinal residual stress is nearly uniform over the plate. In several cases this fact makes it possible to simplify the buckling analysis. *Fig. II-26* also shows schematically how the complicated thermo-mechanical problem can be substituted by a simple mechanical one.

2.3.5.2 Kinetics of angular distortion development

To see how the angular deformation forms, we can examine the butt-welding process in a qualitative sense. In *Fig. II-27* isotherms corresponding to the metal softening temperature on the top surface  $T_*^0$  (firm line) and on the bottom  $T_*^h$  (dotted line) are shown. Let us take a look at a cross-section  $dx$ . We can see that this cross-section consists of three characteristic zones:

- zone (number 1) of softened metal (inside the  $T_*$  isotherm);
- zone (number 2) between  $T_*$  and  $T_0$ , where we have a smooth temperature fall down to the initial temperature  $T_0$ ;
- cold zone (number 3) where the temperature does not change significantly; this zone embraces the heated zone, not allowing it to expand.

The cross-section  $dx$  passes each of these zones. The cold zones (not marked in *Fig. II-27*) are rigidly bound to each other, not allowing the cross-section considered to expand. The heated metal (zones 1 and 2) then tends to expand closer to the *centreline* (CL), causing compression of the zone 1, including its residual plastic deformation.

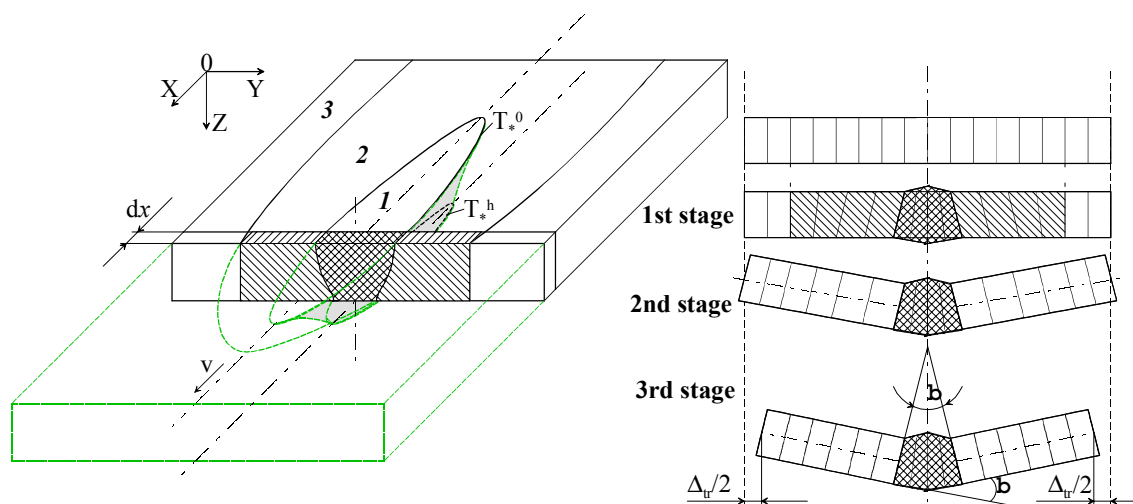


*Fig. II-27. Schematic representation of angular distortion evolution; 1-st stage – shortly after heat source passed through  $dx$ ; 2-nd stage – after fading of the temperature gradient over the plate thickness; 3-rd stage – completely cooled down.*

Because the metal close to the top surface is heated up to a higher temperature, the points belonging to this area shift closer to the CL than the points along the bottom surface.

On the right side of *Fig. II-27* several stages of the angular distortion evolution is shown. The cross section is sectored by the vertical lines. It allows us to see the actual dynamics of the metal movement.

The *1-st stage* is characterised by nonuniform displacements both in the through-thickness and the transverse directions. Points close to the top surface drift towards the CL to a greater extent than points on the opposite surface. This causes a trapezoid shape of the original rectangles.

During the *2-nd stage* the tetragons again become rectangles, but with different widths. As this takes place, the sides of the joining plates bend relative to each other, forming an angle  $\beta$ .

Later on the temperature equalises in the transverse direction, leading to the *3-rd stage* when the whole plate is uniformly shortened in the transverse direction by  $\Delta_{tr}$ . Now the shape of the rectangles is restored, excluding the crosshatched plastically deformed area, corresponding to the softened metal zone.

### 2.3.5.3 Angular distortion

*Fig. II-28* shows the behaviour of angular distortion during completion of the weld joint. It schematically demonstrates how the angle  $\beta$  changes in time.

We can see that in the beginning of the heating stage an area of the plate close to the heat source tends to expand stronger than the cooler regions. It leads to a situation where the outer edges of the plate are "sagging" down. But the expanding region does not have a freedom to expand as much as it needs. The rest of the plate resists, causing plastic deformation of the hot area. This is highlighted in *Fig. II-28* by vertical hatching.

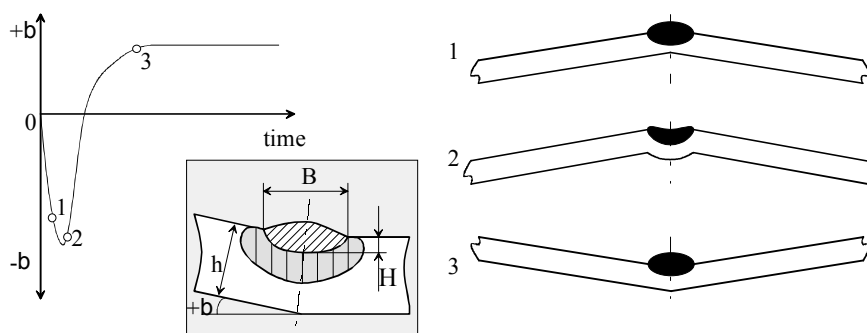


*Fig. II-28. Angular distortion as a function of time during the heating and cooling stages of the joining process, and assigning of joint configuration parameters: H – seam depth; B – seam width.*

The magnitude of the angular distortion depends on a number of factors:

- relative depth of penetration  $H/h$ ;
- relative bead width  $B/h$ ;
- bead shape;
- mechanical- and thermal properties of the base- and filler metal, etc.

The shape of the seam in its turn depends on the concentration and other characteristics of the power source. Results reported in literature often differ greatly from each other. Firstly, it could be explained by the considerable number of acting factors listed above and, secondly, by the uncertainty of the heat source distribution between the two parts of the weld. Different redistribution of the energy between joining parts gives various magnitudes of angular distortion<sup>52</sup>. It is then difficult to predict experimental results and compare them with different practical cases. Predicted results, either by wholly coupled thermal-mechanical analysis or by using simple equations, can serve as a certain approximation of the real one.

As first approximation of the angular distortion in butt welding of a low carbon low alloyed steel plates a diagram suggested by A.S. Kuzminov could be used. This diagram, based on experimental results is shown in *Fig. II-29*.

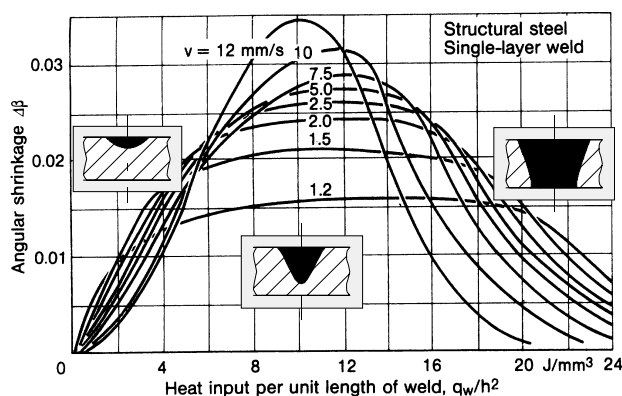


*Fig. II-29. Angular shrinkage  $\Delta\beta$  dependent on heat input per unit length of weld,  $q_w$ , and weld or plate thickness  $h$  for different welding speeds  $v$ .<sup>53,44</sup>*

The diagram shows that from the beginning, with increasing  $q_w/h^2$  parameter, the angle  $\beta$  is increasing, reaching a maximum value at  $q_w/h^2 \approx 10 \text{ J}\cdot\text{mm}^{-3}$ . After reaching the maximum, the angular deformation decreases.

The small value of the angle  $\beta$  at the left part of the diagram is attributable to the heat source not being powerful enough to soften enough metal through the plate thickness. In this case the relatively cold plate is stiff enough to resist the bending force action. The drop in the angle  $\beta$  on the right side of the diagram is caused by the vanishing temperature gradient in the through-thickness direction. In such a situation, layers of the

plate can expand in the transversal  $y$ -direction with less resistance (causing less plastic deformation), and, consequently, reduced angular distortion.

In the case of butt welding with V-shaped edge preparation angular distortion is basically caused by contraction of the filler metal. Assuming that the shape of the seam coincides with the shape of V-groove, it is possible to derive a simple equation for the angle  $\beta$ :

$$\beta = 2\alpha \cdot T_* \cdot \tan\left(\frac{\theta}{2}\right) \quad \text{eq. II-10}$$

where  $\alpha$  is the thermal expansion coefficient,  $T_*$  is the temperature of material softening (for mild steel  $T_* \approx 600^\circ\text{C}$ ) and  $\theta$  is the groove angle<sup>54</sup>.

Another empirical solution was suggested by Okerblom in 1955.<sup>55</sup>

$$\beta = 0.13 \cdot \frac{I \cdot U}{v \cdot h^2} \quad \text{eq. II-11}$$

where  $I$  is current [A],  $U$  is voltage [V],  $v$  is welding speed [ $\text{mm} \cdot \text{s}^{-1}$ ] and  $h$  is plate thickness [mm].

In the case of long plate welding, the temperature distribution along the weld seam varies significantly. The angular deformation will then vary along the plate.

### 2.3.6. Conclusions

In this section the analysis of the deformation process in welding applications is introduced. The main governing mechanisms and deformation classifications are reviewed. The following conclusions can be drawn:

1. Residual deformation of the workpiece is produced in the area along the weld. This area is plastically deformed during the welding process.
2. The overall pattern of rotational distortion during welding depends on the ratio between the weld length and the length of the material softening isotherm (for mild steel  $T_s=600^{\circ}\text{C}$ ).
3. The formation of angular deformation is greatly affected by a number of factors. Among those are: relative depth of penetration, relative bead width, bead shape, mechanical and thermal properties of the base- and filler material.
4. The use of high-heat input welding methods leads to increased deformations that should be investigated carefully. Currently, such thermo-mechanical processes are not sufficiently analysed.

**References**

---

- 1 Rosenthal, D.: "Etude théorique du régime thermique pendant la soudure à l'arc", Congress National des Sciences, Comptes Rendus, Bruxelles, 2, pp.1277-1292, 1935;
- 2 Rosenthal, D., Schmerber, H.: "Thermal study of arc welding" W.J., N4, pp.4-8, 1938;
- 3 Rykalin, N.N.: "Temperature distribution in the elements of the structure during welding", Avtogennoe Delo, N5 and N7, 1938, *Rus.*;
- 4 D. Rosenthal and R. Schmerber: "Thermal study of arc welding . Experimental verification of theoretical formulas", Am. Weld. Journ, Apr. 1938, pp. 2s-8s;
- 5 D. Rosenthal: "Mathematical theory of heat distribution during welding and cutting", Am. Weld. Journ., May 1941, pp. 220s-234s;
- 6 Rykalin, N.N.: "Berechnung der Wärmevergänge beim Schweißen", Berlin, VEB Verlag Technik, 1953;
- 7 J. C. Walter: "Shrinkage distortion in longitudinal welding of beams", The Technical University of Norway, Trondheim, 1963;
- 8 O. Westby: "Temperature distribution in the work-piece by welding", Doctoral Thesis, The technical University of Norway, Trondheim, 1968;
- 9 V. I. Makhnenko, V. A. Oleinik: "Analytical Evaluation of Nominal Stresses and Deformations Preceding the Failure of Round Plates", Prikladnaya Mekhanika, v 10, N 11, Nov. 1974, *Rus.*;
- 10 V. I. Makhnenko, E. A. Velikoivanenko: "Elasto-Plastic Deformations in the Thermal Effect Zone During Butt-Welding of Plates ", Avtomaticheskaya Svarka, N 4, Apr.1975, *Rus.*;
- 11 Y. Ueda, T. Yamakawa: "Analysis of thermal elastic-plastic stress and strain during welding", Trans. Japan Welding Soc., Vol.2, N 2, 1971, pp. 90-100;
- 12 K. M. Gatovskii: "Determination of welding stresses and strain with allowance for structural transformations of the metal", Welding Production (English translation of Svarochnoe Proizvodstvo), v 20, N 11, 1973;
- 13 G. A. Bel'chuk, K. M. Gatovskii, G. Yu. Polishko, Yu. I. Rybin: "Application of the Finite Element Method to Solve Problems of Welding Deformations and Stresses ", Avtomaticheskaya Svarka, N 11, Nov 1977;

- 
- 14 E. Friedman: "Thermo-mechanical analysis of the welding process using the finite element method", Trans. ASME, J. Pressure Vessel Tech., 1975, pp. 206-213;
  - 15 O. Westby: "Anvendelse av elementmetoder på sveisedeformasjoner og egenspeninger", part of the Doctoral Thesis, The technical University of Norway, Trondheim, 1968, *Nor.*;
  - 16 L. Volden: "Residual stress in steel weldments. Experiments, mechanism and modeling", Doctoral Thesis, Trondheim, 1999;
  - 17 T. Moltubakk: "Strength mismatch effect on the cleavage fracture toughness of the heat affected zone of steel welds", Doctoral Thesis, Trondheim, 1999;
  - 18 H. Runnemalm: "Efficient finite element modeling and simulation of welding", Doctoral Thesis, Luleå, 1999;
  - 19 L. Wikander: "Efficient thermomechanical modeling of welding", Doctoral Thesis, Luleå, 1996;
  - 20 Pilipenko, A.Yu.: "Analysis of the temperature distribution during GTA welding of thick-walled pipes", Master Thesis, St-Petersburg Technical University, 1997;
  - 21 J. Goldak, A. Oddy, M. Gu, W. Ma, A. Mashaie, E. Hughes: "Coupling heat transfer, microstructure evolution and thermal stress analysis in weld mechanics", Proc. of IUTAM Symp. Mechanical effects of welding, Springer Verlag, Berlin, 1992;
  - 22 J. Goldak, V. Breiguine, N. Dai, J. Zhou: "Thermal stress analysis in welds for hot cracking", American Society of Mechanical Engineers, Pressure Vessels and Piping Division (Publication) PVP, Proceedings of the 1996 ASME Pressure Vessels and Piping Conference, Jul 21-26 1996, Montreal, 1996;
  - 23 Ø. Gundersen: "Mathematical modeling of welding. A state of the art review", SINTEF Material Technology, Trondheim, 1997;
  - 24 L.-E. Lindgren: "Deformations and stresses in butt-welding of plates", Doctoral Thesis, Luleå, Sweden, 1985;
  - 25 M. O. Näsström: "Thermo-mechanical modeling of welding with experimental verification", Doctoral Thesis, Luleå, Sweden, 1992;
  - 26 ABAQUS Version 5.6, "ABAQUS user's manual", Hibbit, Karlsson & Sorensen, Inc. 1997, Providence, Rhode Island (USA);
  - 27 ANSYS Version 5.3, "ANSYS User's manual", Troy Technology Park, Inc. 1997;
  - 28 "NISA Version 7, User's manual", Engineering Mechanics Research Corporation, Inc. 1997;
-

- 29 Bathe, K.: "Finite element procedures in engineering analysis", Prentice-Hall, New Jersey, 1982;
- 30 Grong, Ø.: "Metallurgical modeling of welding", The institute of materials, Cambridge, 1994;
- 31 V. A. Karkhin: "Principles of heat transfer in weldments", Leningrad Technical University, 1990;
- 32 H. E. Boyer: "Atlas oif stress-strain curves", ASM International, USA, 1987;
- 33 J. N. Harris: "Mechanical working of metals. Theory and practice", Pergamon Press, Oxford, 1983;
- 34 R. W. Cahn: "Physical metallurgy", North-Holland Publishing Company, Amsterdam, 1965;
- 35 N. I. Bezuhov: "Basics of theory of elasticity, plasticity and creep", Visshaya Shkola, Moscow, 1968;
- 36 J. Chakrabarty: "Theory of plasticity", McGraw-Hill Book Company, Singapore, 1987;
- 37 W. Prager: "Introduction to mechanics of continua", Birkhäuser Verlag, Switzerland, 1961;
- 38 K. Hellan: "Plastisitets teori", Tapir Forlag, Trondheim, 1972, *Nor.*;
- 39 J. Chakrabarty: "Applied plasticity", Springer-Verlag, New-York, 2000;
- 40 E. G. Thomsen, C. T. Yang, S. Kobayashi: "Mechanics of plastic deformation in metal processing", The Macmillan Company, New-York, 1965;
- 41 N. N. Malinin: "Applied theory of plasticity and creep", Mashinostroenie, Moscow, 1975, *Rus.*;
- 42 C. R. Boër, N. Rebelo, H. Rydstad, G. Schröder: "Process modelling of metal forming and thermomechanical treatment", Springer-Verlag, Berlin, 1986;
- 43 R. A. C. Slater: "Engineering plasticity. Theory and application to metal forming processes", The Macmillan Press LTD, London, 1977;
- 44 D. Radaj: "Heat effects of welding", Springer-Verlag, Berlin, 1992;
- 45 K. M. Gatovskii, V. A. Karkhin: "Theory of welding stresses and deformations", Leningrad Shipbuilding Institute, 1980, *Rus.*;
- 46 G. A. Bel'chuk, K. M. Gatovskii, B. A. Kokh: "Welding of ship structures", Sudostroenie, Leningrad, 1980, *Rus.*;

- 47 R. Gunnert: "Residual welding stress", Almqvist & Wiksell, Stockholm, 1955;
- 48 K. Masubuchi: "Analysis of welded structures", Pergamon Press, London, 1980;
- 49 V. I. Makhnenko: "Computational methods for investigation of kinetics of welding stresses and deformations", Naukova Dumka, Kiev, 1976;
- 50 E. P. DeGarmo, J. L. Meriam, F. Johanssen: "The effect of weld length upon the residual stresses of unstrained butt welds", *Welding Journal*, 25(8), 1946, pp. 485s-486s;
- 51 S. P. Timoshenko, J. N. Goodier: "Theory of elasticity", McGraw-Hill Book Company, New York, 1970;
- 52 V.A. Vinokurov: "Welding stresses and distortion", Wetherby: British Library 1977 (Original: Svarochnie deformatsii i napryazheniya: metodi ikh ustraneniya. Moscow: Mashinostroenie 1968);
- 53 A.S. Kuzminov: "Calculation principles of total deformation of ship hull structures", Works of Central Scientific Research Institute of Shipbuilding Industry, 1956, N9., *Rus.*;
- 54 N.O. Okerblom: "Technological and structural design of welded structures", Mashinostroenie, Moscow 1964, *Rus.*;
- 55 N. O. Okerblom: "The calculations of deformation of welded metal structures", Mashgiz, Moscow, 1955, *Rus.*;

## CHAPTER III THEORETICAL BACKGROUND

## 1. PROCESS UNDER INVESTIGATION

The main goal of the current dissertation is to investigate the effect of the multi-electrode submerged arc welding process. As an example was chosen a three-electrode one-sided welding technique used for butt-welding of 20mm thick plates. To evaluate this welding technique, it will be compared with single-electrode welding carried out in three passes.

## 1.1. Description of the structure under investigation

The investigated technique is usually used in shipbuilding on panel lines for long welds.<sup>1,2,3,4</sup>

For example, in two blocks of one bulk carrier of 85 000m<sup>3</sup> built in 1992 at Burmeister and Wain Shipyard A/S, 183 meters of a total of 2964 were butt welded. In other words, only 6% of all the welds are related to the process that is in the focus of attention in the present investigation.

In *Fig. III-1* an example of one block assembly method is shown. In this example the investigated method can be used on the stage named "plate fitting and welding". Depending on the facilities of the shipyard, the size of the plates to be joined may vary over a wide range.

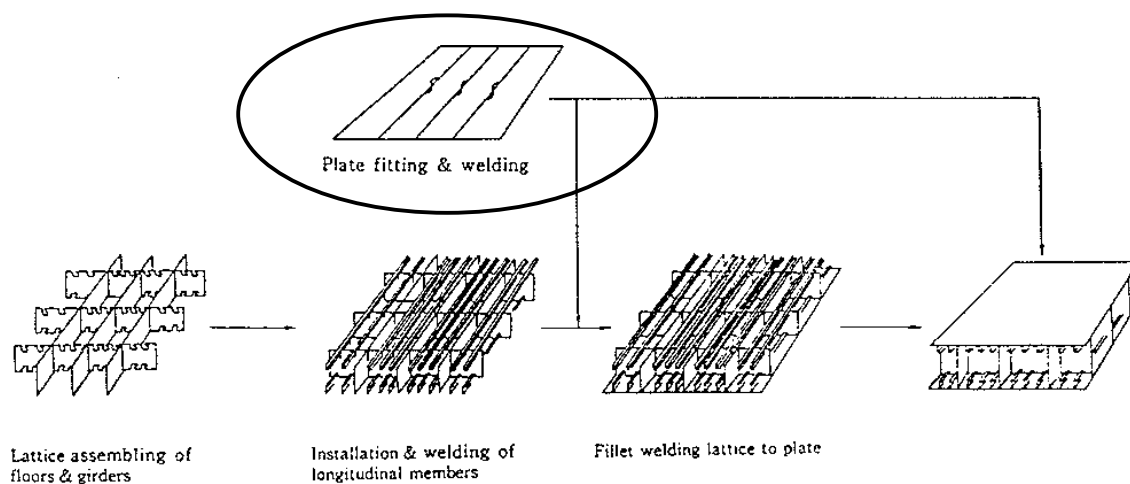


*Fig. III-1. The Waku-Gumi method of block assembly used in Japan.*<sup>5</sup>

For example, the Hitachi Zosen shipyard has a panel line for large panels. Plates 25×4m are welded together to form 25×24m panels, to which stiffeners and then transverse members are added. Similar welds are used in erection of:

- upper deck;
- inner bottom;
- bottom plating;

- side plating;
- inner bulkhead.<sup>5</sup>

The plate thickness for this structure is usually between 20 and 30 millimetres. But, the currently investigated welding technique can be applied to plates from 6mm to 45mm thick.

For simulations a specimen was chosen that is smaller than the commonly used plates in shipbuilding. The scheme of the welding process that has been simulated in our study is shown in Fig. III-2.

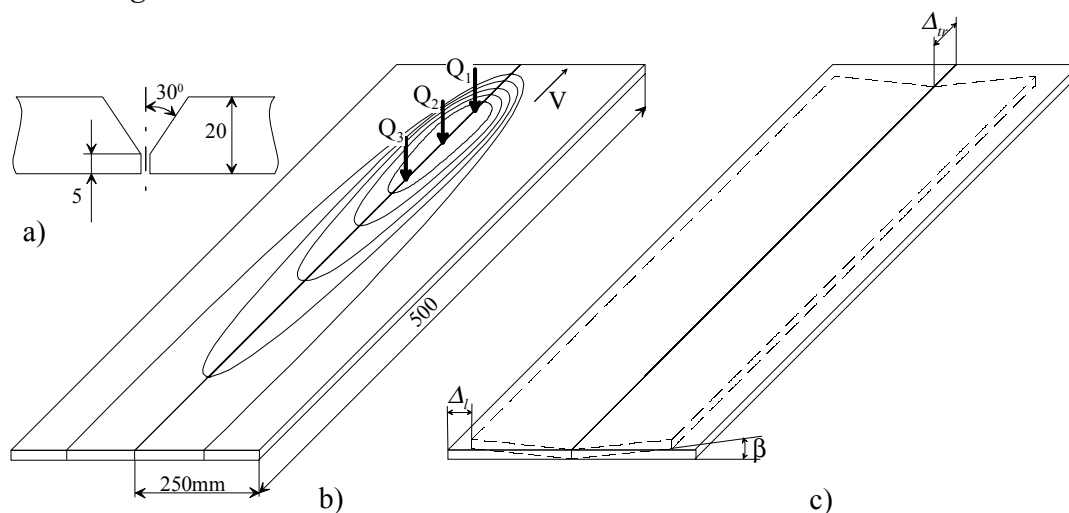


Fig. III-2. Specimen for simulations; (a) – edge preparation; (b) – scheme of the three-electrode welding process; (c) – deformation caused by the welding.

To simulate the real-size plates in 3D would mean to operate FE models that consist of hundreds of thousands 3D elements for the case of similar mesh density that was used in the models of the current dissertation.

## **1.2. Material description**

### **1.2.1. Steels for shipbuilding**

Steels used in shipbuilding must meet the specified minimum of the yield strength values, they must be resistant to the initiation of brittle fracture, and they must be resistant to fatigue.

The steels for commercial ships are subdivided into two strength classes: normal strength (235MPa yield strength) and higher-strength (315 and 355MPa yield strength).<sup>6</sup>

The material investigated in the this dissertation is ASTM A131 steel or the equivalent NVE360 (according to Det Norske Veritas). This steel is *higher-strength steel*. It belongs to the family of *microalloyed high-strength low-alloy steels*. The yield strength in it is elevated by precipitation mechanisms and grain refinement through the presence

of small amounts of vanadium, niobium and copper. The chemical composition of this steel is given in *Table III-1*.

*Table III-1. Chemical composition of ASTM A131 steel.*

Element		Composition, wt%
<b>C</b>	carbon, <i>max</i>	0.18
<b>Mn</b>	manganese	0.90-1.60
<b>P</b>	phosphorous, <i>max</i>	0.035
<b>S</b>	sulphur, <i>max</i>	0.04
<b>Si</b>	silicon	0.10-0.50
<b>Ni</b>	nickel, <i>max</i>	0.40
<b>Cr</b>	chromium, <i>max</i>	0.25
<b>Mo</b>	molybdenum, <i>max</i>	0.08
<b>Cu</b>	copper, <i>max</i>	0.35
<b>Nb</b>	niobium, <i>max</i>	0.05
<b>V</b>	vanadium, <i>max</i>	0.10
<b>Al</b>	aluminium	0.015-0.020

### 1.2.2. Thermal and mechanical properties of the investigated steel

For the following simulations one needs to know the properties of the material under study:

- general properties (density  $\rho$  [ $\text{kg}\cdot\text{m}^{-3}$ ], thermal expansion coefficient  $\alpha$  [ $\text{K}^{-1}$ ]);
- thermal properties (thermal conductivity  $\lambda$  [ $\text{J}\cdot\text{m}^{-1}\cdot\text{s}^{-1}\cdot\text{K}^{-1}$ ], specific heat capacity  $c$  [ $\text{J}\cdot\text{kg}^{-1}\cdot\text{K}^{-1}$ ]);
- elastic mechanical properties (elastic modulus  $E$  [ $\text{N}\cdot\text{m}^{-2}$ ], Poisson's ratio  $\nu$ );
- inelastic mechanical properties (yield stress  $\sigma_Y$  [ $\text{N}\cdot\text{m}^{-2}$ ], including different kinds of hardening if needed).

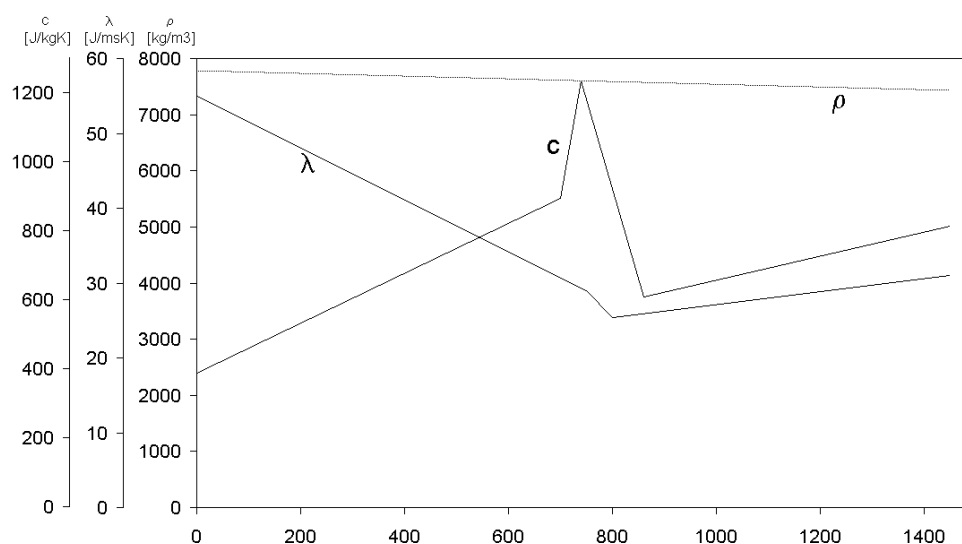


*Fig. III-3. Thermal conductivity  $\lambda$ , density  $\rho$ , and specific heat capacity  $c$  in dependence on temperature for structural C-Mn steel.<sup>7,8,9,10</sup>*

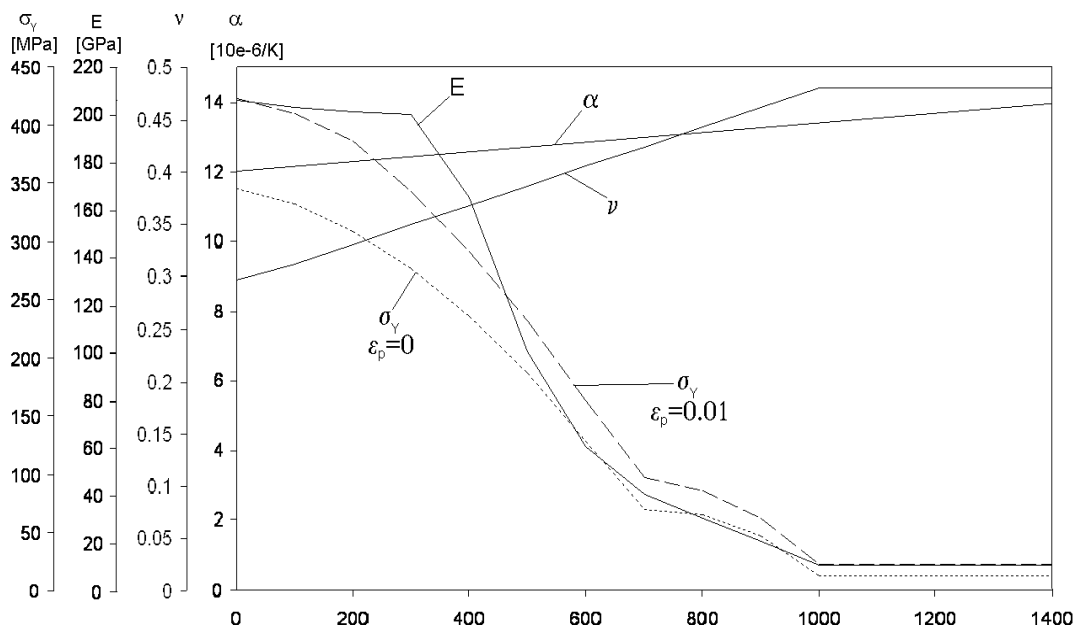


Fig. III-4. Young's modulus  $E$ , Poisson's ratio  $\nu$ , yield strength  $\sigma^y$ , and thermal expansion coefficient  $\alpha$  (microstructural transformations  $\alpha$ - $\gamma$ Fe and  $\gamma$ - $\alpha$ Fe are not taken into account).<sup>7-11</sup>

The graphical representation of the dependence of these properties on temperature is shown in Fig. III-3 and Fig. III-4.

Fig. III-4 includes a demonstration of the hardening of the material subjected to inelastic deformation. The yield stress for the material subjected to plastic deformation ( $\epsilon_p=0.01$ ) is shown by a dashed line. Both kinematic and isotropic hardening models were tested in our investigations.

All the data in Fig. III-3 and Fig. III-4 (excluding yield strength) is for the St52 structural steel, but can be applied to quite a wide range of steels, because minor variations in alloy content have negligible influence on these properties.<sup>12</sup>

The continuous cooling diagram for a material analogous to the investigated one is presented in Fig. III-5. The welding process considered is characterised by a very low cooling rate. It is evident from Fig. III-5 that in the investigated material the transformation ferrite-perlite happens at elevated temperature (approximately 650°C).

A Mises representation of the yield surface (assuming isotropic yielding) was used. Fig. III-6 demonstrates the difference between the kinematic- and isotropic hardening approaches.<sup>13,14,15,16</sup>

Isotropic hardening means that the yield surface changes size uniformly in all directions such that the yield stress increases (or decreases) in all stress directions as plastic straining occurs. Kinematic hardening introduces translation of the yield surface in stress space, leading to the appearance of nonisotropic material properties. It was used in models taking into account cyclic loading.

The plasticity models also need an elasticity definition to deal with the recoverable part of the strain.

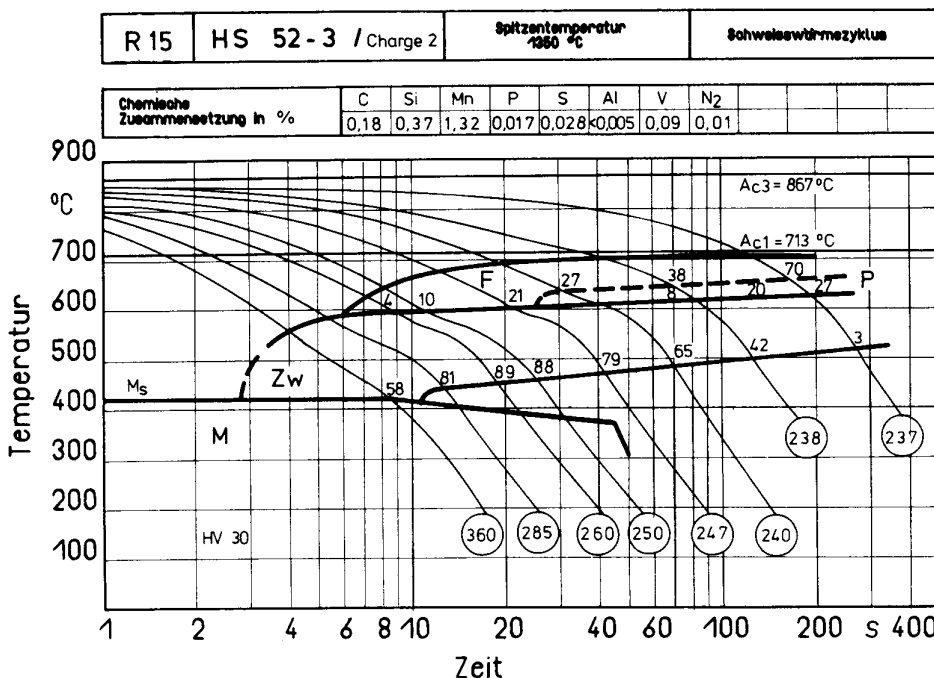


Fig. III-5. Continuous cooling diagram for the material analogous to the investigating one.<sup>17</sup>

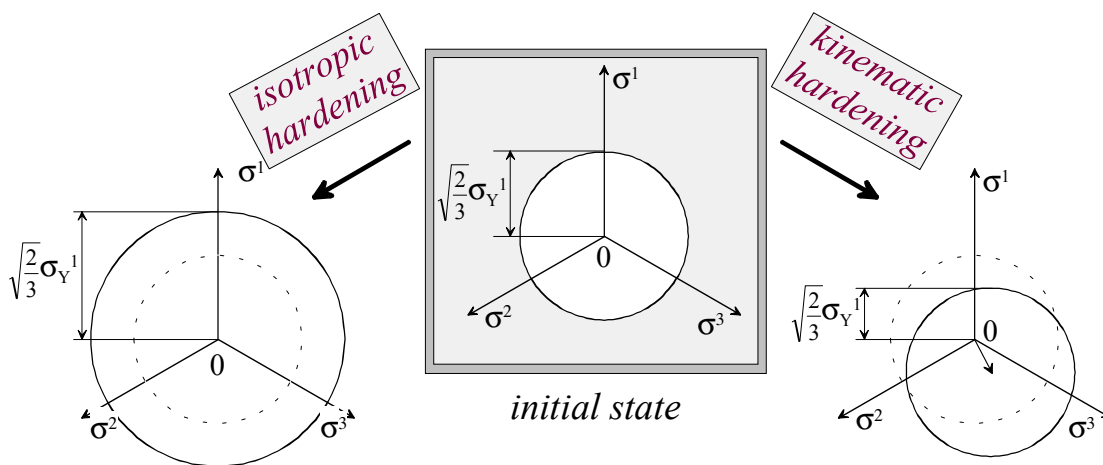


Fig. III-6. Three-dimensional representation of the hardening in the Mises isotropic and kinematic models (for metallic materials).

As mentioned above, the elastic part of the model is characterised by Young's modulus and Poisson's ratio. In our work isotropic linear elastic behaviour was assumed in all the simulations.

Experimenting with different types of hardening did not reveal significant changes in the output data, probably because of rather small deformations during the joining process.

### 1.3. Description of the welding process. Multi-electrode and multi-pass techniques

The present dissertation is dedicated to the investigation of two welding techniques based on the submerged arc welding (SAW) process. These techniques are: the three-electrode one-pass welding and the single-electrode welding completed in three passes.

The conventional SAW process did not change much from the time of its invention in 1935, when electric arc welding under a blanket of granulated welding flux, which completely submerged the welding zone, was first reported. The scheme of the process is shown in *Fig. III-7*.

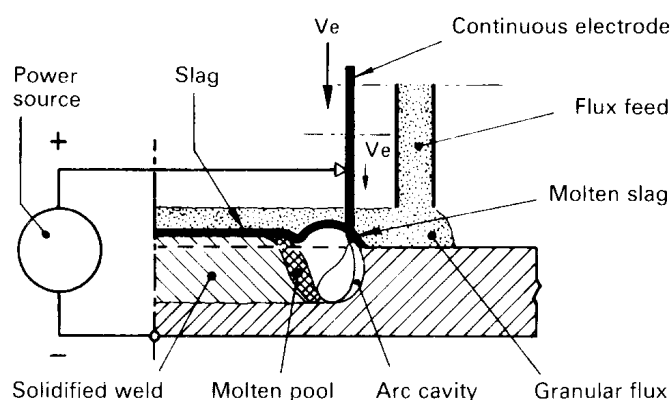


*Fig. III-7. Scheme of submerged arc welding.*<sup>18</sup>

Most small, and some medium-size shipyards, weld their flat panels on both sides, using SAW. The larger shipyards, producing larger flat panels, have developed the one-sided welding process, that involves the use of several heat sources.<sup>19,20,21,22,23,24</sup> In this case, no panel-turning devices are necessary, which gives a productivity increase of up to 50%.

*Fig. III-8* demonstrates a part of the equipment used for one-sided welding. In this figure the plate, which is seen in its cross-section, is clamped by a magnetic table. Under the seam the equipment for the flux copper backing (FCB) is seen.

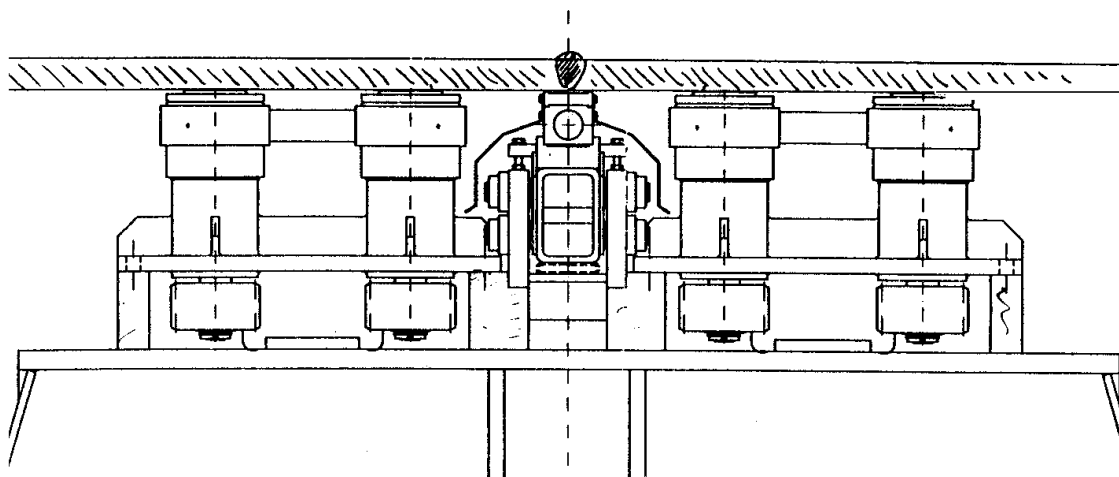


Fig. III-8. Drawing of a TTS one-sided welding station.<sup>3</sup>

The other scheme of the three-electrode one-sided welding process is shown in Fig. III-9. It demonstrates the case corresponding to the currently investigating scheme when the leading electrode is followed by two trailing electrodes. The main welding parameters used for simulations are listed in Table III-2.

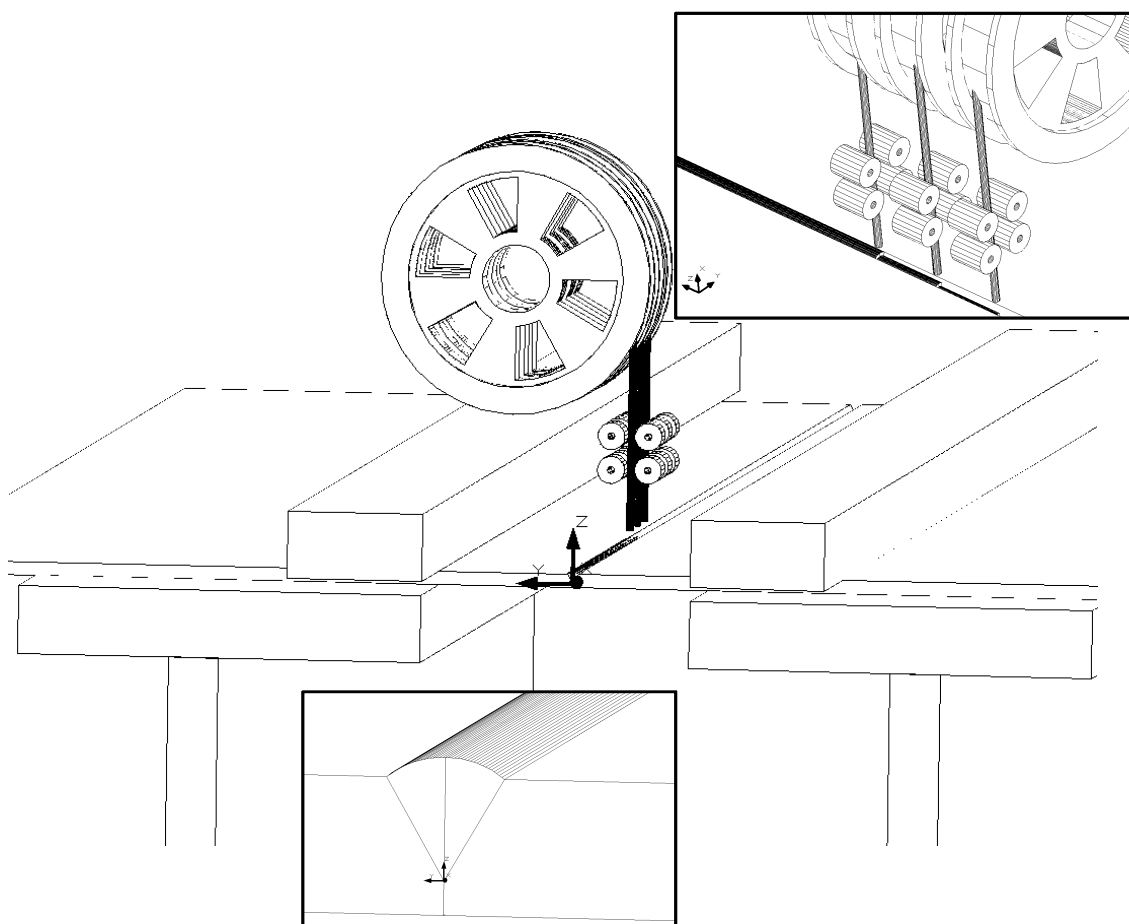


Fig. III-9. Scheme of the three-electrode one-sided welding process.

Table III-2. Welding parameters.

Plate thickness	$h$	20mm
Process		3-electrodes SAW
Welding speed	$v$	10mm/s
Gap between plates		0mm
Edge preparation		Y-60-5
Current, leading electrode (DC+)	$I_1$	$I_1=1200A$
Current, 2 <sup>nd</sup> electrode (AC)	$I_2$	$I_2=600A$
Current, 3 <sup>rd</sup> electrode (AC)	$I_3$	$I_3=700A$
Voltage, leading electrode	$U_1$	$U_1=32V$
Voltage, 2 <sup>nd</sup> electrode	$U_2$	$U_2=36V$
Voltage, 3 <sup>rd</sup> electrode	$U_3$	$U_3=38V$
Electrodes diameter	$d_{el}$	5mm
Distance between leading and 2 <sup>nd</sup> electrode	$l_1$	100mm
Distance between 2 <sup>nd</sup> and 3 <sup>rd</sup> electrode	$l_2$	110mm

#### **1.4. Conclusions**

In this section the process that is investigated in this dissertation is introduced and its main properties are described. Features of the technological implementation of the welding process are described. Based on the results presented in this section the following conclusions can be drawn:

1. The process under investigation (three-electrode submerged arc welding of medium-thick plates) is widely used in shipbuilding for joining plates to be used as parts of the ship hull.
2. A low cooling rate is typical for the considering welding process. Examination of the CCT diagram indicates that during the cooling stage the transformation  $\alpha$ -Fe into  $\gamma$ -Fe happens at elevated temperature (approximately 650<sup>0</sup>C). At this temperature the steel is still soft. This fact allows us to make an assumption about insignificant influence of the hysteresis in the mechanical properties on the residual stress and strain distribution.
3. We investigate the one-sided welding process, which may increase productivity up to 50% compare to two-sided welding, which require heavy panel-turning devices. The use of the tandem SAW allows significantly increase productivity.

## 2. HEAT TRANSFER ANALYSIS METHODS

### 2.1. Analytical solutions

#### 2.1.1. Variety of analytical solutions

The creation of the analytical model consists in finding the function that can describe the temperature field in the body under consideration. At present, many different analytical models are known.

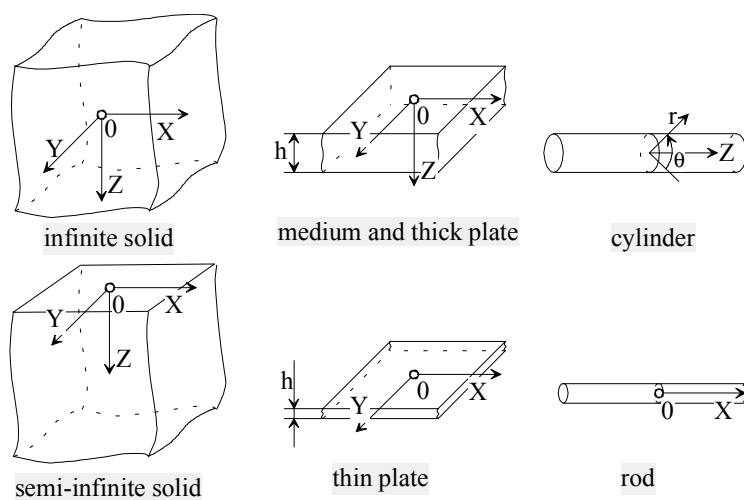


Fig. III-10. Different schemes of idealised body configuration.

To start creating the analytical model we first have to decide what kind of geometry approximation would be most suitable for the our purpose. There are several alternatives:

- infinite body;
- semi-infinite body;
- infinite thin plate;
- infinite medium thick plate;
- infinite rod;
- infinite cylinder.

All of these geometry configurations are shown in *Fig. III-10*. This list can be expanded with additional help of the "method of images".<sup>25</sup> This method allows to limit the body in any direction. At the same time it introduces into the model additional calculating difficulties, the model becomes more complicated.

The next step towards analytical model creation is to choose the heat source approximation. There are three principles of idealised heat source classification. It can be classified by: time of action, mobility and dimensions.

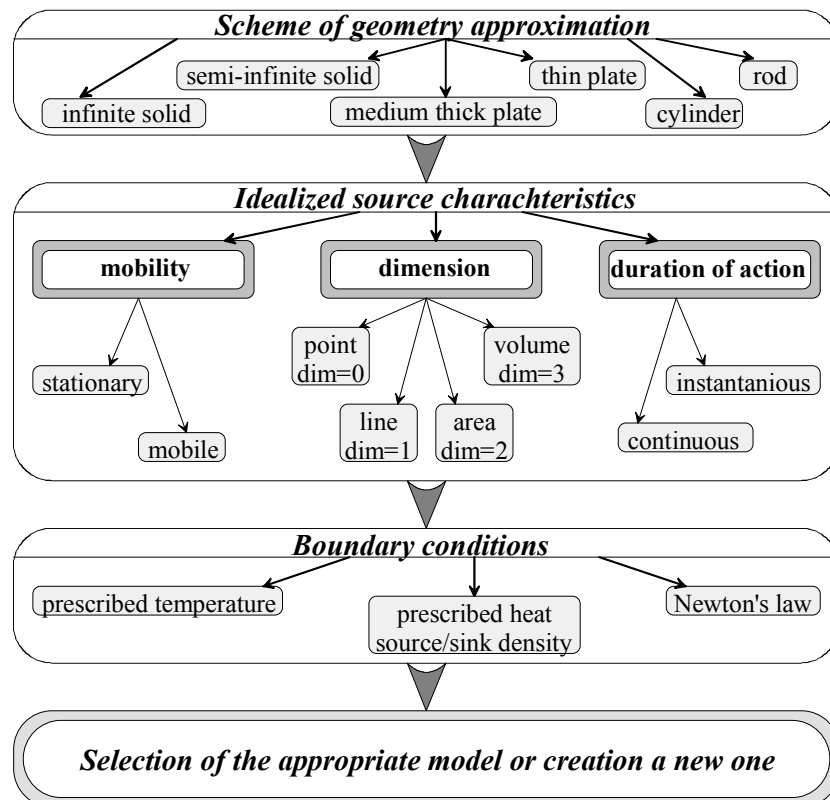


Fig. III-11. Flow chart of the model selection process.

By the time of action the heat source can be instantaneous or continuous. The source can be stationary or mobile. By the area of distribution the source can be presented as a dot (dim=0), line (dim=1), plane (dim=2) and volume (dim=3). To get a general view, all the classifications are presented in the scheme on Fig. III-11.

### 2.1.2. Model of the temperature distribution during multi-electrode SAW

Within the context of this dissertation the variety of the existing analytical models will not be considered in more detail. Instead of reviewing the simple analytical models, we will have a good look at the model corresponding to the experimental case described in CHAPTER III, section 1.

#### 2.1.2.1 Selection of the appropriate model

Briefly about initial data (for more information – see CHAPTER III, section 1.3). The welding process involves multi-electrode submerged arc welding with 3-electrodes used in shipbuilding. The experiments were conducted by Merete Henriksen with the company TTS on two NVE360 (according to the Det norske Veritas designation) 20mm-thick steel plates.<sup>3</sup> The process was characterised by a very high heat input:

- first (leading) electrode: ~35kW;

- second electrode: ~20kW;
- third electrode: ~25kW.

To model the thermal cycles during this process we have to choose most appropriate model from the perspective of expected accuracy of the required data output and relative simplicity of the model. In other words, the input should correspond to the required output. For example, as will be demonstrated further, for the practical applications involving cooling rate predictions below 800<sup>0</sup>C, even a simple 1D solution can be used.

Let us follow the steps described in scheme from *Fig. III-11*. If we are interested in the geometry of the weld seam and the heat affected zone, then experience tells us that for such a combination of plate thickness and heat input we should take a medium thick plate as a real geometry approximation. For example, if this combination were more extreme, such as thicker plate and less powerful source, then the isotherms in the relatively high temperature range (700–1500<sup>0</sup>C) in a cross-section would have the shape of semicircles. Hence the model for a semi-infinite solid would be appropriate.

Going to the idealised source characteristics we can easily decide that the source should be mobile and continuous. To get the most realistic results we need to take a 3D source distribution. But this choice would greatly complicate the creation and consequently the solution of the analytical model. So, we can try to use a line heat source for every acting welding arc. To make it more practical we can introduce into the model a function that would be responsible for the through-thickness heat source distribution. This function introduces as an additional multiplier and will be discussed later in more details.

As a starting point we assume that the plate surfaces are impermeable to heat (special case of the prescribed heat source/sink over the surface).

### 2.1.2.2 Mathematical modelling

The considerations presented above lead us to a model based on several assumptions:

- the plate is isotropic, relatively thick and infinitely wide and long;
- the heat source distribution through the plate thickness  $q_{nm}(z)$  can be arbitrarily chosen but must be specified;
- the material physical properties (i.e. thermal conductivity  $\lambda$  and thermal diffusivity  $a$ ) are temperature independent;
- the initial temperature  $T_0$  is constant.

There is a basic steady state solution for the moving point source in a thin medium thick plate:

$$T(x, y, z) - T_0 = \frac{q_0 / h}{2\pi\lambda} \cdot \exp\left(-\frac{vx}{2a}\right) \cdot \left[ \sum_{i=-\infty}^{i=+\infty} (1/R_i) \exp\left(-\frac{v}{2a} R_i\right) \right] \quad \text{eq. III-1}$$

where:

$R_i = \sqrt{x^2 + y^2 + (z - 2i \cdot h)^2}$  is the distance from real and imaginary heat source to point  $P$ , [m]  
 $q_0$  is source net power, [W];

$v$  is the welding speed, [m·s<sup>-1</sup>];  
 $x, y$  are Cartesian co-ordinates, [m];

In the case of slow convergence of the sum in the *eq. III-1* it can be expanded in the Fourier cosine series. Using the integral number N 3.961.2 in Gradshteyn's hand-book<sup>26</sup>

$$\int_0^{\infty} \exp\left[-\beta\sqrt{\gamma^2 + u^2}\right] (\gamma^2 + u^2)^{-1/2} \cos au \cdot du = K_0(\lambda\sqrt{a^2 + \beta^2}) \quad \text{eq. III-2}$$

it is possible to rewrite *eq. III-1*.<sup>27</sup>

$$T(x, y, z) - T_0 = \frac{q_0/h}{2\pi\lambda} \cdot \exp\left(-\frac{vx}{2a}\right) \cdot K_0\left(\frac{vr}{2a}\right) \cdot F_0(r, z); \quad \text{eq. III-3}$$

$$F_0(r, z) = 1 + 2 \sum_{i=1}^{\infty} \cos \frac{\pi iz}{h} \cdot K_0\left(\frac{vr}{2a} \sqrt{1 + \left(\frac{2\pi ai}{vh}\right)^2}\right) \cdot K_0\left(\frac{vr}{2a}\right)$$

where:

$r$  is the distance from the source ( $r = \sqrt{x^2 + y^2}$ ), [m];

$K_0$  is the modified Bessel function of second kind and zero order.

But we are interested in a multi-source solution which takes into account the line heat source through-thickness distribution. Using the function of the through-thickness power distribution expanded in the Fourier cosine series, the function  $F_0$  can be verified by introducing an additional multiplier  $I_{im}$ . The principle of superposition allows us to sum the effects of individual sources, and in such a manner the *eq. III-3* can be transformed in the following way:<sup>28</sup>

$$T(x, y, z) - T_0 = \sum_{n=1}^N \frac{q_n/h}{2\pi\lambda} \cdot \exp\left(\frac{v(x-x_n)}{2a}\right) \cdot K_0\left(\frac{vr_n}{2a}\right) \cdot F_n(r_n, z); \quad \text{eq. III-4}$$

$$F_n(r_n, z) = 1 + 2 \sum_{i=1}^{\infty} \cos \frac{\pi iz}{h} \cdot K_0\left(\frac{vr_n}{2a} \sqrt{1 + \left(\frac{2\pi ai}{vh}\right)^2}\right) \cdot I_{ni}/K_0\left(\frac{vr_n}{2a}\right)$$

$$I_{ni} = \sum_{m=1}^{M_n} I_{nim} = \sum_{m=1}^{M_n} \int_0^h \frac{q_{nm}(z)}{q_n} \cos \frac{\pi iz}{h} dz;$$

$$r_n = \sqrt{(x-x_n)^2 + (y-y_n)^2};$$

where:

$N$  is the number of welding arcs;

$q_n$  is the total net power of the n<sup>th</sup> heat source [W];

$r_n$  is the distance between the point located at  $x, y, z$  and the axis of the n<sup>th</sup> heat source [m];

$F$  is the function responsible for the heat source distribution effect on the steady state temperature field;

$M_n$  is the number of elementary sections in which the n<sup>th</sup> heat source distribution is divided (see *Fig. III-13*);

$x_n, y_n$  are co-ordinates of the n<sup>th</sup> heat source [m].

The scheme of the process itself and some symbol designations are shown in Fig. III-12.

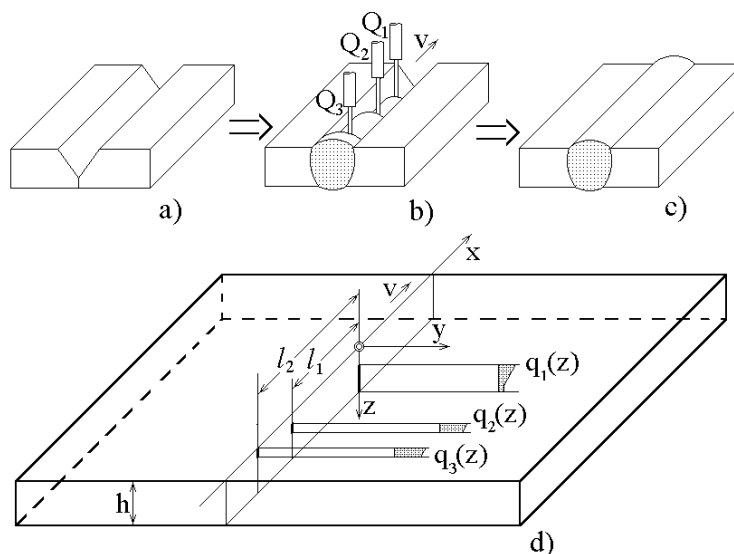


Fig. III-12. Multi electrode SAW process configuration:  
 a) edge preparation;  
 b) welding process;  
 c) welded joint;  
 d) calculation scheme for the welding process.

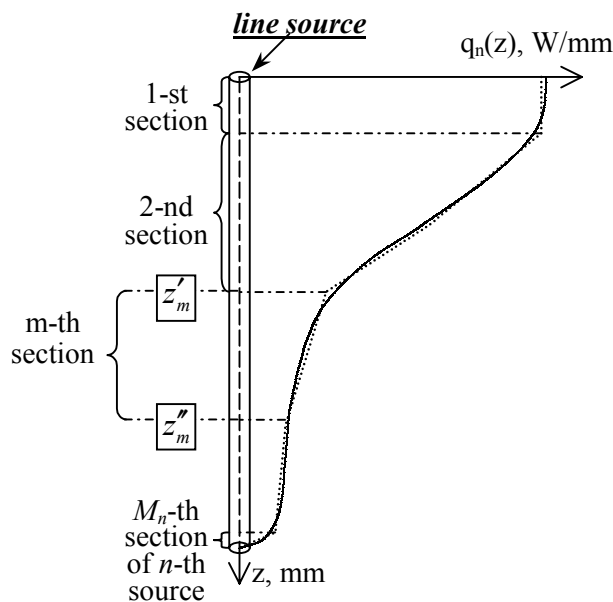


Fig. III-13. Through thickness power distribution of the line heat source;  
 — actual distribution;  
 ..... linear interpolation of the distribution.

If the source is concentrated in one point on the plate surface then  $I_i=q$ . If the power  $q_{nm}(z)$  is distributed linearly in the section  $z'_m, z''_m$ , i.e.  $q_{nm}(z)=A+Bz$  (where A and B are constants), then<sup>27, 29</sup>

$$I_{im} = \frac{h}{\pi i} (A + Bz_m'') \sin \frac{\pi iz_m''}{h} + \left( \frac{h}{\pi i} \right)^2 B \cos \frac{\pi iz_m''}{h} - \frac{h}{\pi i} (A + Bz_m') \sin \frac{\pi iz_m'}{h} - \left( \frac{h}{\pi i} \right)^2 B \cos \frac{\pi iz_m'}{h}; \quad \text{eq. III-5}$$

For more information about the function  $F$  see Proceedings of welding conference LUT Join'99.<sup>28</sup>

eq. III-4 does not take into account the heat loss from the surface. Usually, this kind of heat transfer is negligible, except in the welding of thin plates. However, ME SAW is characterised by very high heat input and low cooling rate, so even for thick plates (tens of millimetres) the heat loss can not be neglected because of very long thermal cycles.<sup>30</sup> Convective heat transfer from the surface can be accounted for approximately by introducing an additional correction factor in eq. III-4:

$$T(x, y, z)|_{\alpha>0} = T(x, y, z)|_{\alpha=0} \cdot \exp(-bt); \quad \text{eq. III-6}$$

where

$$b = \frac{\alpha_1 + \alpha_2}{c\rho h}$$

and  $t$  is the time after the source has passed the cross-section where the point  $x, y, z$  is located [in seconds]. The parameters  $\alpha_1, \alpha_2$  are coefficients of convective and radiation heat transfer from the top and bottom side of the plate, respectively [ $\text{W}\cdot\text{m}^{-2}\cdot\text{K}^{-1}$ ].

The first function on the right hand-side of eq. III-6 corresponds to eq. III-4. The use of a heat loss factor in the form of an additional multiplier is accurate for the 1D flow case. For the 2D case (when  $F$  is equal to unity in eq. III-4), such a procedure gives an error of less than 1% if  $(vr/2a) < 1000$  and  $(4ab/v^2) < 0.01$ . In the following, we shall assume that this correction is valid for the 3D case as well. An exact solution of the 3D problem with boundary conditions of the 3rd kind (Newton's boundary conditions) will largely complicate the analysis, without necessarily contributing to an improved confidence in the predictions.

## **2.2. Finite element analysis**

### **2.2.1. Variety of finite element solutions**

To solve different convective heat transfer problems a variety of finite element models can be applied. The appropriate model should be chosen considering the type of results expected from the model. Within the limits of this dissertation implementation of 2D models in the  $XY$  and  $YZ$  planes (see Fig. III-9 on page 67) and complete 3D heat transfer analysis model will be reviewed.

The basic principles of the ABAQUS are presented in Appendix E in addition to the information highlighted in the following sections.

The 2D models have important advantages in computing time and necessary computer resources.<sup>31,32,33</sup> At the same time a 2D analysis neglects the heat propagation in the direction perpendicular to the considered plane. By this means the calculated temperatures turn out to be over-predicted compared to the analogous 3D scheme. These over-predictions are most noticeable in the high temperature regions where the temperature gradient and, consequently, the heat flow density (see *eq. II-2*) is higher.

The case of butt-welding of plates with Y-shaped edge preparation, investigated in the current dissertation, is obviously symmetrical about the plane passing through the weld centreline perpendicular to the plates surfaces. This fact allows us to consider only one half of the real structure, compensating for the lack of the details by implementation of the corresponding boundary conditions.<sup>34</sup> In the case of heat flow analysis, the surface coincident with the symmetry plane, is assumed to be impermeable to heat. The actual heat input consumed on the joining process is divided by two.

### 2.2.2. "Element birth" technique

If material is added to or removed from a system, certain elements in the model may become "existent" or "non-existent". In ABAQUS coding in the \*MODEL CHANGE option, the parameters ADD and REMOVE can be used to deactivate or reactivate selected elements.

This procedure can be used for modelling the effects of structural changes. In finite element models created for welding applications, it can model the process of filler metal addition. In the case of metal cutting, it can model the parts removed.

To achieve the "element death" effect, the ABAQUS does not actually remove the elements. Instead, it just deactivates them. In the case of the heat flow model, the actual conductivity of the material is set to zero.

In a similar way, when elements are "born", they are not actually added to the model. They are simply reactivated. During the reactivation step the thermal conductivity of heat transfer elements is ramped up from zero over the step. To add an element into the model, first, the model should be created whole. Next step is to remove the desired element in order to reactivate it when needed.

### 2.2.3. 2D YZ-plane model for temperature distribution in the cross-section of the plate

In terms of the calculation time and complexity of the model, the simplest model for the heat transfer analysis is 2D YZ-plane model (gives results for input data to the plane strain thermal stress analysis). This transient problem is handled as totally uncoupled with the mechanical part of the task. In other words, the temperature field is calculated without consideration of the stress/deformation.



third elements are distributed among 13 elements each; the second – among 10 elements.

In the case of rough mesh, the first and second sources are located within only one element each; the last source is assumed to be applied to the two elements situated close to the surface.

In order to simulate the addition of the melted electrode into the weld, the reactivated elements corresponding to the heat sources are introduced with initial temperature chosen to be 2000<sup>0</sup>C. The total heat input is then recalculated to take into account the excessive energy.

### 2.2.3.3 Calculation procedure

Time incrementation in the analysis is controlled automatically by ABAQUS. It means that ABAQUS chooses the time step such as to keep the largest temperature change at every integration point less than an allowed value (here  $\Delta T_{max}=50^0\text{C}$  was used). At the time when the heat source starts to be active, the time step  $\Delta t$  is approximately  $6.5 \cdot 10^{-3}\text{s}$ . By the end of the heating process (0.8<sup>th</sup> – 1.001<sup>th</sup> seconds), the time increment is slightly increased up to  $8.3 \cdot 10^{-3}\text{s}$ . During the cooling stage the time step grows up to the maximum allowed by the user value (500s for this particular problem).

In ABAQUS time integration in transient problems is done with the *backward Euler method* (sometimes also referred to as the modified *Crank-Nicholson operator*). This method is unconditionally stable for linear problems.

Heat transfer problems can be non-linear because the material properties are temperature dependent or because the boundary conditions are non-linear. The nonlinearity associated with the temperature dependence of the material properties is mild because the properties do not change rapidly with temperature.

The problem considered here does not take into account the temperature dependence of the surface heat transfer coefficient. By this means the heat transfer problem is mildly non-linear. ABAQUS uses an iterative scheme to solve non-linear heat transfer problems. This scheme is based on the *Newton iteration method*.

In the model DC2D4 elements (in the ABAQUS specification) are used. These 4-nodes elements with linear interpolation have only the temperature as a degree of freedom. As output the nodal values of the temperature are saved in order to be used as input data for the thermo-mechanical part of the problem.

### 2.2.4. 2D shell-elements model for temperature distribution in the plane of the plate

For calculation of the in-plane deformations (longitudinal- and transverse shrinkage) the temperature calculated with the 2D  $XY$ -plane temperature model can be used. Results from this model would be an input for the plane-stress 2D model.

#### 2.2.4.1 2D solid elements versus 2D shell-elements

Adaptation of the 2D solid elements can not be considered for the case of butt welding of plates. The reason for this is the lack of possibility to introduce the heat exchange between the body and the surroundings by standard methods. Heat exchange with an element can be introduced only in the plane of this element. Meanwhile, the large plate surfaces have a normal perpendicular to the possible 2D element plane.

Heat loss in the 2D models can be taken into account approximately. For this purpose, additional user subroutines, written in FORTRAN, would be needed. Unfortunately, technical problems hindered this alternative.

At the same time, the 2D shell-elements have additional integration points (further explanation below). If the 3D model similar to the 2D model has few elements in the through-thickness direction, then the 2D shell-element model loses its usefulness (reduction of the dimensionality of the problem does not lead to a reduction of the calculation time). For example, the model with only one element in the through-thickness direction is clearly less time-consuming.

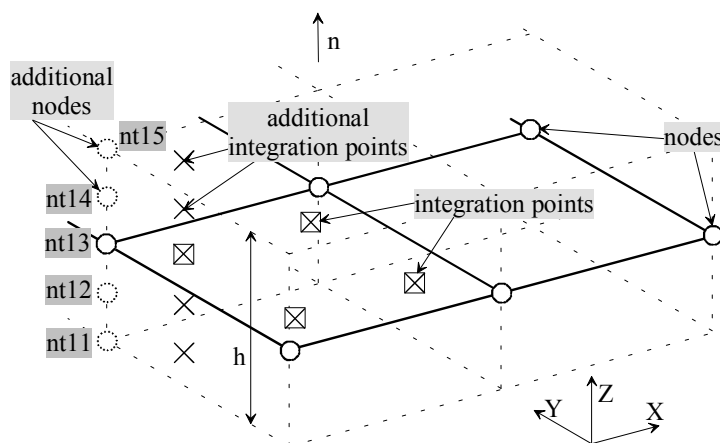


Fig. III-15. Example of shell section definition with five section points in the through-thickness direction; the node temperature is denoted by  $nt$ .

Heat transfer shell elements provide the values of temperature at a number of points through the thickness at each shell node (see Fig. III-15). In ABAQUS specification the temperature on the bottom surface of the shell is degree of freedom 11. The temperature on the top surface is degree of freedom  $10+n_s$ . The parameter  $n_s$  is the total number of

integration points used through the shell section. In such a manner, in the particular case presented in *Fig. III-15*, five values of the node temperature (*nt11–15*) refer to a single integration node.

ABAQUS allows the user to specify the number of section points used for cross-section integration and through-thickness direction temperature interpolation at each node. *Simpson's rule* is used for integration through the shell thickness.

#### 2.2.4.2 Mesh for 2D heat flow analysis with shell-elements

The model considered here is based on the mesh shown in *Fig. III-16*. The mesh has a constant step in the  $x$ -direction. This model consists of elements that are rather long in the welding direction (50mm instead of 10mm in the 3D model of smaller specimens, introduced later).

Along the  $y$ -direction the dimensions of the elements vary. The smallest elements of the presented mesh have dimensions  $5 \times 50$ mm. The small size elements are needed only in the region with high temperature gradient. In such a way the height of the elements increases with the distance from the weld centreline.

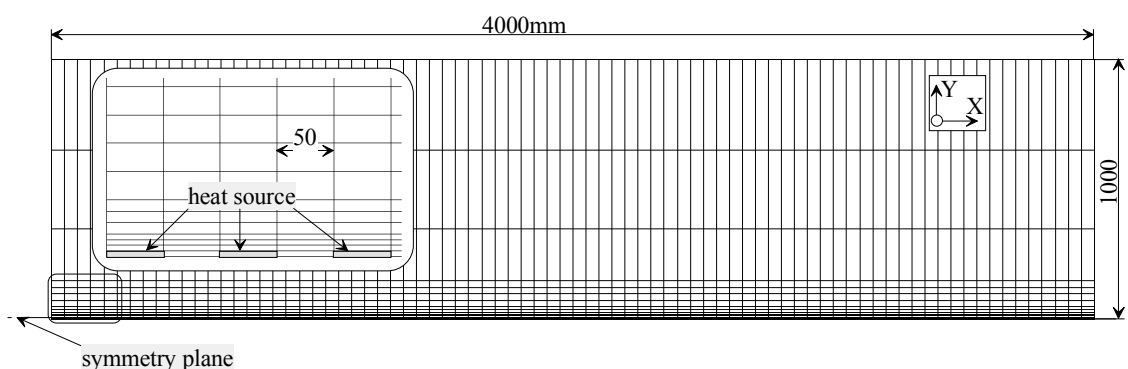


*Fig. III-16. Finite element mesh used for 2D XY-plane heat flow model.*

#### 2.2.4.3 Applied boundary and initial conditions, and calculation procedure

Like other models, the model considered here takes into account heat dissipation by convection from the free surfaces of the plate.

The position of the sources in *Fig. III-16* corresponds to the moment of time between the 20<sup>th</sup> and 25<sup>th</sup> seconds. In order to correspond to the welding conditions in the experiments (welding speed  $v=10\text{mm}\cdot\text{s}^{-1}$ ), the source shifts its position every 5 seconds by one element in the positive  $x$ -direction. The complete welding time is 420s. That is including gradual starting and finishing. Welding begins when the first of the acting three sources begins to function from 0.001 second. The process of heating is completed when the last source is terminated.

During calculation the time incrementation is chosen automatically by ABAQUS. The maximum allowed temperature change at every point of the model is  $\Delta T_{max}=100^{\circ}\text{C}$ . During the starting stage of heating the time step  $\Delta t$  is approximately  $1 \cdot 10^{-1}\text{s}$ . At the more stable stage of heating  $\Delta t \approx 4 \cdot 10^{-1}\text{s}$ . During the cooling stage the time increment automatically increases up to the maximum allowed by the user value, in this particular case  $\Delta t_{max}=500\text{s}$ .

In the model simple DS4 shell elements were applied. The model consists of 1120 elements and 1215 nodes. As an output, five nodal temperature values for every node are saved in order to be used as input data for the thermo-mechanical problem. For temperatures above  $500^{\circ}\text{C}$ , the values of *nt13* is approximately 0.5% higher than corresponding to the free surfaces with convective cooling *nt11* and *nt15* (see *Fig. III-15*). It cannot have a significant influence on the thermo-mechanical processes of metal deformation.

### 2.2.5. 3D heat flow model for butt welding of plates

The 3D model described in this section, is the most complicated, model for heat transfer analysis in this study. It gives results for input data to the complete 3D thermal stress analysis model.

This transient problem is handled as totally uncoupled from the mechanical part of the task. In other words, the temperature field in the model is calculated without consideration of the deformation heat.

No "element birth" technique was implemented, because it would highly complicate the problem.

#### 2.2.5.1 Finite element mesh and applied initial and boundary conditions

The model is based on the mesh shown in *Fig. III-17*. The smallest elements are situated close to the weld. The smallest elements have dimensions  $10 \times 5 \times 4\text{mm}$ . We need to keep a small size of the elements only in the region with high temperature gradient. In such a way, the width of the elements increases with the distance from the joint centreline.

To the surfaces of the elements situated along the plates free surfaces, convective heat exchange with the surroundings is applied. In the case of "steel-air" interface, the coefficient of convective heat transfer is assigned to be  $\alpha_c=30 \text{ J} \cdot \text{m}^{-2} \cdot \text{s}^{-1} \cdot \text{K}^{-1}$  (see *Fig. III-14*). When cooling by water-spraying has to be modelled, the heat transfer coefficient is  $\alpha_c=1000 \text{ J} \cdot \text{m}^{-2} \cdot \text{s}^{-1} \cdot \text{K}^{-1}$ .<sup>35,36</sup>

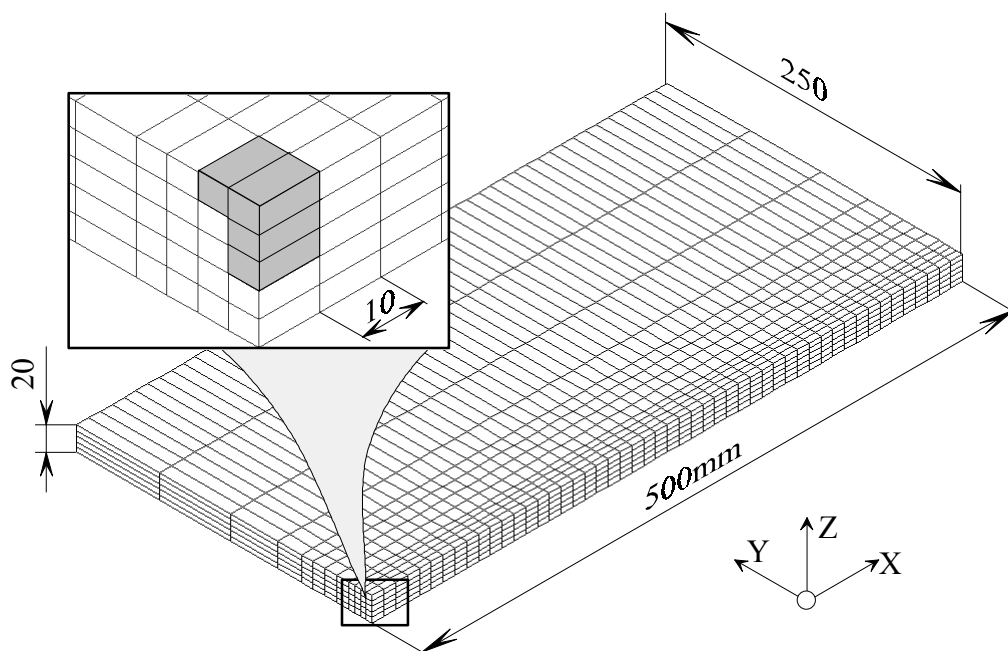


Fig. III-17. Finite element mesh for 3D heat flow analysis.

Each source is distributed among four elements arranged in the shape of the gap between the plates (Y-shaped groove preparation). The sources are specified using the \*DFLUX option (distributed heat flux) of the ABAQUS coding in  $[\text{J}\cdot\text{m}^{-3}\cdot\text{s}^{-1}]$ . The acting three heat sources are spaced along the  $x$ -axis according to the modelling case (100mm between the leading electrode and the second electrodes, and 110mm between the second and third electrodes).

In order to correspond to the welding conditions during the experiments (welding speed  $v=10\text{mm}\cdot\text{s}$ ), the source shifts its position every second by one element in the positive  $x$ -direction. The complete welding time is 70s. That is including gradual starting and finishing. Welding begins when the first source of the acting three begins to function from 0.001 second. The process of heating is completed when the last source is terminated.

#### 2.2.5.2 Calculation procedure

Time incrementation during the analysis is controlled automatically by ABAQUS. It means that ABAQUS chooses the time step such as to keep the largest temperature change in every integration point less than an allowed value (here  $\Delta T_{\max}=50^{\circ}\text{C}$  was used). By the time when the heat source starts to be active, the time step  $\Delta t$  is approximately  $5\cdot 10^{-3}\text{s}$ . By the end of the heating process ( $70^{\text{th}} - 80^{\text{th}}$  seconds), the time increment is slightly increases up to  $8\cdot 10^{-3}\text{s}$ . During the cooling stage the time step grows up to the maximum allowed by the user value (500s for this particular problem).

In ABAQUS time integration in transient problems is done with the *backward Euler method* (sometimes also referred to as the modified *Crank-Nicholson operator*). This method is unconditionally stable for linear problems.

The problem considered here does not take into account the temperature dependence of the surface heat transfer coefficient. By this means the heat transfer problem is mild non-linear. ABAQUS uses an iterative scheme to solve non-linear heat transfer problems. This scheme is based on *Newton iteration method*.

In the model three-dimensional solid DC3D8 elements (in the ABAQUS specification) are used. These 8-nodes brick with linear interpolation have only the temperature as a degree of freedom. As output nodal values of the temperature are saved in order to be used as input data for the thermo-mechanical part of the problem.

## 2.2.6. Methodical example of heat flow analysis

### 2.2.6.1 Purpose of the example

This example serves to determine the mesh accuracy for 2D and 3D simulations. In the case of the 2D model the selection of an appropriate element size is not very important because it is possible to choose finer mesh than necessary. For the 3D scheme the element size, and consequently the number of elements, plays a crucial role in the process of modelling itself. So, to determine the roughest acceptable mesh for the 3D model is one of the first steps on the way towards getting reliable results.

### 2.2.6.2 Method

The best way to determine the accuracy of the mesh would be to compare the calculated results with experiment. Unfortunately, we did not have experimental data that could be used for this purpose. Based on a comprehensive analysis of the problem, the decision was made to compare an approximate numerical solution with an exact analytical solution for a specially formulated problem. A significant criterion would be the maximum temperature distribution in a cross-section of the weld.

### 2.2.6.3 Exact solution

As mentioned, the analytical solution was chosen to be the reference for the approximate 2D and 3D models based on finite element analysis. The analytical model presented in *Fig. III-18* takes into account finite dimensions in  $z$ - and  $y$ -direction. The plate is supposed to be infinite in the  $x$ -direction. The width of each of the two joining plates equals 250mm. In order to introduce a cooling process, the most realistic would be to take into consideration convective heat loss from the free surfaces. But, unfortunately, this would make the solution not exact. The decision about keeping the

outer surfaces at a constant zero temperature ( $T(t)=0$ ) was made. As seen from Fig. III-18, in order to keep the temperature on a zero level at the outer surfaces, two additional heat sinks of similar capacity (-80kW each) were entered.

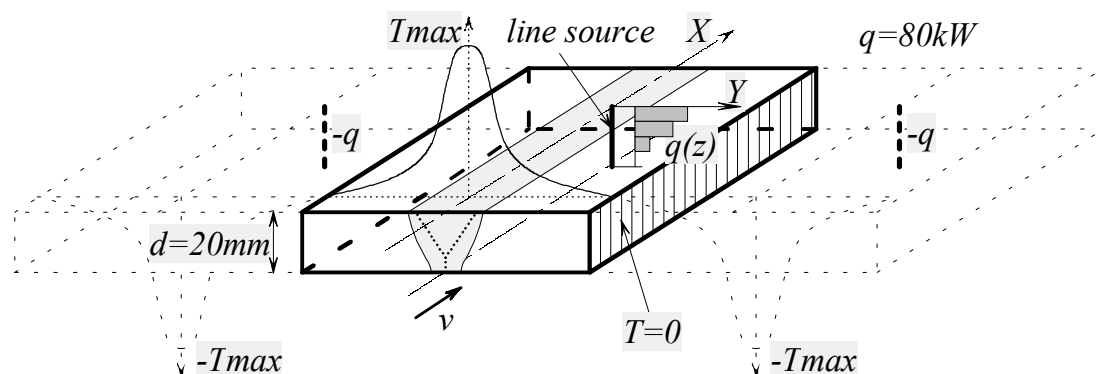


Fig. III-18. Scheme of the analytical model for the methodical example.

In order to reproduce the real heat source distribution in space, a line source with a nonuniform through-thickness power distribution was introduced.

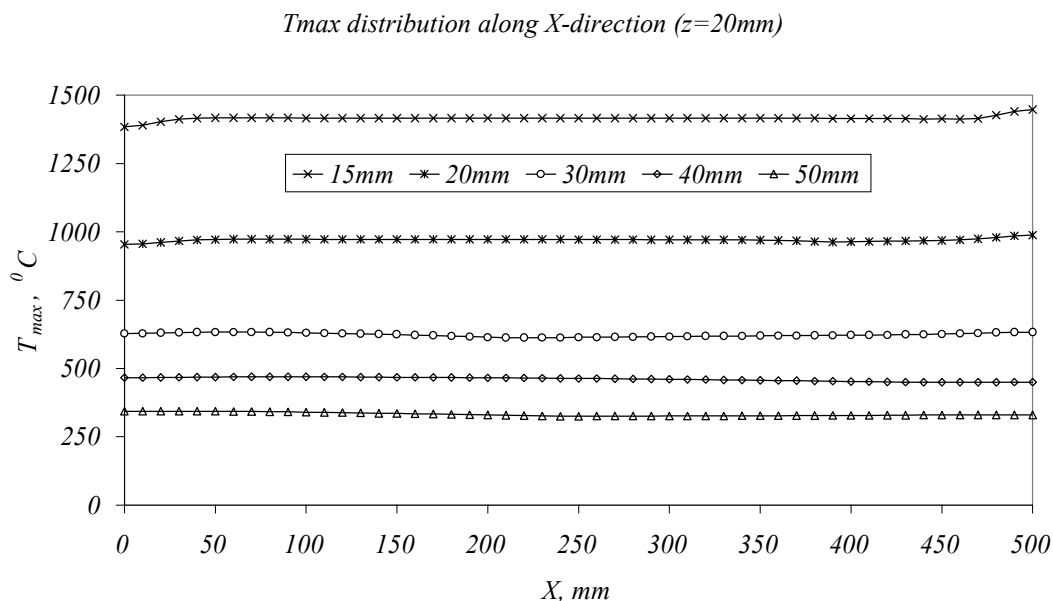
The material and process characteristics are listed in Table III-3. Thermal properties were chosen equivalent to low-alloyed steel properties. The welding process characteristics were chosen similar to the process investigated in this thesis. The main difference was that this example involves a one-electrode process instead of a three-electrode process.

Table III-3. Material properties and parameters of welding process.

Characteristic	Abbreviation	Value
Net power	$q$	80kW
Welding speed	$v$	10mm/s
Thermal diffusivity	$a$	$5 \cdot 10^{-6} \text{m}^2/\text{s}$
Thermal conductivity	$\lambda$	$25 \text{W}/\text{m} \cdot ^\circ\text{C}$
Volume heat capacity	$c\rho$	$5 \cdot 10^6 \text{J}/\text{m}^3 \cdot ^\circ\text{C}$

#### 2.2.6.4 3D FEA heat flow model

In the 3D model a relatively rough mesh was used. The smallest elements had dimensions  $4 \times 5 \times 10 \text{mm}$  ( $h \times w \times l$ ). Based on a great number of experiments with simulations, it can be concluded that much longer elements could be used with no serious harm done to the solution accuracy. This fact makes sense because of the very long thermal cycles (very elongated isotherms) and, hence, the almost 2D character of the heat flow at some distance behind the moving source. Totally the model consists of 3000 elements and 3978 nodes. Similarly to the analytical model, the nodes lying on the outer surfaces of the plate were forced to have a constant zero temperature.



*Fig. III-19. Distribution of the  $T_{max}$  along x-direction at some distances from the weld centreline.*

The heat source was arranged as a column of elements, not as an infinitely thin line in the case of analytical model. It is wise to assume that the influence of this difference vanishes at the distance approximately equal to the diameter of the column. It corresponds to a temperature range  $T < 1500^{\circ}\text{C}$ . So, for the temperature range  $1500 < T_{max} < 0^{\circ}\text{C}$ , the models can be considered to be identical.

*Fig. III-19* demonstrates that the finite length of the plate, under consideration in the 3D model, does not have an effect after a 50mm distance from the beginning and the end of the weld, at least for the temperature range  $T < 1500^{\circ}\text{C}$ . We can clearly see this by the horizontal area on the graphs corresponding to the  $T_{max}$  distribution in a direction parallel to the welding. The curve corresponding to the 15- and 20mm distance from weld centreline, clearly indicates the expected  $T_{max}$  distribution. Compared to the rest of the curve, in the first 50mm zone  $T_{max}$  has lower values. This can be explained by a gradual entering into a pseudo-steady state of the heat flow.  $T_{max}$  increases near the end of the weld due to an end effect (the edge of the plate acts as a “mirror” for the heat flow).

Summing up the above it can be concluded that the problem definition for the 3D model is identical to the exact analytical solution. This is true at least for temperatures  $1500 < T_{max} < 0^{\circ}\text{C}$ . The only source of error is an error due to the roughness of the mesh and accuracy of the method.

### 2.2.6.5 2D FEA heat flow model

The solution of the 3D model is very time consuming. For optimisation of the welding process technique it is better to use a 2D model from which we can expect quite reliable results, too. For better comparison of the simulations, the mesh density in the case of the 2D model was chosen to be the same as for the 3D model. For later calculations the mesh density can be significantly increased, because it will not affect calculations cost much.

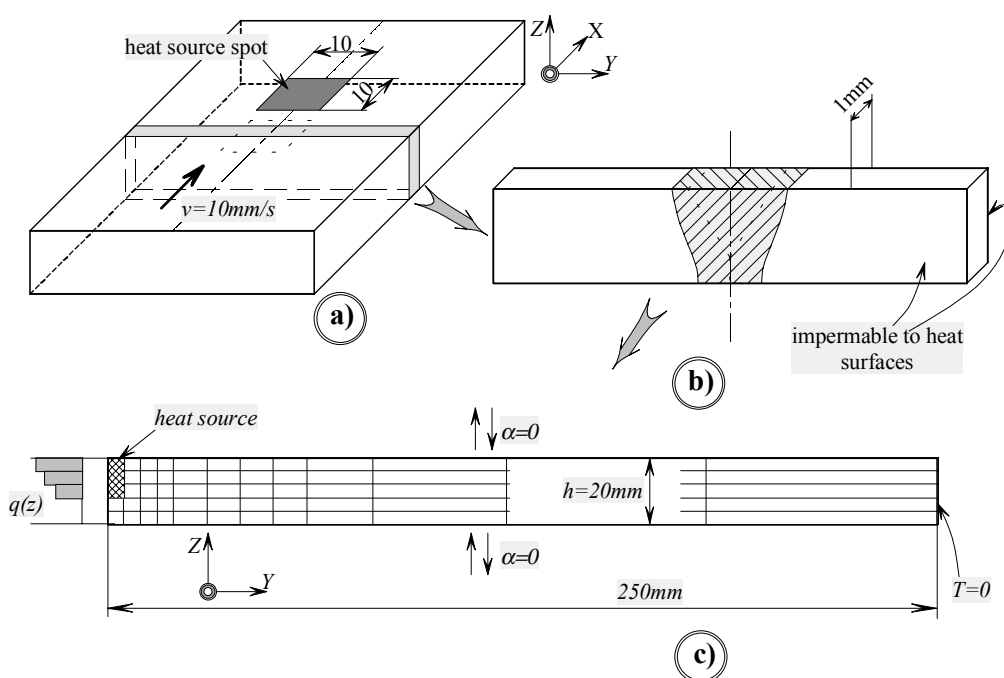


Fig. III-20. Scheme of 2D heat flow model; (a) – 3D plate; (b) – extracted thermally isolated cross-section of the plate; (c) – 2D finite element model.

In Fig. III-20 the scheme of the 2D heat flow model is presented. In the model a cross-section of the plate from 3D model is considered. The size of the acting heat source spot is assumed to be a square  $10 \times 10 \text{ mm}$ . In order to have comparable models, the heat source retention time is assumed to be 1s (the time needed for the heat source to cross the thin cross-section). As for all the models under consideration, the way to cool the plate down is to keep the outer edge of the plate at constant zero temperature.

Quite simple DC2D4 (after ABAQUS coding system) heat conduction elements were used in the model.

### 2.2.6.6 Discussion of results

In Fig. III-21 the results from all three models under investigation are presented. The comparison reveals a very good agreement of the approximate 2D and 3D numerical models with analytical model results.

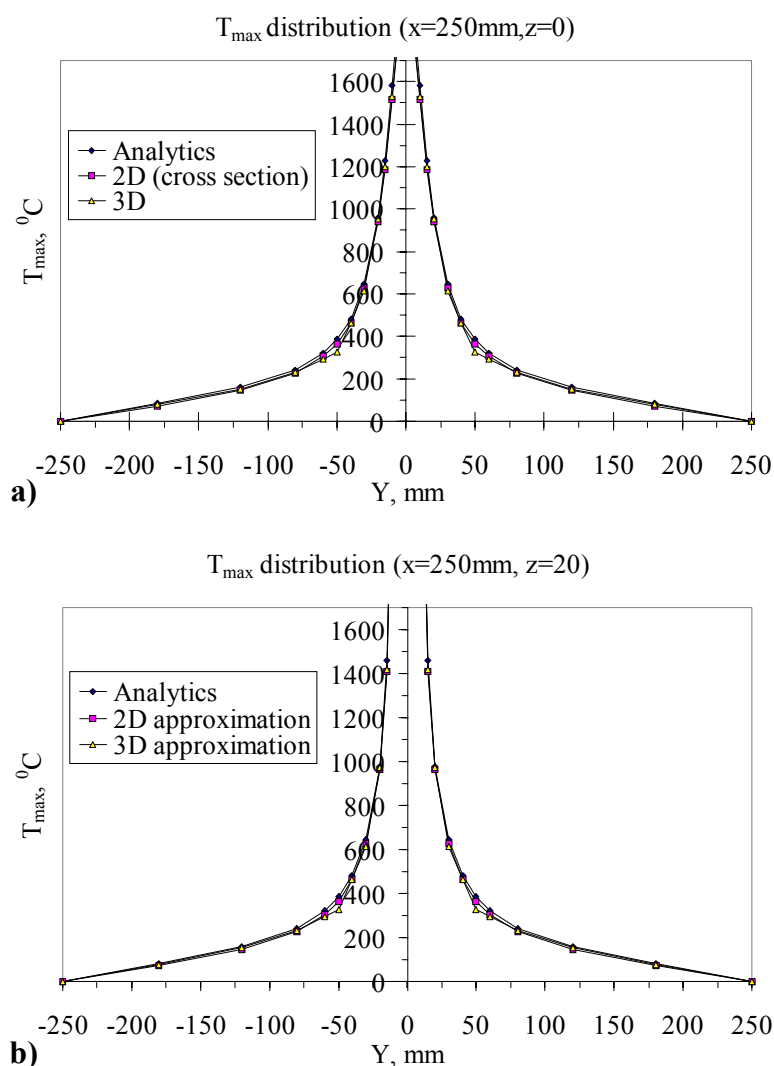


Fig. III-21. Distribution of the maximum temperatures at the points laying along the line perpendicular to the weld CL; (a) – on the bottom surface ( $z=0\text{mm}$ ); (b) – on the top surface ( $z=20\text{mm}$ ).

Fig. III-22 shows the direct representation of the error of the method depending on the  $T_{max}$  magnitude. Mostly the level of error is about 5%. It is an excellent demonstration of the heat flow model accuracy. Overall, the 3D model shows a better agreement, except at two points around  $T_{max}=300^{\circ}\text{C}$ . This could be due to a missed maximum value of the  $T_{max}$  because the temperature field data were not recorded at every increment in time. We had to keep the file size under 2Gb (actual limitation on a file size) and the 3D solution is not only a time-consuming but a hard-disk space consuming process too.

The error peaks occur in the  $T_{max}<400^{\circ}\text{C}$  temperature region for both models. This can be explained by the too rough mesh in the corresponding part of the plate. Anyhow, the maximum value of the error is 16%. This figure is quite acceptable for our purpose.

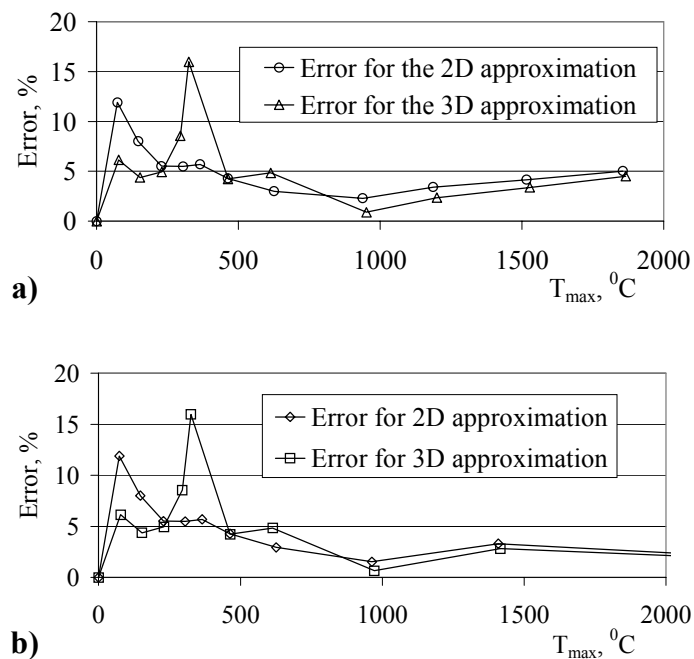


Fig. III-22. 2D and 3D heat flow model error as a function of actual values of  $T_{max}$ : (a) – for the temperature distribution on the bottom surface of the plate ( $z=0\text{mm}$ ); (b) – for the temperature distribution on the top surface of the plate ( $z=20\text{mm}$ ).

### **2.3. Conclusions**

In this section both analytical and numerical methods of the heat flow analysis, adapted for investigating welding procedure, are presented. Typical features of the different solutions are described. Based on the context of this section the following conclusions can be drawn:

1. The 2D model, suggested for the heat flow analysis in the cross-section of the plate, includes an "element birth" technique, allowing to simulate the filler metal addition.
2. An analytical scheme, taking into account an arbitrary through-thickness moving heat source distribution and convective heat loss from the free surfaces, was suggested for evaluation of the accuracy of the numerical methods.
3. Based on the methodical example, we can state that the suggested mesh and time incrementation for 2D and 3D heat flow models approximate the exact solution with 95% accuracy in the temperature interval  $500^{\circ}\text{C} < T < 1500^{\circ}\text{C}$  (in the temperature interval  $0^{\circ}\text{C} < T < 500^{\circ}\text{C}$  the accuracy drops down to 84%).
4. The smallest element of the 3D model has dimensions  $4 \times 5 \times 10 \text{mm}$  ( $h \times w \times l$ ), but considerably longer elements could be used because of almost 2D character of the heat flow at some distance behind the arc.

### 3. STRESS AND STRAIN FIELDS ANALYSIS MODEL

#### 3.1. Variety of models for stress and strain fields analysis

In this work both residual and transient stress-strain fields caused by the welding procedure described in section 1 of the current chapter were analysed. In the context of this dissertation several models were tested:

- 2D sequentially coupled thermal-stress analysis involving plane strain elements models with different mesh density;
- 2D sequentially coupled thermal-stress analysis involving generalised plane strain elements models with different mesh density;
- 3D sequentially coupled thermal-stress analyses with different mesh density.

It should be mentioned that the 2D plane strain model is not reliable for the prediction of the angular deformation magnitude. Meanwhile, it can be used for comparison of how the different welding and boundary conditions affect the response of the structure. For one example, it is possible to determine how the final angular distortion will change due to modification of the edge preparation (varying the through-thickness power source distribution).

The main advantage of the 2D-scheme implementation is that it allows using a high-density mesh, without expecting the computational time to be days.

#### 3.2. Metal plasticity in ABAQUS

Plastic deformation in the thermal stress models, described in this section, is taken into account based on the incremental plasticity theory. Plasticity models used for calculations are written in ABAQUS as *rate independent models*. In other words, the response of the structure does not depend on the rate at which the material is strained. This is a default option in ABAQUS.

The rate dependent models can be included in the model by specifying the additional option (\*CREEP, \*RATE DEPENDENT, etc.).

A basic assumption of the elastic-plastic models is that the deformation can be divided into an elastic part and an inelastic part. It can be written in the additive strain rate decomposition:

$$\dot{\epsilon} = \dot{\epsilon}^{el} + \dot{\epsilon}^{pl} \quad \text{eq. III-7}$$

where  $\dot{\epsilon}$  is the total mechanical strain rate,  $\dot{\epsilon}^{el}$  is the elastic strain rate and  $\dot{\epsilon}^{pl}$  is the plastic strain rate.

The plasticity models have a region of purely elastic response. The yield function  $f$  defines the limit to this region of purely elastic response:

$$f(\sigma, T, H_{iso}) < 0 \quad \text{eq. III-8}$$

where  $s$  is the stress,  $T$  is the temperature and  $H_{iso}$  is *isotropic hardening* parameter. Models including *kinematic hardening* were also tested. The results are not represented in this dissertation.

Isotropic hardening is a default option. To include kinematic or combined hardening, the parameters HARDENING=KINEMATIC or HARDENING=COMBINED, should be included in the \*PLASTIC option.

Stress states with positive yield function can not occur because we have rate independent models. And, we have the yield constraint  $f=0$  during plastic flow.

When the material is flowing plastically the plastic part of the deformation is defined by the flow rule:

$$d\epsilon^{pl} = \sum \lambda \frac{\partial g}{\partial \sigma} \quad \text{eq. III-9}$$

where  $g(\sigma, T, H_{iso})$  is the flow potential,  $\lambda$  is the plastic flow rate whose value is determined by the requirement to satisfy the consistency condition  $\dot{f}=0$ .

In the models described below, the direction of flow is the same as the direction of the outward normal to the yield surface. Such models are called “*associated flow*” plasticity models. These models are accurate for materials in which dislocation motion provides the fundamental mechanisms of plastic flow. It fits the modern conception of the plasticity of the most metals.

### **3.3. 2D sequentially coupled thermal-stress model (plane strain and generalized plane strain)**

#### **3.3.1. Meshes for 2D plane strain and generalised plane strain analysis**

A scheme of 2D-plane strain model is presented in *Fig. III-23*. The mesh and the boundary conditions for the generalised plane strain model are the same, the only difference is implementation of different kind of elements.

Two meshes with different densities were tested. The smallest elements of fine mesh close to the weld have dimensions  $1 \times 1.67$ mm. The rough mesh has  $5 \times 4$ mm elements. In order to decrease the number of elements, the width of the elements increases significantly with the distance from the centreline. The texts of input files specially written for simulations under ABAQUS are presented in Appendix A3-A6.

The rough mesh for generalised plane strain analysis consists of 60 elements and 78 nodes. The fine mesh consists of 192 elements and 221 nodes.

It must be emphasised that computational time required for running the simulations was quite insignificant (see Table III-4). It allows us to say that the use of rough meshes in similar models for the sake of saving time is not necessary.

Table III-4. Comparative magnitude of CPU time for 2D-plane strain models, (in minutes).

	thermal analysis	stress analysis	$\Sigma$
fine mesh	18.5	8.0	26.5
rough mesh	12.5	5.0	17.5

### 3.3.2. Applied boundary conditions

Two types of boundary conditions were applied during simulations. One of them was with the presence of a total constraint applied to the point under the root of the weld during the heating period (drawn by grey dashes). In the second case, the plate was not restricted in vertical movement neither during heating period nor during cooling.

The first case assumes a stiff plate, not allowing the considered cross-section to go up along the centreline during the heating stage. The second case is linked to an assumption of fast completion of the seam (the whole plate is warmed up along the centreline).

The existence of the additional restrictions during the heating stage leads to the determination of the maximum possible value of angular deformation. It happens because we completely eliminate the lifting of the weld during heating.

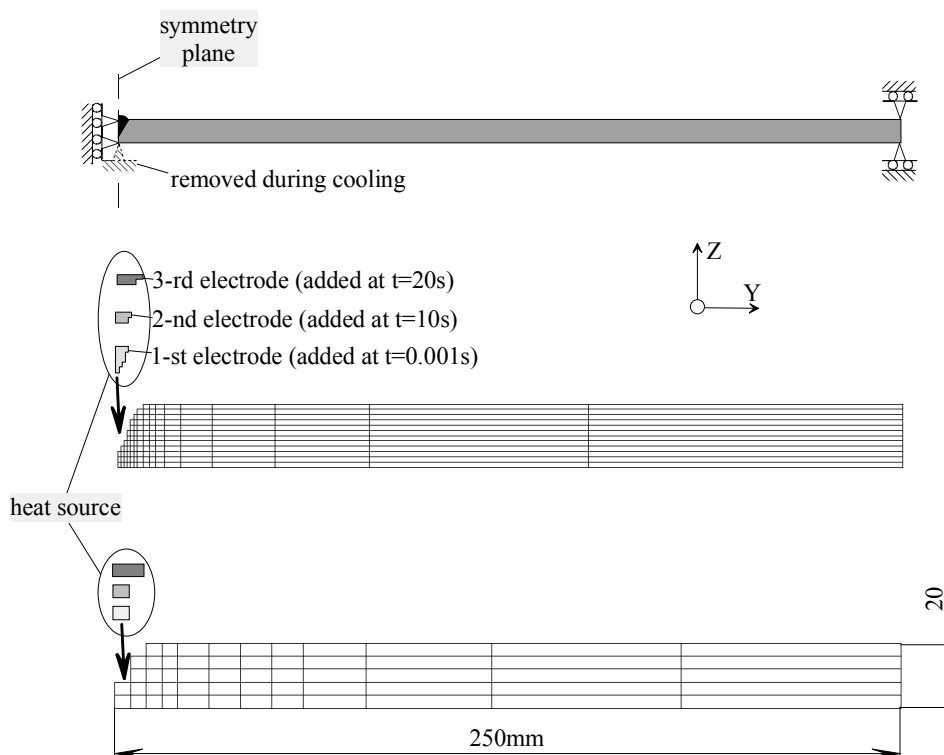


Fig. III-23. Scheme of boundary conditions application and two different finite element analysis meshes for 2D welding simulations.

### 3.3.3. Utilisation of the "element birth" technique

In the mechanical part of the model, as well as in the heat flow model, the "element birth" technique was applied (more information in section 2.2.2). In *Fig. III-23* two meshes for the case involving three-electrode submerged arc welding process are shown.

In this case, the elements corresponding to the filler metal from the three sources, are added at intervals  $\Delta t=10s$ . In the case of the single-electrode welding procedure with subsequent completion of the three passes, the time interval between passes is extended up to 7000s. This is done in order to achieve complete cooling between passes.

To achieve the "element death" effect, the ABAQUS does not actually remove the elements. Instead, it just deactivates them by changing the properties. In the case of the generalised plane strain model, the stiffness of the removed elements is set to zero.

In the models, used in this dissertation, elements were reactivated "strain-free". Inactive elements do not accumulate plastic deformation while they are deactivated. During activation they are reset to an "annealed" state (zero stress, strain, plastic strain, etc.).

The "element birth" technique introduces serious problems into the thermal stress analysis. These problems are caused by large displacements induced by the heating process. An element that is being reactivated strain-free fits into whatever configuration is given by its nodes at the moment of reactivation. *Fig. III-24*. demonstrates a possible conflict during element reactivation. Three nodes of the grey element are attached to the surrounding elements (designated by the crosses) and, hence, forced to appear at the positions prescribed by the rest of the model. The node designated by the circle, is free.

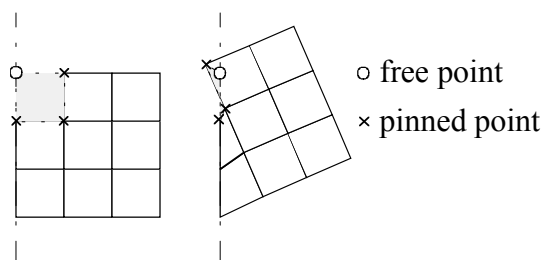


*Fig. III-24. Problem associated with element birth.*

The "element-birth" technique, described here, is included in ABAQUS as a standard. The other way of doing it is to multiply the stiffness of the removed region by a reducing factor not equal to zero. Calculations in the ANSYS environment are organised this way.

The model without implementation of the "element birth" technique was used in the current dissertation as well. In this case, all the elements of the mesh hold their properties unchanged during the whole process.

3.3.4. Elements used in 2D models

In Fig. III-25 the numbering of the element nodes and integration points are shown. As a standard, the nodes are numerated following the counter-clockwise direction, starting from the left bottom corner. Faces of the elements are numbered in the same manner. The integration points are numbered differently.

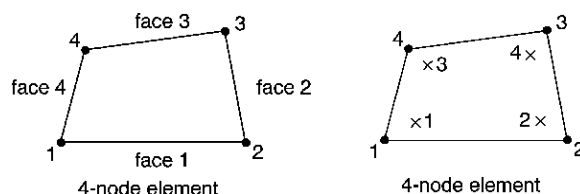


Fig. III-25. Node ordering and face numbering on elements, and numbering of integration points for output.<sup>37</sup>

In the case of the plane strain model, simple 4-node bilinear CPE4 elements with full integration were used. These plane strain elements have two translational degrees of freedom ( $u_x$  and  $u_y$ ).

Plane strain elements can be used when it can be assumed that the strains in a loaded body are functions of planar co-ordinates alone and the out-of-plane normal and shear strains are equal to zero. Plane strain elements must be defined in the  $XY$  plane, and all loading and deformation is also restricted to this plane. Since plane strain theory assumes zero strain in the thickness direction, isotropic thermal expansion may cause large stresses in the thickness direction.

In the case of the generalised plane strain model, 6-node bilinear quadrilateral CGPE6 elements with full integration were used. These elements have additional nodes (see Fig. III-26). One of these nodes is carrying information about expansion in  $z$ -direction  $\Delta u_z$ . The other reference node has information about the rotation of the plane  $\Delta \phi_x$  and  $\Delta \phi_y$ .

The mesh of generalised plane strain elements is similar to a single layer of three-dimensional elements between two rigid planes. The motion of the planes is controlled by two reference nodes. The nodes of the elements can move within the planes but must remain on them.

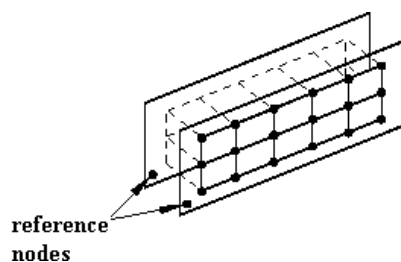


Fig. III-26. Generalised plane strain elements with reference nodes.

These elements may provide several output variables. Some types of output variables that could be relevant to the topic of this dissertation are listed in *Table III-5*.

ABAQUS uses numerical techniques to integrate variables over the volume of each element. Using Gaussian quadrature ABAQUS evaluates the material response at each integration point in each element. The value of temperatures at the integration points used to compute the thermal stresses depends on whether first-order or second-order elements are used. In our case we have linear elements. By this means an average temperature is used at the integration points so that the thermal strain is constant throughout the element. An approximate linearly varying temperature distribution is used in higher-order elements with full integration.

*Table III-5. Selected output variables for the thermal-stress analysis.*

ABAQUS code	Physical meaning
$S_{ij}$	Stress components ( $i,j=1\div 3$ )
$SP_n$	Minimum, intermediate and maximum <i>principal stress</i> ( $SP1\leq SP2\leq SP3$ )
<i>MISES</i>	<i>Mises equivalent stress</i>
<i>TRESC</i>	<i>Tresca equivalent stress</i>
$ALPHA_{ij}$	<i>kinematic hardening shift tensor components</i> ( $i,j=1\div 3$ )
$E_{ij}$	Strain components ( $i,j=1\div 3$ )
$EP_n$	Minimum, intermediate and maximum <i>principal strains</i> ( $EP1\leq EP2\leq EP3$ )
$ER_{ij}$	Mechanical <i>strain rate</i> components ( $i,j=1\div 3$ )
$EE_{ij}$	<i>Elastic strain</i> components ( $i,j=1\div 3$ )
$IE_{ij}$	<i>Inelastic strain</i> components ( $i,j=1\div 3$ )
$THE_{ij}$	<i>Thermal strain</i> components ( $i,j=1\div 3$ )
$U_m, UR_n$	<i>Displacement</i> components, including rotations at nodes
<i>NT</i>	<i>Temperature</i> value at a node
$RF_m, RM_n$	Components of <i>reaction forces</i> , including reaction moments

### 3.3.5. Contact analysis implementation

In the scope of the current dissertation, the models involving contact analysis and applied gravitational forces, were also explored.

To reconstruct the real welding process, into the mechanical part of the model, the interaction between the plate and "ground" was included. In a finite element analysis contact conditions are a special class of discontinuous constraint, allowing forces to be transmitted from one part of the model to another. The constraint is discontinuous because it is applied only when the two surfaces are in contact. When the two surfaces separate, no constraint is applied. Solving the problem including contact analysis significantly complicates the simulation. For example, the problem described here takes about twice as much CPU time as a similar problem without contact analysis.

The "ground" was modelled through the use of an analytical rigid surface. The use of rigid surface is cost-effective since the only variables associated with a rigid surface are the translation and rotation on a single node, known as a rigid body reference node. In addition, ABAQUS does not need to calculate the stiffness or stresses within the rigid

body. Analytical rigid surface is computationally more efficient than the one modelled with rigid elements. In contact analysis friction between the surfaces ( $\mu=0.6$ ) was taken into account.

### **3.4. 3D sequentially coupled thermal-stress model**

In the scope of this dissertation several meshes with different density were tested. The difference between the tested meshes was the element size in the  $x$ -direction. Elements 5, 10 and 20mm long were tested.

#### **3.4.1. Meshes for 3D thermal-stress analysis**

The scheme of the selected 3D sequentially coupled thermal-stress analysis's model is presented in *Fig. III-27*. The smallest elements situated close to the weld have dimensions 10×5×4mm ( $dx \times dy \times dz$ ). Similarly to the 2D model, with a distance from a centreline, element dimensions in the  $y$ -direction change significantly. The elongated elements may cause overstiff behaviour of the structure.<sup>38</sup>

A 3D static analysis model was created in order to demonstrate the locking phenomenon causing abnormally stiff behaviour of the 3D 8-nodes linear brick elements (C3D8 in ABAQUS specification). A square plate was analysed. One side of the plate was cantilevered. The concentrated bending forces were applied to the other side of the plate. In separate computer runs the plate was approximated by elongated elements and by cubic elements. The results demonstrated that the elongated elements work well in the direction of the short edge of the element. But, are too stiff in the direction along the element. More information is presented in *Appendix F*.

The elongated elements present in the 3D thermal-stress analysis model (illustrated in *Fig. III-27*) will not work along the long edges of the elements (see *Fig. IV-32*). In other words, the areas remote from the weld seam will not be subjected to bending around the direction of welding (the  $x$ -direction). It is shown in *Appendix F* that elongated elements work well in the element's short-edge direction.

Totally the mesh consists of 3000 elements and 3978 nodes. Some examples of input files are presented in Appendix A1-A2. The data about the necessary CPU resources are listed in *Table III-6*.

*Table III-6. Comparative magnitude of CPU time for 3D models, (in hours).*

	thermal analysis	stress analysis	$\Sigma$
fine mesh ( $dx=5mm$ )	38.0	20.0 [first 45s of the welding process]	58.0
normal mesh ( $dx=10mm$ )	16.5	14.5	31.0
rough mesh ( $dx=20mm$ )	5.0	4.5	9.5

The meshes differ from each other by a doubled mesh density in the welding direction ( $x$ -direction). The element length is marked in *Table III-6* in italics.

Additionally, a model consisting of two parts was tested. One part consists of material with elastic-plastic properties and other part is purely elastic. Most of the elements are concentrated in the plastically deformed zone (60% of all the elements). Simulations were done to check the efficiency of this approach. The reduction in stress analysis time, however, was less than 10%.

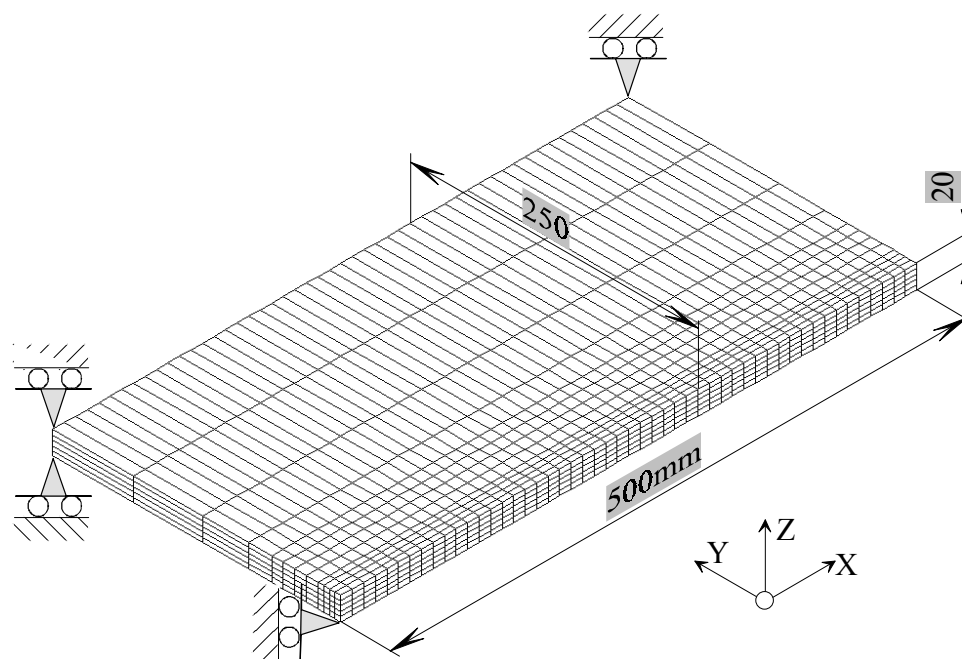


*Fig. III-27. Scheme of boundary conditions application and selected finite analysis mesh for 3D welding simulations (boundary condition corresponding to the plane symmetry is not shown).*

Another technique for reducing the calculation time could also be used. It would consist of the same elastic-plastic part, while the purely elastic elements would be substituted by springs.<sup>39,40</sup> We estimate that this kind of simulation may reduce calculation time by approximately 30%. But, problems that would be faced, such as changing the stiffness of the springs according to the averaged temperature of that area, discouraged further development of this model. This technique may, however, be useful for the case of very wide specimens.

With increasing mesh density, the number of elements doubles. At the same time, the calculation time does not double, but approximately triples. This happens because not only the number of elements has increased, but, the fine mesh requires smaller time steps during the calculations. Consequently, in the case of finer mesh, the number of time increments increases.

### 3.4.2. Applied boundary conditions

The applied boundary conditions are schematically shown in *Fig. III-27*. The only thing that is missing is the boundary condition corresponding to the plane symmetry relatively the plane passing through the weld centreline and perpendicular to the  $y$ -axis. This condition restrict movement of the nodes lying in this plane, not allowing them to move in the  $y$ -direction.

The first node from the beginning of the seam, belonging to the root of the weld, is fixed in its movement in the  $x$ -direction. The vertices, situated far from the weld centreline, are restricted to move in the  $XY$ -plane.

Such an arrangement of the boundary conditions allows us to simulate the plate freely lying on the base (no gravitational forces are taken into account).

### 3.4.3. Elements used in 3D models

In *Fig. III-28* the numbering of the element nodes and integration points are shown. As a standard, the nodes are numerated following the counter-clockwise direction, starting from the left bottom corner of the lowest level. Then, in a similar way, the second level of the nodes is numerated. Numeration of the faces of the elements is more complicated than in the 2D case. The integration points are numbered similarly to the 2D case.

In the model simple 8-node linear brick C3D8 elements with full integration were used. These elements have three translational degrees of freedom ( $u_x$ ,  $u_y$  and  $u_z$ ).

ABAQUS uses numerical techniques to integrate variables over the volume of each element. Using Gaussian quadrature ABAQUS evaluates the material response at each integration point in each element. The value of temperatures at the integration points used to compute the thermal stresses depends on whether first-order or second-order elements are used. In our case we have linear elements. By this means an average temperature is used at the integration points so that the thermal strain is constant throughout the element. An approximate linearly varying temperature distribution is used in higher-order elements with full integration.

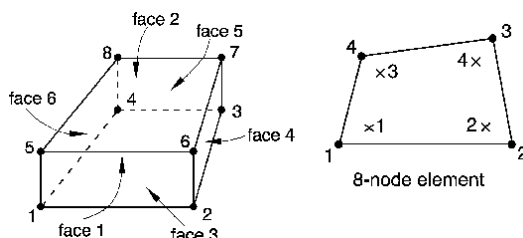


*Fig. III-28. A 3D linear brick node ordering and face numbering, and numbering of integration points for output.*<sup>37</sup>

### 3.4.4. Different sources of non-linearity in the models

Similarly to the 2D-model, for the sake of exploring different techniques, contact analysis was introduced into the simulation. It was done in order to evaluate the effect of the gravitational forces, acting on the welding details. From the experience gained from the large number of experimental simulation runs it can be concluded that including this type of analysis significantly complicates the problem, extending the CPU time two-three times. In addition contact modelling introduces some model developing difficulties, such as over-constraining the model and preventing rigid body motion. An overconstraint occurs when a contact constraint on the displacements at a slave node conflicts with a prescribed boundary condition on that degree of freedom at the node.

Contact analysis introduces additional *boundary nonlinearity* into the model with *material-* and *geometric nonlinearity*, thus gathering all three sources of nonlinearity in the structural mechanics simulations into the mechanical part of simulations.

The source of material nonlinearity lies in the included plastic behaviour of the workpiece material described above (see *Fig. III-4* and *Fig. III-29*). In the thermal and the mechanical analyses all the material properties depend on the temperature (*Fig. III-3* and *Fig. III-4*) value introducing nonlinearity into the thermal problem.

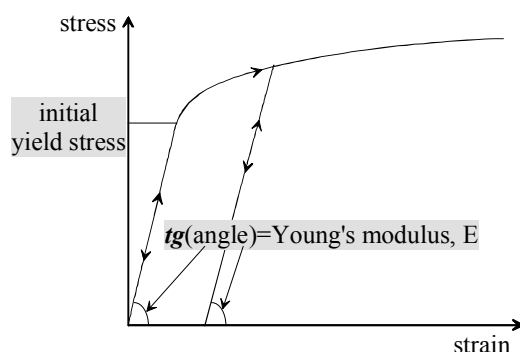


*Fig. III-29. Elastic-plastic behaviour of the material.*

The models, used for 3D sequentially coupled thermal stress analysis, implement the large-displacement analysis. It is one of the sources of non-linearity in the models.

Representing large-displacement effects by including the NLGEOM parameter on the \*STEP option (see Appendix A1-A6) is an alternative to a "small-displacement" analysis. When NLGEOM is specified, most elements are formulated in the current configuration using current nodal positions. Elements therefore distort from their original shapes as the deformation increases. Omission of the NLGEOM parameter means that geometric non-linearity is ignored – the kinematic relationships are linearized. The elements are formulated in the reference (original) configuration, using original nodal co-ordinates.

### 3.4.5. Mesh accuracy

#### 3.4.5.1 Purpose of the evaluation

The purpose of this section is to justify the accuracy of the mechanical part of the 3D thermal stress model. For the 3D scheme presented the element size, and consequently the number of elements, plays a crucial role in the process of modelling itself. On the one hand, too rough a mesh may lead to wrong results and, on the other hand, too many elements in the model will lead to a non-solvable problem because of the limited computer capacity. So, to determine the roughest acceptable mesh for the model is one of the first steps on the way to getting reliable results.

#### 3.4.5.2 Method

In the case of heat-flow analysis, the maximum temperature distribution in the cross-section of the weld was chosen to be the key parameter for analysis. The 2D and 3D FE approximate results were compared with exact analytical solution.

For the mechanical part of the problem, the task is more complicated. First of all, we do not have any analytical solution that could be used as an exact solution of the mechanical problem analogous to the considered case of welding. Exact solutions are available only to elasticity problems for geometrically very simple bodies. Comparison of the ABAQUS simulations with an analytical solution of a simple problem will not give more confidence in the complicated thermo-mechanical model.

Secondly, there are more variables that should be analysed in the mechanical part of the model than in the thermal one.

Finite element model results should converge toward exact results as a mesh is repeatedly refined. The computed results from two or more analyses can be extrapolated to yield an improved result.<sup>41</sup> This fact, called "convergence in itself", can be used for determination of the mesh accuracy.

#### 3.4.5.3 Discussion of the results

During model exploration it was revealed that the model presented in *Fig. III-27* is most sensitive to change of the element density in the weld-longitudinal direction. So, the results of the three models with different element density in  $x$ -direction were used for evaluation of the mesh accuracy. Meshes with steps in  $x$ -direction of  $h_x=5, 10$  and  $20\text{mm}$  were used.

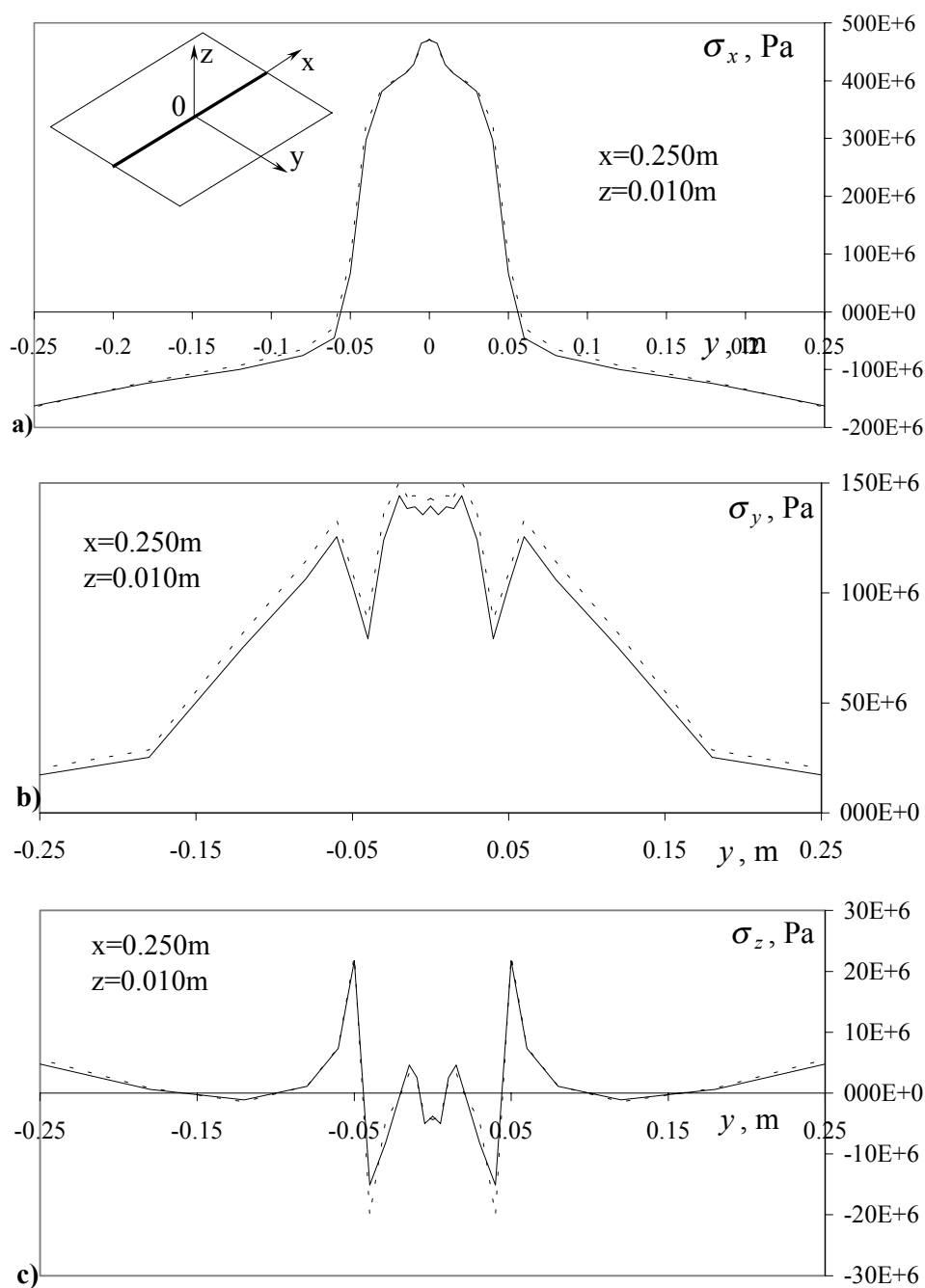


Fig. III-30. Effect of the mesh density on calculated residual stress distribution (according to meshes with 10 and 20mm step in  $x$ -direction); (a) – longitudinal stress  $\sigma_x$ ; (b) – transverse residual stress  $\sigma_y$ ; (c) – transverse residual stress  $\sigma_z$ :

——— -  $h_x = 10\text{mm}$   
 - - - - - - -  $h_x = 20\text{mm}$

The influence of the mesh density on the residual stress distribution is illustrated in Fig. III-30 (solid line curves correspond to  $h_x = 10\text{mm}$  and the dashed lines correspond to  $h_x = 20\text{mm}$ ). It is evident that the stress distribution is not seriously affected by the too course mesh.

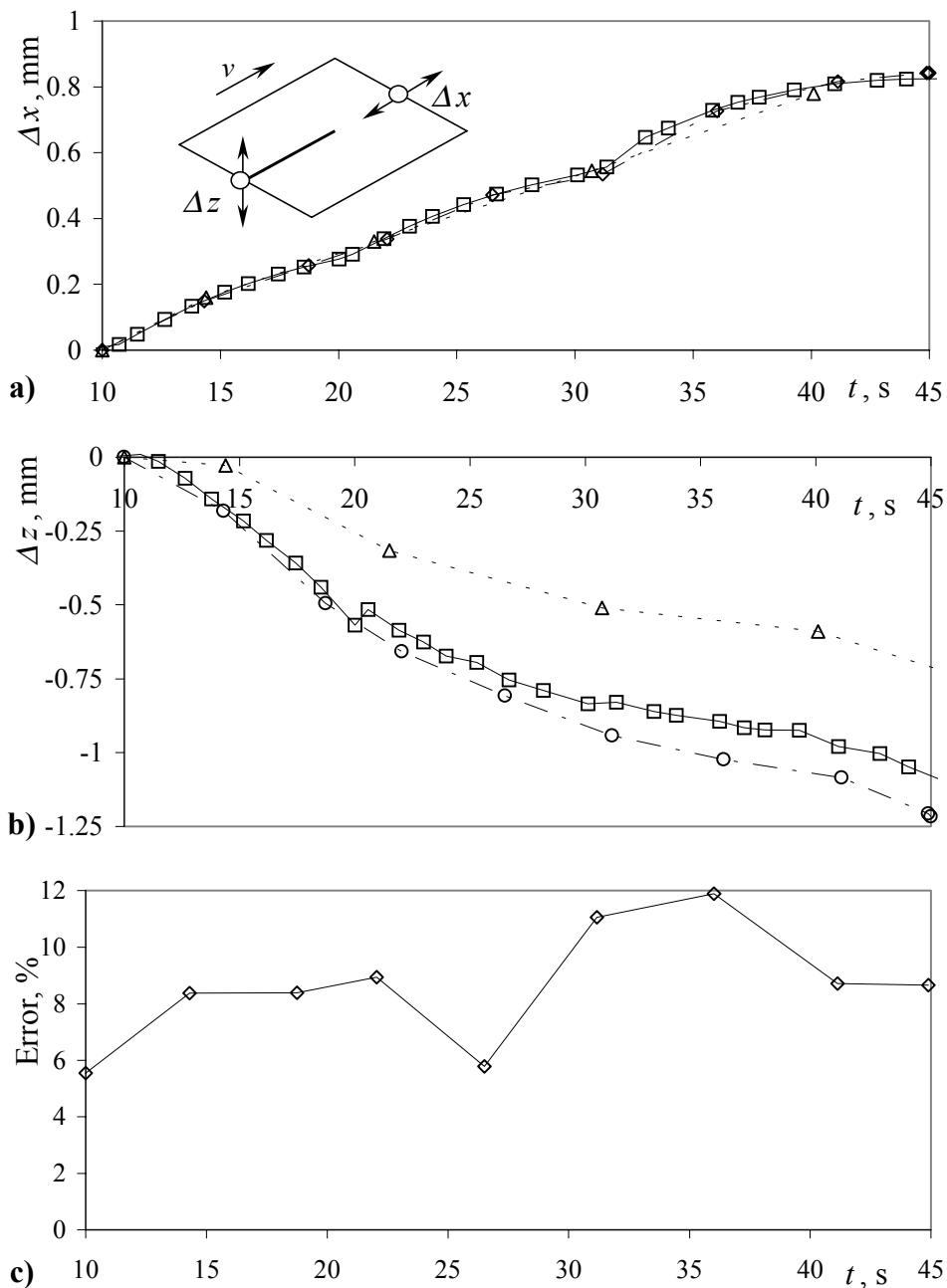


Fig. III-31. Effect of the mesh density on calculated plate deformation during beginning of the heating stage (according to meshes with 5, 10 and 20mm step in  $x$ -direction); (a) – longitudinal elongation along the weld centreline; (b) –  $z$ -displacement (angular deformation); (c) – error of the 10mm-mesh compare to 5mm (according to angular deformation):

- $h_x = 5\text{mm}$
- $h_x = 10\text{mm}$
- $h_x = 20\text{mm}$

For the investigated case of butt welding the deformation is more sensitive to the mesh density.

In Fig. III-31 the results from only the first 45s of the welding process are shown. This is due to technical problems met during solution of the thermo-mechanical task with the finest mesh, characterised by  $h_x=5\text{mm}$ . Demands on computation time and hard disk capacity were too severe. This model consists of 6000 volumetric elements. Calculation of the first 45s of the thermal process took approximately 3000 time increments. The whole thermal history had to be stored on the hard disk in order to be used as an input data for the mechanical simulations. Totally almost 10Gb of the hard disk was used for this task.

Analysing the beginning stage of the welding process, we may assume that the further behaviour of the system has the same tendency.

Fig. III-31.a demonstrates the non-significant influence of the mesh density on the longitudinal elongation. But, the results on angular deformation, presented in Fig. III-31.b, demonstrate the strong effect of the element length on this kind of deformation.

Using too rough elements ( $h_x>50\text{mm}$ ) leads to completely wrong results concerning the angular deformation of the welded plate. According to calculations with such rough mesh steps, the plate is not exposed to angular deformation at all. It happens because the model is too stiff in the  $x$ -direction. At the same time, the residual stress distribution is not affected by such drastic change of the element length.

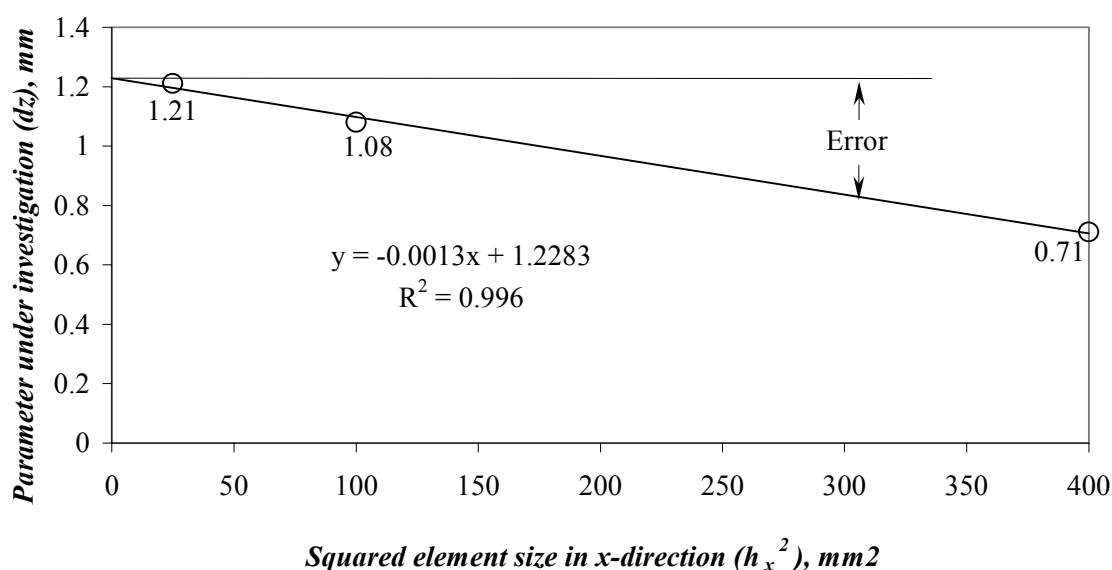


Fig. III-32. Extrapolation of the real  $z$ -displacement with error proportional to  $h_x^2$ .

To demonstrate the mesh accuracy in Fig. III-32, the angular deformation results on the 45<sup>th</sup> second of the welding process were used.

In order to find the exact angular deformation, we can presume that the convergence of the solution is monotonic and that the convergence rate is known. In our case, we assume that the error is proportional to  $h_x^2$ . Use of the results from three models allows us to demonstrate that it is true. The straight line describes quite well the tendency shown in Fig. III-32 (with average standard deviation  $R^2=0.996$ ).

According to *Fig. III-32*, the error of the model with  $h_x=10\text{mm}$  is 12%. The spread of the error shown in *Fig. III-31* does not exceed this limit.

We cannot be sure that the demonstrated tendency will be the same by the end of the welding process. In order to get assured, we can state that the mechanical part of the thermal-stress model is not less than 80-85% accurate.

### **3.5. Conclusions**

In this section a variety of numerical methods of the sequentially coupled thermal stress analysis, adapted for the welding procedure investigated, is presented. Typical features of the different solutions are described. Based on the context of this section the following conclusions can be drawn:

1. The suggested 2D plane strain model and generalised plane strain models are not reliable for the prediction of the angular deformation magnitude. Meanwhile, it can be used for comparison of how the different welding and boundary conditions affect the response of the structure.
2. The "element birth" technique, in the case of the mechanical part of the sequentially coupled thermal stress analysis model, introduces serious numerical problems. These problems are caused by large displacements induced by the heating process, and the impossibility to reactivate new-born elements at their prescribed location.
3. The models with contact analysis implementation were also explored in the scope of this dissertation. It was done in order to evaluate the effect of the gravitational forces, acting on the welding details. Contact analysis significantly complicate the solution, approximately doubling computation time, not demonstrating significant influence on the stress-strain development.
4. The mechanical part of the simulation, in contrast to the heat flow analysis, cannot use elements elongated along the weld line. For better accuracy elements near the centreline must be nearly cubic.
5. Forming criteria about the accuracy of the FE model, we first need to determine what is in the focus of attention. If the main problem concerns stress distribution (corrosion problem, brittle fracture, fatigue strength), then a relatively coarse mesh can be used. Problems that concern about deformation processes in welding demand finer mesh.
6. By varying the mesh density, it was demonstrated that convergence to the exact value of the angular deformation is achieved "from below". It demonstrates that a rough mesh is too stiff, and does not allow the structure to respond to the thermal load in a proper way.
7. Analysing the deformation of the plate during the first 45 seconds of the welding process, the accuracy of the method can be claimed to be 88%. But there is no guaranty that this tendency will be the same by the end of the welding process. In order to get assured, we can state that the mechanical part of the thermal-stress model is not less than 80-85% accurate.

**References**

- 
- 1 G. A. Bel'chuk, V. D. Matskevich: "Welding in shipbuilding", Sudprom GIZ, Leningrad, 1961, *Rus.*;
  - 2 B. Altemühl: "Welding duplex chemical tankers the ESAB way", Svetsaren, V 54, N 1-2, 1999, pp. 15-21;
  - 3 M. Henriksen: "Simulation and measurements of thermal stresses in one side submerged arc welding of steel plates", Engineer Thesis, Norwegian University of Science and Technology, Trondheim, 1997;
  - 4 V. V. Andreev: "General technology of shipbuilding", Sudostroenie, Leningrad, 1984;
  - 5 R. Boekholt: "Welding mechanization and automation in shipbuilding worldwide", Abington Publishing, Cambridge England, 1996;
  - 6 G. Tither: "The development and applications of niobium-containing HSLA steels", Proc. Processing, Properties and Applications, 1992, pp. 61-80;
  - 7 Rothman, M.F.: High-temperature property data: ferrous alloys. American Society for Metals, USA, 1988;
  - 8 Davis, J.R.: Materials handbook, 10th edn., Vol.1. American Society for Metals, USA, 1990;
  - 9 D. Radaj: "Heat effects of welding", Springer-Verlag, Berlin, 1992;
  - 10 L. Karlsson: "Plane stress fields induced by moving heat sources in butt-welding", J. Appl. Mech. (ASME), 99, 1977, pp. 231-236;
  - 11 Muzukami, H. and Miyashita, Y.: Mechanical properties of continuously cast steel at high temperatures. Tetso-to-Hagane (Iron and Steel), 63:46, 1994. (in Japanese);
  - 12 Michaleris, P. and DeBiccari, A.: Prediction of welding distortion. Welding Journal, April 1997, 172-s – 181-s;
  - 13 N. N. Malinin: "Applied theory of plasticity and creep", Mashinostroenie, Moscow, 1975, *Rus.*;
  - 14 J. N. Harris: "Mechanical working of metals. Theory and practice", Pergamon Press, Oxford, 1983;
  - 15 J. Chakrabarty: "Theory of plasticity", McGraw-Hill Book Company, Singapore, 1987;

- 16 J. Chakrabarty: "Applied plasticity", Springer-Verlag, New-York, 2000;
- 17 P. Seyffarth: "Atlas Schweiss-ZTU-Schaubilder", VEB Verlag Technik and Dusseldorf, Berlin, 1982;
- 18 P. T. Houldcroft: "Submerged-arc welding", 2nd edn, Abington Publishing, Cambridge, 1989;
- 19 B. I. Medovar: "Two-arc automatic welding at high speeds", Avtogennoe Delo, 1950, Vol.11, 20-23;
- 20 D. E. Knight: 'Multiple electrode welding by "unionmelt" process', The Weld. J., Apr. 1954, 303-312;
- 21 Y. Kitamura, S. Fujimori, T. Yatake: "Dynamic observation of a molten pool in arc welding with high travel speed", IIW Asian Pacific Regional Welding Congress, 1988, pp. 557-569;
- 22 D. S. Taylor, C. E. Thornton: "High deposition rate submerged arc welding", Welding Review, Aug. 1989, pp. 167-180;
- 23 B. G. Sidorenko, S. L. Mandel'berg: "Selection of the optimum number of electrodes in multi-arc welding at high speed", Welding International, N 4, 1989, pp. 289-291;
- 24 N. U. Ahmed, B. J. Jarvis: "Thermal cycles in multiple electrode submerged arc welding", Welding Journal, Jan. 1996, pp. 15s-23s;
- 25 Rosenthal, D.: Transactions ASME, N68, pp.849-866, 1946;
- 26 Gradshtein, I.S., Ryzhik, I.M.: "Tables of integrals, sums, series and factorizations", 1971, Moscow, Science, *Rus.*;
- 27 V. A. Karkhin: "Principles of heat transfer in weldments", 1990, Leningrad, Leningrad Technical University;
- 28 Pilipenko, A.Yu, Karkhin, V.A., Grong, Ø., Halmøy, E.: "Simulation of thermal cycles in multielectrode submerged arc welding", Welding conference Join'99, Lappeenranta, pp. 91-98, August 1999;
- 29 V. A. Karkhin and A. Yu. Pilipenko: "Modeling thermal cycles in the weld metal and the heat affected zone in beam methods of welding thick plates", Welding International, 1997, Vol.11, 401-403;
- 30 P. L. Mangonon, M. A. Mahimkar: "A three-dimensional heat transfer finite element model of submerged arc welding of HSLA steels", Advances in Welding Science and Technology - TWR '86: Proceedings of an International Conference on Trends in Welding Research, Gatlinburg, USA, 1986;
- 31 O. C. Zienkiewicz: "The finite element method", Vol. 1, McGraw-Hill Book Company, London, 1989;

- 32 O. C. Zienkiewicz, R. L. Taylor: "The finite element method", Vol. 1, Butterworth-Heinemann, Oxford, 2000;
- 33 N. Ottosen, H. Petersson: "Introduction to the finite element method", Prentice Hall, London, 1992;
- 34 K. M. Gatovskii, V. A. Karkhin: "Theory of welding stresses and deformations", Leningrad Shipbuilding Institute, 1980, *Rus.*;
- 35 G. E. Totten, M. A. Howes: "Steel heat treatment handbook", Marcel Dekker, New York, 1997;
- 36 G. F. Hewitt, G. L. Shires, Y. V. Polezjaev: "International encyclopedia of heat and mass transfer", CRC Press, New-York, 1997;
- 37 ABAQUS version 5.6, ABAQUS user's manual, Vol.1. Hibbit, Karlson & Sorensen, Inc. 1997;
- 38 O. C. Zienkiewicz, R. L. Taylor: "The finite element method", Vol. 1 and 2, Butterworth-Heinemann, Oxford, 2000;
- 39 H. Murakawa: "Theoretical prediction of residual stress in welded structures", *Welding International*, 1997, 11 (8), pp. 599-604;
- 40 Yu. Luo, H. Murakawa, Yu. Ueda: "Prediction of welding deformation and residual stress by elastic FEM based on inherent strain", *Trans. JWRI*, Vol. 26, 1997, No. 2, pp. 467-475;
- 41 Robert D. Cook, "Finite element modeling for stress analysis", John Wiley & Sons, Inc., USA, 1995;

## CHAPTER IV EXAMINATION OF MODELS AND DISCUSSION OF RESULTS

### 1. HEAT FLOW ANALYSIS

The heat supplied by the arc induces complex thermal cycles in the weldment. This process causes several important transformations in the structure. These transformations are:

- changes in the microstructure of the heat affected zone (HAZ);
- transient thermal stress and metal movement;
- creation of residual stress and distortion in the structure.

In order to analyse the above mentioned problems, the heat flow during welding should be analysed first.

#### **1.1. Results of the analytical model of the temperature distribution during ME SAW, assuming the case of infinitely wide and long medium-thick plates and moving heat source**

For visualisation of the analytical model corresponding to *eq. III-6*, a series of simple programs were written in Turbo Pascal 7.0. Some listings of the programs are presented in Appendix D. For the calculations the following values of variables were taken:

heat loss coefficient  $\alpha=30\text{W/m}^2\cdot\text{K}$ ;<sup>1,2</sup>

thermal diffusivity  $a=5\cdot 10^{-6}\text{m}^2/\text{s}$ ;<sup>3</sup>

thermal conductivity  $\lambda=25\text{W/m}\cdot\text{K}$ ;<sup>3</sup>

The temperature fields on the top and bottom sides of the plate are shown in *Fig. IV-1.a*. Note that the scales along the *x*- and *y*-axes differ by a factor of ten. From *Fig. IV-1.b* it is seen that the weld width varies over the thickness (29mm on the top and 19mm on the bottom), while the width of heat affected zone (delimited by the 1500 and the 700°C isotherms) on the top of the plates is smaller than on the bottom side (13mm and 18.5mm, respectively).

The analytical model indicates that the weld pool on the top side of the plate is 580mm long, and the material softening isotherm, corresponding to approximately 700°C, has a length of 2000mm.

From *Fig. IV-1.b* it is also evident that in the region characterised by  $T_{max}<900^\circ\text{C}$ , the temperature gradient in the through-thickness direction almost vanishes. This can be seen from the vertical lines corresponding to the 900°C isotherm. This fact and the fact of the very elongated 900°C isotherm allow us to conclude that if the research is concentrated on the areas with  $T_{max}<900^\circ\text{C}$ , then the problem can be simplified to a 1D analytical heat flow model.

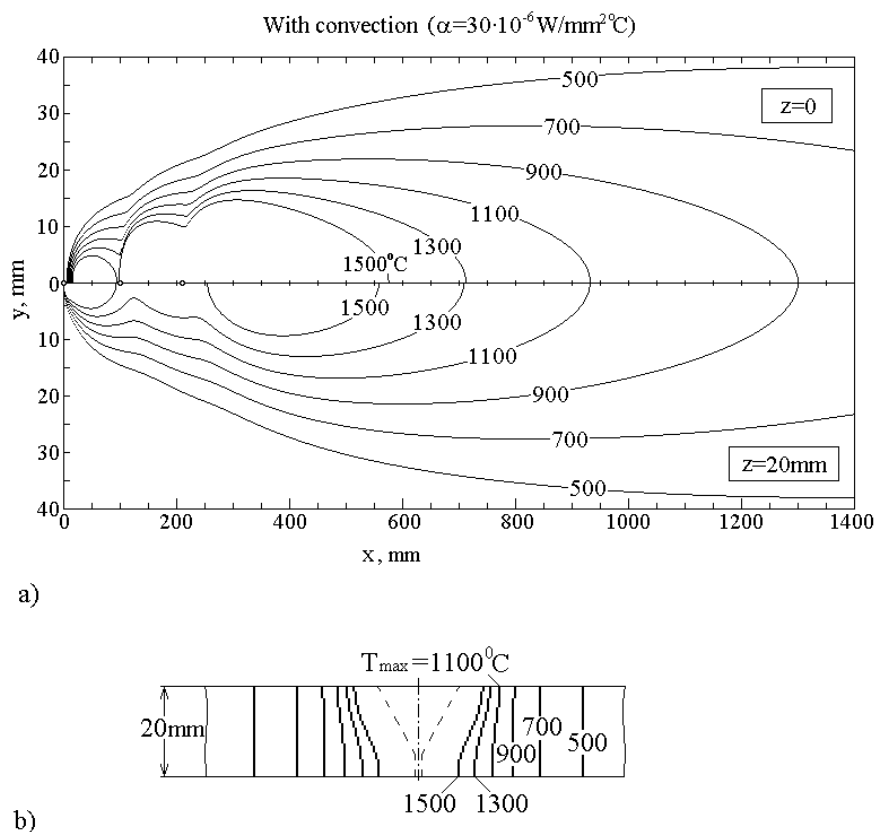


Fig. IV-1. Calculated temperature field during ME-SAW of a 20mm thick steel plate; (a) Isothermal contours on the top ( $z=0$ ) and the bottom side ( $z=20\text{mm}$ ) of the plate, (b) peak temperatures in the cross-section of the plate.

The analytical model can be used for prediction of weld metal and HAZ properties. For this purpose information about cooling rates and characteristic time intervals (e.g. the cooling time from  $800$  to  $500^{\circ}\text{C}$ ,  $\Delta t_{8/5}$ ) are needed. These welding process characteristics are illustrated in Fig. IV-2. In general, high-power ME SAW is characterised by very slow cooling rates, typically one order of magnitude lower than that commonly observed in ordinary fusion welding.

It was previously mentioned that a simple 1D scheme describing the temperature distribution can be a suitable alternative for prediction of the temperature-time pattern. In Fig. IV-2 the two different approaches are compared. The letters in the graphs correspond to the points assigned in the upper diagrams showing the peak temperatures in the cross-section (3D scheme on the left hand-side, 1D scheme on the right hand-side). A comparison with the 3D model reveals that the deviation in the cooling rate, as calculated from the 1D model, is less than 10% if the temperature does not exceed 80% of the peak temperature in a given position.

This fact once again confirms the possibility to use a simple 1D model for class of tasks of the heat flow analysis considered here.

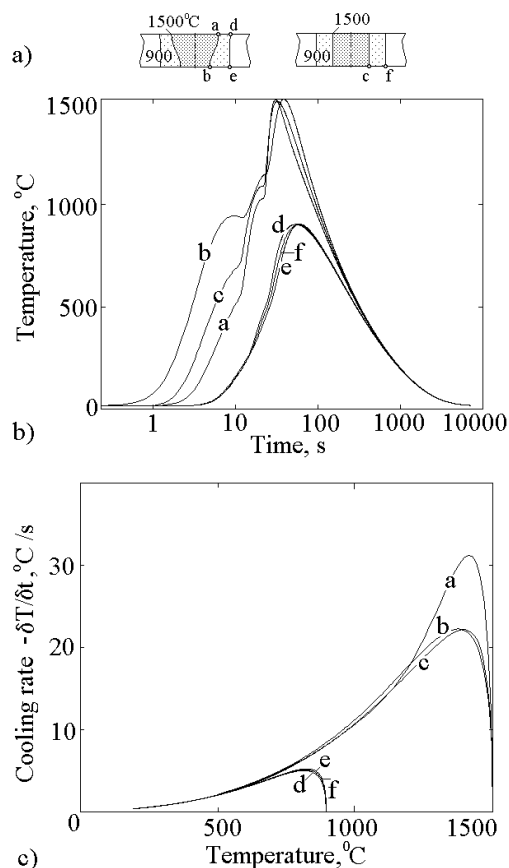


Fig. IV-2. Examples of outputs from the 3D and 1D heat flow models; (a) Peak temperatures in the cross-section of the plate, (b) Weld thermal cycles, (c) Cooling rate vs. temperature for the points indicated in (a).

## **1.2. Results of the 2D model for temperature distribution in the cross-section of the weld, assuming simultaneous seam completion**

This dissertation covers both complete 3D thermal models and a simplified 2D model. The 2D models have important advantages in computing time and necessary computer resources. At the same time a 2D analysis neglects the heat propagation in the direction perpendicular to the considered plane. By this means the calculated temperatures turn out to be over-predicted compared to the corresponding 3D scheme. These over-predictions are most noticeable in the high temperature regions where the temperature gradient and, consequently, the heat flow are higher.

Fig. IV-3 and Fig. IV-4 represent the results from the 2D heat transfer model with fine mesh but without “element birth” technique implementation. For the complete scheme of sequentially coupled thermo-mechanical analysis, this technique was used alone with rougher mesh for thermal and mechanical analysis. The accuracy of the rough mesh was evaluated in section 2.2.2., and was found to be acceptable.

In Fig. IV-3 the temperature distribution in the cross-section of the plate is shown. The temperature is represented as a function of the time and the spatial co-ordinates. As we

see, the shape of the weld is not formed by the time the heat source is terminated (the heat source is active from 0.001s to 1.000s). In fact, by this time the liquid metal not yet been formed on the bottom side of the plate. *Fig. IV-4.b* also points out that the node situated close to the boundary of the weld on the top surface of the plate reaches its maximum temperature value at ~10s. The temperature in the similar node on the bottom of the plate passes its maximum at ~15s. We can see a gradual temperature equalisation.

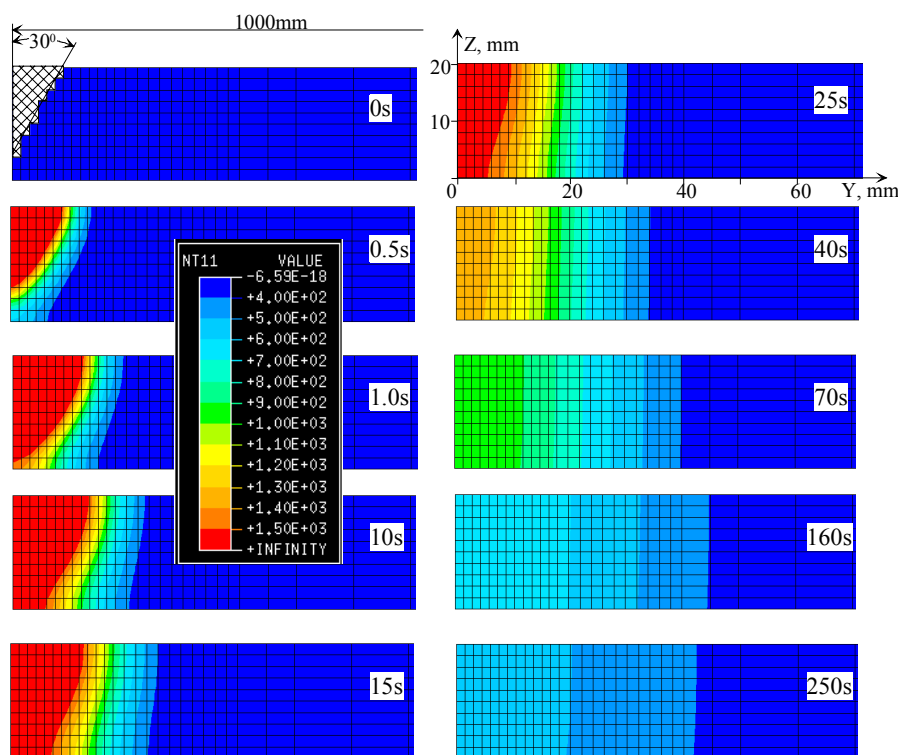


*Fig. IV-3. Temperature distribution after 2D YZ-plane model at some points in time; Heat source acts from 0.001 till 1.001 second.*

Comparison of the values of the cooling rate (see *Fig. IV-4.c*) to the results of the analytical solution (see *Fig. IV-2.c*) reveals a difference about 35% of the maximum value calculated in the analytical model.

The weld width varies over the thickness from 27mm on the top to 15mm on the bottom of the plate. The HAZ width on the bottom is 17mm and on the top 11mm. The small difference from the analytical solution results can be explained by the use of the temperature dependent material properties in the finite element model. The reason for this conclusion is that the error of the finite mesh was evaluated in *section 2.2.6 of Chapter III*, and was found to be insignificant.

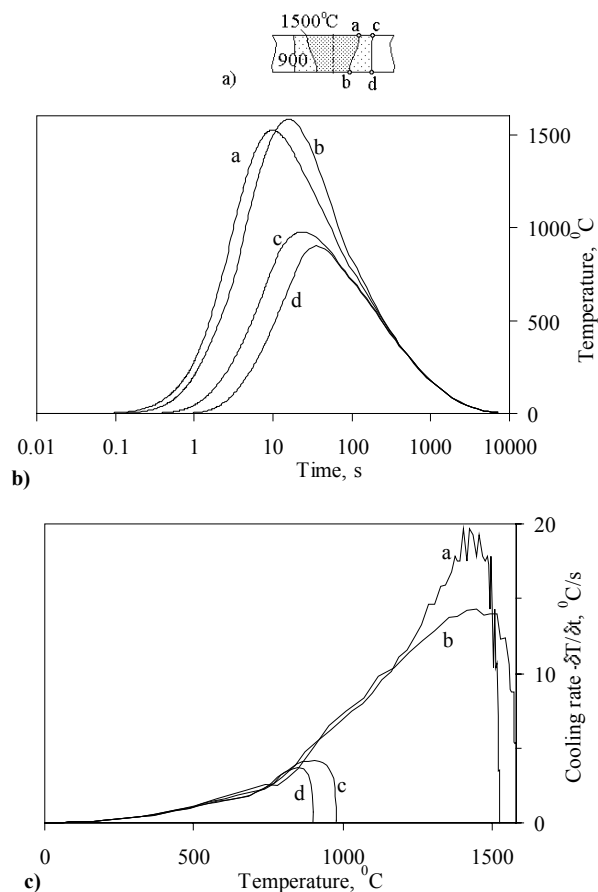


Fig. IV-4. (a) Points designation on peak temperature distribution in the cross-section of the plate; (b) Weld thermal cycles; (c) Cooling rates vs. temperature.

### **1.3. Results of the 2D model involving “element birth” technique for temperature distribution in the cross-section of the weld (comparison of the multi-electrode- and the multi-pass welding procedures)**

One of the main points of this dissertation is to compare two welding techniques widely used in ship-building. These techniques are the three-electrode single pass welding, and the single-electrode three-pass welding. Both these techniques are used for one-side welding.

The “element birth” technique, allowing to simulate weld metal deposition, gives more realistic results in terms of the thermal history of the welding process. This technique was chosen to be used for comparison of the two welding procedures under consideration.

Fig. IV-5 represent the results from the 2D heat transfer model with “element birth” technique implementation. The accuracy of the mesh was evaluated in *section 2.2.6. of Chapter III*, and was found to be acceptable.

The points for consideration, designated in *Fig. IV-5.a*, were chosen to be close to the boundary of the weld seam ( $T_{max} \approx 1500^{\circ}\text{C}$ ) after each pass in the case of multi-pass welding.

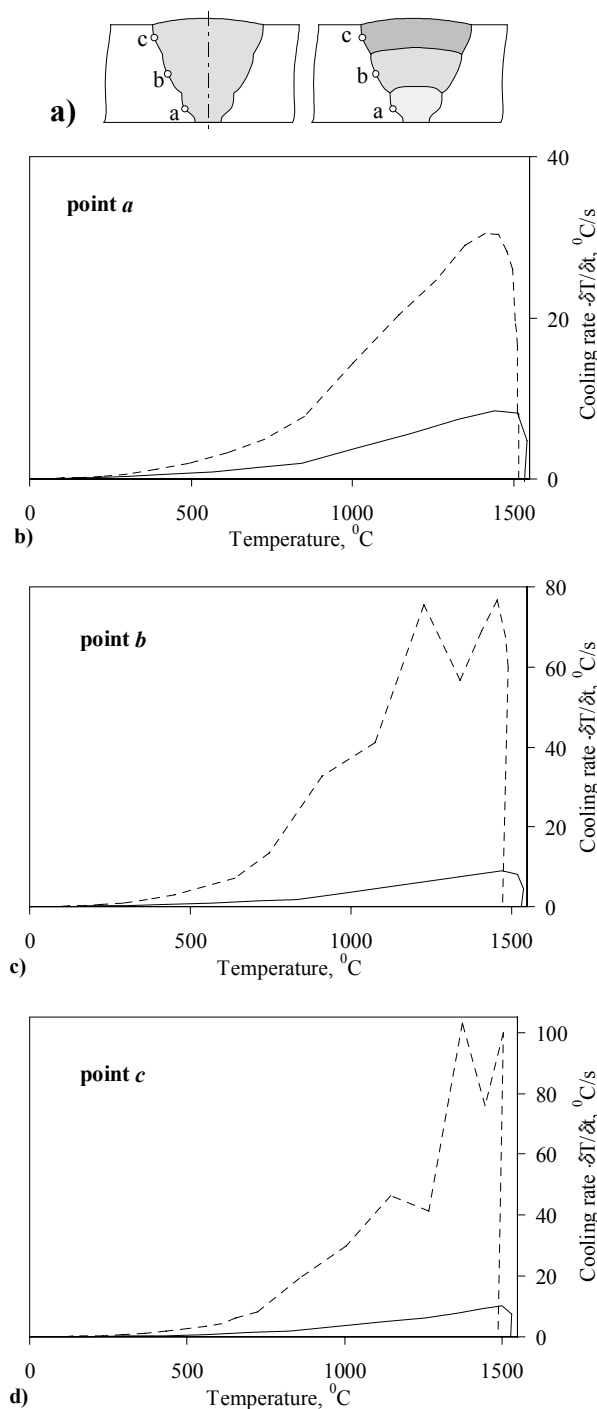


*Fig. IV-5. Comparison of the cooling rates for two considered welding techniques; (a) – points designation on the cross-section of the weld; (b-d) – cooling rate vs. temperature for three considered points (--- single-electrode multi-pass welding procedure, — three-electrode one-pass technique).*

The results presented in *Fig. IV-5* reveal significant differences in cooling rates for the two investigated welding techniques. This difference is quite important both in the high-temperature region and in the temperature interval of the solid phase transformation.

In the case of three-electrode welding, designated by the solid lines in *Fig. IV-5.b-d*, the cooling rate does not vary much in the three points considered. Only in the high-temperature region (1400-1500<sup>0</sup>C) does this difference exceed 10-15%.

In the single electrode three-pass technique the peak cooling rate at point *c* (3<sup>rd</sup> pass) is approximately three times higher than at point *a* (1<sup>st</sup> pass). The more rapid cooling in the last weld run can be explained by the fact that the heat dissipates into a larger amount of surrounding cold metal.

In comparing two welding techniques the great difference in the cooling rates should be mentioned. The three-electrode single-pass welding gives from four to ten times slower cooling than the multi-pass welding techniques with similar parameters.

#### **1.4. Results of the complete 3D heat flow model for butt welding of plates**

To solve the most realistic sequentially coupled thermo-mechanical problem, the 3D heat flow model was created. This model is described in detail in *section 2.2.5 of Chapter III*.

This model was used to simulate the three-electrode one-pass welding technique only. In order to get realistic results in simulation of the other welding procedure (single electrode multi-pass welding), the "element birth" technique must be used. This technique quite complicates the solution in the case of 3D simulations.

In *Fig. IV-6* the results from the 3D thermal model are presented. *Fig. IV-6.a* clearly indicates the existence of three peaks corresponding to the three heat sources moving along the *x*-axis. This peaks are visible only at high temperature.

It is seen from the graphs that in the regions where  $T_{max} < 700^{\circ}\text{C}$ , the effect of three distinct arcs (spaced over 210mm distance along *x*-axis) diminishes. This means that the thermal cycles corresponding to the points with  $T_{max} < 700^{\circ}\text{C}$  are smooth (without distinctive humps caused by the distributed heat source).

According to the 3D model, the length of the weld pool on the top side of the plate is 450mm. On the bottom side the melted metal appears only after the third source contribution, and the pool is 100mm long. The width of the weld pool on the top and bottom sides is 26mm and 5mm respectively.

The width of heat affected zone (delimited by the 1500 and the 700<sup>0</sup>C isotherms) on the top of the plates is smaller than on the bottom side (10mm and 18mm, respectively).

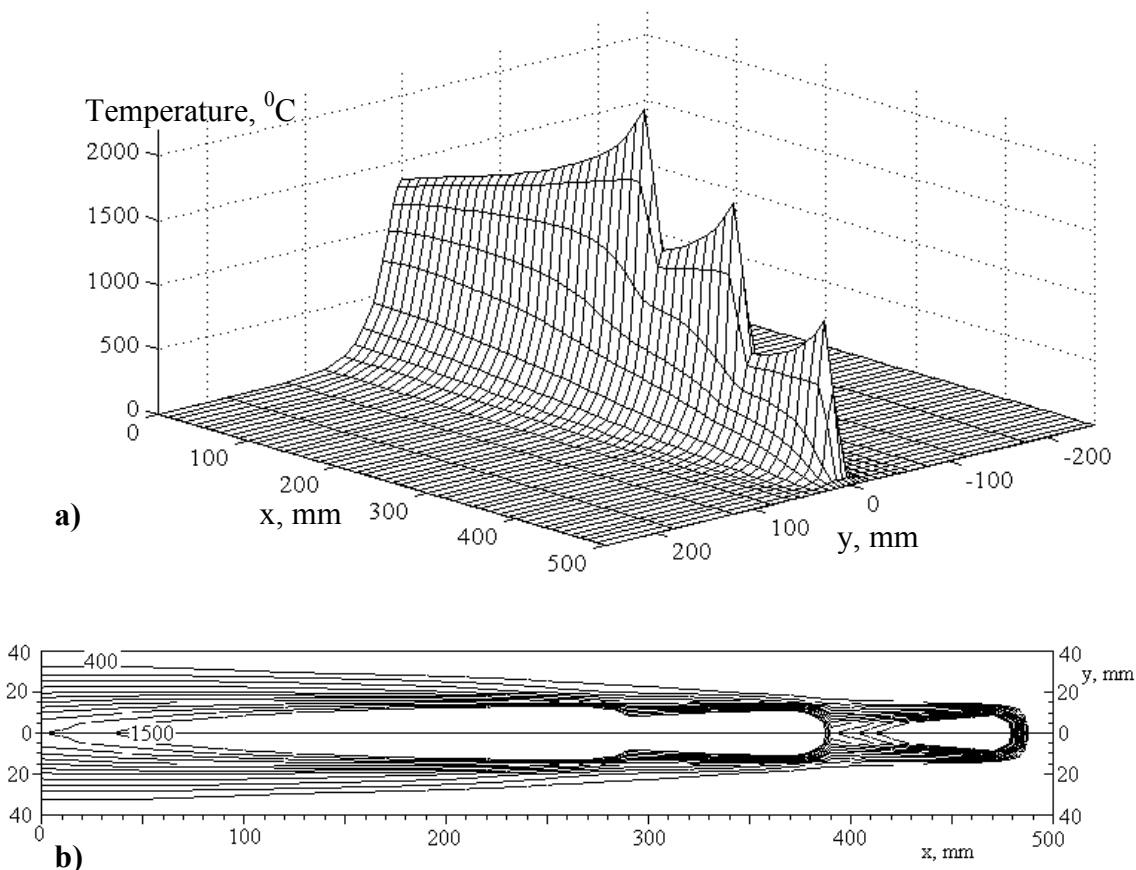


Fig. IV-6. Temperature distribution in a 20mm thick plate at the 58<sup>th</sup> second of the process in the case of the three-electrode welding procedure; (a) – 3D results representation over the bottom side of the plate; (b) – 2D results representation over the top side.

### **1.5. Solid phase transformations due to three-electrode welding procedure and multi-pass welding procedure**

The results from the 2D model with "element birth" implementation, presented in section 2.2.2 of Chapter III, pointed out the important difference in cooling rates between the two welding process under consideration.

According to those results, the three-electrode technique is accompanied by a very slow cooling process in the temperature region corresponding to the solid phase transformation in the steel. According to the continuous cooling diagram for a steel similar to steels used in ship building, presented in Fig. III-5, this temperature interval lies between 800 and 400<sup>o</sup>C.

The two considered welding techniques differ in the cooling rates from three to nine times in the above mentioned temperature interval. This fact causes significant difference in the metallographic structure of the joints welded with the two techniques.

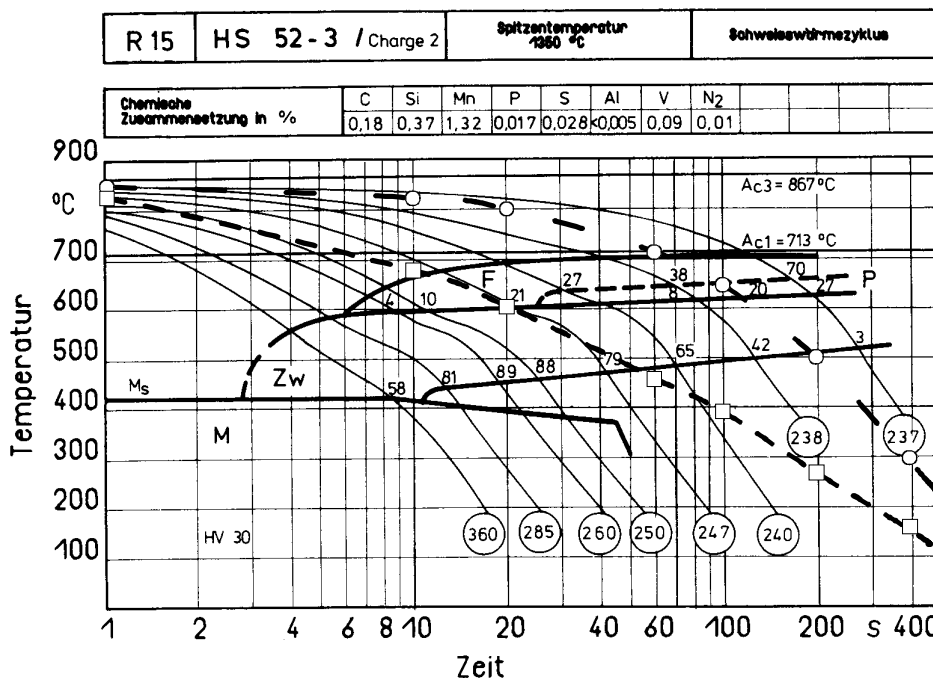


Fig. IV-7. Continuous cooling diagram by Seyffarth<sup>4</sup> with superimposed cooling curves corresponding to: — — three-electrode welding procedure, - - - multi-pass welding procedure.

In Fig. IV-7 the continuous cooling diagram is presented. Besides the cooling curves originally present on the diagram, two curves, corresponding to the two welding processes under consideration, are added. These curves correspond to the points situated in the heat-affected zone (HAZ) close to the top surface. The three-electrode one-pass welding technique is represented by the dashed curve with longer dashes.

According to the diagram, in the HAZ of the joint completed with the multi-pass technique, the structure can be expected to be composed of 25% ferrite and 75% bainite. For such a microstructure a hardness of 245HV can be expected.

The three-electrode welding procedure leads to the formation of a mixture of 50% ferrite, 20% perlite and 30% bainite in the HAZ. The HAZ for this welding procedure is even softer (237HV).

Due to the slow cooling, the solid phase transformation in both cases is complete, and no residual austenite can be expected in the microstructure of the HAZ.

For both welding procedures a coarse grain structure in the HAZ and long columnar crystals in the solidified weld metal can be expected.

These expectations can be confirmed by the diagram presented in Fig. IV-8. According to this diagram, along the weld centreline the existence of the equiaxed-dendritic crystals is possible. The cellular-dendritic microstructure can be expected in the areas situated closer to the heat affected zone.

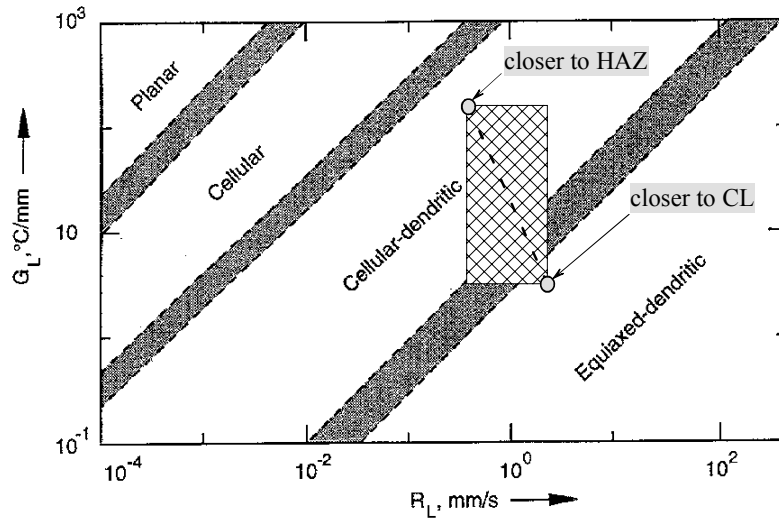


Fig. IV-8. Variation of weld metal solidification microstructure with  $G_L$  and  $R_L$ .<sup>3</sup> The area corresponding to the three-electrode welding procedure is marked by rectangular crosshatched region.

The local temperature gradient in the weld pool is marked as  $G_L$ , and it can be estimated from the simulated temperature distribution. The local crystal growth rate is marked by  $R_L$ , and it can be estimated according to the shape of the  $T=1500^{\circ}\text{C}$  isotherm and the following equation:

$$R_L \approx v \cdot \cos \gamma \quad \text{eq. IV-1}$$

where  $v$  is the welding speed and  $\gamma$  is the angle between the welding direction and the direction of the crystal growth (see Fig. IV-9).

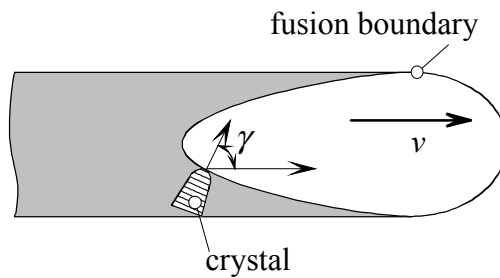


Fig. IV-9. Definition of the angle  $\gamma$  in eq. IV-1.

### **1.6. Conclusions**

In this section the temperature field for two welding procedures (multi-electrode and multi-pass welding) used in shipbuilding are investigated and compared. The investigation was based both on an analytical heat flow model and 3D and 2D finite element analysis. Based on the results presented in this section the following conclusions can be drawn:

1. According to calculations, the weld pool width in the case of the three-electrode welding, calculated based on analytical and 2D and 3D FEA, does not vary much from one solution to another (29mm from analytical model; 28mm from 2D cross-sectional model and 26mm from 3D model). The weld pool length turned out to be much more sensitive to the solution (580mm in the analytical model; 350mm in the 2D cross-sectional model and 450mm in the 3D model).
2. The length of the material softening isotherm ( $700^{\circ}\text{C}$ ) calculated for the case of the three-electrode welding procedure varies between 1500mm according to the 2D FE thermal model and 2000mm according to the analytical model (the most realistic 3D FE thermal model shows the  $700^{\circ}\text{C}$  isotherm to be 1700mm long). This fact indicates that for successful computer and experimental modelling of real welding processes, used for completion of long weld runs, the length of the specimen should not be shorter than 2000mm. Otherwise, the stiffness of the structure would not be reproduced in the experiment.
3. The effect of the choice of model on the cooling rate is not significant. In the high temperature region the cooling rate differs by maximum 30%. At temperatures corresponding to the solid phase transformation ( $800 > T > 400^{\circ}\text{C}$ ), this difference almost vanishes. This fact allows us to conclude that both analytical and finite element analysis can be used for successful prediction of the microstructure evolution.
4. According to the 2D model with the "element birth" technique, the cooling rate in the case of conventional single-electrode three-pass welding is 4-10 times higher in the temperature interval  $500\text{-}1500^{\circ}\text{C}$  than in the case of the three-electrode process.
5. The cooling rate in the case of the first run of multi-pass welding is 3 times lower than during last weld run. It can be explained by variation in the effective heat diffusion area due to difference in the groove geometry.
6. In comparison the two welding techniques cause significantly different microstructure transformations in the HAZ. The metallographic structure after three-electrode one pass welding is predicted to be 50% ferrite, 20% perlite and 30% bainite. In the case of the single-electrode technique, the perlite phase is fully eliminated, and the microstructure is composed of 25% ferrite and 75% bainite.
7. The hardness in the HAZ for both welding techniques is rather low (237HV for the three-electrodes and 245HV for the single-electrode).

## 2. STRESS FIELDS

### 2.1. Overall stress fields description

Due to the non-uniform heating process during butt-welding of the plates, a stress state with a high level of volumetric stress may arise. In the case investigated in this dissertation, the most important temperature gradient is the one in the direction transverse to the welding ( $y$ -axis direction in *Fig. III-8* in *Chapter III*). Correspondingly, the case reviewed here is characteristic of the butt-welding of relatively thick and long plates at rather high welding speed.

Existing methods of butt-welding can produce joints with different widths of the plastically deformed zone. This variation is possible due to: heat sources with different input power densities; edge preparation techniques, etc. Usually it is possible to estimate the width of the plastically deformed zone from the width of the weld seam. A *reduced seam width* usually leads to:

- lower total deformations of the structure;
- less energy overhead;
- better properties of the HAZ metal.

At the same time, *increased seam width* is characterised by:

- improved weldability;
- utilisation of more convenient and cheap equipment;
- simplified welding technology.

Currently, the ship building industry employs submerged arc welding (SAW) to produce long butt-welds and, sometimes, fillet-welds. In ship building medium thick plates often need to be welded. The present investigation covers SAW of 20mm thick steel plates. Two different welding procedures are compared. The first procedure involves three-electrode SAW in one pass. The second one uses convenient one-electrode SAW, but the weld is completed in three passes with complete cooling between passes.

Both welding procedures are characterised by a wide plastically deformed zone and high heat input.

*Fig. IV-10-Fig. IV-12* give an overall representation of the residual stress distributions calculated for the three-electrode process. These figures are the result of 3D-model runs. In *Fig. IV-10* the distributions of the longitudinal stress  $\sigma_x$  over the bottom ( $z=0\text{mm}$ ) and the top ( $z=20\text{mm}$ ) sides of the plate are presented. *Fig. IV-11* and *Fig. IV-12* demonstrate the residual transverse stress distributions. These three figures clearly indicate the two-dimensionality of the stress-state of the plate. *Fig. IV-12* reveals a very low magnitude of the residual stress  $\sigma_z$  in the through-thickness direction. These figures help to create an overall impression of the complexity of stress-state caused by the welding procedure.

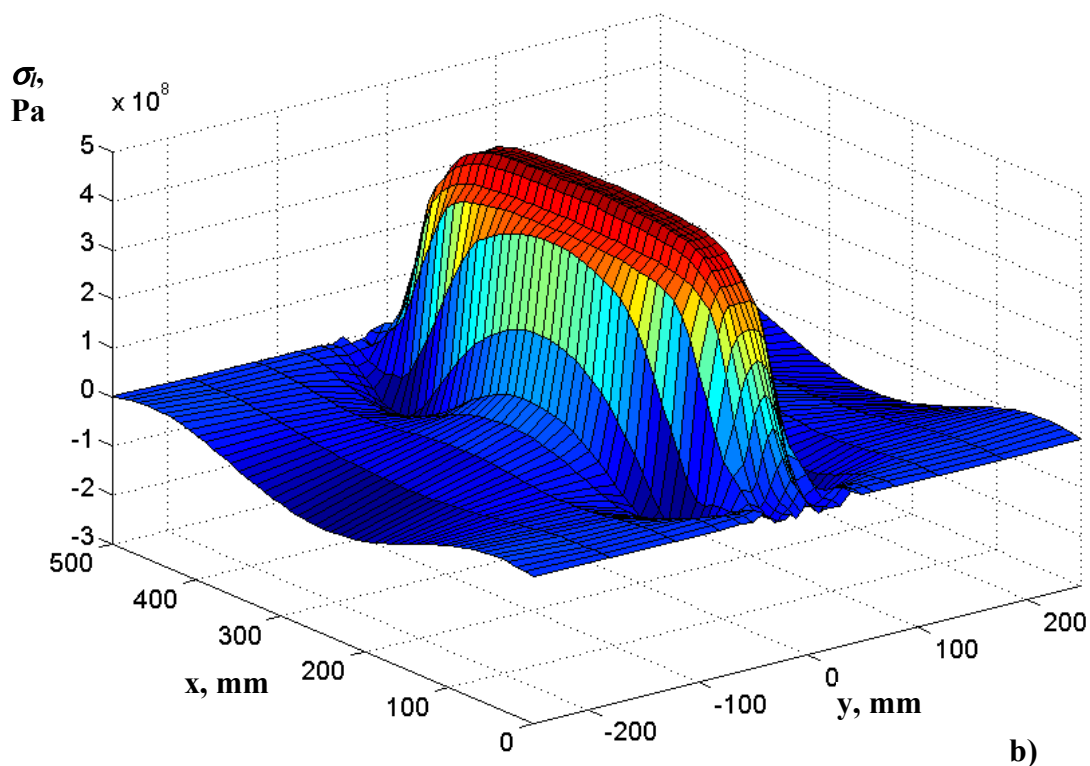
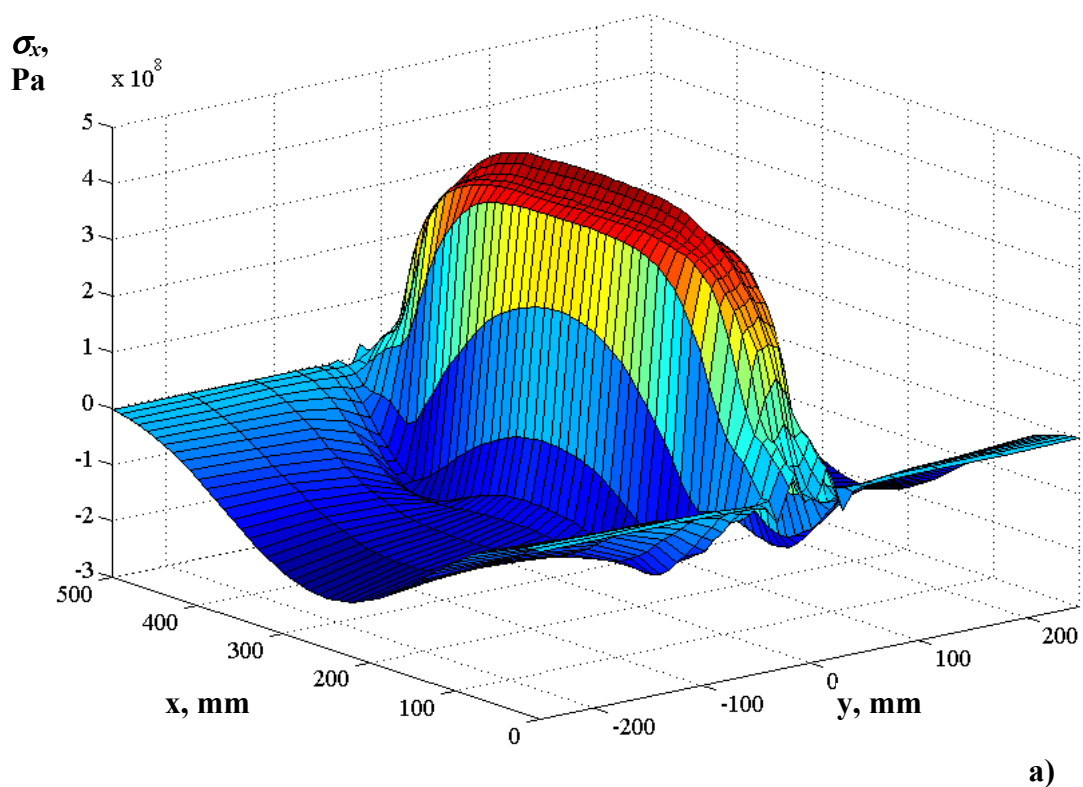


Fig. IV-10. Distribution of the longitudinal stress  $\sigma_x$ ; (a) – on the bottom side ( $z=0\text{mm}$ ) and (b) – the top side ( $z=20\text{mm}$ ) of the plate.

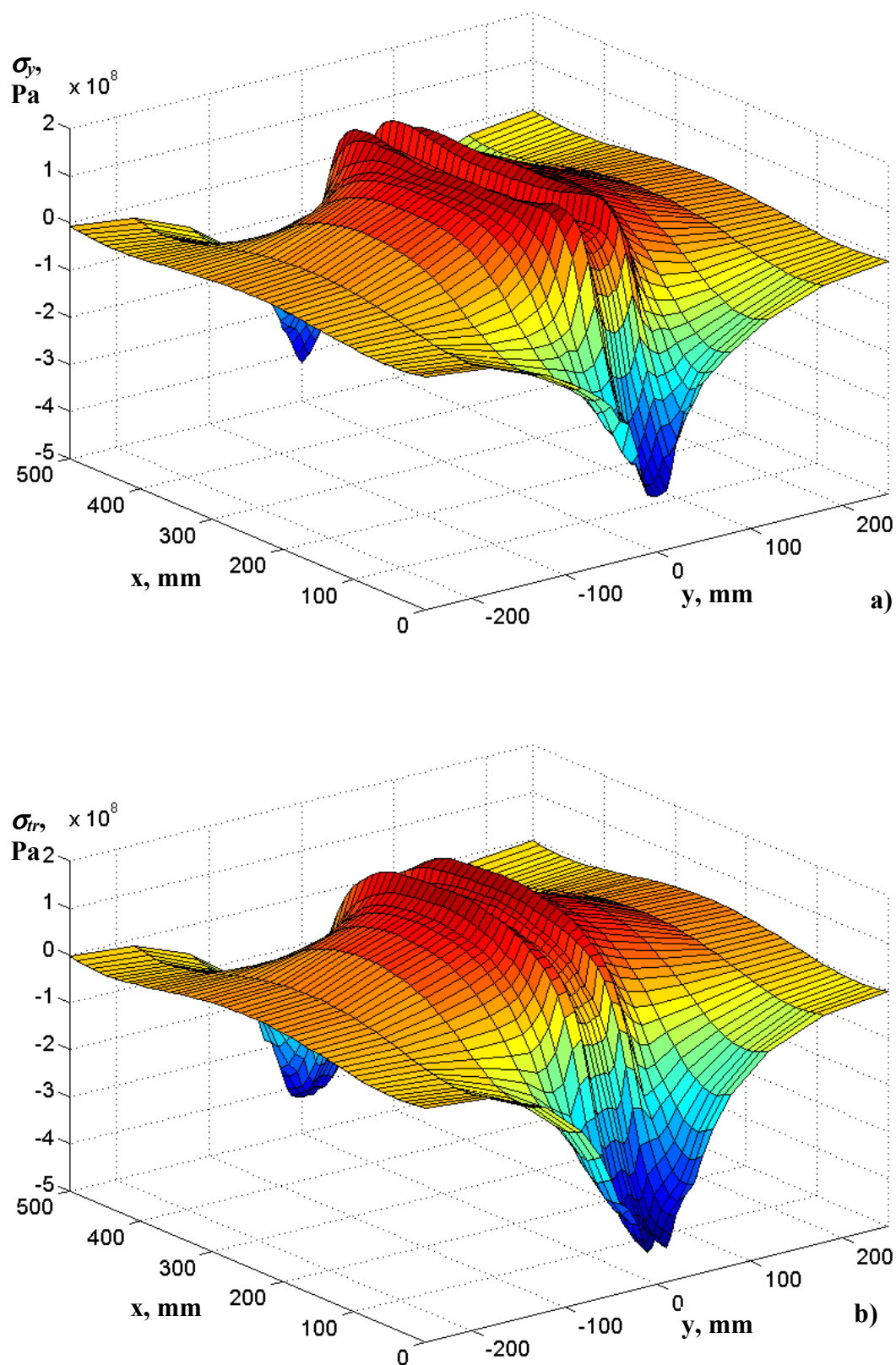


Fig. IV-11. Transverse stress  $\sigma_y$ ; (a) – on bottom side ( $z=0$ mm) and (b) – topside ( $z=20$ mm) of the plate.

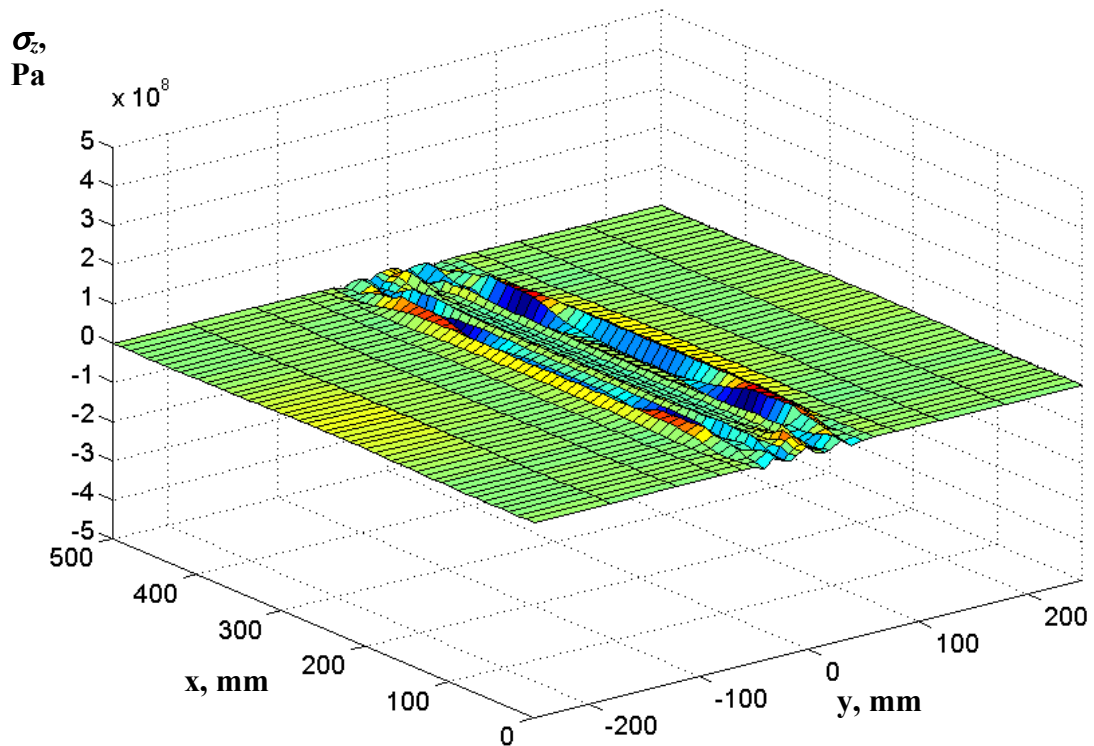


Fig. IV-12. Transverse through-thickness stress  $\sigma_z$  in a midsection of the plate.

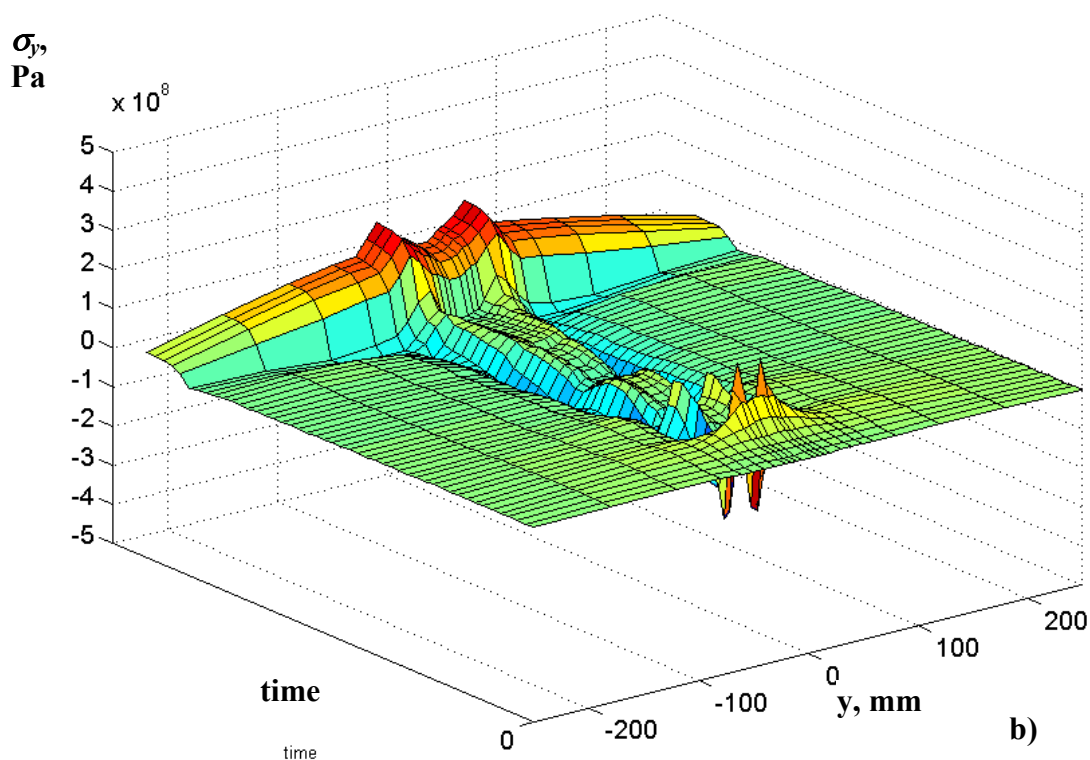
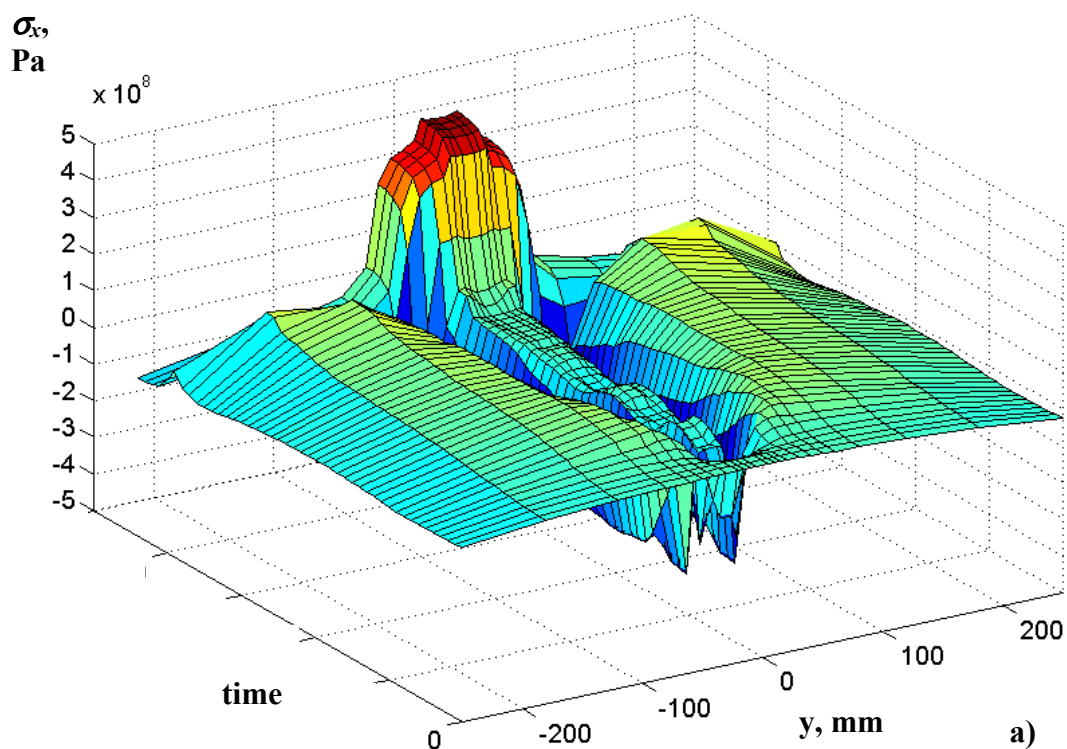


Fig. IV-13. Time development of longitudinal (a) and transverse (b) stresses ( $x=250\text{mm}$ ,  $z=20\text{mm}$ ).

The diminishing of end effects agrees with Saint-Venant's principle. "For bodies extended in two or three dimensions the stress or strain due to loading on a small part of the body may be expected to diminish with distance on account of "geometrical divergence" whether or not the resultant is zero".<sup>5</sup> It is evident from *Fig. IV-10* and *Fig. IV-11* that the length of the chosen specimens is not sufficient to clearly decouple the stress distribution in the middle of the plate from the end effects. In other words, if the length were great enough, the stress distribution would not change with  $x$  co-ordinate after some distance from the edge.

*Fig. IV-13* shows the development in time of the longitudinal ( $\sigma_x$ ) and transverse ( $\sigma_y$ ) stresses. The development is traced along the line on the top side of the plate ( $x=250\text{mm}$ ,  $z=20\text{mm}$ ). Hence, the residual state corresponds to *Fig. IV-10.b* and *Fig. IV-11.b* with  $x=250\text{mm}$ .

As was analysed in the *Chapter II*, with rising temperature ahead of the moving heat source, the points close to the weld line start to experience compression in the longitudinal direction. Then, with rising temperature and, consequently, lower yielding point, the value of the longitudinal stress grows up to zero. Stresses in the regions a short distance from the arc are compressive, because the expansion of these areas is restrained by the surrounding metal where the temperature is lower. However, stresses in the areas further away from the weld arc are tensile and balance with compressive stresses in the areas near the weld.

Going further, at some distance behind the weld arc, the temperature drops sufficiently for the material to be stiff enough to resist the deformation caused by the temperature change. Due to cooling the areas close to the weld contract and cause tensile stresses.

After a certain time, the temperature change due to welding diminishes. High tensile longitudinal stresses are produced near the weld. The longitudinal stresses reach a value ca. 15% higher than the yielding point for room temperature. Also, in the regions away from the weld, compressive stresses arise, which balance the temperature along the weldment.

Ahead of the heat source, we first meet a hump in the tensile stresses, while the temperature is still close to zero. Further follows an abrupt fall down to compression, reaching the yield limit at slightly elevated temperatures. Then with rising temperature and, hence, lower yield limit, the transverse stresses climb up close to a zero values. This highly compressed region just ahead of heat source is in the equilibrium state with the tensile hump. Thus, the region in tension is in equilibrium with the unavoidable compression area around the hot elements trying to expand.

Following further along the time axis, at some distance behind the welding arc, the temperature drops sufficiently for the material to be stiff enough to resist the deformation caused by the temperature change. Due to cooling the areas close to the weld contract and cause gradually growing tensile stresses.<sup>6</sup>

## **2.2. Characteristic features of two welding procedures under investigation**

### **2.2.1. Stress development**

A thorough approach to the selection of welding procedure has to include a careful analysis of several aspects. One of them is the investigation of weld stress dynamics in the areas close to the weld.

During the heating period, when the temperature distribution in the transverse directions is non-uniform, triaxial stresses of significant magnitude can occur in the areas close to weld. This is why the dynamics of the stresses should be paid attention to.

In *Fig. IV-14* the dynamics of the stresses at the points situated on the bottom surface close to the weld is represented. These results are from 3D simulation of the welding of two 500×250×20mm plates. The maximum temperature in the point for all the considered cases was ca. 700<sup>0</sup>C. For the multi-pass welding procedure only the first and the last passes are mapped in *Fig. IV-14.b* and *Fig. IV-14.c*. In *Fig. IV-14.c* the time scale starts from zero and not from 14000s as it was during calculations. It is conditioned by the logarithmic scale for the time in *Fig. IV-14*.

Analysis of the data presented allows us to conclude that in the HAZ during the temperature equalisation stage, the correlation between stresses  $\sigma_x$ ,  $\sigma_y$  and  $\sigma_z$  may differ significantly from that of the final residual state. Initially, during the heating stage the maximum compression stresses is  $\sigma_y$  in the transverse direction. Later on the longitudinal stress  $\sigma_x$  becomes dominant, first in the compressive and then in the tensile region. The tensile transverse stress  $\sigma_z$ , acting in the through-thickness direction, is quite significant during the first stage of the heating and cooling process. They almost diminish with further heating and cooling.

The behaviour described above is similar both for the multi-electrode and the multi-pass welding procedures investigated in the thesis. For multi-pass welding the maximum value of the tensile stress  $\sigma_z$  (about 30% of yielding point  $\sigma_y$ ) during the heating stage is 1.5 times higher than in the case of multi-electrode welding. This fact can be explained by the existence of a higher temperature gradient in the through-thickness direction in the case of multi-pass welding. A similar effect is demonstrated for the transverse stress  $\sigma_y$ . Only the longitudinal  $\sigma_x$  stress behaviour is very similar for both welding procedures.

In addition, the development of the longitudinal stresses in time is more “stable”. The behaviour of the transverse stresses in the case of multi-electrode welding procedure is obviously affected by the action of the following electrodes (ca. 10<sup>th</sup> and 20<sup>th</sup> seconds on the  $\sigma_y$  and  $\sigma_z$  curves in *Fig. IV-14.a*). Regardless of the temperature ( $T$  curve) having a little disturbance caused by the next sources, the curves for  $\sigma_y$  and  $\sigma_z$  change their tendencies at these moments. At the same time,  $\sigma_x$  curve do not seemed to be affected.

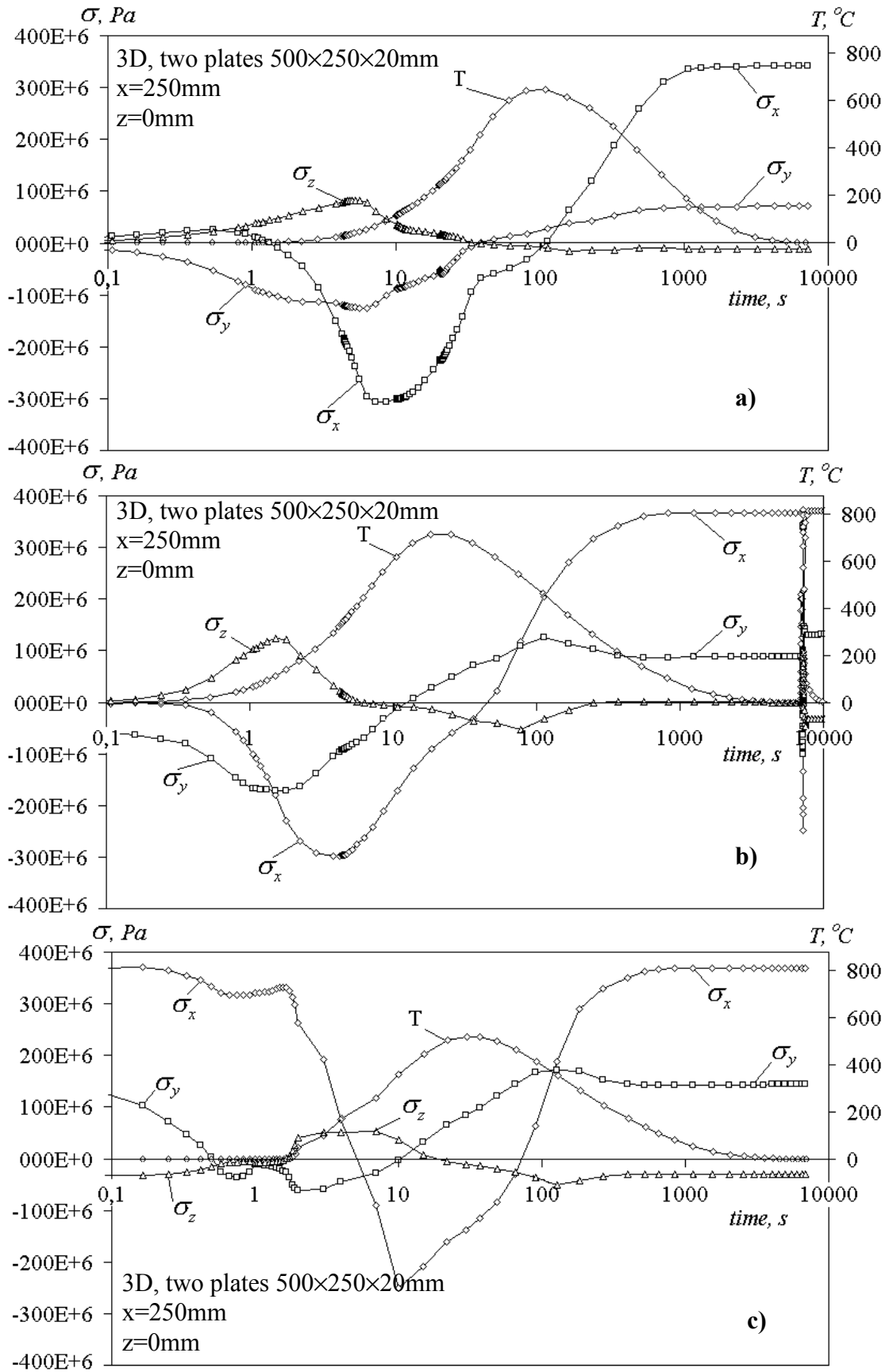


Fig. IV-14. Temperature and stresses development in the point situated in the heat affected zone; (a) – ME SAW; (b) – first pass and (c) – last pass of the multi-pass welding.

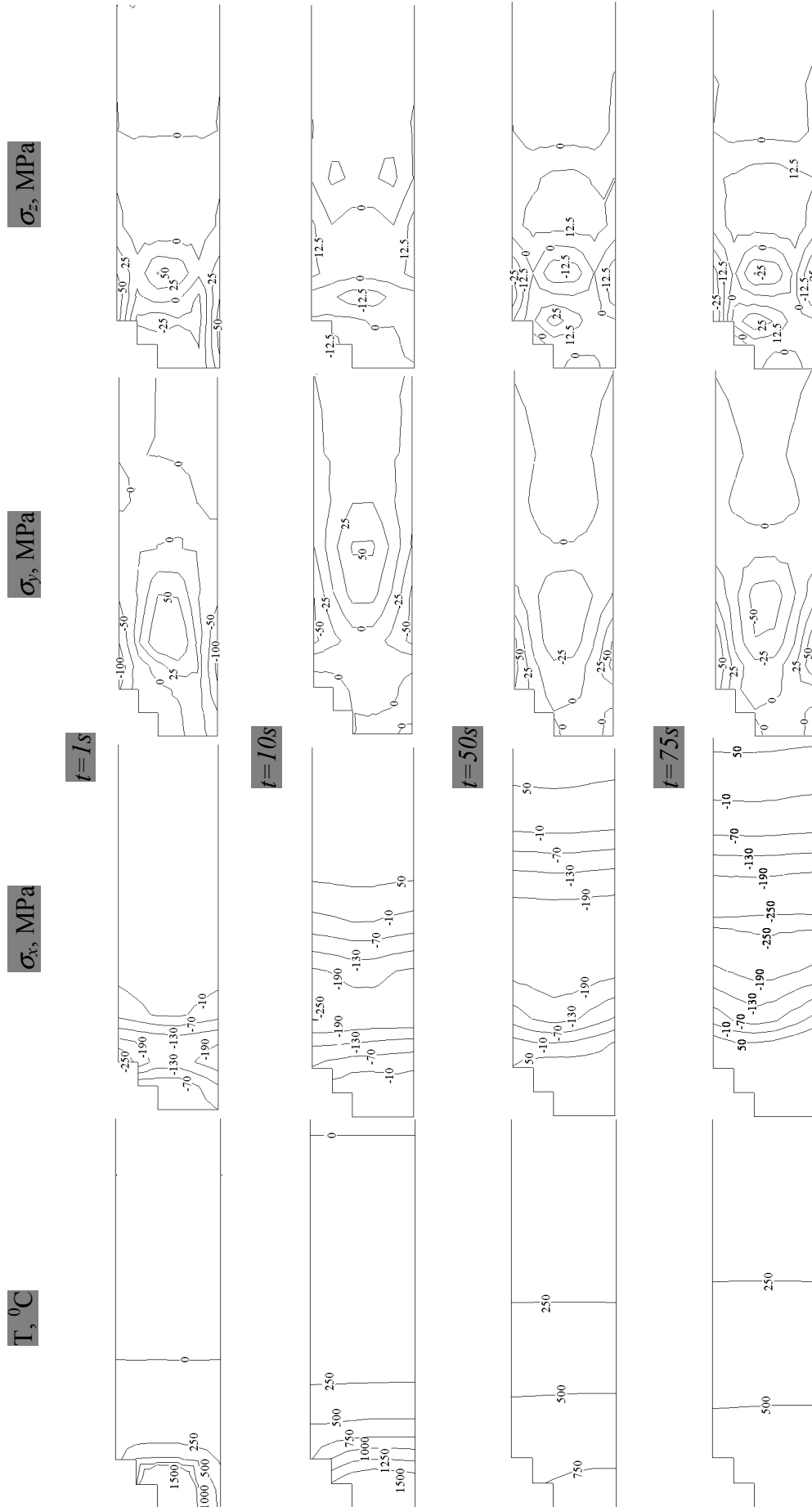


Fig. IV-15. Stress distribution in the cross-section of the joint after the first pass of the single electrode multi-pass welding procedure.

The time dependence of the stress caused by any welding procedure has several features. *Fig. VI-15* may help to understand some of them. During the initial stage of heating, a highly non-uniform temperature distribution exists. This fact causes the existence of a stressed state close to triaxial. In its turn, the triaxial stressed state hinders the plastic flow of the material (for more information see *Fig. II-4* in *Chapter II*), and allows the existence of stresses much higher than the yield point at the actual elevated temperature. In *Fig. VI-15* in the diagram corresponding to the  $\sigma_x$  distribution at  $t=10s$ , some locations in the area close to the weld are subjected to a stress about twice as high as yield point. This fact may lead to the initiation of defects (hot micro-cracks and propagating cracks) in the above indicated zone.

The features described above are especially significant in the case of high-strength steel welding. These steels have a yield point close to the ultimate tensile stress.

### 2.2.2. Residual stresses

During cooling (after ca. 100 seconds in *Fig. IV-14*) the longitudinal stress  $\sigma_x$ , in the areas close to the weld, becomes dominant over the transverse stresses  $\sigma_y$  and  $\sigma_z$ .

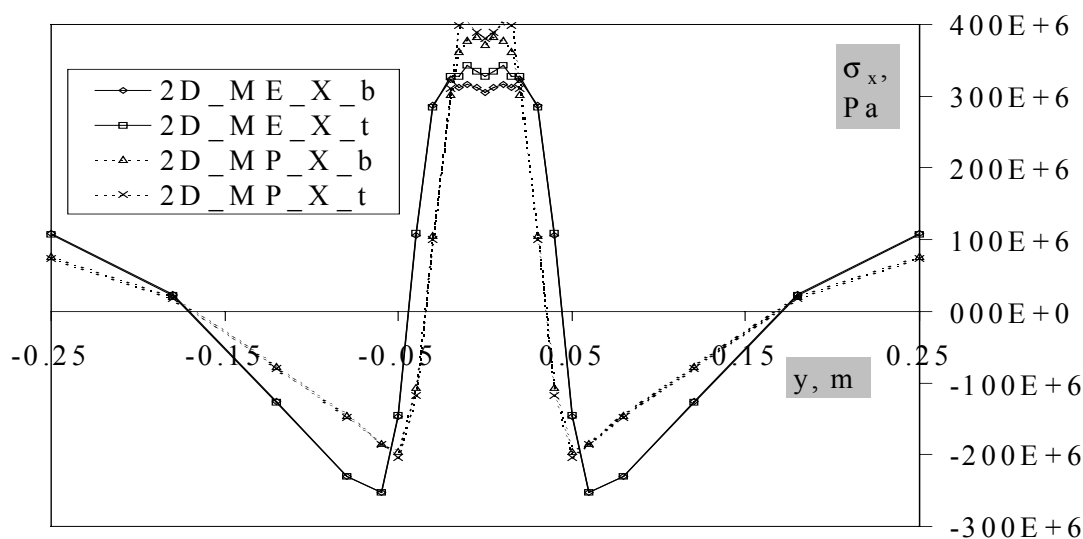


*Fig. IV-16. Longitudinal residual stress distributions along the transverse direction on the bottom and top sides of the plate.*

The data presented in *Fig. IV-16* show the difference between the residual longitudinal stress distributions after the two welding procedures under investigation. In *Fig. IV-17* the residual transverse stresses are shown. In the graphs the letters “MP” correspond to the single electrode multi-pass welding procedure (weld is completed in three passes), and “ME” corresponds to the multi-electrode welding procedure (three-electrode welding). The “2D” in the curves names in *Fig. IV-16* means that the results were obtained from 2D thermal stress model. The letters “b” and “t” correspond to the stress distributions on the bottom side and the top side of the plate.

Considering *Fig. IV-16* and *Fig. IV-17*, it is evident that longitudinal stresses are dominating in the welded structure. The maximum values of the transverse stress  $\sigma_y^{max}$  correspond to 32% of  $\sigma_x^{max}$  for the case of multi-pass welding procedure, and 24% for the case of multi-electrode welding procedure. The transverse stresses  $\sigma_z$  in the through-thickness direction are even less significant. They correspond to 10% and 9% of  $\sigma_x$  respectively.

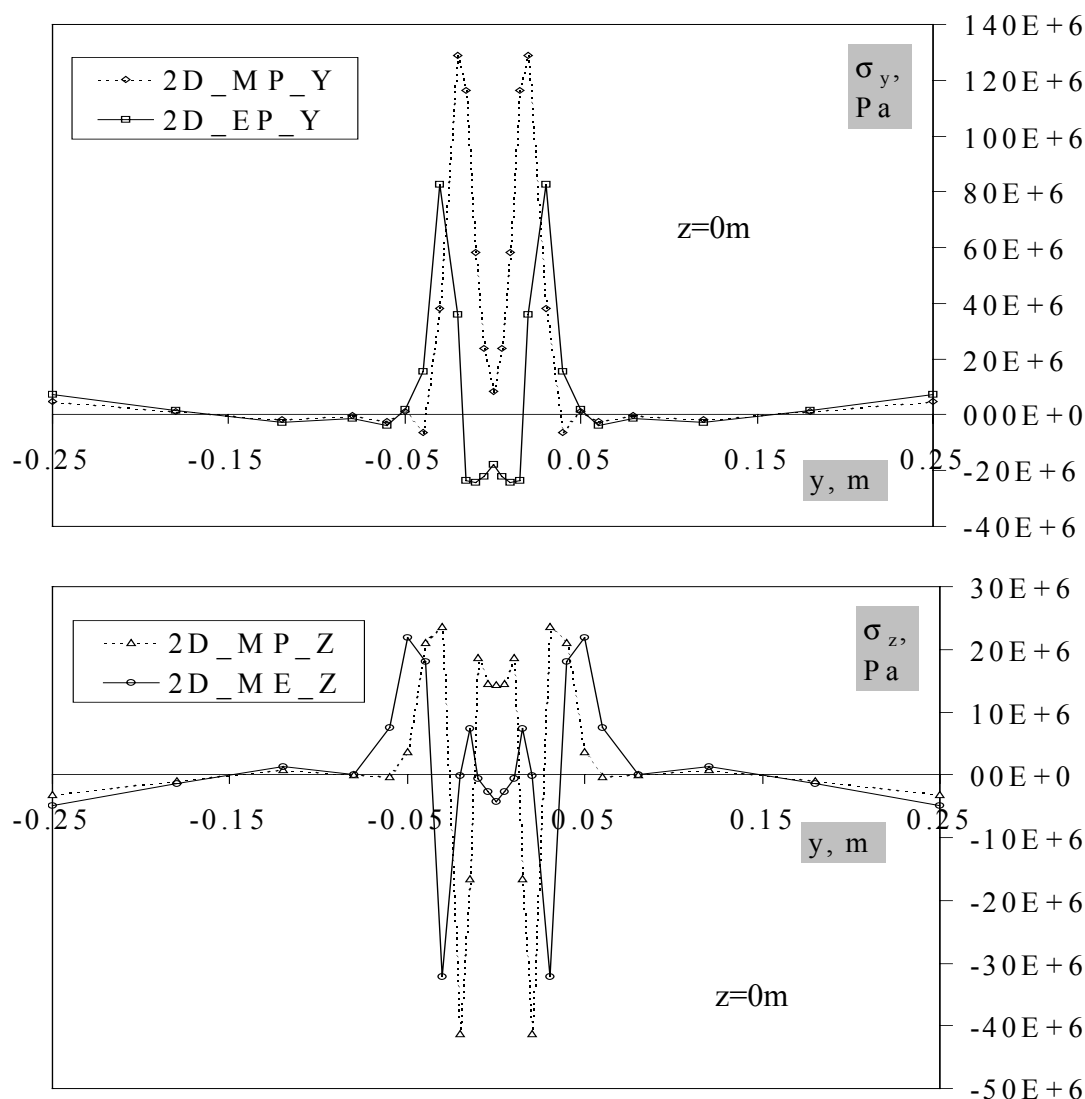


*Fig. IV-17. Residual transverse stresses distributions along transverse direction on bottom side of the plate.*

Both the longitudinal and transverse stress distributions in *Fig. IV-16* and *Fig. IV-17* demonstrate some similarities between the two welding procedures. The stress distribution corresponding to multi-pass welding, has a pronounced pattern characterised by higher maximum values for all the stress components, and a narrower area of plastically deformed zone (ca. 5 plate thicknesses against 6 thicknesses in the case of the three-electrode welding). It is affected by the width of the isotherm  $T_{max} \approx 200^{\circ}\text{C}$ . The areas heated above the  $200^{\circ}\text{C}$  limit were subjected to plastic flowing.

### **2.3. Conclusions**

In this section both the transient and the residual stress distributions for two welding procedures (multi-electrode and multi-pass welding) employed in shipbuilding are investigated and compared. The investigation was based both on 3D and 2D finite element sequentially coupled thermal stress models. Based on the results presented in this section the following conclusions can be drawn:

1. Residual stress fields typical of the high-power SAW employed in shipbuilding for the joining of medium-thick plates, can be characterised by a plane stress state ( $\sigma_z^{max}$  is about 10% of  $\sigma_y$ ).
2. Based on 3D-model results, the non-volumetric stress state leads to the conclusion that the existence of maximum residual longitudinal stresses higher than the yield point ( $\sigma_x^{max} \approx 1.15 \sigma_y$ ) can be explained by, firstly, the material hardening and, only secondly, by a feebly marked volumetric stress-state.
3. Very high heat input produces a relatively wide plastically deformed zone (relatively to the thickness). This fact explains the low level of the residual transverse stress in the through-thickness direction of the plate ( $\sigma_z^{max} \approx 0.1 \sigma_y$ ).
4. Compared to multi-pass welding, multi-electrode welding is characterised by a more pronounced dominance of the longitudinal stresses over the transverse stresses.
5. In the area close to the weld, at some distance from the plate surface, the transient stresses state can be pronouncedly volumetric. The tri-axial stress hinders the plastic flow of the material and gives rise to stresses much higher than the yield point at the actual elevated temperature ( $\sigma_x \approx 2 \sigma_y$ ). This fact can lead to the initiation of defects (hot micro-cracks and propagating cracks) in the above indicated zone.
6. Multi-electrode welding is characterised by a wider plastically deformed zone (ca. 6 plate thicknesses) compare to the multi-pass welding (5 thicknesses). It is affected by the width of the isotherm  $T_{max} \approx 200^{\circ}\text{C}$ . The areas heated above the  $200^{\circ}\text{C}$  limit were subjected to plastic flowing.

### 3. OVERALL DEFORMATION OF WELDED STRUCTURES

#### **3.1. In-plane deformation**

Welding stresses, discussed in the previous section, and deformations, discussed in this section, are closely related phenomena. During heating and cooling, thermal strains occur in the weld and adjacent area. The strains produced during the heating stage of welding are always accompanied by plastic deformation of the metal. The stresses resulting from these strains combine and react to produce internal forces that cause a variety of welding distortions.

Residual deformations introduce severe problems in the assembly of welded structures and reduce their quality. In some cases mechanical or thermal post weld treatment is required to reduce deformation to specifications. On the other hand, pre-weld misalignment of the parts to be welded, correct clamping and choice of welding procedure can significantly reduce deformations. Distorted shape and incorrect dimensions of welded components and structures may make them useless. In shipbuilding the extra cost of adjusting for deformations in joining together sections may be comparable to the cost of the actual welding itself.<sup>7</sup>

Mathematical modelling, providing quantitative prediction of and methods to reduce deformations can therefore improve quality and reduce costs in welded constructions.

Referring to experiments conducted on small specimens, the transverse shrinkage is often claimed to be insignificant compared to the longitudinal shortening.<sup>20</sup> The main focus of the present dissertation is the investigation of submerged arc welding procedures employed in shipbuilding. This welding process is used for butt welds of long plates. The longitudinal shrinkage is proportional to the length of the weld. Thus, in the case of long plates, the longitudinal shrinkage is also significant.

The present dissertation is intended to highlight the advantages and disadvantages of two different welding procedures. This section serves to demonstrate the influence of welding technique on the deformation dynamics and the residual distortion of the structure, caused by the non-uniform heating during welding.

##### **3.1.1. Transverse shrinkage**

Three-electrode one-sided submerged arc welding is considered first. *Fig. IV-18* shows the in-plane transverse shrinkage. The diagrams in *Fig. IV-18* indicate U-shaped form of the transverse shrinkage distribution along the outer edges parallel to the welding direction.

In *Fig. IV-18* the results from the sequentially coupled 2D generalised plane strain thermo-mechanical model, described in *section 3.2 of Chapter III*, are also shown. They are marked by short horizontal lines (in reality it is just a single point, because coordinate  $x$  is omitted in the 2D models). Compare to the 3D model, described in *section 3.3 of Chapter III*, the line for the three-electrode one-pass welding technique obtained

from the 2D model indicates underpredicted result (from 25 % up to 65%). In *Fig. IV-18* the results from the 2D and the 3D models of the three-electrode welding are assigned as *2D\_ME* and *3D\_ME* respectively. Results from 2D model of the single-electrode welding are marked by *2D\_MP*.

Nevertheless, this result can be used for comparison with the similarly organised 2D model of the single-electrode multi-pass welding procedure. The result for this technique is also marked in *Fig. IV-18*.

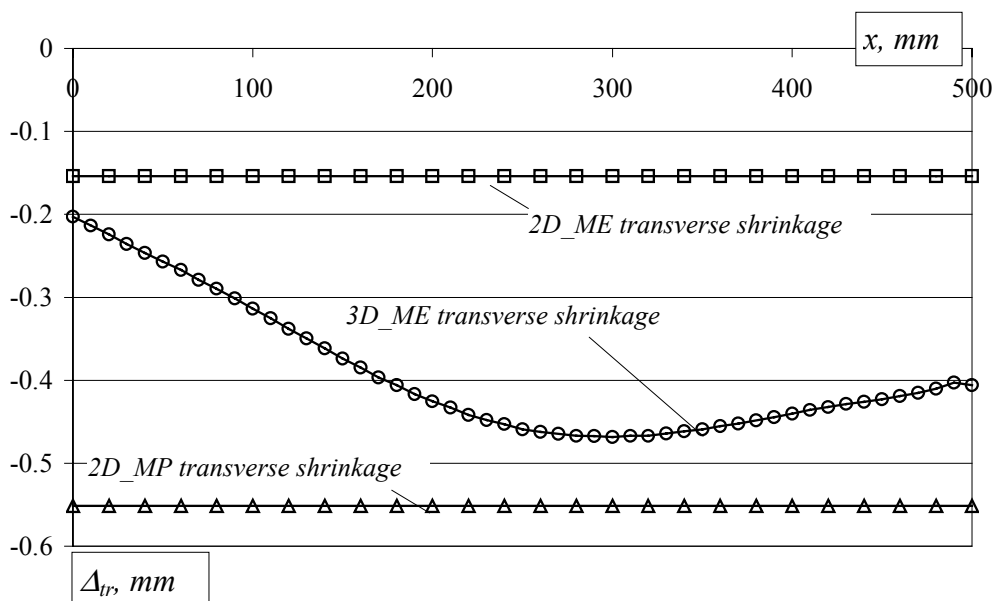


*Fig. IV-18. Transverse shrinkage distribution along the longitudinal edge of the plate ( $y=250\text{mm}$ ,  $z=10\text{mm}$ ).*

Comparison reveals that the multi-electrode welding procedure causes approximately three times less transverse shrinkage than the single-electrode multi-pass procedure. These results were obtained for exactly the same heat sources characteristics (net heat power, distribution in space, etc.). The only difference was the time interval between the action of three sources.

These values for the curve from the 3D sequentially coupled thermo-mechanical model are recalculated keeping in mind the angular deformation. The scheme explaining the recalculation procedure is shown in *Fig. IV-19*.

As an output from the ABAQUS we get the translation of the nodes in space. In *Fig. IV-19* the translation of point *A* in the *y* and *z* directions respectively are designated by  $u_2$  and  $u_3$ . Angular deformation alone would correspond to point *A* shifting to the *A'* position. Additional transverse shrinkage brings about a new position *A''*. For the case of insignificant angular deformations, the transverse shrinkage  $\Delta_{tr}$  equals with good accuracy the translation of nodes in *y*-direction. In ABAQUS designation the *y*-axis corresponds to the axis number two and, hence, for this case  $\Delta_{tr}=u_2$ .

In the case of significant angular deformation a correction to the  $u_2$  translation should be taken into account. The equation shown in *Fig. IV-19* allows us to calculate the real transverse shrinkage  $\Delta_{tr}$  based on the node translations  $u_2$  and  $u_3$ .

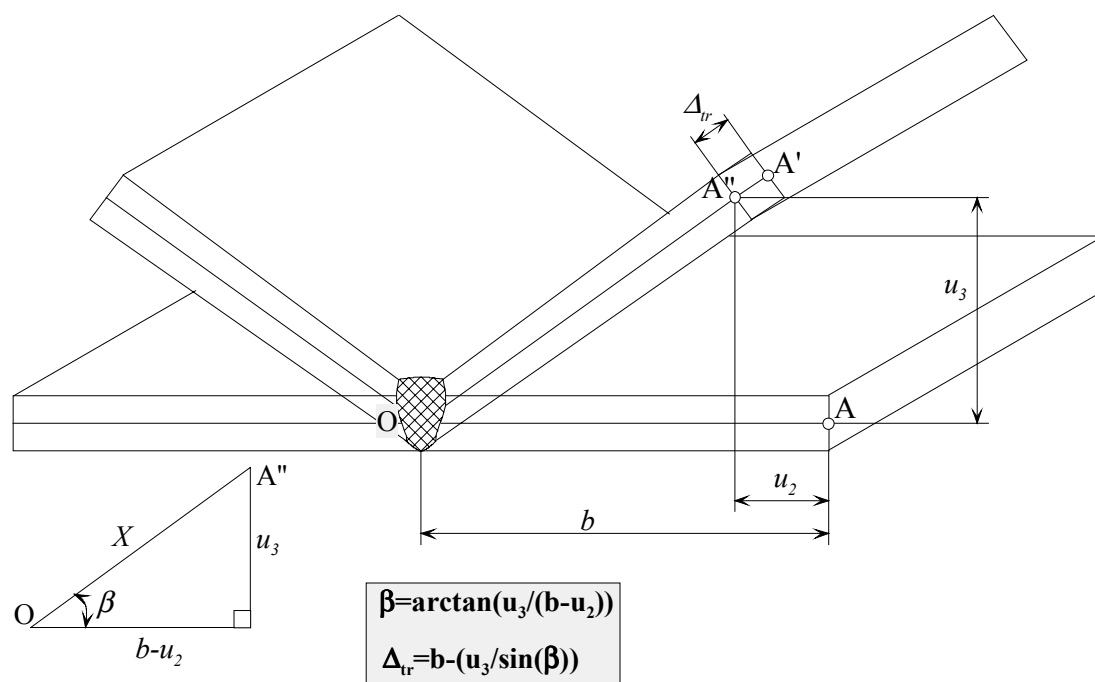


*Fig. IV-19. Recalculation scheme for the transverse shrinkage.*

### 3.1.2. Longitudinal shrinkage

*Fig. IV-20* shows the results from both the 3D and the 2D generalised plane strain models. The longitudinal shrinkage results from the 3D model are plotted as a function of the  $y$  co-ordinate. The results from the 2D models are indicated by two horizontal lines. Compared to 3D model the residual longitudinal shrinkage results from the 2D model for the three-electrodes one pass welding procedure are overpredicted by approximately 20%.

The 3D model clearly indicates a localised character of the residual longitudinal shrinkage. The plate has been distorted in the longitudinal direction mostly in the area close to the weld centreline. This area is approximately 50mm wide. The rest of the plate width in the longitudinal direction was insignificantly distorted.

Based on *Fig. IV-20* we can compare the two welding techniques (the three-electrode one pass welding and the single-electrode multi pass welding). Based on the 2D generalised plane strain model, we can conclude that for the investigated welding parameters and the plates geometry, the multi-electrode procedure causes 50% greater longitudinal shrinkage.

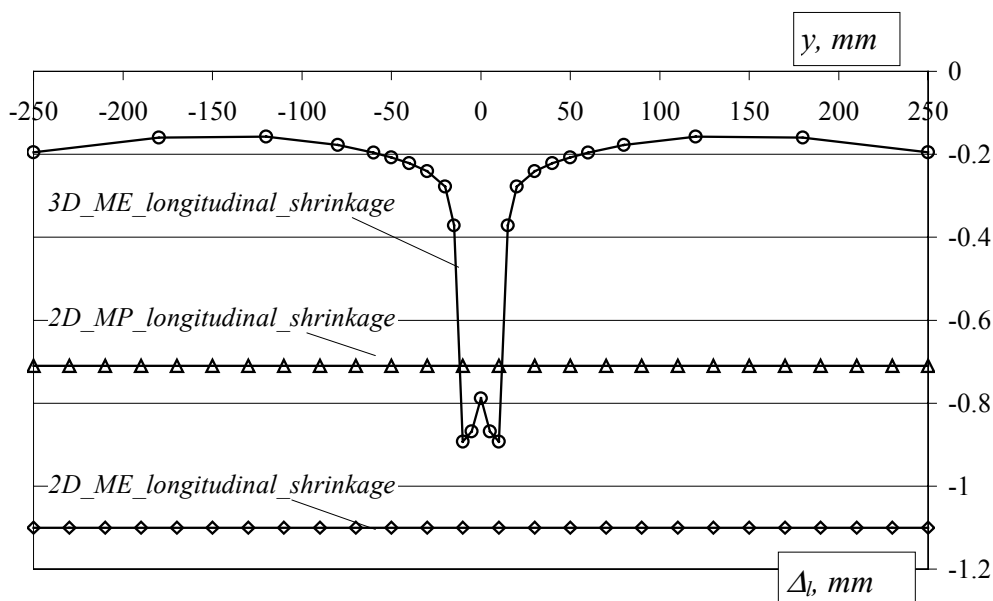


Fig. IV-20. Longitudinal shrinkage distribution along the transverse direction.

### 3.2. Inherent strain as a source for elastic finite element analysis

When the welded structure is small, the more or less thorough 3D thermal-elastic-plastic finite element analysis can be used for welding deformation and residual stress prediction. However, in the case of large and complicated structures, it is difficult to analyse non-linear time-dependent problems. Despite swiftly growing computer capacity, the solution of such problems demand too much computer time and hard disc space. The concept of inherent strain was introduced in the middle 1970s by Yukio Ueda.<sup>8,9</sup> Later on, this concept was used and developed mostly by Japanese and American scientists.<sup>10,11,12,13,14,15</sup>

Generally, the inherent strain can be considered as a source for both deformations and residual stresses produced by welding. If the inherent strain for an individual welding process is known, the deformation and residual stress distribution can be estimated based on simple elastic finite element analysis instead of using highly complicated thermal-elastic-plastic (TEP) models. At the same time, to determine the inherent strain with a good accuracy, a thorough TEP analysis or experimental results are needed. To resolve the problem, Ueda in early 1990s suggested the possibility of approximation of the inherent strain distribution in large complicated structures based on the experimental data or on the FE analysis conducted on smaller specimens.

In general, the total strain  $\varepsilon$  is composed of the elastic strain  $\varepsilon^e$  (EE), the inelastic strain  $\varepsilon^i$  (IE), and the thermal strain  $\varepsilon^{th}$  (THE). The inelastic strain  $\varepsilon^i$ , in its turn, consists of the plastic strain  $\varepsilon^p$  (PE) and the creep strain  $\varepsilon^c$  (CE). The ABAQUS notation is given in the brackets.

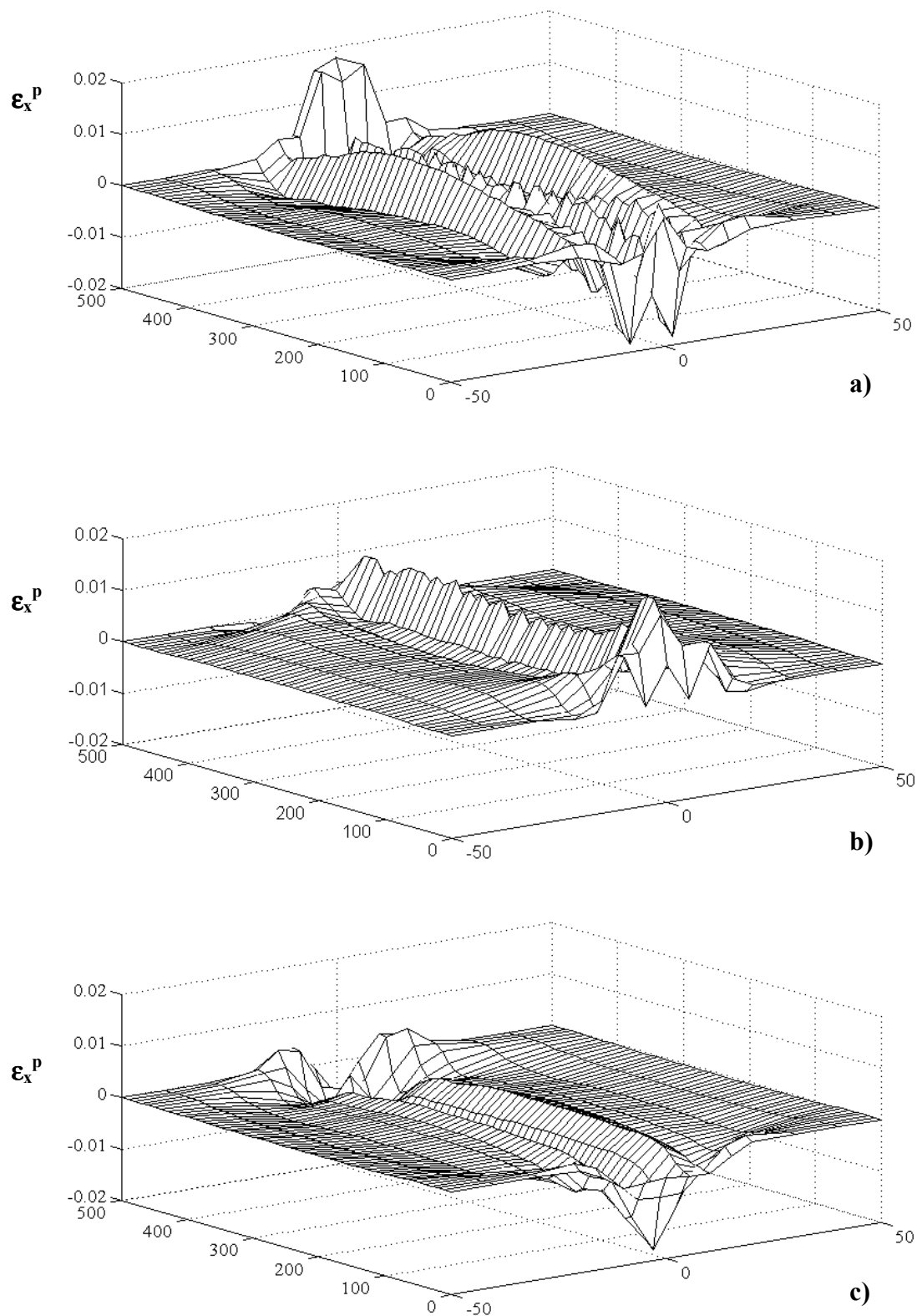


Fig. IV-21. Residual plastic strain in the weld longitudinal direction  $\varepsilon_x^p$  distribution over the plane of the plate (results from the 3D model of the three-electrode welding); (a) – top surface; (b) – middle-section; (c) – bottom surface.

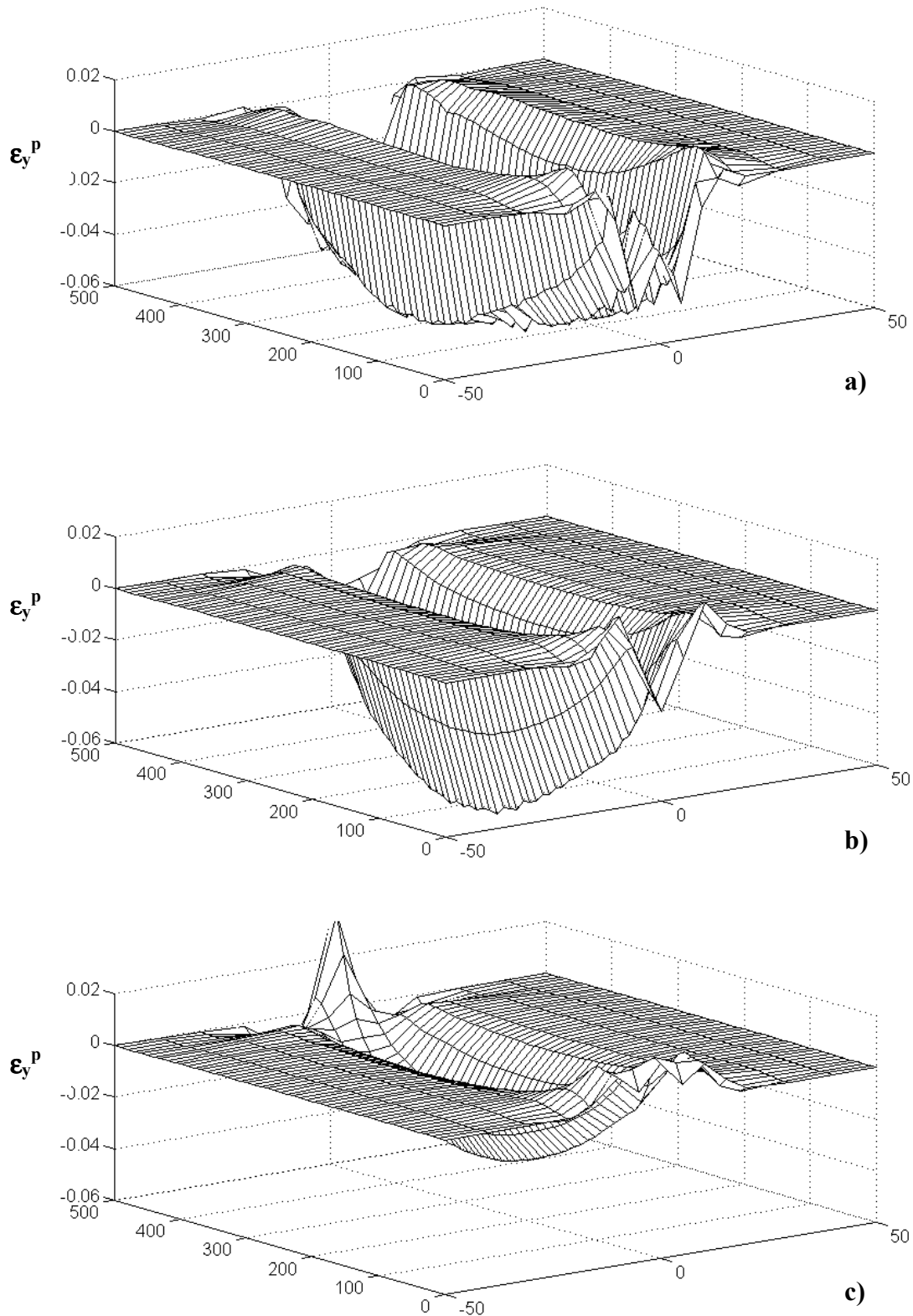


Fig. IV-22. Residual plastic strain in the weld transverse direction  $\epsilon_y^p$  distribution over the plane of the plate (results from the 3D model of the three-electrode welding); (a) – top surface; (b) – middle-section; (c) – bottom surface.

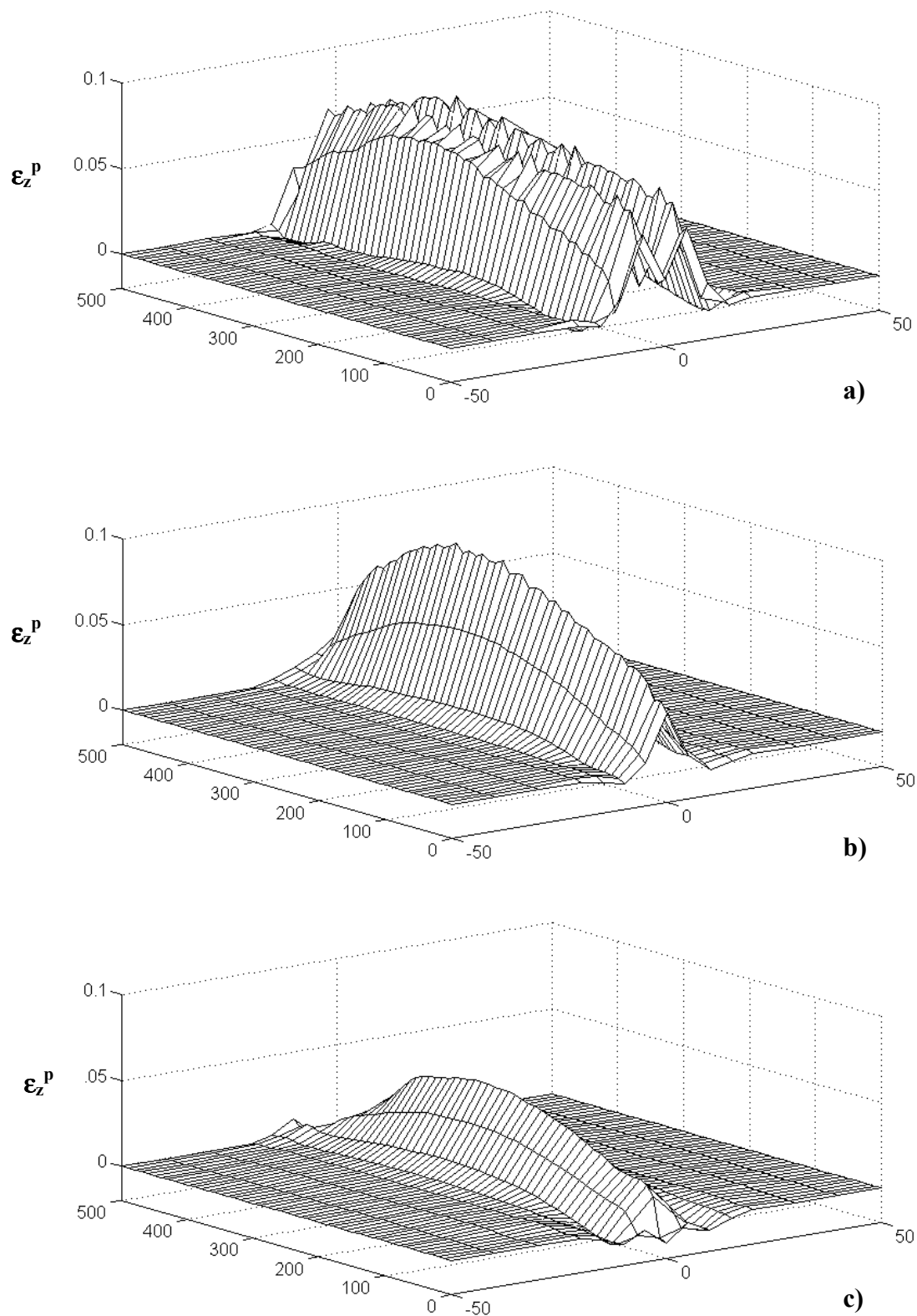


Fig. IV-23. Residual plastic strain in the through-thickness direction  $\epsilon_z^p$  distribution over the plane of the plate (results from the 3D model of the three-electrode welding); (a) – top surface; (b) – middle-section; (c) – bottom surface.

The present dissertation is concentrated with the cases of thermo-mechanical models of welding applications. In such instances the model usually does not include creep analysis. Our models are not exceptions to this rule. Hence, for the completely cooled down welded structure, the inherent, or in other words, incompatible, strain consists purely of plastic strain  $\epsilon^p$ .

This section is assigned to analyse the inherent strain distribution based on TEP FEM of the three-electrode submerged arc welding of plates in a butt-joint. These results can be used for further investigation of the welding deformation phenomena in large plate welding.

In *Fig. IV-21*, *Fig. IV-22* and *Fig. IV-23* the distribution of the residual plastic strain over the plane of the plate specimen is shown. It should be emphasised that the graphs cover only a 100mm wide stripe along the weld centreline. This region was chosen because the plastic deformation is concentrated in this zone.

These figures demonstrate the complexity of the plastic strain distribution. All these figures include the distribution over three parallel planes (the top surface ( $z=20\text{mm}$ ), the bottom surface ( $z=0\text{mm}$ ) and the plane with  $z=8\text{mm}$ ). While preserving the overall character of the distribution, the shape of the distribution changes significantly with the through-thickness co-ordinate ( $z$  co-ordinate).

The analysis of the inherent strain distribution indicates extreme complications regarding the inherent strain generalisation.

### **3.3. Plastic strain evolution**

The main criterion for the initiation of hot cracks is the evolution of the plastic strain in the high temperature region.

The plastic strain ( $\epsilon_x^p$ ,  $\epsilon_y^p$  and  $\epsilon_z^p$ ) evolution for the points of the heat affected zone is a quite characteristic feature. *Fig. IV-24* shows the kinetics of these characteristics as a function of temperature during heating and cooling stages in the points situated in the middle of the plate ( $T_{max} \approx 850^\circ\text{C}$ ).

The plastic strain in all three normal directions ( $\epsilon_x^p$ ,  $\epsilon_y^p$  and  $\epsilon_z^p$ ) appear in the heating stage of the process after reaching some temperature (ca.  $100^\circ\text{C}$  for the case of 2D model and  $200^\circ\text{C}$  for the case of 3D model in *Fig. IV-24.b*). It means that the 2D model predict a wider plastically deformed zone. In other words, according to the 2D model, the plastics deformation occurs in areas exposed to lower temperatures.

This effect is caused by different constraints applied to the plate according to the models. In the case of 2D generalised plane strain model, the plate is almost free to expand in the transverse  $y$ - and  $z$  directions. In the 3D model, the expansion in these directions is constrained to a higher degree because of the cold and, consequently, stiff part of the plate ahead of the moving heat source.

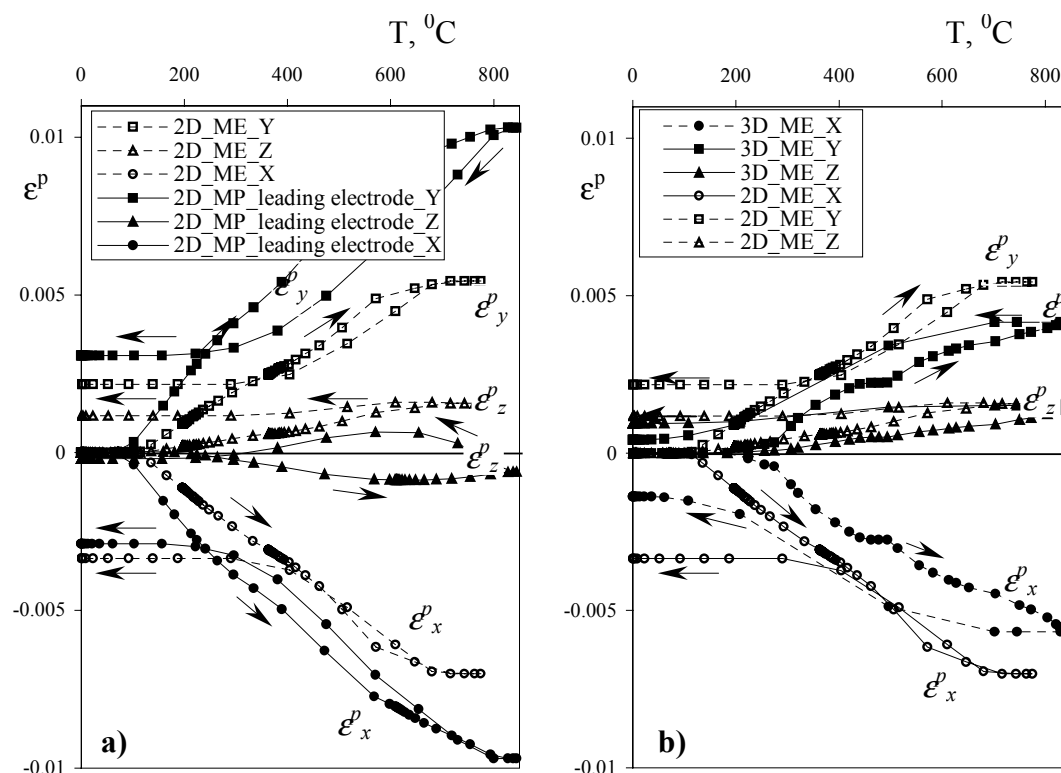


Fig. IV-24. Plastic strain  $\epsilon_x^p$ ,  $\epsilon_y^p$ ,  $\epsilon_z^p$  kinetics as a function of temperature for the points situated in the HAZ; (a) – comparison of multi-electrode and single-electrode welding procedure; (b) – comparison of results from 3D and 2D generalised plane strain model for three-electrode one pass welding.

In Fig. IV-24.a the results from the 2D generalised plane strain model for the two different welding techniques are presented. The three-electrode welding procedure is represented by dotted lines.

In both cases presented, after reaching some critical temperature, the plastic strain in  $y$ -direction  $\epsilon_y^p$  is positive, and the plastic strain component in the longitudinal  $x$ -direction  $\epsilon_x^p$  is negative. The  $z$ -direction component  $\epsilon_z^p$  in the case of three-electrode welding is non-significant and always positive. In the case of single-electrode welding, during the heating stage  $\epsilon_z^p$  is growing insignificantly in negative values. After reaching the maximum temperature in the point considered in the HAZ, plastic strain in through-thickness  $z$ -direction is turning to be positive. Such a correlation is based on the highest temperature gradient in  $y$ -direction.

Plastic deformations  $\epsilon_x^p$  and  $\epsilon_y^p$  for the cases considered (three-electrode welding and multi-pass welding) differ significantly from each other numerically. At the same time, they are qualitatively quite similar.

The tendencies described above are applicable for points in the HAZ with higher  $T_{max}$  as well. Hence, in the base metal close to the fusion line compressive stresses arise. These stresses cause significant negative plastic deformation in the longitudinal direction  $\epsilon_x^p$  (in the direction with lower temperature gradient). In order to fulfil the rule of

incompressibility ( $\epsilon_x^p + \epsilon_y^p + \epsilon_z^p = 0$ ), the plastic deformation  $\epsilon_y^p$  in the transverse direction is positive, while the plastic deformation in  $z$ -direction is kept close to zero.

Consequently, during the cooling stage of welding, in the points considered in HAZ, the stresses in the longitudinal direction turn out to be tensile. Also, in certain situations, tension along the melting boundary may cause crack-like defects in the HAZ. Such defects are typical for the medium-alloyed steels.

### **3.4. Conclusions**

In this section the strain fields for two welding procedures (multi-electrode and multi-pass welding) employed in shipbuilding are investigated and compared. The investigation was based both on 3D and 2D generalised plane strain finite element sequentially coupled thermal stress models. Based on the results presented in this section the following conclusions can be drawn:

1. The three-electrode one pass welding procedure causes approximately 70% less transverse shrinkage than the single-electrode three pass technique.
2. In the case of near square shape of the welded plates (length  $\approx$  width), the longitudinal shrinkage distribution has a localised character. Only a narrow zone close to the weld line (approximately two plate thicknesses) shrinks significantly.
3. The single-electrode three pass welding procedure gives less longitudinal shrinkage. The longitudinal shrinkage in the case of the three-electrode welding is 50% higher than in the case of single-electrode three pass welding technique.
4. The data presented in *section 3.2* indicates a significant non-linear behaviour of the residual inherent (plastic) strain. To further explore the possibilities of using the inherent strain concept in welding stress and deformation calculations, more effort should be put into inherent strain generalisation.
5. The 2D generalised plane strain model reveals a wider plastically deformed zone than the 3D model. In other words, according to the 2D model, the plastic deformation occurs in areas exposed to lower maximum temperatures. In the case considered, according to the 2D model plastic deformation occurred in the areas with  $T_{max} > 100^{\circ}\text{C}$ . For the 3D model this interval is narrowed down to  $T_{max} > 200^{\circ}\text{C}$ .
6. Considering the plastic strain development in the HAZ of the weld, it was demonstrated that the single-electrode welding procedure for the investigated conditions exposes the weld to higher plastic strain at elevated temperatures. The maximum transient plastic strain in the transverse direction  $\epsilon_y^p$  at  $800^{\circ}\text{C}$  is twice as high in the case of the multi-pass welding as in the multi-electrode technique. This fact indicates that the multi-pass welding procedure is more favourable in terms of hot crack initiation.

#### 4. OUT-OF-PLANE DEFORMATION

Just like any other welding deformation, the angular deformation is caused by non-uniform heating and cooling during welding. The reason for the angular changes in the butt-welded plates is the existence of a temperature gradient in the through-thickness direction.

The residual angular deformations introduce severe problems into the process of welded structure assembly. At the same time, correct arrangement of the prefabrication and welding procedures (selection of the rational welding parameters, using counter-aligning measures, etc.) may prevent unacceptable deformations. Distorted shape and dimensions also reduce the usefulness of the structure.

The above mentioned allows us to see the importance of the angular deformation development modelling on the design and manufacturing stages. It is important for estimation of the reliability of the structure, and development of suitable methods for improving the dimensional accuracy of the welded structure.

##### 4.1. Variation of the data reported in literature

Results reported in literature often differ much from each other. This may be due to the great number of influencing factors. All these factors have a non-linear effect on the angular deformation. Respectively, it is quite complicated to take into account these effects in the experimental investigation of the problem. In such instances it is difficult to predict experimental results and compare them with different practical cases. Results predicted by sequentially coupled thermal-mechanical analysis can serve as an approximation of the real one.

In *Fig. IV-25* the results of experimental investigation by Kuzminov<sup>16</sup> are shown. This illustration is based on a curve from *Fig. II-29* in *Chapter II* for 10 mm/s welding speed (corresponding to our investigation). The heat input per unit length corresponding to the considered welding conditions and a typical value of the arc efficiency coefficient  $\eta$  is represented by the fine vertical line in *Fig. IV-25*.

Boundaries of a possible  $q_w/h^2$  area depending on a range of  $\eta$  values are highlighted as well. This area shows how the angular shrinkage is affected by variations in the arc efficiency. We can clearly see that relying upon Kuzminov's investigations for studying example we can get a range of possible  $\Delta\beta$  values from 0.0025rad up to 0.0060rad.

In the graphs from Kuzminov's work the maximum angular deformation is 0.035rad. At the same time, Kuzminov reports angular deformation as large as  $20^\circ$  ( $\approx 0.35\text{rad}$ ) in the case of long plate welding. That is ten times higher than the claimed maximum in *Fig. II-29* and *Fig. IV-25*. Once again, this fact accentuates the complexity of our problem.

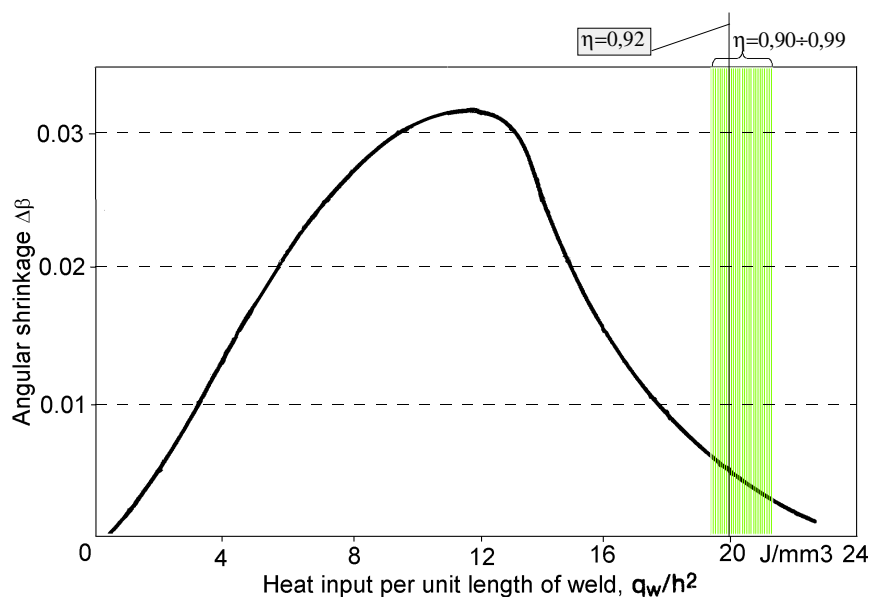


Fig. IV-25. Angular shrinkage  $\Delta\beta$  as a function of heat input per unit length of weld,  $q_w$ , and weld or plate thickness  $h$  for welding speeds  $v=10\text{mm/s}$  with marked area corresponding to the investigated three-electrode process and range of the arc efficiency coefficient.<sup>17</sup>

Ueda, in one of his works, reports on the mechanical effects of the four-electrode welding procedure on 19.5mm thick plates of large size.<sup>18</sup> He reports the angular deformation to vary between 0.025rad and 0.040rad. According to the welding parameters used in the experiments, these values are more than ten times higher than predicted from the diagram shown in Fig. IV-25.

This fact means that there are more welding parameters that affect the formation of the angular deformation than are taken into account in Fig. IV-25. Also, these parameters have quite a strong influence. One of such parameter is the weld length. With constantly increasing weld length the angular deformation is increasing until it reaches some maximum value.<sup>16</sup> This fact was also confirmed by the experiments conducted in our laboratory on 6mm thick plates.

#### **4.2. Comparison of the 3D FEA results with different experimental data**

In an effort to verify the models presented in section 3 of Chapter III several computer runs with various combinations of boundary conditions and applied forces were conducted. In the current section these results will be compared with different experimental data.

In his work Kuzminov states that the formation of the angular deformation depends on the parameter representing the through-thickness temperature non-uniformity. This parameter is the heat input per unit length of weld, divided by the squared plate thickness, i.e.  $q_w/h^2$ .

Based on the above-mentioned criterion of similarity  $q_w/h^2$ , experiments on 6mm plates were conducted in the laboratory. The heat source characteristics were chosen in order to keep the  $q_w/h^2$  parameter on the same level as in the case of three-electrode welding procedure simulated on 20mm plates. In-plane dimensions were chosen to be the same (two plates 500×250mm). The welding speed was 10mm/s.

Fig. IV-26 shows both the results from the 3D thermo-mechanical models and the experimental data. The predicted angular deformation in 6mm plates came out to be under predicted by 45% compare to experimental results. The calculated angular deformation for 20mm plates is only 13% off the experimental value for 6mm plates.

The mesh for both 3D models (6mm plates and 20mm plates) was essentially the same. The only difference was that in the case of thin plates the elements were 1.2mm long in the through-thickness direction instead of 4mm in the case of 20mm plates.

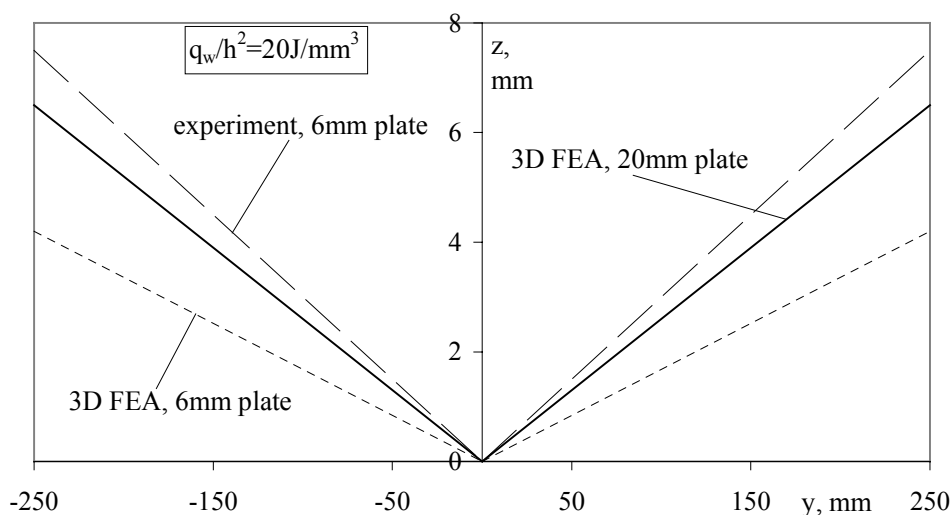


Fig. IV-26. Comparison of the two similar (in terms of  $q_w/h^2$ ) welding cases. Angular deformation of 6mm plate (experiment and simulation) and 20mm plate (simulation).

The poor accuracy in the case of 6mm plate can be explained by the flattened elements situated close to the weld. This kind of elements cause a locking phenomenon as described in detail in *Appendix F*. In order to avoid this we would have to increase the thickness of elements, but it would reduce the number of the elements in the through-thickness direction.

The other source of inaccuracy is the relatively rough mesh compared to the size of the weld pool. The weld pool was approximately 25-30mm long and 7mm wide. The smallest elements situated near the weld centreline have dimensions 5×10mm. In other words the weld pool was three elements long and less than two elements wide. This fact caused some errors in temperature field determination, probably including the temperature region where  $400 < T < 1000^\circ\text{C}$ . This temperature interval is the most important for the mechanical part of the thermo-mechanical simulation.

Fig. IV-27 shows the out-of-plane deformation caused by the welding of two 6mm thick plates. In Fig. IV-27 both results of the experiment and simulated data are presented.

It is clearly seen that the overall shape of the plates was predicted quite accurately by 3D model. At the same time, as already mentioned, the absolute value of angular change turned out to be under-predicted by 45%.

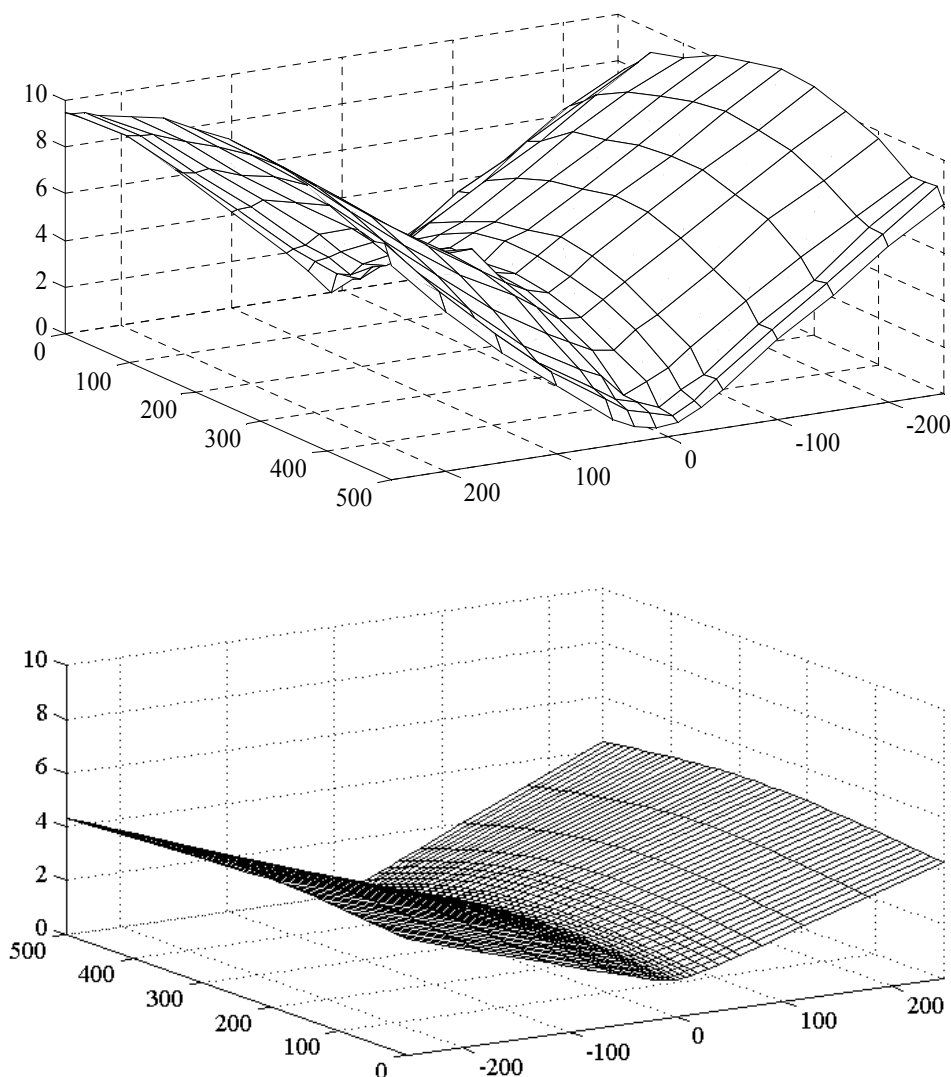


*Fig. IV-27. Comparison of out-of-plane deformation in 6mm plates; (a) – experimental results; (b) – results of the 3D FEA.*

Ueda, in his previously mentioned work<sup>18</sup>, published results of the investigations carried on 19.5mm thick large plates. His experiments were similar to our multi-electrode submerged arc welding technique. Of course, his results cannot be used for evaluation of the FE model accuracy. But, they can show the similarity of the tendencies evaluated by our 3D sequentially coupled thermo-mechanical.

In *Fig. IV-28* both the experimental results published by Ueda and those calculated with the 3D model data are shown. These results are in a good qualitative agreement. The absolute value of the angular deformation measured in the experiment is 35÷60% of the calculated value based on the model.

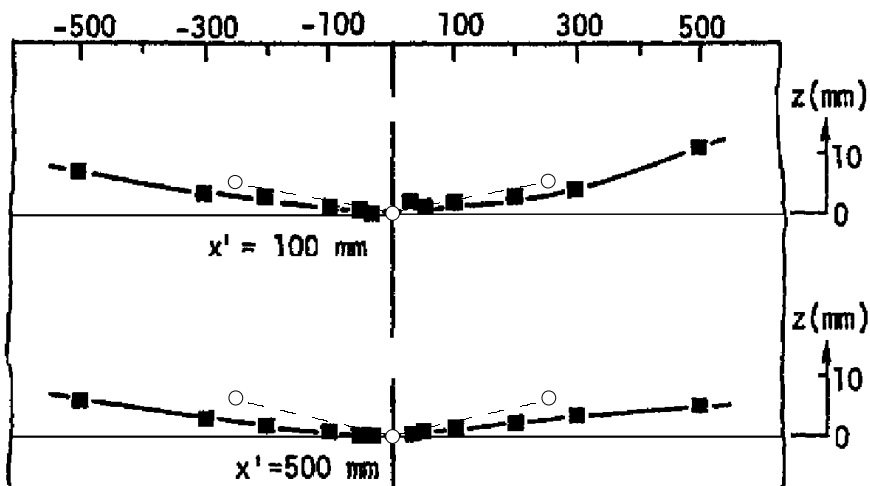


Fig. IV-28. Experimentally evaluated by Ueda<sup>18</sup> out-of-plane deformation (firm lines and squares) and simulated results (dashed lines and circles).

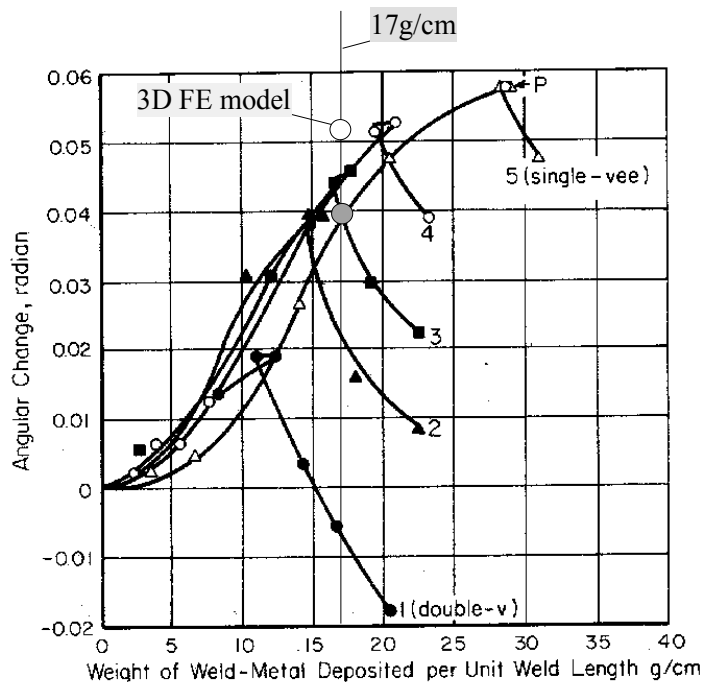


Fig. IV-29. Effect of groove shape on angular change;<sup>19,20</sup> values corresponding to the investigated welding procedure ( $w=17g/cm$ ) are superimposed.

Kihara and Masubuchi analysed distortion produced in a ring-type specimen by angular change due to butt-welding.<sup>21</sup> The measured effect of the shape of the groove on angular change is demonstrated in Fig. IV-29. In one set of experiments, a single-vee-type bevel was prepared in the ring-type specimen with 600mm outer diameter, 300mm inner diameter, and 19mm plate thickness.

A comparison between calculated and experimentally measured results reveals that in some cases simulations give overestimated values (as in the case of two Japanese sources) and in some cases the deformation turns out to be underestimated (as in the case of our own experiments). It is difficult to exactly simulate experiments in detail because the deformation is quite sensitive to variations in welding conditions. These problems are discussed in more details in *section 4.1* of the current chapter and in *section 2.3.5.3* of *Chapter II*.

The weight of the electrode consumed in the case of the steel welding can be calculated according to the following equation.<sup>20</sup>

$$w=0.058D_f^2$$

where  $w$  is the weight of the electrode consumed;  $D_f$  is the weld size.

In *Fig. IV-29* the data corresponding to our three-electrode welding procedure electrode consumption is marked by the solid vertical line. The intersection of this line and the curve for the single-vee bevel (number 5) corresponds to our of the welding parameters (for more information see *section 1* of *Chapter III*).

The angular change calculated according to the 3D thermo-mechanical model is approximately 30% higher than those corresponding to the experiments by Kihara and Masubuchi.

The angular deformation calculated according to the empirical equation suggested by Okerblom<sup>22</sup> (*eq. 11* in *Chapter II*) is  $\beta=0.046$ rad. That means that this value is only 8% lower than the angular change calculated according to the 3D thermo-mechanical model.

### **4.3. Overall shape of the plates deformed by welding**

The angular change in the cross-section of the weld starts to grow right after the heat source has passed over this section. The formation period of the angular deformations is longer than the period of formation of residual longitudinal deformations. This happens because the temperature equalisation in the through-thickness direction comes much earlier than in the plate-width direction.

The amount of the angular deformation can change the final overall shape of the structure. In other words, angular deformations followed by the longitudinal shrinkage affects the overall shape of the plates.

In *Fig. IV-30* the residual out-of-plane deformation of the welded plates caused by three-electrode one-pass welding is shown. The deformed longitudinal  $x$ -axis has a convex form. The development of such a shape is illustrated in *Fig. IV-31*.

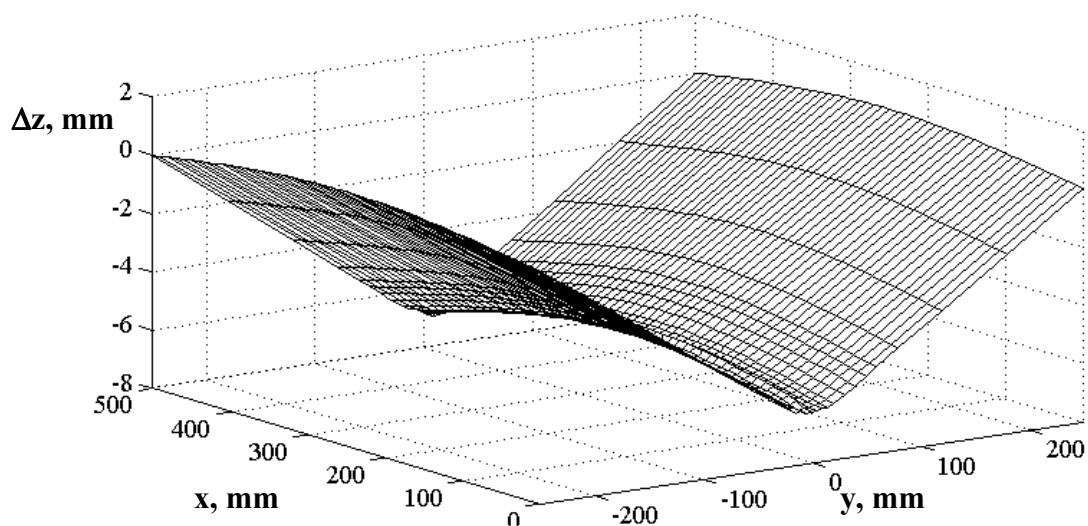


Fig. IV-30. Out-of-plane deformation caused by the three-electrode one-pass welding of 20mm thick plates (results after 3D thermo-mechanical model).

If the angular deformations are not significant (like in the case demonstrated in Fig. IV-31.a) then the centre of the plastically deformed zone lies higher than the median plane. Hence, the  $x$ -axis has a concave shape. In the case illustrated in Fig. IV-30 the angular deformations are significant, and the centre of plastically deformed zone lies lower than the median plane. It corresponds to the case in Fig. IV-31.b. That is why the plate in Fig. IV-30 has the convex shape.

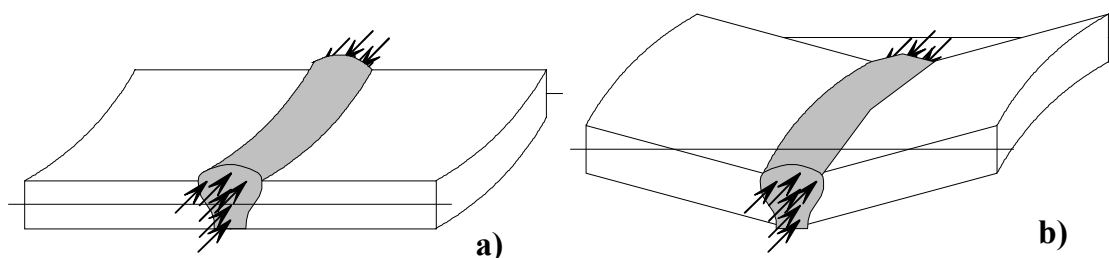


Fig. IV-31. Scheme of formation of “convex” and “concave” out-of-plane deformation.

#### **4.4. The effect of heat source distribution on the angular deformation**

Among other factors, the angular deformation depends on a shape of the seam. The shape of the seam in its turn depends on the concentration and other characteristics of the power source.

*Fig. IV-32* shows the effect of the shape of the weld pool. This effect was investigated on the 2D plane strain model of the welding of the 6mm steel plates. In all three cases considered the heat input per unit length of the weld is kept on the same level. The voltage-amperage characteristics were the same and the welding speed was the same. The only difference was in the heat source distribution.

In the first case (*Fig. IV-32.a*) the heat source was assumed to be distributed as a column starting from the top surface and extended over  $\frac{3}{4}$  of the plate thickness. It is evident, that in this case the through-thickness temperature distribution has almost uniform character. In this case a melt-through was achieved.

The curve corresponding to this case is marked by number **1**. It is clearly seen that in this case the angular change is quite insignificant compared to the other two cases. It is nine and a half times lower than in the third case.

In the second case (*Fig. IV-32.b*) the source was assumed to be distributed as a thick spot on the top surface of the plates. The source was extended over  $\frac{1}{6}$  of the plate thickness. In this case the weld pool in the cross-section has approximately the shape of a semi-circle. This case is accompanied by a very strong temperature gradient in the through-thickness direction in the area close to the weld centreline.

The curve in *Fig. IV-32.d* corresponding to this case is marked by number **2**. It shows the significant increase in the angular deformation compared to the first case.

The third case corresponds to the some hypothetical situation when the source is spread over a large area close to the top surface (*Fig. IV-32.c*). In this case the weld pool itself does not extend deeper than  $\frac{1}{3}$  of the plate thickness. In this case we have extreme conditions when even higher angular deformation can be achieved.

The curve corresponding to this extreme case in *Fig. IV-32.d* is marked by number **3**.

A quite interesting fact is that the angular deformation in the third case starts to grow rapidly later than in the second case. In the second case the rapid increase happened 0.5s after the source had passed the cross-section, and in the third case it happened 1.0s after the source.

The temperature equalisation in the through-thickness direction in the third case is lagging behind compared to the second case. It demonstrates that significant angular deformation growth starts only when the plates are sufficiently heated on the bottom side as well as on the top. In other words, a softened region of the metal should exist along the centreline of the cross-section.

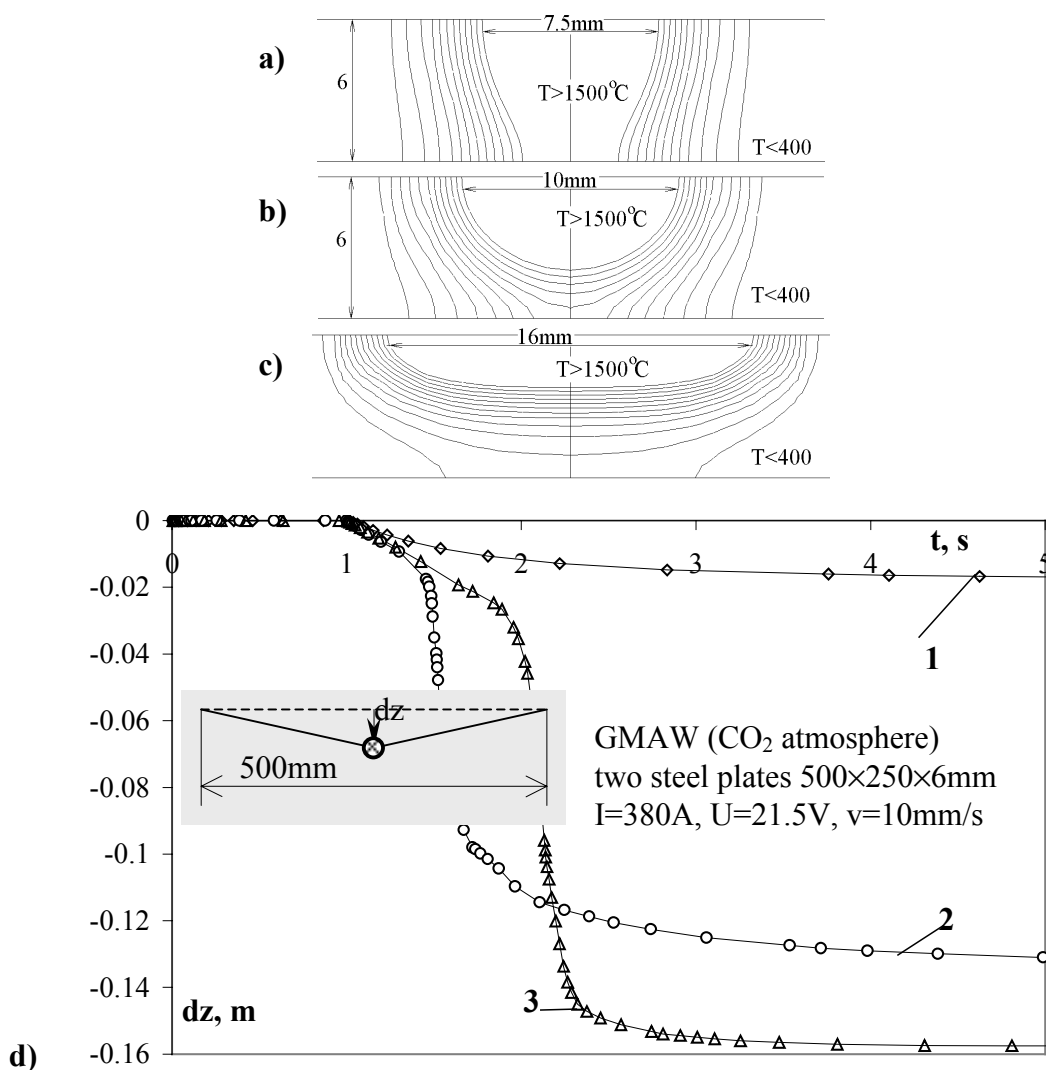


Fig. IV-32. Effect of the shape of the weld pool; (a-c) – temperature distribution in the cross-section of the weld with three different heat source distributions; (d) – kinetics of the z-displacement of the weld ( $dz$ ).

#### 4.5. Evolution of the out-of-plane distortion

For the case of three-electrode welding Fig. IV-33 gives an idea of the behaviour of the plate Z-displacement with time. The plate shape is shown for several moments in time during and after the welding. The first four diagrams are shown with the same scale. Starting from the diagram corresponding to the 50<sup>th</sup> second of the process, the scale has been changed because of the high values of out-of-plane distortions.

Starting from the moment when the heat source has passed some cross-section, the positive angular deformation started to grow significantly in this cross-section. As the heat source travels along the x-axis, the angular deformation continues to rise.

When the first source reaches the end of the plate, the whole plate is warmed up to a certain temperature and softened along the weld line. About this time, the angular deformation of the plate changes the most.

After the last source is terminated, corresponding to the 70<sup>th</sup> second of the process, the angular deformation of the plate is largely formed.

Further change of the plate shape is caused by the longitudinal shortening. It becomes noticeable after the plate is cooled significantly down. Until this time (approximately after 1000 seconds), the outer edges of the plate and centreline of the weld were straight lines during cooling (50<sup>th</sup> and 70<sup>th</sup> seconds).

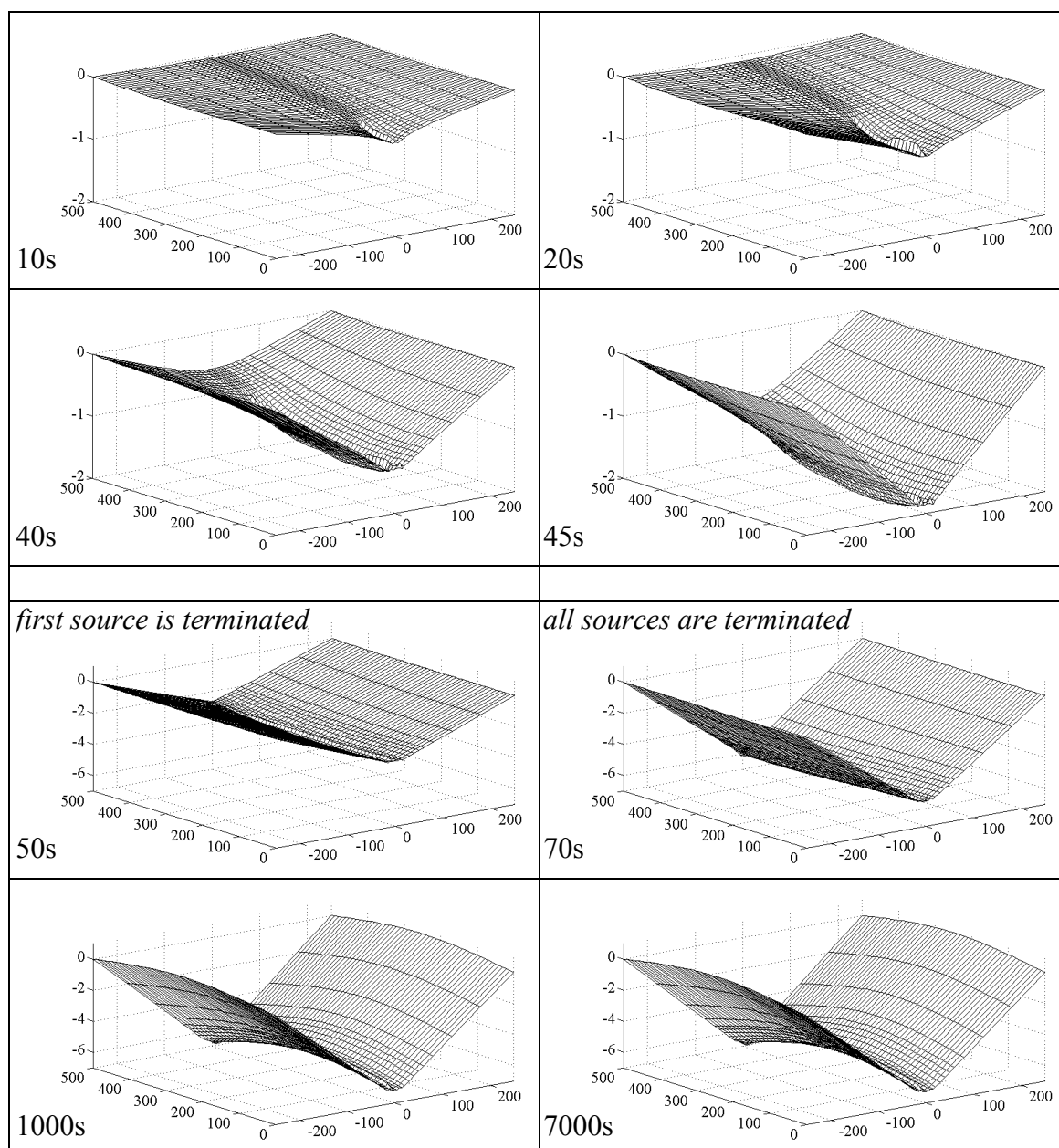


Fig. IV-33. The continuous evolution of out-of-plane distortion for the considered experimental procedure (results from the 3D FEM of 20mm thick steel plates welding).

After the maximum temperature in the plate reaches a certain level (approximately  $100\div 150^{\circ}\text{C}$ ), the overall shape of the plate changes swiftly to a convex-like shape ( $1000^{\text{th}}$  second in *Fig. IV-33*). From now on, the out-of-plane deformation of the plate does not change much with further cooling.

The transition from  $70^{\text{th}}$  to  $1000^{\text{th}}$  second gives a vivid example of convex shape plate formation. The mechanism of the formation is explained in *section 4.3*

The formation of the angular deformation occurs in rather soft material ( $T > 1000^{\circ}\text{C}$ ) and ends long before the structure completely cools down. Hence, clamping the plates, not allowing them to deflect in the out-of-plane direction, gives significant reduction of the angular deformation. It happens because the same forces caused by the non-uniform temperature distribution in the through-thickness direction, can cause larger deformation if they are applied to the softer material.

#### **4.6. Angular deformation caused by multi-electrode and multi-pass welding**

Based on the 2D generalised plane strain model taking into account the “element birth” technique, the two welding techniques, investigated in the current dissertation, were analysed.

The analysis showed that single-electrode welding in three passes causes 170% higher angular deformation than three-electrode one-pass welding with parameters described in *section 1.3 of Chapter III*.

#### **4.7. Conclusions**

In this section the development of out-of-plane distortion in plates using two welding procedures (multi-electrode and multi-pass welding) employed in shipbuilding are investigated and compared. The results of the simulations were compared with a number of experimental data. The investigation was based both on 3D and 2D finite element sequentially coupled thermal stress models. Based on the results presented in this section the following conclusions can be drawn:

1. The comparison between calculated and experimentally measured results reveals that in some cases simulations give overestimated values of angular deformation and in some cases underestimated values. It is difficult to exactly simulate experiments in detail because the deformation is quite sensitive to variations in welding conditions. Important systematic error in the simulation model would tend to give either systematic over- or underestimates.
2. According to the 3D model, the intensive formation of the angular deformation starts right after the source has passed over the cross-section under consideration (cold metal ahead of the moving source restrains the free development of the angular deformation). Formation continues until the maximum temperature in the cross-section drops down to approximately 1000<sup>0</sup>C (in the considered case of three-electrode welding it takes a little more than 70s).
3. The formation of the angular deformation occurs in rather soft material ( $T > 1000^0\text{C}$ ) and ends long before the structure completely cools down. Hence, clamping the plates, not allowing them to deflect in the out-of-plane direction, gives significant reduction of the angular deformation. It happens because the same forces caused by the non-uniform temperature distribution in the through-thickness direction, can cause larger deformation if they are applied to the softer material.
4. The significant angular deformation growth starts only when the plates are sufficiently heated on the bottom side as well as on the top. In other words, in order to proceed with angular change formation, a softened region of the metal should exist along the centreline of the cross-section.
5. The three-electrode welding procedure causes 65% less angular change in the 20mm thick steel plates compared to single-electrode welding in three passes.

## References

- 1 G. E. Totten and M. A. Howes: "Steel heat treatment handbook", Marcel Dekker, New York, 1997;
- 2 G. F. Hewitt, G. L. Shires, Y. V. Polezjaev: "International encyclopedia of heat and mass transfer", CRC Press, New-York, 1997;
- 3 Ø. Grong: "Metallurgical modeling of welding", The institute of materials, Cambridge, 1994;
- 4 P. Seyffarth: "Atlas Schweiss-ZTU-Schaubilder", VEB Verlag Technik and Dusseldorf, Berlin, 1982;
- 5 S. P. Timoshenko, J. N. Goodier: "Theory of elasticity", McGraw-Hill Book Company, New York, 1970;
- 6 R. Gunnert: "Residual welding stress", Almqvist & Wiksell, Stockholm, 1955;
- 7 R. Boekholt: "Welding mechanization and automation in shipbuilding worldwide", Abington Publishing, Cambridge England, 1996;
- 8 Y. Ueda, K. Fukuda, K. Nakacho, S. Endo: "A new measuring method of residual stress with the aid of finite element method of reliability of estimated values", J. Soc. Naval Architects of Japan, V 2, 1971, N 2, pp. 499-507, *jap.*;
- 9 Y. Ueda, K. Fukuda, M. Tanigawa: "A new measuring method of three dimensional stress based on theory of inherent strain", Trans. JWRI, V 8, 1979, N 2, pp. 89-96;
- 10 Y. Ueda, M. G. Yuan: "The characteristics of the source of welding residual stress (inerent strain) and its application to measurement and prediction", Mechanical Effects of Welding, IUTA Symp., Springer Verlag, 1991, pp. 105-121;
- 11 Y. Ueda, M. G. Yuan: "Prediction of residual stress in butt welded plates using inherent strains", J. of Engineering Materials and Technology, ASME Vol.115, 1993, pp. 417-423;
- 12 M. G. Yuan, Y. Ueda: "Prediction of residual stress in welded T- and I-joints using inherent strains", J. of Engineering Materials and Technology, ASME Vol.118, 1996, pp. 229-234;
- 13 M. Mochizuki, M. Hayashi, T. Hattori: "Welding residual stress estimation by inherent strain analysis and thermal elastic plastic analysis and its verification using neutron diffraction measurement", Nippon Kikai Gakkai Ronbunshu, A Hen/Transactions of the Japan Society of Mechanical Engineers, Part A, Vol. 63, Issue 612, Aug. 1997, pp. 1675-1680;

- 14 C.-H. Chien, H.-J. Chen, Y.-T. Chiou: "Estimation of welding residual stresses by using simulated inherent strains", Transactions of the Japan Welding Society, Vol. 20, Issue 1, Apr. 1989, pp. 52-59;
- 15 T. Terasaki, H. Kamikihara: "Difference between deformation of cutting and one of edge welding", Yosetsu Gakkai Ronbunshu/Quarterly Journal of the Japan Welding Society, Vol. 18, Issue 4, 2000, pp. 674-679;
- 16 A.S. Kuzminov: "Calculation principles of total deformation of ship hull structures", Works of Central Scientific Research Institute of Shipbuilding Industry, 1956, N9., *Rus.*;
- 17 D. Radaj: "Heat effects of welding", Springer-Verlag, Berlin, 1992;
- 18 Y. Ueda, H. Murakava, S. M. Gu, Y. Okumoto, R. Kamichika: "Simulation of welding deformation for precise ship assembling (report I)", Trans. of JWRI, 21, 2, 1992, pp. 125-135;
- 19 K. Masubuchi: "Analysis of welded structures", Pergamon press, London, Great Britain, 1980;
- 20 L. P. Connor: "Welding handbook", 8th edn., Vol. 1, American Welding Society, USA, 1991;
- 21 H. Kihara, K. Masubuchi: "Studies on the shrinkage and residual welding stress of constrained fundamental joint", Reports of Transportation Technical Research Institute, no. 7, 1954, no. 20, 1956;
- 22 N. O. Okerblom: "The calculations of deformation of welded metal structures", Mashgiz, Moskow, 1955, *Rus.*;

**CHAPTER V MITIGATION TECHNIQUES**

Welding stresses and deformations have various effect on the welded structure performance. Mostly, they have negative influence.<sup>1,2,3,4,5</sup>

Triaxial tensile residual stresses in combination with defects promote brittle fracture. Uniaxial or biaxial tensile residual stresses reduce corrosion resistance, and, at the same time, improve the structure stability limit. The compressive residual stress increases the fatigue strength.

Residual stresses in combination with welding deformations significantly affect the dimensional precision of the structure and its usefulness and costs. These facts show the necessity, in many cases, of including different mitigation techniques in the welding procedures. These techniques are applied to keep the welding residual stresses and deformation below specified limits.

The problem here is that, to a large extent, welding residual stresses and distortions behave in contrary ways. For example, if the parts were rigidly fixed during welding, the overall distortion of the structure is low. Residual stresses, however, will be higher than in the case of freely welded parts. Consequently, we have to distinguish methods that keep the residual stresses low, and those which reduce distortion. This section will concentrate mostly on the stress relieving measures.

There are many different methods of welding deformation and stress reduction. At the same time, the main principles are the same. Classification of the mitigation techniques helps to understand its performance capabilities and limitations. According to the basic mechanisms on which the techniques are based, three *fundamental principles* are known:

1. Reduction of the volume of the plastically strained zone and the values of the plastic strains *during the heating stage*.
2. In order to compensate for the plastic shortening produced during the heating stage, plastic elongation may be introduced *during the cooling stage or after the weld has been completed*.
3. Compensation of the welding deformation by preweld misalignment and using larger parts, taking into account welding deformations.

The first principle can be achieved by regulation of the thermal action and mechanically. The measures are:<sup>6</sup>

- preheating;
- reduction of the size and number of welds;
- reduction of the net heat input per unit length of the weld;
- introduction of additional heat sinks;
- welding of the pre-stretched parts;<sup>7,8,9,10,11,12</sup>

The second principle is reduction of the residual plastic deformation volume achieved during heating period. The measures are:<sup>13,14,15,16,17</sup>

- successive forging treatment;
- successive rolling treatment;

- stretching and bending;
- high-temperature tempering.

From the third group of mitigation techniques should mentioned:<sup>18</sup>

- prealignment taking into consideration estimated deformations;
- symmetrical joint arrangement (X-groove preparation, double-fillet weld)
- other design measures.

The following section will concentrate on the finite element thermo-mechanical models of some of the above mentioned mitigation techniques.

## **1. MECHANICAL STRAIGHTENING**

Mechanical straightening can be applied during welding and after the joining has been completed. Quite significant residual stress relief can be achieved with this method. At the same time, the use of this technique is often difficult in practice. For example, for mechanical straightening of 20mm thick and 1000mm wide plates, equipment able to clamp and stretch the plates with approximately  $4 \cdot 10^6$ N force would be needed to reach the effect illustrated in *Fig. V-3*. At present, such equipment does not exist. The case introduced below serve as a more or less hypothetical example helping to understand principles and mechanism of stress relieving methods.

### **1.1. Model of post-welding mechanical stretching**

*Section 1.2.2.2 of Chapter II* explains how the process of welding can be represented by a simple three-rod model. The post-welding mechanical straightening can also be illustrated based on this simple model.

It is well known that in plates made of a material without phase transformation during cooling at lower temperatures high tensile stresses (close to the yielding point) are set up in the region close to the weld due to the welding process. Hence, in order to simulate welding, the self-balanced system of three rods should consist of the central rod subjected to a high tensile stress  $\sigma_t$ , and the two limiting rods under half as high compressive stress  $\sigma_c = \sigma_t/2$  (see *Fig. V-1.c*).

To model the process of stretching, an external load with a tensile stress  $\sigma$  is applied to the three-rod system. The stress development for both the central and the limiting rods is shown in *Fig. V-1.a*. Starting from the initial points ( $I^C$ ,  $I^T$  and  $I$  corresponding to the compressed rod, the tensed rod and the external load) the stresses grow with increasing strain.

If the structure is stretched in the elastic region only (up to points  $2^C$ ,  $2^T$  and  $2$ ) then, the structure returns to its initial state after the load removing. This means that in order to achieve stress reduction we need to produce plastic deformation of the elements of the structure.

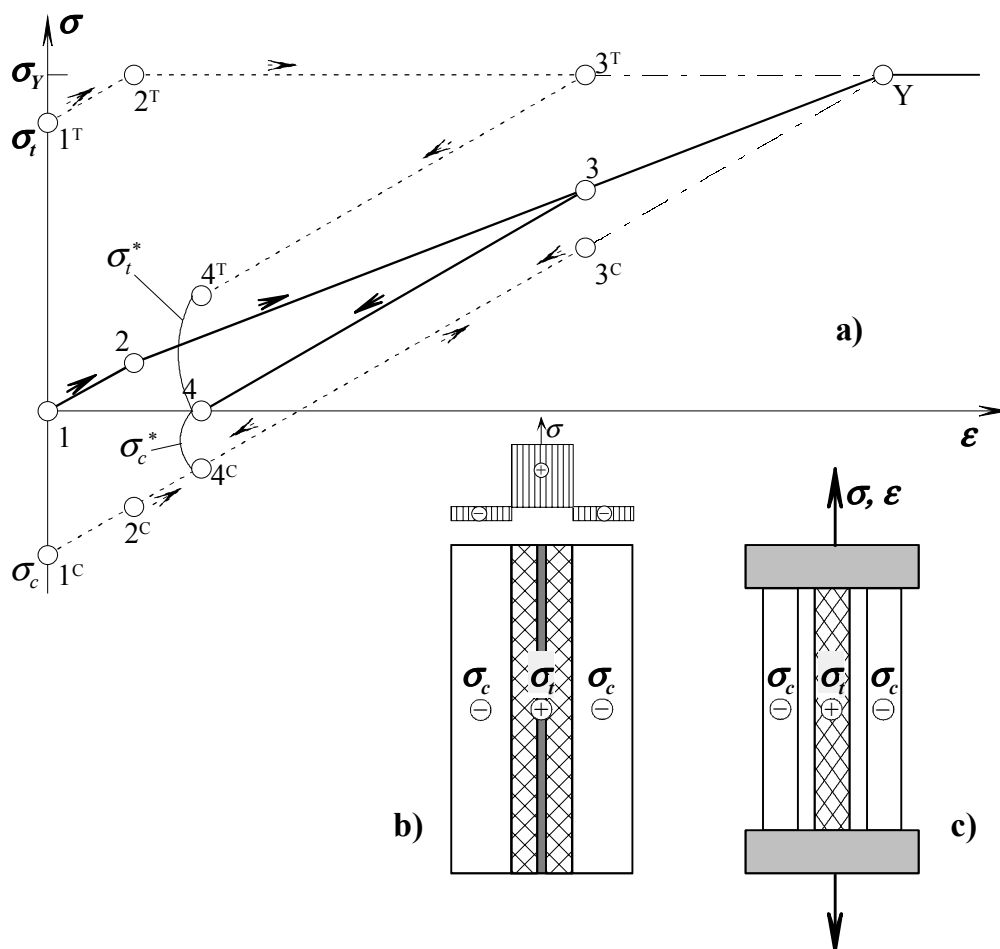


Fig. V-1. Three-rod system demonstrating the principle of mechanical straightening; (a) – tensile and compressive loading and unloading resulting in residual stress relief ( $\sigma_c^*$  and  $\sigma_t^*$  are residual stresses after treatment); (b) – plates "as welded"; (c) – three-rod system.

After the tensile stress in the central element has reached the yielding point, the stiffness of the structure is reduced because the central element is “flowing” without further increase of the stress with deformation. Hence, the trajectory of the stress corresponding to the external load (designated by a thick line in Fig. V-1.a) changes its slope.

If the structure is released from the external load after reaching some stress-strain state designated by  $3^T$ ,  $3^C$  and 3, the stress corresponding to the load diminishes, while the structure has some residual elongation. Relaxation of the elastically deformed limiting rods follows the same trajectory for loading and unloading down to point  $4^C$ . In the central rod we get significant tensile stress relief. The residual stress in the central element corresponds to point  $4^T$ .

As a consequence, the elements of the structure have residual stresses  $\sigma_t^*$  and  $\sigma_c^*$  that are significantly lower than in the initial state.

According to the model, after reaching yielding in all three elements of the system (this state corresponds to the point *Y* in *Fig. V-1.a*), the residual stresses  $\sigma_t^*$  and  $\sigma_c^*$  will vanish completely.

## **1.2. 3D model of mechanical stretching**

In *Fig. V-3* the effect of the mechanical stretching is demonstrated. These results were calculated based on the 3D mechanical model for non-linear static stress/displacement analysis.

In the model the edge of the plate at  $x=0\text{mm}$  was clamped, while distributed forces were applied to the edge at  $x=500\text{mm}$ . The force applied to a 20mm thick and 500mm wide plate was equal to  $2 \cdot 10^6\text{N}$  (that corresponds to  $\sigma=200\text{N}\cdot\text{mm}^{-2}$ ). The scheme of the mechanical stretching process is shown in *Fig. V-2*.

In *Fig. V-3.a* and *Fig. V-3.b* the longitudinal stress distribution over an internal plane at  $z=8\text{mm}$  is shown with the same scale for stress. These graphs indicate a significant residual longitudinal stress relief caused by a simple longitudinal stretching (approximately 45% of the initial  $\sigma_x^{max}$ ). The peak of  $\sigma_x$  in the case of 1D stressed state should have been reduced exactly by  $200\text{N}\cdot\text{mm}^{-2}$  (see *Fig. V-1*). But, existence of the complex 3D stressed state results in a slightly more significant reduction ( $\sigma_x^{max}$  is reduced by  $209\text{N}\cdot\text{mm}^{-2}$ ).

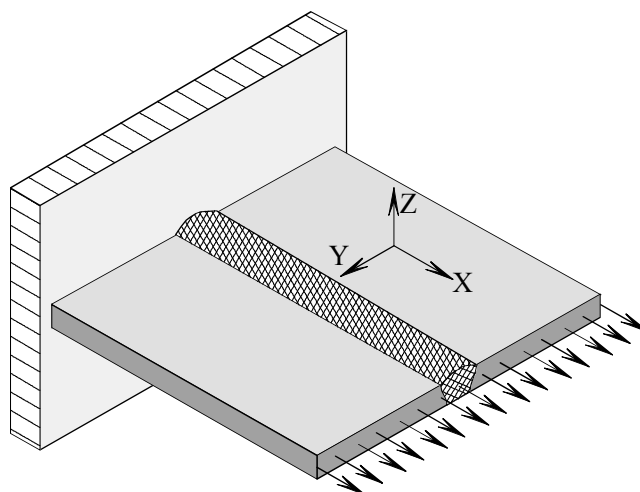


*Fig. V-2. Scheme of the mechanical stretching.*

*Fig. V-3.b* and *Fig. V-3.c* reveals that mechanical stretching reduces the longitudinal stress  $\sigma_x$  rather evenly. In other words, after the treatment, the stress distribution has a form quite similar compared to the "as-welded" condition. The main difference is the additional stress field disturbances *close* to the beginning and the end of the weld. After the stretching, the longitudinal stress at these areas rise approximately ten times, and equals about 8% of  $\sigma_Y$  in tension and 30% in compression ( $\sigma_x=0$  along the edges perpendicular to the weld).

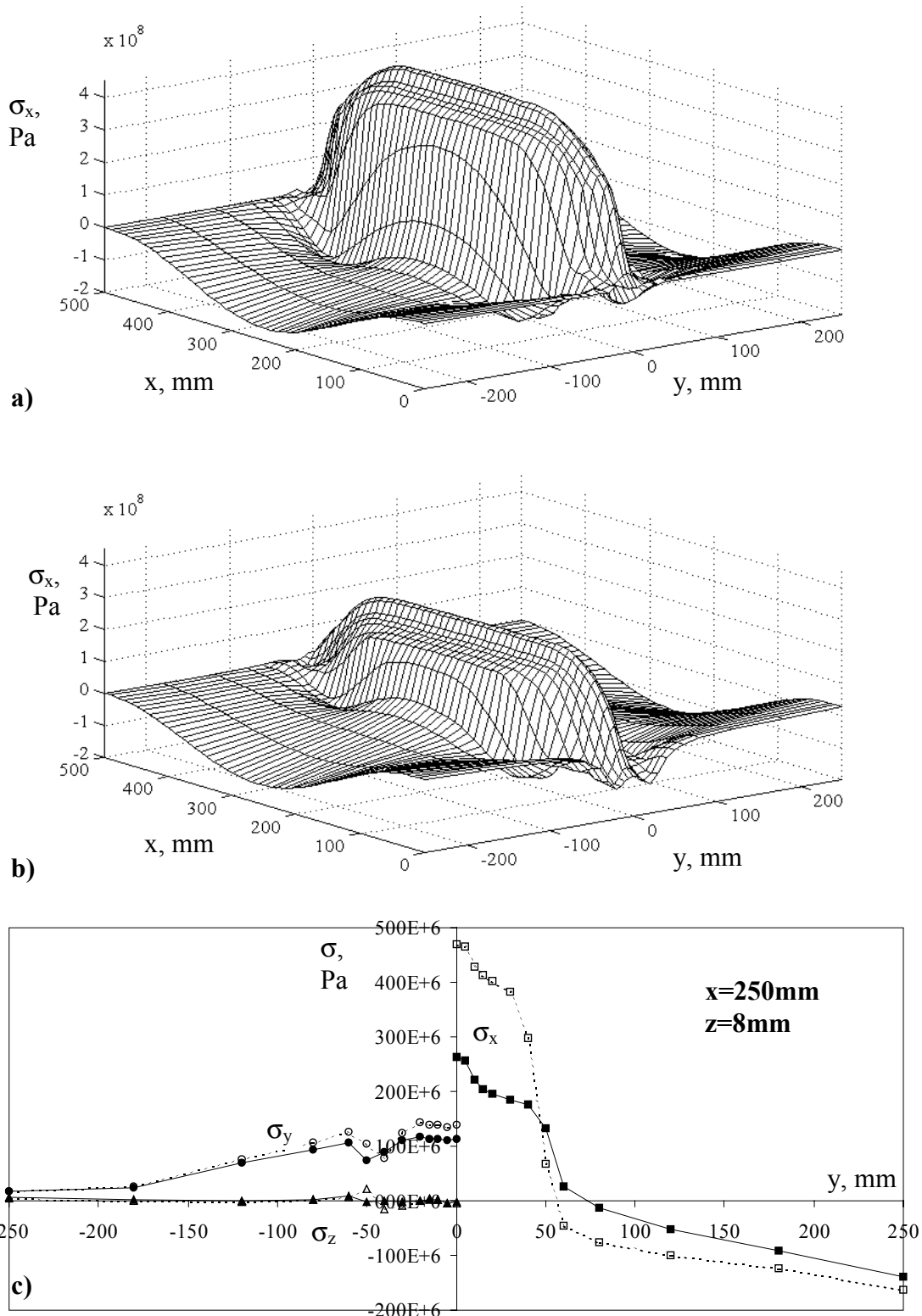
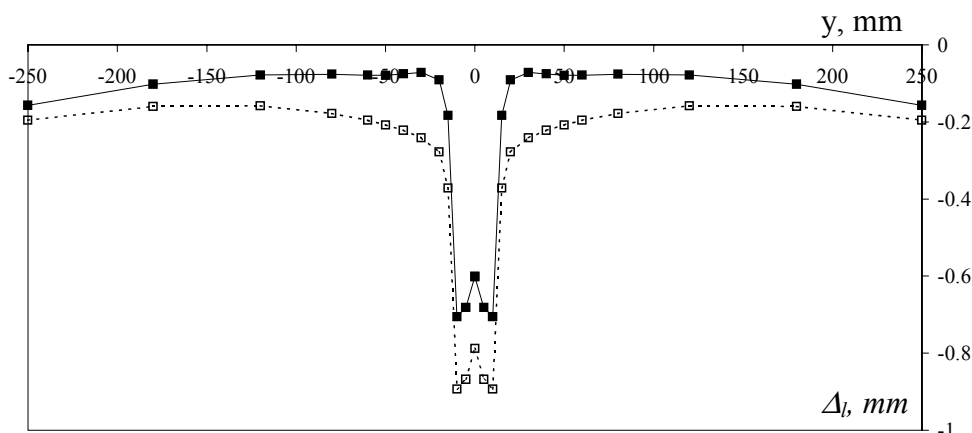


Fig. V-3. Mechanical straightening effect; (a) – longitudinal residual stress  $\sigma_x$  distribution as welded ( $z=8\text{mm}$ ); (b) – longitudinal residual stress  $\sigma_x$  distribution after mechanical straightening ( $z=8\text{mm}$ ); (c) – mechanical straightening effect on all three stress components (--- - as welded, — - after mechanical straightening).

As a result of the mechanical stretching, the transverse stresses  $\sigma_y$  and  $\sigma_z$  are also reduced (see *Fig. V-3.c*).

The mechanical stretching also has a beneficial effect on the residual deformations. This effect is demonstrated in *Fig. V-4*. The maximum longitudinal shrinkage is reduced by 20%. The transverse welding shrinkage is reduced insignificantly.



*Fig. V-4. Effect of the post-welding mechanical stretching on longitudinal residual shrinkage (--- - as welded;— - after mechanical straightening).*

## 2. THERMAL TENSIONING

As was previously mentioned, the residual stresses can be reduced by the introduction of additional plastic elongation in the areas close to the weld. Elongation of the seam can be achieved not only by mechanical means, but also by low temperature heating of the zones that were not plastically deformed during welding. Schemes of thermal tensioning processes based on this principle are shown in *Fig. V-5*.

### 2.1. Factors affecting selection of the thermal load

There are several variables in the thermal tensioning process. During the design stage the most important of them are:

- maximum temperature;
- width of the heating area;
- heating time;
- distance from the seam.

In order not to induce a new plastic shortening in the heating areas, the heating should be kept below some critical level. This level can be easily evaluated based on a simple model demonstrated in *Fig. V-6*.

Assuming that the plate is rigidly constrained a simple 1D model is sufficient for evaluating the maximum heating temperature  $T_h^{max}$ . According to the Fig. V-6 in order not to achieve plastic deformation, the thermal strain induced in the heated element should be kept below the limit  $\epsilon^T = \sigma_Y/E$ . Based on this model, the maximum allowed heating temperature for the steel should be approximately 170°C.

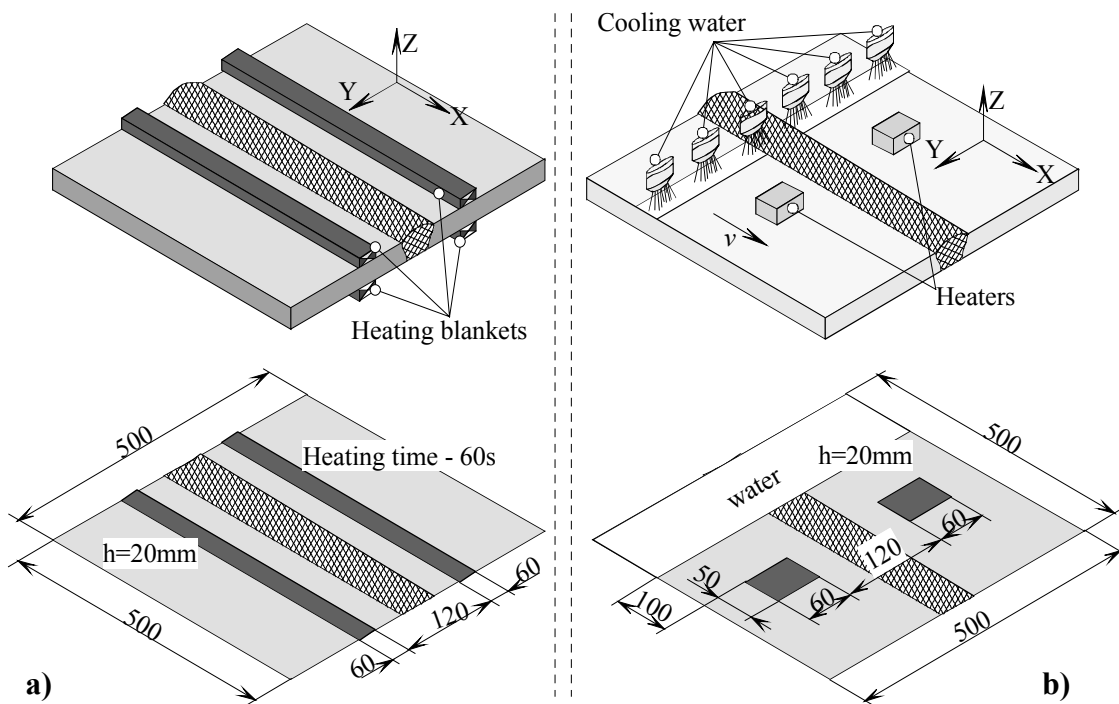


Fig. V-5. Schemes of the thermal tensioning techniques; (a) – with stationary heating blankets; (b) – with moving system of heaters and water sprays.

In the case of real structures the plate is not absolutely stiff, allowing some additional elastic expansion. Hence, the  $T_h^{max}$  can be slightly higher than predicted based on the simple model shown in Fig. V-6.

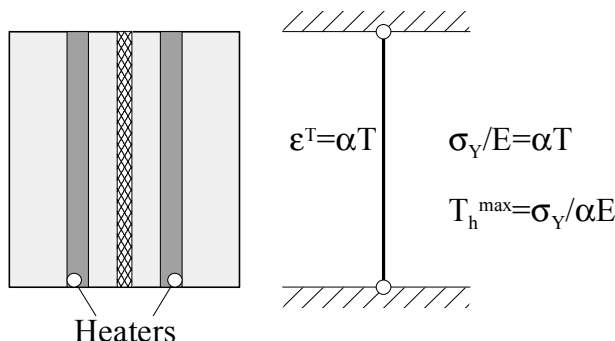
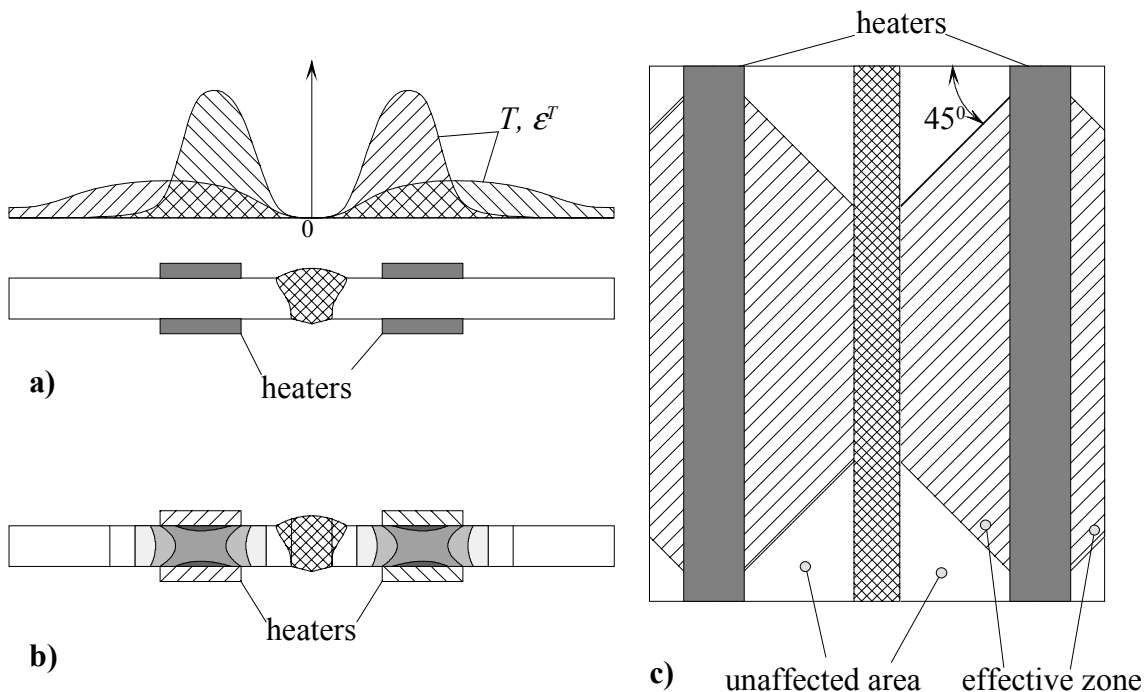


Fig. V-6. Scheme for determination of maximum heating temperature.

The effect of the width of the heating area is demonstrated in *Fig. V-7.a*. Application of narrow heaters gives a localised temperature rise, while wide heaters give a wider distributed temperature rise. The resulting force, caused by the heating, is proportional to the area under the temperature curve (illustrated by the crosshatched region).



*Fig. V-7. Illustrations of the effect of the main factors affecting the selection of the heaters; (a) – width of the heating area; (b) – heating time; (c) – distance from the seam.*

Considering the above mentioned, we can conclude that the wider the region heated up to the allowed temperature, the more significant is the effect of the treatment. Of course, we must keep in mind that the area with high tensile residual stress should be kept at as low as possible temperature. For economic reasons we cannot always use the heating over large areas. Heaters with some reasonable width are able to provide enough effect, reducing the peak tensile stress down to a some acceptable level.

The heating time and the intensity of the heating process determine the temperature distribution. This combination should lead to the resulting temperature field with low temperature gradient in the through-thickness direction (as it shown in *Fig. V-7.b*). At the same time, if we spend too much time on getting smooth through-thickness temperature distribution, the temperature will rise in the region with high tensile stress. This variant is not acceptable.

Some optimum combination of the heating time and the intensity of the heating should be found for every specific case.

The distance from the weld centreline to the heater cannot be defined uniquely either. In order to avoid temperature rise in the tensile region along the weld seam, we can move

the heaters further away from it. But, another acting factor limits this possibility. This factor is based on the Saint-Venant's principle (is illustrated in *Fig. V-7.c*). This principle allows us to determine the extent of the area where the effect of the thermal loading is active. According to this principle, moving the heaters away from the weld centreline, we reduce the effectiveness of the treatment.

## **2.2. Implementation of stationary heating blankets and moving heating sources**

In this dissertation two 3D thermo-mechanical models of thermal tensioning were created. These models correspond to the two different techniques demonstrated in *Fig. V-5*.

In the first model, corresponding to *Fig. V-5.a*, 60mm wide heaters were introduced along the weld centreline at 60mm distance from it. The heaters were applied on both sides of the plates. The maximum temperature during heating was achieved by the end of the heating stage (about 190°C).

In the model the resulting stress and deformation fields from the 3D model of welding described in *sections 3.2 and 3.3 of Chapter III* were used as initial conditions. The heaters were producing energy during the first 60 seconds. Afterwards, complete cooling was achieved by introducing a convective heat loss from the free surfaces ( $\alpha_c=30\text{W}\cdot\text{m}^{-2}\cdot\text{K}^{-1}$ )<sup>19,20</sup>. The heating and cooling process took 4000s.

The results from this model are presented in *Fig. V-8* similarly to the representation of the mechanical stretching results in *Fig. V-3*. These graphs also indicate a significant residual longitudinal stress relief caused by the thermal tensioning with stationary heating blankets.

The concave top of the graph corresponding to the longitudinal stress  $\sigma_x$  after the treatment, shown by the solid line in *Fig. V-8.c*, can be explained by the principle of the method. The stretching of the area close to the weld produces additional compression of the adjacent area. Also, the area that is stretched enough to reach the yielding point is limited. In the example this area is limited by a 80mm wide strip along the weld. It is indicated by an unchanged value of  $\sigma_x$  at the point with  $y=40\text{mm}$ . At points closer to the weld centreline the residual longitudinal stress  $\sigma_x$  was reduced due to the thermal treatment.

The other thermal tensioning technique considered in this dissertation corresponds to the scheme illustrated in *Fig. V-5.b*. In the model two 60×60mm heaters were moving at the welding speed along the weld centreline at 90mm distance from it. The heaters were applied on both sides of the plate. At 100mm distance behind the heaters water sprays were moving along the top surface with the same speed  $v=10\text{mm}\cdot\text{s}^{-1}$ . The cooling due to water sprayed over the top surface of the plate was modelled by introducing an additional convective heat loss from the top surface with  $\alpha_c=1000\text{W}\cdot\text{m}^{-2}\cdot\text{K}^{-1}$ .<sup>19,20</sup> The heating and cooling process took about 500s.

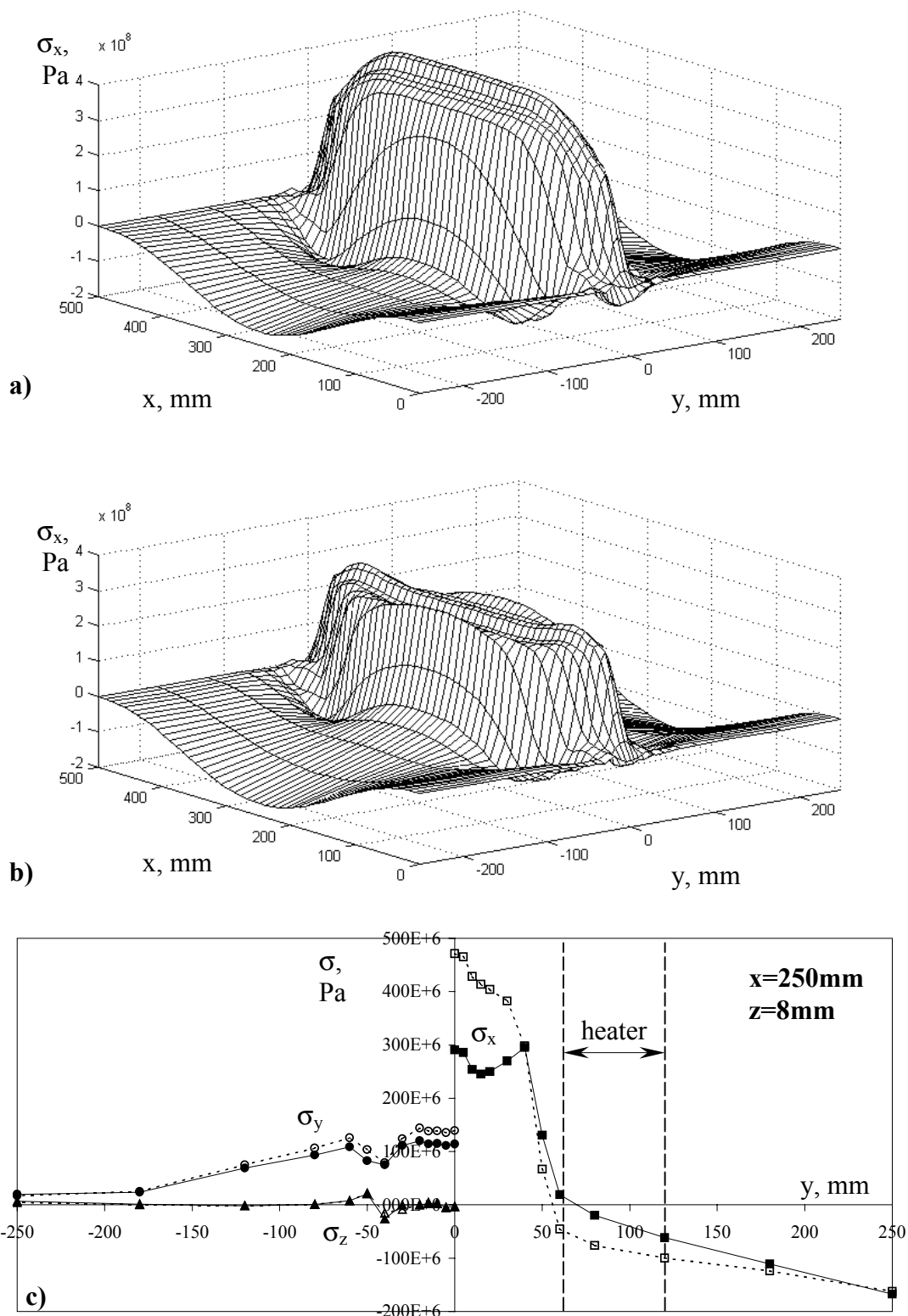


Fig. V-8. Effect of the thermal tensioning with stationary heating blankets; (a) – longitudinal residual stress  $\sigma_x$  distribution as welded ( $z=8$ mm); (b) – longitudinal residual stress  $\sigma_x$  distribution after thermal tensioning ( $z=8$ mm); (c) – thermal tensioning effect on all three stress components (----- - as welded, ——— - after thermal tensioning).

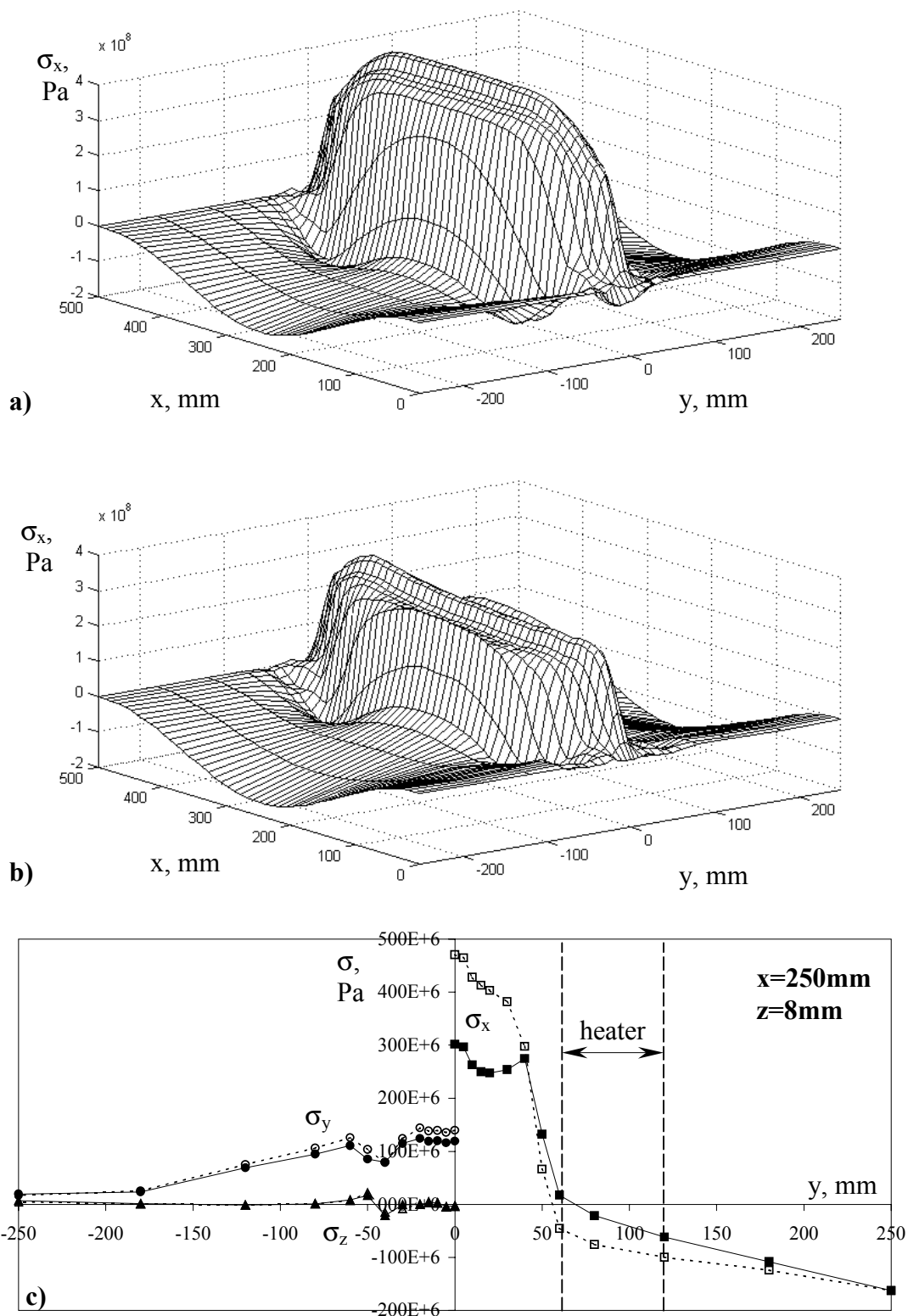


Fig. V-9. Effect of the thermal tensioning with moving heaters and water sprays; (a) – longitudinal residual stress  $\sigma_x$  distribution as welded ( $z=8\text{mm}$ ); (b) – longitudinal residual stress  $\sigma_x$  distribution after thermal tensioning ( $z=8\text{mm}$ ); (c) – thermal tensioning effect on all three stress components (----- - as welded, ——— - after thermal tensioning).

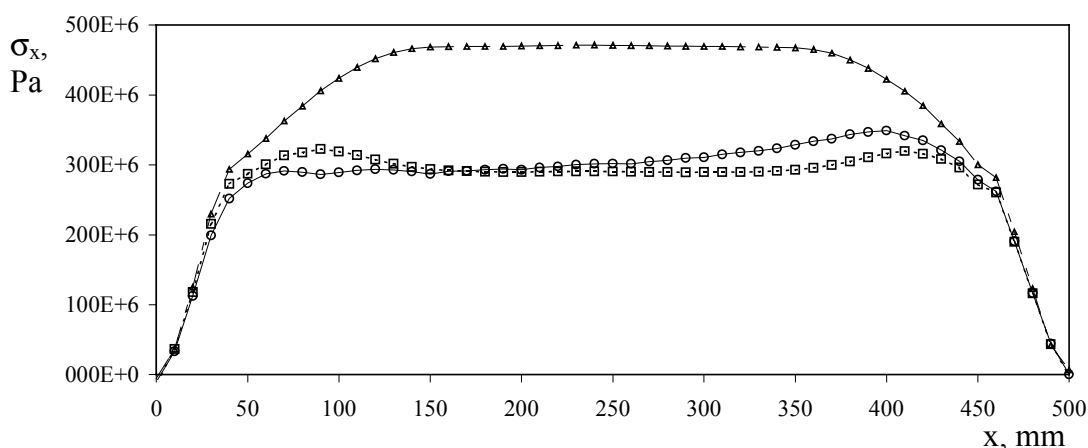


Fig. V-10. Longitudinal stress distribution along the centreline of the weld (-○- - moving heaters and water sprays; -□- - stationary heating blankets; -△- - as welded).

The results achieved by the thermal tensioning with moving heaters are quite similar to the results for the case of stationary heating blankets. The main difference is that the maximum value of  $\sigma_x$  on the centreline near the final end is 20% higher with moving heat source compared to stationary ones (see Fig. V-10). The opposite is true near the start.

In these examples thermal tensioning gave less reduction in longitudinal shrinkage than did mechanical stretching. The reduction is approximately 10-15% of the initial shrinkage.

### 2.3. Mechanism of thermal tensioning

The mechanism of the thermal tensioning is demonstrated in Fig. V-11. Two points are considered. One of them is situated close to the centreline of the weld seam, and the other is under the heater. The development of the temperature rise  $T$ , the longitudinal stress  $\sigma_x$  and the plastic strain in the  $x$ -direction  $\epsilon_x^p$  are presented in Fig. V-11 for the case of stationary heating blankets.

We do not claim that the technique suggested in section 2.2 is optimal. As seen from Fig. V-11.a, the temperature close the centreline began to rise already during the heating stage, reducing the effectiveness of the treatment.

Compressed regions under the heaters with rising temperature are subjected to further compression (without appearance of plasticity in the region).

At the same time, the highly stretched region close to the centreline feels a slight relief, caused by the change of the 3D stressed state (we sliding down along the sides of the cylinder presented in Fig. II-4). This region undergoes some reduction of the plastic compression during the heating stage (see Fig. V-11.c), leading to the reduction of such integral characteristic as longitudinal shrinkage.

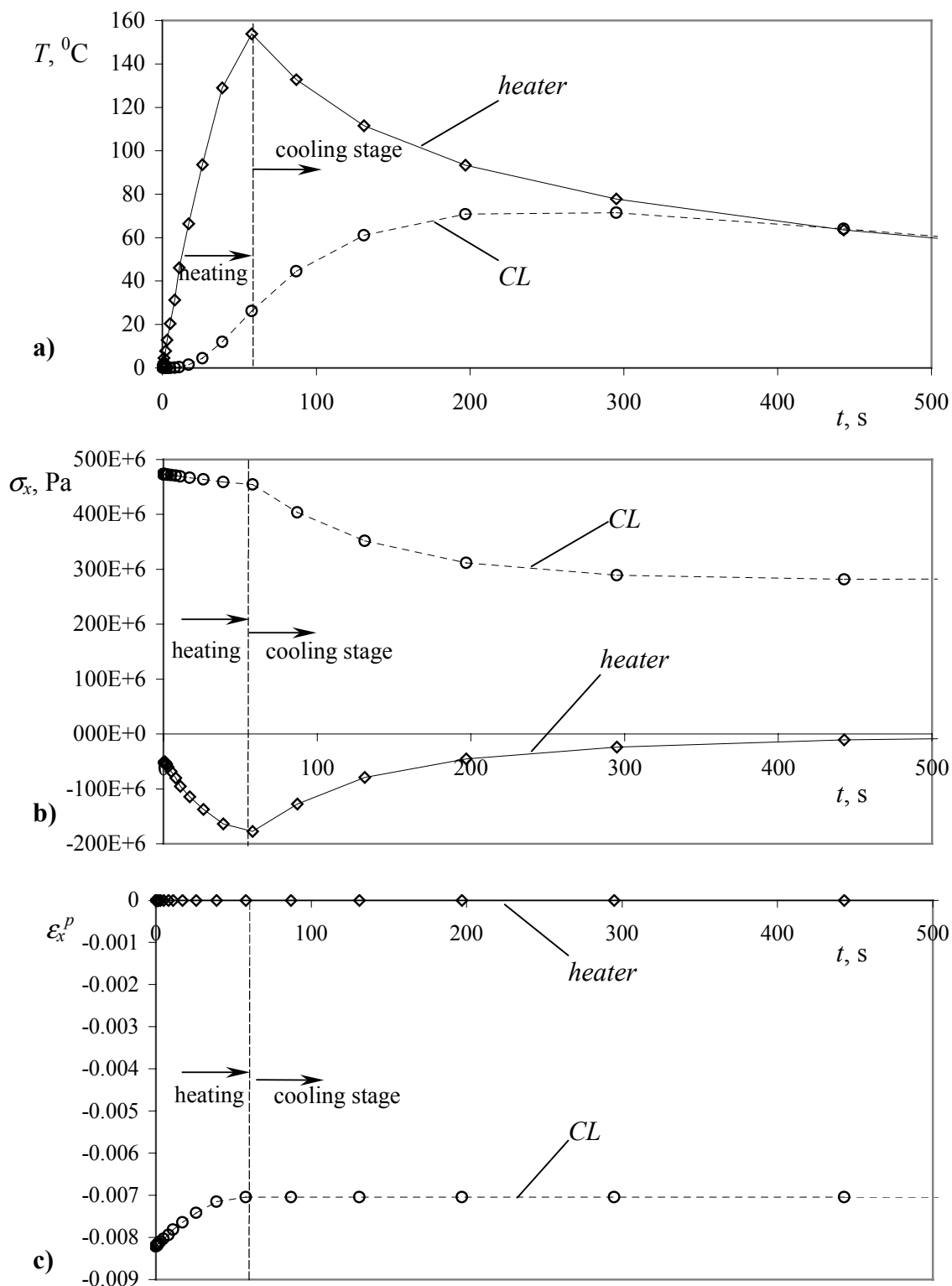


Fig. V-11. Mechanism of the thermal tensioning; (a) – temperature evolution; (b) – longitudinal stress evolution; (c) –  $\epsilon_x^p$  plastic strain evolution;  
 ---○--- for the point situated close to the weld centreline ( $x=250\text{mm}$ ,  $y=1\text{mm}$ ,  $z=9\text{mm}$ );  
 —◇— for the point situated under the heater ( $x=250\text{mm}$ ,  $y=76\text{mm}$ ,  $z=9\text{mm}$ ).

The tensile stress along the weld centreline is being gradually relieved during the cooling stage. The stress in the area under the heater also changes in order to keep the self-equilibrium state described in *eq. II-6* on *page 30*.

Only first 500 seconds of the treatment process is illustrated in *Fig. V-11*. Complete cooling leads to the slight gradual change of the longitudinal stress  $\sigma_x$ .

### 3. TECHNIQUES FOR MITIGATION OF ANGULAR DEFORMATIONS

In order to reduce angular deformation several techniques can be suggested. These techniques are suggested based on a careful analysis of the formation of the out-of-plane deformation.

First of all, the angular deformation development depends on the through-thickness temperature gradient (in other words, non-uniformity of the temperature field in through-thickness direction). Different transverse shrinkage forces acting on the top and the bottom surfaces of the workpiece affect the magnitude of the angular change.

In order to reduce angular deformation we need to reduce the temperature non-uniformity in the through-thickness direction. One way is to use a welding technique involving two-sided welding. If the welding must be carried on one side only, then the technique illustrated in *Fig. V-12* can be used in order to reduce the angular change.

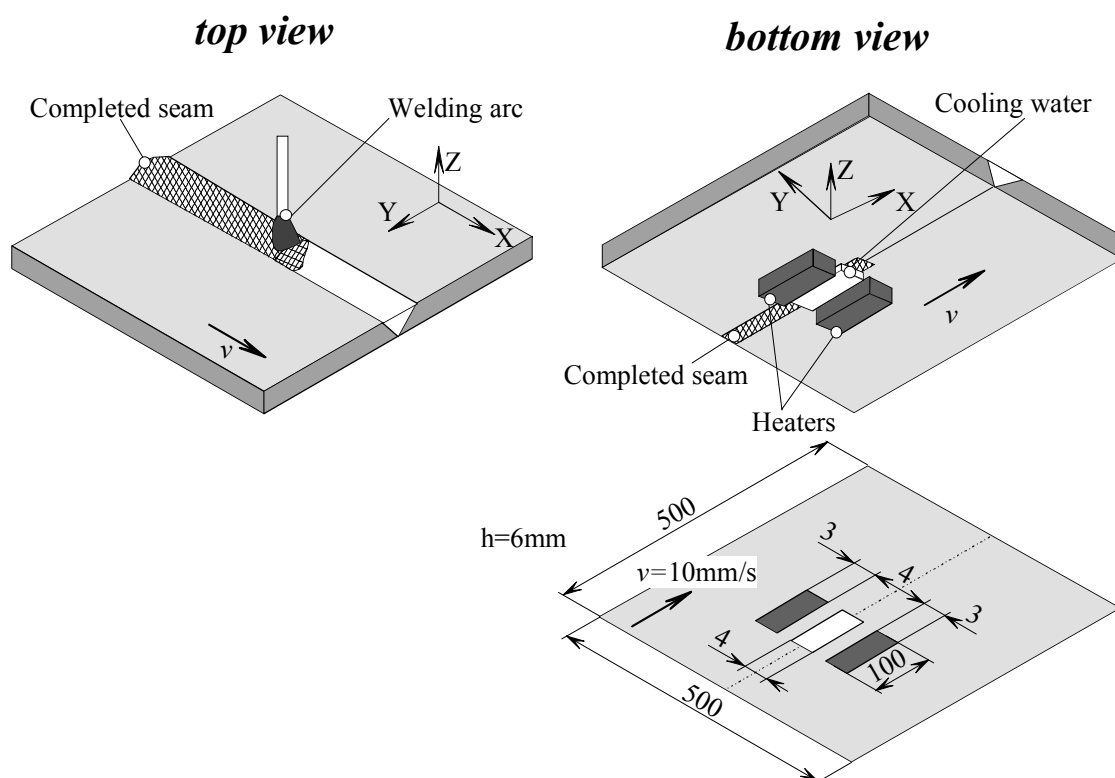


*Fig. V-12. Technique of angular deformation reduction, implementing moving cooler and additional heaters along the bottom side of the weld.*

Results of the implementation of this technique based on the 2D FE plane strain model are presented in *Fig. V-13*.

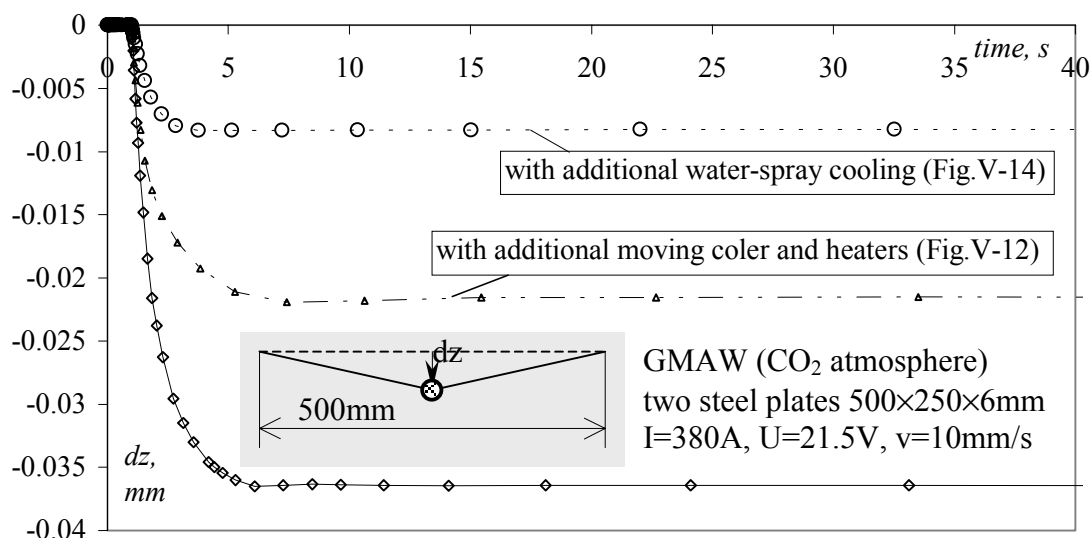


*Fig. V-13. Effect of the techniques directed towards limitation of the angular deformation (evolution of z-displacement of the weld seam in 6mm thick plates).*

The effect of the technique is quite significant. In *Fig. V-13* the effect is shown on 6mm thick steel plates.

In this example, simultaneously with the welding arc acting on the top surface of the plate, the cooler and two additional heaters were moved along the bottom side at the welding speed  $v=10\text{mm}\cdot\text{s}^{-1}$ . The cooler was assumed to be 4mm wide and 100mm long. Both heaters were 3mm wide and 100mm long.

The length of the heaters and cooler was chosen based on angular deformation kinetics. It is seen from *Fig. V-13* that by the 10<sup>th</sup> second the angular change is already formed and remains at the same level during further cooling.

Cooling was introduced into the model by convective cooling from the surface with  $\alpha_c=1000\text{W}\cdot\text{m}^{-2}\cdot\text{K}^{-1}$  <sup>19,20</sup>, corresponding to "water-steel" interaction. For modelling the heaters, the corresponding elements at the bottom surface were heated up to 1000<sup>o</sup>C.

The results demonstrate that the above-explained technique reduces the residual angular deformation by 40%.

*Fig. V-13* also contains the information about the effect of the other technique, which, according to this illustration, is even more efficient.

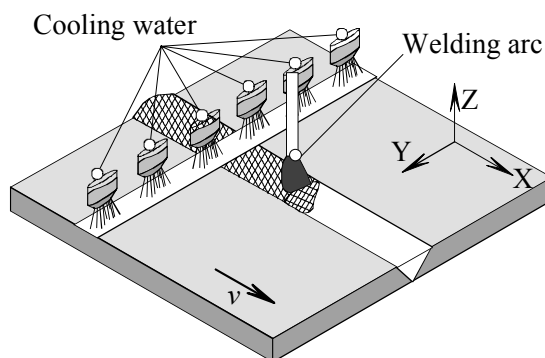


Fig. V-14. Technique of angular deformation reduction, implementing moving water sprays behind the heat source along the top side of the weld.

This technique is illustrated in Fig. V-14 and also based on the principle of temperature equalisation in the through-thickness direction. It is quite simple. Only water sprays are needed. At the same time, this technique is mostly hypothetical because it requires cooling directly behind the travelling heat source. If cooling is applied after the weld pool solidifies, almost no positive effect is visible.

According to calculations, this technique is capable to reduce the angular deformation by 75% in the case of 6mm thick steel plates (see Fig. V-13).

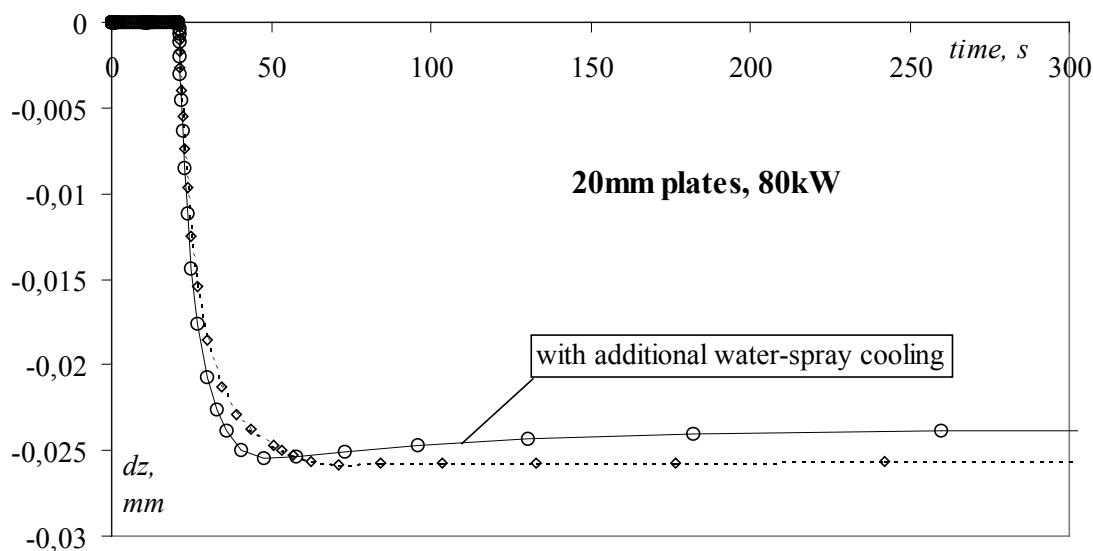


Fig. V-15. Effect of the techniques directed towards limitation of the angular deformation (evolution of z-displacement of the weld seam in 20mm thick plates).

The effectiveness of the above-introduced technique vanishes with increasing plate thickness. This because it is impossible to affect from the surfaces the temperature distribution through the plate thickness. As demonstrated in *Fig. V-15* the effect of the water-spraying technique implemented on 20mm thick plates shows only 7% reduction of the angular deformation.

Nevertheless, the preweld alignment of the parts to be joined is still the most efficient technique of the measures directed towards reduction of the angular shrinkage. For the successful implementation of this method, the *a priori* estimated angular shrinkage should be found as precise as possible.

#### 4. CONCLUSIONS

In this section several techniques for reducing welding stresses and deformation are investigated and compared. The investigations were based on 3D finite element mechanical (in the case of mechanical stretching) and sequentially coupled thermal stress models. The data from previous welding simulations were used as initial conditions for the calculations. Based on the results presented in this section the following conclusions can be drawn:

1. For the considered class of methods significant effect on the residual stress distribution was demonstrated. The suggested techniques gave a reduction of the peak residual stress of 45% with mechanical stretching and of 35% with thermal tensioning.
2. With mechanical stretching, while reducing the peak stress, new local residual stresses were generated in previously stress free areas near the plate ends.
3. The different techniques (mechanical stretching, thermal tensioning with the stationary heating blankets and the moving heat sources) gave similar results with regard to the distribution and maximum values of residual stress and deformation.
4. To avoid additional plastic deformation the maximum heating temperature should not exceed a certain level. The maximum heating temperature depends on the yielding point  $\sigma_y$ , the thermal expansion coefficient of the material  $\alpha$  and the stiffness of the structure (for the higher-strength steel ASTM A131  $T_h^{max}=170^{\circ}\text{C}$  in the case of absolutely stiff structure).
5. Suggested techniques, directed towards reduction of the angular deformations, are expected to demonstrate significant improvement of the joint in terms of angular deformation magnitude. The effect of the techniques increases with decreasing plate thickness. It was demonstrated that for the case of 6mm thick plates a reduction up to 75% can be achieved.

**References**

- 
- 1 K. Masubuchi: "Analysis of welded structures", Pergamon Press, London, Great Britain, 1980;
  - 2 T. N. Nguyen, M. A. Wahab: "The effect of residual stress on fatigue of butt joints", *Welding Journal*, Febr. 1996, pp. 55s-61s;
  - 3 D. Radaj: "Design and analysis of fatigue resistant welded structures", Abington Publishing, Cambridge, 1990;
  - 4 M. I. Onsøien, O. M. Akselsen, Ø. Grong, P. E. Kvaale: "Prediction of cracking resistance in steel weldments", *Welding Journal*, Jan. 1990, pp. 45-51;
  - 5 O. I. Steklov: "Strength of welded structures in corrosive medium", Mashinostroenie, Moscow, 1976;
  - 6 N. O. Okerblom: "Technological design of the welded structures", Mashinosroenie, Leningrad, 1964;
  - 7 Y. I. Burak, L. P. Besedina, Y. P. Romanchuk, A. A. Kazimirov, V. P. Morgun: "Controlling the longitudinal plastic shrinkage of metal during welding", *Avtomaticeskaya Svarka*, N3 (288), 1977, pp. 27-29, *Rus.*;
  - 8 Y. I. Burak, Y. P. Romanchuk, A. A. Kazimirov, V. P. Morgun: "Selection of the optimum field for preheating plates before welding", *Avtomaticeskaya Svarka*, N5 (314), 1979, pp. 15-19, *Rus.*;
  - 9 P. Michaleris, X. Sun: "Finite element analysis of thermal tensioning techniques mitigating weld buckling distortion", *Welding Journal*, Nov. 1997, pp. 451s-457s;
  - 10 P. Michaleris, J. Dantzig, D. Tortorelli: "Minimisation of welding residual stress and distortion in large structures", *Welding Journal*, Nov. 1999, pp. 361s-366s;
  - 11 P. Dong, J. K. Hong, P. Rogers: "Analysis of residual stresses in Al-Li repair welds and mitigation techniques", *Welding Journal*, Nov. 1998, pp. 439s-445s;
  - 12 C. Conrardy, R. Dull: "Control of distortion in thin ship panels", *Journal of Ship Production*, Vol. 13, Issue 2, May 1997, pp. 83-92;
  - 13 G. E. Tummers: "Summary report on stress relaxation data", *Brit. Weld. J*, 10 (1963), pp. 292-303;
  - 14 V. M. Sagalevich: "Methodes of elimination of welding stresses and deformations", Mashinostroenie, Moskva, 1974;

- 15 G. P. Wozney, G. R. Crawler: "An investigation of vibrational stress relief in steel", *Welding Journal*, Sept. 1968, pp. 441s - 449s;
- 16 R. W. Nichols: "Overstressing as a means of reducing the risk of subsequent brittle failure", *Brit. Weld. J.*, 15 (1968), No. 1, pp. 21-42 and No. 2, pp. 75-84;
- 17 S. J. Maddox: "Improving the fatigue strength of welded joints by peeing", *Met. Constr.*, 1985, No. 4, pp. 220-224;
- 18 K. M. Gatovskii, V. A. Karkhin: "Theory of welding stresses and deformations", Leningrad Shipbuilding Institute, 1980;
- 19 G. E. Totten and M. A. Howes: "Steel heat treatment handbook", Marcel Dekker, New York, 1997;
- 20 G. F. Hewitt, G. L. Shires, Y. V. Polezjaev: "International encyclopedia of heat and mass transfer", CRC Press, New-York, 1997;

---

**CHAPTER VI CONCLUSIONS**

This dissertation is devoted to the theoretical and experimental investigation and the comparison of two welding techniques used mostly for long fillet- and butt-welds. These techniques are: the three-electrode one-side SAW and the single-electrode multi-pass SAW.

This work was mostly based on computer simulation of residual stress and distortion of thick plates. Some mitigation techniques directed towards reduction of the negative mechanical effects were also investigated in this dissertation.

The main conclusions that can be drawn, based on the investigations carried out by the author during the last four years, are gathered in this chapter:

1. Based on the methodical example, we can state that the suggested mesh and time incrementation for 2D and 3D heat flow models approximate the exact solution with 95% accuracy in the temperature interval  $500^{\circ}\text{C} < T < 1500^{\circ}\text{C}$ . In the temperature interval  $0^{\circ}\text{C} < T < 500^{\circ}\text{C}$  the accuracy drops down to 84%.
2. The smallest element of the 3D model has dimensions  $4 \times 5 \times 10 \text{ mm}$  ( $h \times w \times l$ ), but considerably longer elements could be used because of almost 2D character of the heat flow at some distance behind the arc.
3. The models with contact analysis implementation were also explored in the scope of this dissertation. It was done in order to evaluate the effect of the gravitational forces, acting on the welding details. Contact analysis significantly complicates the solution, approximately doubling computation time, not demonstrating significant influence on the stress-strain development.
4. The mechanical part of the simulation, in contrast to the heat flow analysis, cannot use elements elongated along the weld line. For better accuracy elements near the centreline must be nearly cubic.
5. In forming criteria about accuracy of the FE model, we first need to determine what is in the focus of attention. If the main problem concerns stress distribution (corrosion problem, brittle fracture, fatigue strength), then a relatively coarse mesh can be used. Problems that concern about deformation processes in welding demand finer mesh.
6. Analysing the deformation of the plate during the first 45 seconds of the welding process, the accuracy of the method can be claimed to be 88%. But there is no guaranty that this tendency will be the same by the end of the welding process. To be on the safe side, we can state that the mechanical part of the thermal-stress model is not less than 80-85% accurate.
7. According to calculations, the weld pool width in the case of the three-electrode welding, calculated based on analytical and 2D and 3D FEA, does not vary much from one solution to another (29mm from analytical model; 28mm from 2D cross-

sectional model and 26mm from 3D model). The weld pool length turned out to be much more sensitive to the solution (580mm in the analytical model; 350mm in the 2D cross-sectional model and 450mm in the 3D model).

8. The length of the material softening isotherm (700<sup>0</sup>C) calculated for the case of the three-electrode welding procedure varies between 1500mm, according to the 2D FE thermal model, and 2000mm, according to the analytical model. The most realistic 3D FE thermal model shows the 700<sup>0</sup>C isotherm to be 1700mm long. This fact indicates that for successful computer and experimental modelling of real welding processes, used for completion of long weld runs, the length of the specimen should not be shorter than 2000mm. Otherwise, the stiffness of the structure would not be reproduced in the experiment.
9. According to the 2D model with the "element birth" technique, the cooling rate in the case of conventional single-electrode three-pass welding is 4-10 times higher in the temperature interval 500-1500<sup>0</sup>C than in the case of the three-electrode process.
10. In comparison the two welding techniques cause significantly different microstructure transformations in the HAZ. The metallographic structure after three-electrode one pass welding is predicted to be 50% ferrite, 20% perlite and 30% bainite. In the case of the single-electrode technique, the perlite phase is fully eliminated, and the microstructure is composed of 25% ferrite and 75% bainite.
11. Based on 3D-model results, the non-volumetric stress state leads to the conclusion that the existence of maximum residual longitudinal stresses higher than the yield point ( $\sigma_x^{max} \approx 1.15\sigma_y$ ) can be explained by, firstly, the material hardening and, only secondly, by a feebly marked volumetric stress-state.
1. Very high heat input produces a relatively wide plastically deformed zone, relatively to the plate thickness. This fact explains the low value of the residual transverse stress in the through-thickness direction of the plate ( $\sigma_z^{max} \approx 0.1\sigma_y$ ).
13. Multi-electrode welding is characterised by a slightly wider plastically deformed zone (ca. 6 plate thicknesses) compared to multi-pass welding (5 thicknesses). It is affected by the width of the isotherm  $T_{max} \approx 200^0\text{C}$ . The areas heated above the 200<sup>0</sup>C limit were subjected to plastic flowing.
14. The single-electrode three pass welding procedure gives less longitudinal shrinkage. The longitudinal shrinkage in the case of the three-electrode welding is 50% higher than in the case of single-electrode three pass welding technique.
15. The data presented in *section 3.2* indicates a significant non-linear behaviour of the residual inherent (plastic) strain. To further explore the possibilities of using the inherent strain concept in welding stress and deformation calculations, more effort should be put into inherent strain generalisation.
16. The 2D generalised plane strain model reveals a wider plastically deformed zone than the 3D model. In other words, according to the 2D model, the plastic deformation occurs in areas exposed to lower maximum temperatures. In the case considered, according to the 2D model plastic deformation occurred in the areas with  $T_{max} > 100^0\text{C}$ . For the 3D model this interval is narrowed down to  $T_{max} > 200^0\text{C}$ .

1. Considering the plastic strain development in the HAZ of the weld, it was demonstrated that the single-electrode welding procedure for the investigated conditions exposes the weld to higher plastic strain at elevated temperatures. The maximum transient plastic strain in the transverse direction  $\epsilon_y^p$  at  $800^{\circ}\text{C}$  is twice as high in the case of the multi-pass welding as in the multi-electrode technique. This fact indicates that multi-pass welding procedure is more favourable in terms of hot crack initiation.
18. The comparison between calculated and experimentally measured angular deformation reveals that in some cases simulations give overestimated value and in some cases deformation turns out to be underestimated. It is difficult to exactly simulate experiments in detail because the deformation is quite sensitive to variations in welding conditions.
19. The three-electrode welding procedure causes 65% less angular change in the 20mm thick steel plates compared to single-electrode welding in three passes.
20. For the considered class of methods significant effect on the residual stress distribution was demonstrated. The suggested techniques gave a reduction of the peak residual stress of 45% with mechanical stretching and of 35% with thermal tensioning.
21. The different techniques (mechanical stretching, thermal tensioning with the stationary heating blankets and the moving heat sources) gave similar results with regard to the distribution and maximum values of residual stress and deformation.
22. Suggested techniques, directed towards reduction of the angular deformations, are expected to demonstrate significant improvement of the joint in terms of angular deformation magnitude. The effect of the techniques increases with decreasing plate thickness. It was demonstrated that for the case of 6mm thick plates a reduction up to 75% can be achieved.

### ***RECOMMENDATIONS FOR FURTHER WORK***

Each step of the progress in hardware technology allows solving increasingly more complicated problems. The real phenomena under consideration of weldability analysis have a very complicated nature. Together with expanding horizons of our capabilities in computational science, we get the possibility to include more and more nuances in the formulation of the problems. It means that with time we will be able to solve more detailed approximations, taking into account more parameters of the process.

Investigations presented in this dissertation are limited by the following computer resources:

- 500MHz Pentium III processor;
- 256Mb random access memory;
- 30Gb hard driver disk (with IDE controller).

With such resources we were limited to the mesh consisting of 3000 elements. Size of the specimen was limited by  $500 \times 250 \times 20$ mm.

Implementation of the “inherent strain solution” (introduced in section 3.2. of Chapter IV) in order to investigate residual stresses and deformations of the real-size specimens (for example  $10.000 \times 4.000 \times 20$ mm) is a feasible prospect. Even the above mentioned computer resources would be sufficient for solution of such a problem (elastic finite element analysis) with  $10^5$  elements.

In order to solve directly a thermo-mechanical problem for such specimen, much more computational power would be needed.

With the increasing availability of more computer resources, one can try to include into the formulation of the problem the low-temperature microstructure transformations and increased mesh density.

More detailed data on the thermo-mechanical properties of the material and implementation of the “element birth technique” (described in section 2.2.2 of Chapter III) for the 3D analysis can improve reliability of the results.

For investigation of the weldability in terms of the hot and cold microcrack formation the submodelling technique should be included into the analysis. This technique involves two separate sets of solutions. First, the overall stresses of the structure subjected to a thermal load are calculated using a relatively rough mesh. After that the focus is switched to the small volume for investigation of microcrack initiation (mesh density now is much higher). The results from the solution for overall stress distribution serve as boundary conditions for the submodel.

**APPENDIX A**

Parts from the ABAQUS input files used for simulations are listed in this section. There are several sections in this Appendix A:

1. A1 – input file for thermal part of the 3D model of the three-electrode welding procedure (two 500×250×20mm steel plates).
2. A2 – input file for mechanical part of the 3D model of the three-electrode welding procedure (two 500×250×20mm steel plates).
3. A3 – input file for thermal part of the 2D model of the three-electrode welding procedure (steel plates with cross-section 250×20mm). This part is for calculation of the first 10 seconds of the process (1<sup>st</sup> source).
4. A4 – input file for thermal part of the 2D model of the three-electrode welding procedure (steel plates with cross-section 250×20mm). This part is for calculation of the time interval 10s< $t$ <20s of the process (2<sup>nd</sup> source).
5. A5 – input file for thermal part of the 2D model of the three-electrode welding procedure (steel plates with cross-section 250×20mm). This part is for calculation of the time interval 20s< $t$ <7000s of the process (3<sup>rd</sup> source and cooling process).
6. A6 – input file for mechanical part of the 2D model of the three-electrode welding procedure (steel plates with cross-section 250×20mm).

## A1 Input file for thermal part of the 3D model of the three-electrode welding procedure (two 500×250×20mm steel plates)

```

*HEADING
ABAQUS. Temperature part of the sequentially coupled analysis.
4x5x10mm elements.
[t_5_10.inp]
**
*NODE
    1,          0.,          0.
    2,          0.01,         0.
    3,          0.02,         0.
    4,          0.03,         0.
    5,          0.04,         0.

.....
.....

    3974,        0.46,        0.25,        0.02
    3975,        0.47,        0.25,        0.02
    3976,        0.48,        0.25,        0.02
    3977,        0.49,        0.25,        0.02
    3978,        0.5,         0.25,        0.02
**
**
*ELEMENT, TYPE=DC3D8, ELSET=PLATE
    1,          1,          2,          53,          52,          664,          665,
    716,        715
    2,          2,          3,          54,          53,          665,          666,
    717,        716
    3,          3,          4,          55,          54,          666,          667,
    718,        717
    4,          4,          5,          56,          55,          667,          668,
    719,        718
    5,          5,          6,          57,          56,          668,          669,
    720,        719

.....
.....

    2996,        3259,        3260,        3311,        3310,        3922,        3923,
    3974,        3973
    2997,        3260,        3261,        3312,        3311,        3923,        3924,
    3975,        3974
    2998,        3261,        3262,        3313,        3312,        3924,        3925,
    3976,        3975
    2999,        3262,        3263,        3314,        3313,        3925,        3926,
    3977,        3976
    3000,        3263,        3264,        3315,        3314,        3926,        3927,
    3978,        3977
**
**
*SOLID SECTION, ELSET=PLATE, MATERIAL=CMN_STEEL
**
*ELSET, ELSET=BOTTOM, GENERATE
1, 600, 1
*ELSET, ELSET=TOP, GENERATE
2401, 3000, 1
*ELSET, ELSET=LEFT, GENERATE
1, 2951, 50

```

```

*ELSET, ELSET=RIGHT, GENERATE
50, 3000, 50
*ELSET, ELSET=BACK, GENERATE
 551, 600, 1
1151, 1200, 1
1751, 1800, 1
2351, 2400, 1
2951, 3000, 1
**////////////////////////////////////
*ELSET, ELSET=SRC1
2401, 2451, 1801, 1201
**
*****
*ELSET, ELSET=SRC2
2402, 2452, 1802, 1202
**
*****
*ELSET, ELSET=SRC3
2403, 2453, 1803, 1203
**
*****
*ELSET, ELSET=SRC4
2404, 2454, 1804, 1204
**
*****
*ELSET, ELSET=SRC5
2405, 2455, 1805, 1205
**
*****

.....
.....

*****
*ELSET, ELSET=SRC66
2446, 2496, 1846, 1246
**
*****
*ELSET, ELSET=SRC67
2447, 2497, 1847, 1247
**
*****
*ELSET, ELSET=SRC68
2448, 2498, 1848, 1248
**
*****
*ELSET, ELSET=SRC69
2449, 2499, 1849, 1249
**
*****
*ELSET, ELSET=SRC70
2450, 2500, 1850, 1250
**
*****
** CMn_steel*****
**
*MATERIAL, NAME=CMN_STEEL
**
*DENSITY
 7800., 0.
 7438., 1450.

```

```

7438., 3000.
**
*CONDUCTIVITY, TYPE=ISO
  55., 0.
  29., 750.
  25.4, 800.
  31., 1450.
  31., 3000.
**
*SPECIFIC HEAT
  388., 0.
  894., 700.
  1234., 740.
  610., 860.
  814., 1450.
  814., 3000.
**
***LATENT HEAT
**247E3,1465,1544
**
*****
** T_src
**
*AMPLITUDE, NAME=S1, DEFINITION=TABULAR
  10., 0., 10.01, 1., 11., 1.,
11.01, 0.
**
*AMPLITUDE, NAME=S2, DEFINITION=TABULAR
  11., 0., 11.01, 1., 12., 1.,
12.01, 0.
**
*AMPLITUDE, NAME=S3, DEFINITION=TABULAR
  12., 0., 12.01, 1., 13., 1.,
13.01, 0.
**
*AMPLITUDE, NAME=S4, DEFINITION=TABULAR
  13., 0., 13.01, 1., 14., 1.,
14.01, 0.
**
*AMPLITUDE, NAME=S5, DEFINITION=TABULAR
  14., 0., 14.01, 1., 15., 1.,
15.01, 0.
**
.....
.....
*AMPLITUDE, NAME=S66, DEFINITION=TABULAR
  75., 0., 75.01, 1., 76., 1.,
76.01, 0.
**
*AMPLITUDE, NAME=S67, DEFINITION=TABULAR
  76., 0., 76.01, 1., 77., 1.,
77.01, 0.
**
*AMPLITUDE, NAME=S68, DEFINITION=TABULAR
  77., 0., 77.01, 1., 78., 1.,
78.01, 0.
**
*AMPLITUDE, NAME=S69, DEFINITION=TABULAR

```



```
**
**
*CONTROLS, ANALYSIS=DISCONTINUOUS
*CONTROLS, PARAMETERS=TIME INCREMENTATION
,,,,,,,,,9
**
*RESTART, WRITE, FREQUENCY=20
**
*NODE PRINT, FREQ=1
NT,
*NODE FILE, FREQ=1
NT,
**
*END STEP
```

## A2 Input file for mechanical part of the 3D model of the three-electrode welding procedure (two 500×250×20mm steel plates)

```

*HEADING
ABAQUS. Mechanical part of the sequentially coupled analysis.
4x5x10mm elements.
[mc_5_10.inp]
**
*NODE
    1,          0.,          0.
    2,          0.01,         0.
    3,          0.02,         0.
    4,          0.03,         0.
    5,          0.04,         0.

.....
.....

    3974,        0.46,         0.25,         0.02
    3975,        0.47,         0.25,         0.02
    3976,        0.48,         0.25,         0.02
    3977,        0.49,         0.25,         0.02
    3978,        0.5,          0.25,         0.02
**
**
*ELEMENT, TYPE=C3D8, ELSET=PLATE
    1,          1,          2,          53,          52,          664,          665,
    716,        715
    2,          2,          3,          54,          53,          665,          666,
    717,        716
    3,          3,          4,          55,          54,          666,          667,
    718,        717
    4,          4,          5,          56,          55,          667,          668,
    719,        718
    5,          5,          6,          57,          56,          668,          669,
    720,        719

.....
.....

    2995,        3258,        3259,        3310,        3309,        3921,        3922,
    3973,        3972
    2996,        3259,        3260,        3311,        3310,        3922,        3923,
    3974,        3973
    2997,        3260,        3261,        3312,        3311,        3923,        3924,
    3975,        3974
    2998,        3261,        3262,        3313,        3312,        3924,        3925,
    3976,        3975
    2999,        3262,        3263,        3314,        3313,        3925,        3926,
    3977,        3976
    3000,        3263,        3264,        3315,        3314,        3926,        3927,
    3978,        3977
**
**
*SOLID SECTION, ELSET=PLATE, MATERIAL=CMN_STEEL
**
**
*NSET, NSET=FRONT, GENERATE
    1, 51, 1
    664, 714, 1

```

```

1327,1377,1
1990,2040,1
2653,2703,1
3316,3366,1
**
**   constrained in Z-direction nodes   *****
*NSET,NSET=POINTS
613,663
**
**////////////////////////////////////
**
** CMn_steel*****
**
**MATERIAL, NAME=CMN_STEEL
**
**DENSITY
      7800.,
**
**ELASTIC, TYPE=ISO
      2.06E+11,      0.296,      0.
      2.03E+11,      0.311,      100.
      2.01E+11,      0.330,      200.
      2.00E+11,      0.349,      300.
      1.65E+11,      0.367,      400.
      1.00E+11,      0.386,      500.
      6.00E+10,      0.405,      600.
      4.00E+10,      0.423,      700.
      3.00E+10,      0.442,      800.
      2.00E+10,      0.461,      900.
      1.00E+10,      0.480,     1000.
      1.00E+10,      0.480,     3000.
**
**EXPANSION, TYPE=ISO, ZERO=0.
      1.2E-5,      0.
      1.4E-5,     1450.
      1.4E-5,     3000.
**
**
**PLASTIC
      344.64E+6,      0.,      0.
      422.64E+6,      0.1,      0.
      331.93E+6,      0.,      100.
      409.93E+6,      0.1,      100.
      308.30E+6,      0.,      200.
      386.30E+6,      0.1,      200.
      276.07E+6,      0.,      300.
      342.57E+6,      0.1,      300.
      235.22E+6,      0.,      400.
      290.22E+6,      0.1,      400.
      185.77E+6,      0.,      500.
      230.77E+6,      0.1,      500.
      127.71E+6,      0.,      600.
      162.71E+6,      0.1,      600.
      68.55E+6,      0.,      700.
      96.05E+6,      0.1,      700.
      64.35E+6,      0.,      800.
      84.35E+6,      0.1,      800.
      45.65E+6,      0.,      900.
      60.65E+6,      0.1,      900.
      11.32E+6,      0.,      1000.
      21.32E+6,      0.1,      1000.

```



**A3 Input file for thermal part of the 2D model of the three-electrode welding procedure (steel plates with cross-section 250×20mm). This part is for calculation of the first 10 seconds of the process (1<sup>st</sup> source)**

```

*RESTART,WRITE,FREQ=1
*NODE,NSET=BOTTOM_LINE
1, 0.,
1001, 0.005,
2001, 0.010,
3001, 0.015,
4001, 0.020,
5001, 0.030,
6001, 0.040,
7001, 0.050,
8001, 0.060,
9001, 0.080,
10001, 0.120,
11001, 0.180,
12001, 0.250,
*NODE,NSET=TOP_LINE
501, 0., 0.02
1501, 0.005, 0.02
2501, 0.010, 0.02
3501, 0.015, 0.02
4501, 0.020, 0.02
5501, 0.030, 0.02
6501, 0.040, 0.02
7501, 0.050, 0.02
8501, 0.060, 0.02
9501, 0.080, 0.02
10501, 0.120, 0.02
11501, 0.180, 0.02
12501, 0.250, 0.02
**
*NFILL, NSET=MIDDLE
BOTTOM_LINE,TOP_LINE, 5, 100
**
*ELEMENT, TYPE=DC2D4
1, 1,1001,1101,101
*ELGEN,ELSET=ALLELS
1,12,1000,1000,5,100,100
**
*SOLID SECTION, ELSET=ALLELS, MATERIAL=CMN_STEEL
0.001,
**
*ELSET,ELSET=BOTTOM, GENERATE
1,11001,1000
*ELSET,ELSET=RIGHT, GENERATE
11001,11401,100
*ELSET,ELSET=TOP, GENERATE
401,11401,1000
**
*ELSET,ELSET=SRC1
201
*ELSET,ELSET=SRC2
301
*ELSET,ELSET=SRC3
401,1401
*NSET,NSET=SRC1

```





**A4 Input file for thermal part of the 2D model of the three-electrode welding procedure (steel plates with cross-section 250×20mm). This part is for calculation of the time interval  $10s < t < 20s$  of the process (2<sup>nd</sup> source)**

```

*RESTART,WRITE,FREQ=1
*NODE,NSET=BOTTOM_LINE
1, 0.,
1001, 0.005,
2001, 0.010,
3001, 0.015,
4001, 0.020,
5001, 0.030,
6001, 0.040,
7001, 0.050,
8001, 0.060,
9001, 0.080,
10001, 0.120,
11001, 0.180,
12001, 0.250,
*NODE,NSET=TOP_LINE
501, 0., 0.02
1501, 0.005, 0.02
2501, 0.010, 0.02
3501, 0.015, 0.02
4501, 0.020, 0.02
5501, 0.030, 0.02
6501, 0.040, 0.02
7501, 0.050, 0.02
8501, 0.060, 0.02
9501, 0.080, 0.02
10501, 0.120, 0.02
11501, 0.180, 0.02
12501, 0.250, 0.02
**
*NFILL, NSET=MIDDLE
BOTTOM_LINE,TOP_LINE, 5, 100
**
*ELEMENT, TYPE=DC2D4
1, 1,1001,1101,101
*ELGEN,ELSET=ALLELS
1,12,1000,1000,5,100,100
**
*SOLID SECTION, ELSET=ALLELS, MATERIAL=CMN_STEEL
0.001,
**
*ELSET,ELSET=BOTTOM, GENERATE
1,11001,1000
*ELSET,ELSET=RIGHT, GENERATE
11001,11401,100
*ELSET,ELSET=TOP, GENERATE
401,11401,1000
**
*ELSET,ELSET=SRC1
201
*ELSET,ELSET=SRC2
301
*ELSET,ELSET=SRC3
401,1401
*NSET,NSET=SRC1

```





**A5 Input file for thermal part of the 2D model of the three-electrode welding procedure (steel plates with cross-section 250×20mm). This part is for calculation of the time interval  $20s < t < 7000s$  of the process (3<sup>rd</sup> source and cooling process)**

```

*RESTART,WRITE,FREQ=1
*NODE,NSET=BOTTOM_LINE
1, 0.,
1001, 0.005,
2001, 0.010,
3001, 0.015,
4001, 0.020,
5001, 0.030,
6001, 0.040,
7001, 0.050,
8001, 0.060,
9001, 0.080,
10001, 0.120,
11001, 0.180,
12001, 0.250,
*NODE,NSET=TOP_LINE
501, 0., 0.02
1501, 0.005, 0.02
2501, 0.010, 0.02
3501, 0.015, 0.02
4501, 0.020, 0.02
5501, 0.030, 0.02
6501, 0.040, 0.02
7501, 0.050, 0.02
8501, 0.060, 0.02
9501, 0.080, 0.02
10501, 0.120, 0.02
11501, 0.180, 0.02
12501, 0.250, 0.02
**
*NFILL, NSET=MIDDLE
BOTTOM_LINE,TOP_LINE, 5, 100
**
*ELEMENT, TYPE=DC2D4
1, 1,1001,1101,101
*ELGEN,ELSET=ALLELS
1,12,1000,1000,5,100,100
**
*SOLID SECTION, ELSET=ALLELS, MATERIAL=CMN_STEEL
0.001,
**
*ELSET,ELSET=BOTTOM, GENERATE
1,11001,1000
*ELSET,ELSET=RIGHT, GENERATE
11001,11401,100
*ELSET,ELSET=TOP, GENERATE
401,11401,1000
**
*ELSET,ELSET=SRC1
201
*ELSET,ELSET=SRC2
301
*ELSET,ELSET=SRC3
401,1401

```





### A6 Input file for mechanical part of the 2D model of the three-electrode welding procedure (steel plates with cross-section 250×20mm)

```

*RESTART, WRITE, FREQUENCY=1
*NODE,NSET=BOTTOM_LINE
1, 0.,
1001, 0.005,
2001, 0.010,
3001, 0.015,
4001, 0.020,
5001, 0.030,
6001, 0.040,
7001, 0.050,
8001, 0.060,
9001, 0.080,
10001, 0.120,
11001, 0.180,
12001, 0.250,
**
*NODE,NSET=TOP_LINE
501, 0., 0.02
1501, 0.005, 0.02
2501, 0.010, 0.02
3501, 0.015, 0.02
4501, 0.020, 0.02
5501, 0.030, 0.02
6501, 0.040, 0.02
7501, 0.050, 0.02
8501, 0.060, 0.02
9501, 0.080, 0.02
10501, 0.120, 0.02
11501, 0.180, 0.02
12501, 0.250, 0.02
**
*NODE
9998, -0.001,
9999, -0.001, 0.001
**
*NFILL, NSET=MIDDLE
BOTTOM_LINE,TOP_LINE, 5, 100
*NSET,NSET=ALLNS
BOTTOM_LINE,TOP_LINE,MIDDLE
**
**
*ELEMENT, TYPE=CGPE6
1, 1,1001,1101,101, 9998,9999
*ELGEN,ELSET=PLATE
1,12,1000,1000,5,100,100
**
*SOLID SECTION, ELSET=PLATE, MATERIAL=CMN_STEEL
0.001,
**
*NSET,NSET=LEFT, GENERATE
1,501,100
*NSET,NSET=CLAMP
12001
**
*ELSET,ELSET=SRC1
201

```

```

*ELSET, ELSET=SRC2
301
*ELSET, ELSET=SRC3
401, 1401
**
**
*ELSET, ELSET=BOTTOM, GENERATE
1, 11001, 1000
**
**
*NSET, NSET=SRC1
201, 301, 1201, 1301
*NSET, NSET=SRC2
301, 401, 1301, 1401
*NSET, NSET=SRC3
401, 501, 1401, 1501, 2401, 2501
** CMn_steel*****
**
*MATERIAL, NAME=CMN_STEEL
**
*DENSITY
      7800.,
**
*ELASTIC, TYPE=ISO
      2.06E+11,      0.296,      0.
      2.03E+11,      0.311,      100.
      2.01E+11,      0.330,      200.
      2.00E+11,      0.349,      300.
      1.65E+11,      0.367,      400.
      1.00E+11,      0.386,      500.
      6.00E+10,      0.405,      600.
      4.00E+10,      0.423,      700.
      3.00E+10,      0.442,      800.
      2.00E+10,      0.461,      900.
      1.00E+10,      0.480,     1000.
      1.00E+10,      0.480,     3000.
**
*EXPANSION, TYPE=ISO, ZERO=0.
      1.2E-5,      0.
      1.4E-5,     1450.
      1.4E-5,     3000.
**
**
*PLASTIC
      344.64E+6,      0.,      0.
      422.64E+6,      0.1,      0.
      331.93E+6,      0.,     100.
      409.93E+6,      0.1,     100.
      308.30E+6,      0.,     200.
      386.30E+6,      0.1,     200.
      276.07E+6,      0.,     300.
      342.57E+6,      0.1,     300.
      235.22E+6,      0.,     400.
      290.22E+6,      0.1,     400.
      185.77E+6,      0.,     500.
      230.77E+6,      0.1,     500.
      127.71E+6,      0.,     600.
      162.71E+6,      0.1,     600.
      68.55E+6,      0.,     700.
      96.05E+6,      0.1,     700.
      64.35E+6,      0.,     800.

```





## APPENDIX B

Some illustrations of the program written in DELPHI 2 and then modified in DELPHI 5 are presented in this section.

This application is created as a part of the dissertation. The application allows briefly and roughly estimate deformations in the plate due to welding process. It also helps to make a step to better understanding of the physics of this process.

The screenshot shows a software interface for calculating plate deformation. It includes input fields for power, welding speed, and plate thickness, as well as material properties. A result box displays a calculated transverse shrinkage value. Below the interface is a diagram illustrating the types of deformation: transverse shrinkage ( $\Delta_{tr}/2$ ), longitudinal shrinkage ( $\Delta l/2$ ), and angular shrinkage ( $\beta$ ).

Parameter	Symbol	Value
Power input [kW]	q	80
Welding speed [mm/s]	v	10
Plate thickness [mm]	h	20
Thermal expansion coefficient [1/K]	$\alpha$	12E-6
Specific heat capacity [J/gK]	C	640E-3
Density [g/mm <sup>3</sup> ]	$\rho$	7800E-6
Transver stiffness factor	$\mu$	0.7

**RESULT**

$$\Delta_{tr} = \mu \cdot \frac{2\alpha \cdot q \cdot l \cdot v}{c\rho \cdot h}$$

$\Delta_{tr} = 1.34615384$

**Diagram Labels:**  
 Transverse shrinkage:  $\Delta_{tr}/2$   
 Longitudinal shrinkage:  $\Delta l/2$   
 Angular shrinkage:  $\beta$

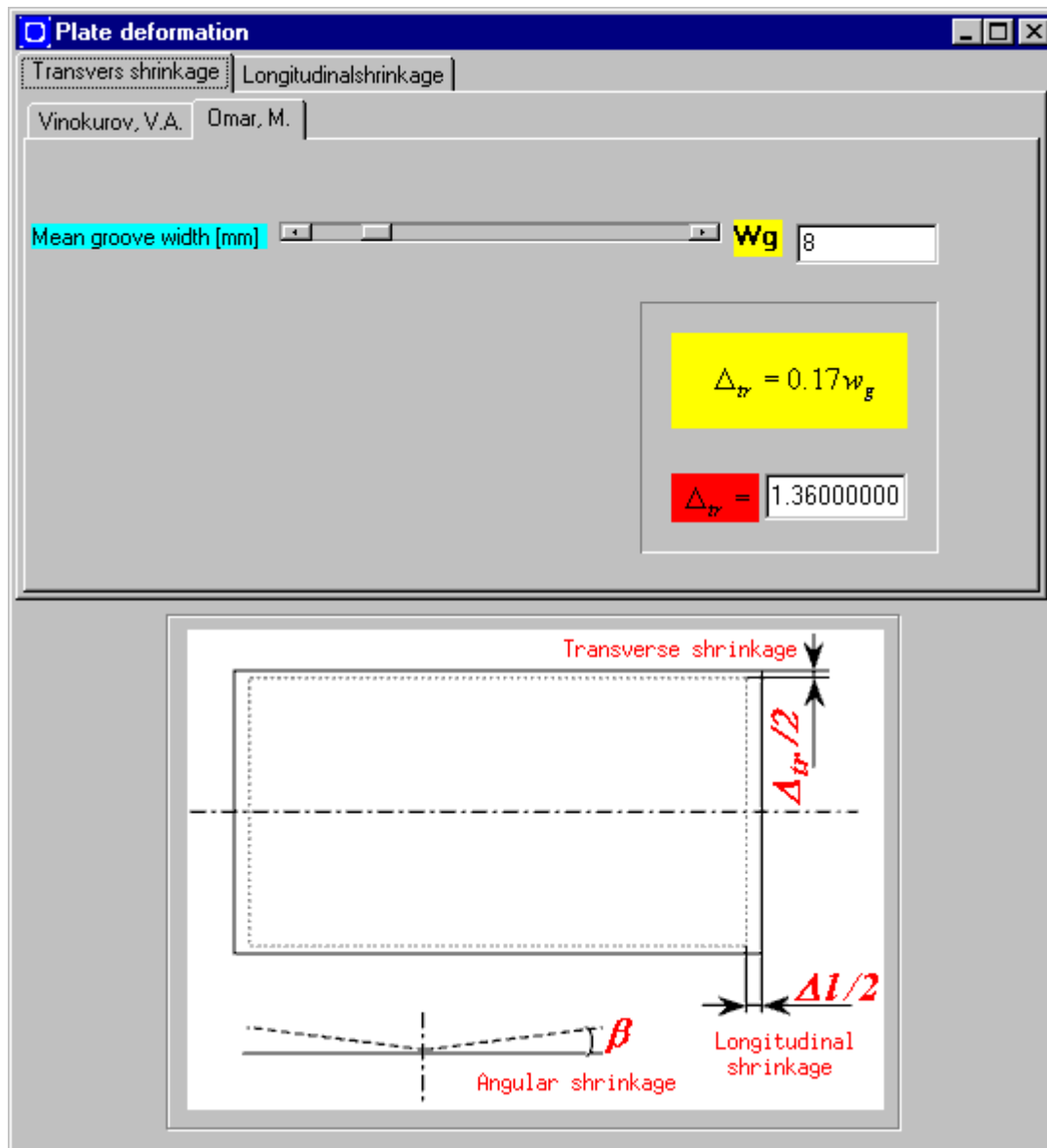


**Plate deformation**

Transvers shrinkage  Longitudinalshrinkage

Radaj, D. |

Heat input [kW]  **q**

Welding speed [mm/s]  **v**

Plate length [mm]  **l**

Cross section area [mm<sup>2</sup>]  **A**

Elastic modulus [N/mm<sup>2</sup>] **E**

$$\Delta l = \frac{F_s l}{EA}$$

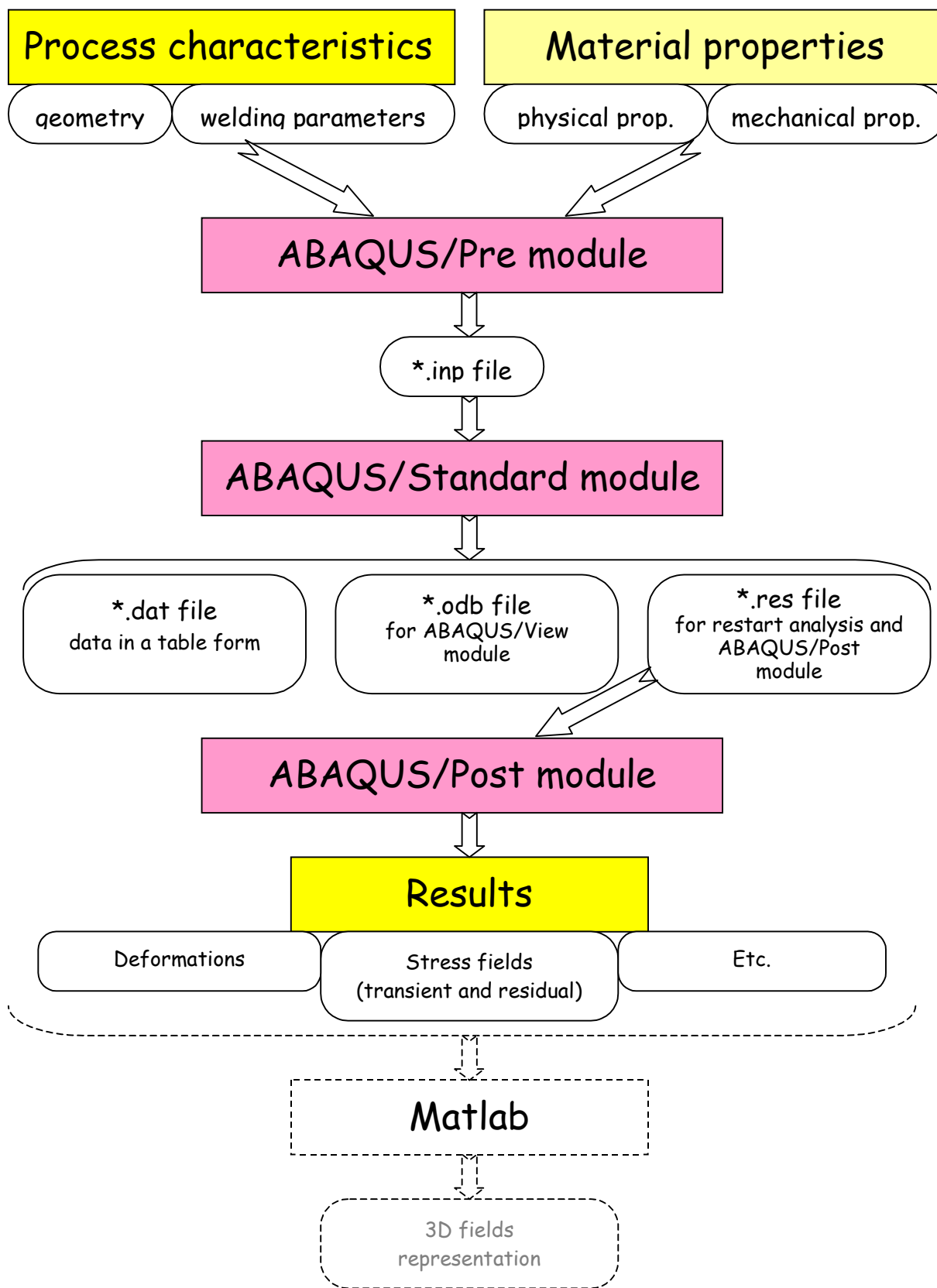
where  $F_s$  is shrinkage force:  $F_s = 1.7 \frac{q}{v}$

**$\Delta l = 1.699999999$**



## APPENDIX C

Abaqus post-processing capabilities do not satisfy all the needs concerning simulation of the thermo-mechanical processes in welding applications. Here the scheme, explaining the complicated way of getting some graphs presented in the dissertation.



## APPENDIX D

```

Program Three_electrodes;

uses graph, crt;
label Out;
const s=20; lia=0.025; v=10; a1=5; alpha=30E-6; cro=0.005;
        q11=4470; q12=32010; q2=20520; q3=25270; dX=2; dY=0.2;

var Gd,Gm,i,j,i1,j1,N,ix,NX,NY,NY1500,NY1300,NY1100,NY900,NY700,NY500,
        NX1500,NX1300,NX1100,NX900,NX700,NX500 :integer;
x,y,z,r,z1,z2,t,I0,r1,x1,A,B,SQR1,Frz,zm1,zm2,h1,h2,h3,h4,h5,h6,
res,h7,h8,h9,h10,CR,b1,t1,Td15 ,Td13 ,Td11 ,Td9 ,Td7, Td5
:real;
TMP,T_1500,Td1500 :ARRAY[1..640] OF REAL;

Function pow(x2,y2:real):real;
begin
  if x2 > 0 then
    res := exp(y2*ln(x2))
  else
    if y2 = Trunc(y2) then
      begin
        res := 1;
        for i := 1 to Round(ABS(y2)) do res := res*x2;
        if y2 < 0 then res := 1.0/res;
      end
    else
      begin
        HALT;
      end;
    pow := res
end;

function K0(z0:real):real; {K0(u) multiplied by exp(u)}
begin
  t:=z0/3.75;
  if z0 < 2 then
    begin
      I0:=1+3.5156229*t*t+3.0899424*t*t*t*t+1.20675*pow(t,6)+0.26597*pow(t,8
    );
      K0:=exp(z0)*(-ln(z0/2)*I0-
      0.57721566+0.4227842*(z0/2)*(z0/2)+0.23069*pow(z0/2,4)+
      0.03488*pow(z0/2,6)+0.00262698*pow(z0/2,8)+0.0001075*pow(z0/2,10));
    end;
    if z0 >= 2 then
      begin
        K0:=(1/pow(z0,0.5))*(1.25331414-0.07832358*(2/z0)+
        0.02189568*(2/z0)*(2/z0)+0.01062446*pow(2/z0,3)+0.00587872*pow(2/z0,4)
        -
        0.00251540*pow(2/z0,5));
      end;
    end;

```

```

end;

function Iim(i2:integer;qi,z4:real):real;
begin
  if qi=q3 then
    begin A:=10256; B:=-613; zml:=0; zm2:=2.7 end;

    if qi=q2 then
      begin A:=9715; B:=-580.4; zml:=2.7; zm2:=5.5 end;

    if qi=q12 then
      begin A:=8638; B:=-516.2; zml:=5.5; zm2:=15 end;

    if qi=q11 then
      begin A:=894; B:=0; zml:=15; zm2:=20 end;

  h5:=(s/(pi*i2));
  h6:= h5* (A+B*zm2)*sin((pi*i2*zm2)/s) + h5*h5* B
*cos((pi*i2*zm2)/s);
  Iim:=h6-h5* (A+B*zml)*sin((pi*i2*zml)/s) - h5*h5* B
*cos((pi*i2*zml)/s);
  end;

function F(qf,r3,z3:real):real;
begin Frz:=1; h4:=(v*r3)/(2*a1);h9:=K0(h4);
  for i1:=1 to 20 do
    begin

SQR1:=sqrt(1+((2*pi*a1*i1)/(v*s))*((2*pi*a1*i1)/(v*s)));
      h3:=h4*SQR1;
      if ((h4-h3)<0) and ((h4-h3>-70)) then

h7:=exp(h4-h3);h8:=1;
      if ((h4-h3)<70) and ((h4-h3>-140)) then

h7:=exp(h4-h3+70);h8:=exp(-70);
Frz:=Frz+2*(cos(pi*i1*z3/s)*K0(h3)*h8*h7*(1/qf)*Iim(i1,qf,z3)/h9);
      end;
    F:=Frz;
  end;

function Tmain(qt,x1,y1,z1:real):real;
begin
  r1:=sqrt(sqr(x1)+sqr(y1));
  h1:=(v*r1)/(2*a1); h2:=(v*x1)/(2*a1);
  b1:=2*alpha/(cro*s);
  if x1<0 then t1:=-x1/v
  else t:=0;

  if h2>30 then Tmain:=0
  else
  Tmain:= ((qt/s)/(2*pi*lia))*exp(-h2-
h1)*K0(h1)*F(qt,r1,z1)*exp(-b1*t1);
  end;

```

**BEGIN**

```

Gd:=detect;
InitGraph(Gd,Gm,' ');
setBkcolor(0);cleardevice;

```

```

FOR NX:=340 TO 640 DO
  BEGIN
    FOR NY:=0 TO 230 DO
      BEGIN
        X:=1-NX*dX;
        Y:=0+NY*dY;
        Z:=20;

        TMP[NY]:=20+Tmain(q11,x,y,z)+Tmain(q12,x,y,z)+
          Tmain(q2,x+100,y,z)+Tmain(q3,x+210,y,z);

        END;

Td15:=100;Td13:=100;Td11:=100;Td9:=100;Td7:=100;Td5:=100;

    FOR NY:=0 TO 230 DO
      BEGIN

        IF (TMP[NY]>1400) AND (TMP[NY]<1600) THEN
          BEGIN
            IF (ABS(TMP[NY]-1500)<Td15) THEN
              BEGIN
                NY1500:=NY;
                Td15:=TMP[NY]-1500;
              END;
            END;

            IF (TMP[NY]>1200) AND (TMP[NY]<1400) THEN
              BEGIN
                IF (ABS(TMP[NY]-1300)<Td13) THEN
                  BEGIN
                    NY1300:=NY;
                    Td13:=TMP[NY]-1300;
                  END;
                END;

                IF (TMP[NY]>1000) AND (TMP[NY]<1200) THEN
                  BEGIN
                    IF (ABS(TMP[NY]-1100)<Td11) THEN
                      BEGIN
                        NY1100:=NY;
                        Td11:=TMP[NY]-1100;
                      END;
                    END;

                    IF (TMP[NY]>800) AND (TMP[NY]<1000) THEN
                      BEGIN
                        IF (ABS(TMP[NY]-900)<Td9) THEN
                          BEGIN
                            NY900:=NY;
                            Td9:=TMP[NY]-900;
                          END;
                        END;

                        IF (TMP[NY]>600) AND (TMP[NY]<800) THEN
                          BEGIN
                            IF (ABS(TMP[NY]-700)<Td7) THEN
                              BEGIN
                                NY700:=NY;
                                Td7:=TMP[NY]-700;
                              END;
                            END;
                          END;
                        END;
                      END;
                    END;
                  END;
                END;
              END;
            END;
          END;
        END;
      END;
    END;
  END;

```

## APPENDIX D

---

```
      END;
    END;

    IF (TMP[NY] >400) AND (TMP[NY] <600) THEN
    BEGIN
    IF (ABS(TMP[NY] -500) <Td5) THEN
    BEGIN
    NY500 :=NY;
    Td5 :=TMP[NY] -500;
    END;
    END;

    END;

    END;

    PUTPIXEL(0+NX,200+NY1500,15);
    PUTPIXEL(0+NX,200-NY1500,15);

    PUTPIXEL(0+NX,200+NY1300,15);
    PUTPIXEL(0+NX,200-NY1300,15);

    PUTPIXEL(0+NX,200+NY1100,15);
    PUTPIXEL(0+NX,200-NY1100,15);

    PUTPIXEL(0+NX,200+NY900,15);
    PUTPIXEL(0+NX,200-NY900,15);

    PUTPIXEL(0+NX,200+NY700,15);
    PUTPIXEL(0+NX,200-NY700,15);

    PUTPIXEL(0+NX,200+NY500,15);
    PUTPIXEL(0+NX,200-NY500,15);

    END;          line(30,200,630,200); line(30,20,30,400);

    FOR NX:=0 TO 30 DO BEGIN
    LINE(30+NX*20,197,30+NX*20,203);
    LINE(27,20+NX*20,33,20+NX*20);
    END;

    READLN;

    END.
```

## APPENDIX E

### ABAQUS. HOW DOES IT WORK? A BRIEF OVERVIEW <sup>1</sup>

A basic concept in the ABAQUS is the division of the problem into *steps*. A step is any convenient phase of the history.

A step starts with the \*STEP option and ends with the \*END STEP option.

For each step user chooses an *analysis procedure*. This choice defines the type of analysis to be performed during the step (static stress analysis, eigenvalue buckling, transient heat transfer analysis, etc.). Any combination of procedures can be used from step to step, but only one procedure is allowed per step. Since the state of the model (stress, strain, temperature, etc.) is updated throughout all general analysis steps, the effects of previous history are always included in the response in each new analysis step.

The most obvious reason for using several steps in an analysis is to change the analysis procedure type. However, several steps can also be used as a matter of convenience – for example, to change output request, boundary conditions, or loading.

Each step in an analysis is divided into multiple *increments*. In non-linear problems ABAQUS will increment and iterate as necessary to analyse the step, depending on the severity of the non-linearity. In most cases the user has two options for controlling the solution: automatic time incrementation or user-specified fixed time incrementation.

In transient cases with a physical time scale, the user can provide parameters to indicate a level of accuracy in the time integration, and ABAQUS will chose the time increments to achieve this accuracy. For example, the maximum change of the temperature in the point was limited by the  $\Delta T_{max}$  during the heat flow analysis of the models described in section 2.2 of Chapter III. Direct control can be useful when automatic control has trouble with convergence in non-linear problems. This method was used in this work for the models with "element birth" technique in the development stage of the model.

In non-linear analysis ABAQUS uses *extrapolation* to speed up the solution. The guess is determined by the size of the current time increment and by whether linear, parabolic or no extrapolation is chosen. The EXTRAPOLATION parameter with values LINEAR, PARABOLIC, or NO is used for this purpose. By default the linear 100% of the previous incremental solution extrapolation is used in the first increment of a step.

A large class of stress analysis problems can be solved with ABAQUS. A fundamental division of such problems is into static or dynamic response. Dynamic problems are those in which inertia effects are significant. The following *analysis types* are available:

- static stress analysis;

- dynamic analysis;
- steady-state transport analysis;
- heat transfer analysis;
- electrical analysis;
- coupled pore fluid diffusion and stress analysis;
- mass diffusion analysis;
- acoustic and coupled acoustic-structural analysis;
- ABAQUS/Aqua analysis;
- underwater shock analysis.

In addition, the following *analysis techniques* are provided:

- restarting analysis;
- using substructure/superelements;
- submodelling;
- element and contact pair removal and reactivation;
- rezoning;
- introducing a geometric imperfection into a model;
- transferring results between ABAQUS/Explicit and ABAQUS/Standard;
- symmetric model generation;
- transferring results from a symmetric mesh to a three-dimensional mesh;
- transferring results from an axisymmetric mesh to an asymmetric mesh;
- fracture mechanics;
- modelling fluid-filled cavities.

ABAQUS generally uses Newton's method to solve non-linear problems and the stiffness method to solve linear problems. In both cases the stiffness matrix is needed.

Non-linear stress analysis problems can contain up to three sources of non-linearity: material non-linearity, geometric non-linearity, and boundary non-linearity. Some of the models presented in this dissertation contain all of these sources.

### ***Heat transfer and thermal-stress analysis***

ABAQUS can solve the following types of heat transfer problems:

*Uncoupled heat transfer analysis:* Heat transfer problems involving conduction, forced convection, and boundary radiation can be analysed. In these analyses the temperature field is calculated without knowledge of the stress/deformation state or the electrical field in the bodies being studied. Pure heat transfer problems can be transient or steady-state and linear or non-linear.

*Sequentially coupled thermal-stress analysis:* If the stress/displacement solution is dependent on a temperature field but there is no inverse dependency, a sequentially coupled thermal-stress analysis can be conducted. Sequentially coupled thermal-stress analysis is performed by first solving the pure heat transfer problem, then reading the temperature solution into a stress analysis as a predefined field. This kind of analysis was involved in the models used in this dissertation.

*Fully coupled thermal-stress analysis:* A coupled temperature-displacement procedure is used to solve simultaneously for the stress/displacement and the temperature fields. A coupled analysis is used when the thermal and mechanical solutions affect each other strongly. For example, in rapid metalworking problems the inelastic deformation of the material causes heating.

*Adiabatic analysis:* An adiabatic mechanical analysis can be used in cases where mechanical deformation causes heating, but the event is so rapid that this heat has no time to diffuse through the material.

*Coupled thermal-electrical analysis:* A fully coupled thermal-electrical analysis capability is provided for problems where heat is generated due to the flow of electrical current through a conductor.

*Cavity radiation:* Cavity radiation effects can be included in uncoupled heat transfer problems.

Heat transfer problems can be non-linear because the material properties are temperature dependent or because the boundary conditions are non-linear. Usually the non-linearity associated with temperature dependent material properties is mild because the properties do not change rapidly with temperature. However, when latent heat effects are included, the analysis may be severely non-linear.

To conduct a *steady-state analysis* the STEADY STATE parameter on the \*HEAT TRANSFER option should be included. Steady-state analysis means that the internal energy term (the specific heat term) in the governing heat transfer equation is omitted.

To conduct a *transient heat transfer analysis* the STEADY STATE parameter from the \*HEAT TRANSFER option should be omitted (it is default parameter). Time integration in transient problems is done with the backward Euler method (modified Crank-Nicholson operator) in the pure conduction elements. This method is unconditionally stable for linear problems.

By default, the *initial temperature* of all nodes is zero. In order to specify nonzero initial temperature, the TYPE=TEMPERATURE parameter on the \*INITIAL CONDITIONS option should be used.

The \*BOUNDARY option can be used to prescribe temperatures at nodes in a heat transfer analysis. Shell elements have additional temperature degrees of freedom through the thickness (see section 2.2.4. of Chapter III).

The following types of *loading* can be prescribed in a heat transfer analysis:

- concentrated heat fluxes can be prescribed by using the \*CFLUX option;
- body fluxes and distributed surface fluxes can be prescribed by using the \*DFLUX option;
- convective film conditions and radiation conditions can be defined by using the \*FILM and \*RADIATE options.

The thermal conductivity and density of the *materials* in a heat transfer analysis must be defined. The specific heat must also be defined for transient heat transfer problems. Latent heat can be defined for diffusive heat transfer elements if changes in internal energy due to phase changes are important.

The heat transfer element library includes diffusive heat transfer elements, which allow for heat storage (specific heat and latent heat effects) and heat conduction.

The second-order heat-transfer elements usually give more accurate results for the same number of nodes in the mesh. First-order diffusive elements are preferred in cases involving latent heat effects since they use a special integration technique to provide accurate solutions with large latent heats.

Thermal interaction between adjacent surfaces and thermal interface elements are also provided to model heat transport across the boundary layer between a solid and fluid or between two closely adjacent solids.

### ***Sequentially coupled thermal-stress analysis***

A sequentially coupled heat transfer analysis is performed by using the `*HEAT TRANSFER` option (described in the previous section) followed by a stress/deformation analysis run.

Temperature is calculated in an uncoupled heat transfer analysis and nodal temperature are stored as a function of time in the heat transfer results file (\*.fil) by using the `*NODE FILE` option and specifying output variable NT.

The temperatures are then read into the stress analysis as a predefined field; the temperature varies with position and usually time dependent. Such predefined fields are always read into ABAQUS at the nodes. They are then interpolated to the calculation points within elements as needed.

To define the temperature field at different times in the stress analysis, the `*TEMPERATURE` option should be used:  
`*TEMPERATURE, FILE=file_name`

### ***Fully coupled thermal-stress analysis***

A fully coupled thermal-stress analysis is performed by using the `*COUPLED TEMPERATURE-DISPLACEMENT` option.

This kind of analysis is usually non-linear because of the nature of the coupling terms. It requires the use of elements with temperature and displacement degrees of freedom.

The temperatures are integrated using a backward-difference scheme, and the coupled system is solved using Newton's method. A fully coupled thermal-stress analysis automatically invokes the non-symmetric matrix storage and solution scheme.

The time increments can be selected automatically based on a user-prescribed maximum allowable nodal temperature change in an increment specified by the DELTMX parameter. ABAQUS will restrict the time increments to ensure that this value is not exceeded at any node.

The accuracy of the integration of time-dependent material behaviour (creep) is governed by the CETOL parameter. CETOL is used to prescribe the maximum strain rate change allowed at any point during an increment. The CETOL parameter can be used together with the DELTMX parameter.

### ***Static stress analysis procedures***

A static stress procedure is one in which inertia effects are neglected. Several static stress analysis procedures are available in ABAQUS:

*static analysis* is used for stable problems and can indicate linear or non-linear response;

*eigenvalue buckling analysis* is used to estimate the critical load of stiff structures. It is a linear perturbation procedure;

*unstable collapse and postbuckling analysis* is used to estimate the unstable, geometrically non-linear collapse of a structure.

*quasistatic analysis* is used to analyse transient response to time-dependent material behaviour (creep and swelling, viscoelasticity, and viscoplasticity).

### ***Static stress analysis***

Static stress analysis ignores time-dependent material effects (creep, swelling, viscoelasticity) but takes rate-dependent plasticity and hysteretic behaviour for hyperelastic materials into account.

During a \*STATIC step the user assigns a time period to the analysis. This is necessary for cross-references to the amplitude options, which can be used to determine the variation of loads and other externally prescribed parameters during a step.

*Linear static analysis* involves the specification of load cases and appropriate boundary conditions. If all or part of a problem has linear response, substructuring is a powerful capability for reducing the computational cost of large analyses.

Non-linearities can arise from large-displacement effects, material non-linearity, and boundary non-linearities such as contact and friction. If geometrically non-linear behaviour is expected (as in the all models included in this dissertation), the \*STEP, NLGEOM option should be used.

ABAQUS uses Newton's method to solve the non-linear equilibrium equations. Many problems involve history-dependent response. Therefore, the solution usually is

obtained as a series of increments, with iterations to obtain equilibrium within each increment.

In most cases the *automatic incrementation* scheme is preferred because it will select increment sizes based on computational efficiency. This is default option.

*Initial values* of stress, temperature, field variables, solution-dependent state variables, etc. can be specified using the \*INITIAL CONDITIONS option.

*Boundary conditions* can be applied to any of the displacement or rotation degrees of freedom (1-6). During the analysis prescribed boundary conditions can be varied using an amplitude definition.

In the linear static analysis concentrated *load forces* can be applied to the displacement degrees of freedom (1-6) using the \*CLOAD option. Distributed pressure forces or body forces can be applied using \*DLOAD option.

Any of the stress/displacement elements in ABAQUS can be used in a static stress analysis.

The element output available for a static stress analysis includes stress; strain; energies; the values of state, field, and user-defined variables; and composite failure measures. The nodal output available includes displacements, reaction forces, and co-ordinates.

### ***Solving non-linear problems***

ABAQUS combines incremental and iterative procedures for solving non-linear problems. This process involves:

- using Newton's method to solve the non-linear equations;
- determining convergence;
- defining loads as a function of time;
- choosing suitable time increments automatically.

In a non-linear analysis the solution can not be calculated by solving a single system of linear equations, as would be done in a linear problem. Instead, the solution is found by specifying the loading as a function of time and incrementing time to obtain the non-linear response. Therefore, ABAQUS breaks the simulation into a number of time increments and finds the approximate equilibrium configuration at the end of each time increment. Using Newton's method, it often takes ABAQUS several iterations to determine an acceptable solution to each time increment.

---

1 ABAQUS version 5.6, ABAQUS user's manual, Vol.1. Hibbit, Karlson & Sorensen, Inc. 1997;

## APPENDIX F

## LOCKING PHENOMENON

A 3D static stress analysis model illustrated in *Fig. F-1* was created in order to demonstrate the locking phenomenon causing abnormally stiff behaviour of the 3D 8-node linear brick elements (C3D8). This kind of behaviour is typical for elongated elements.

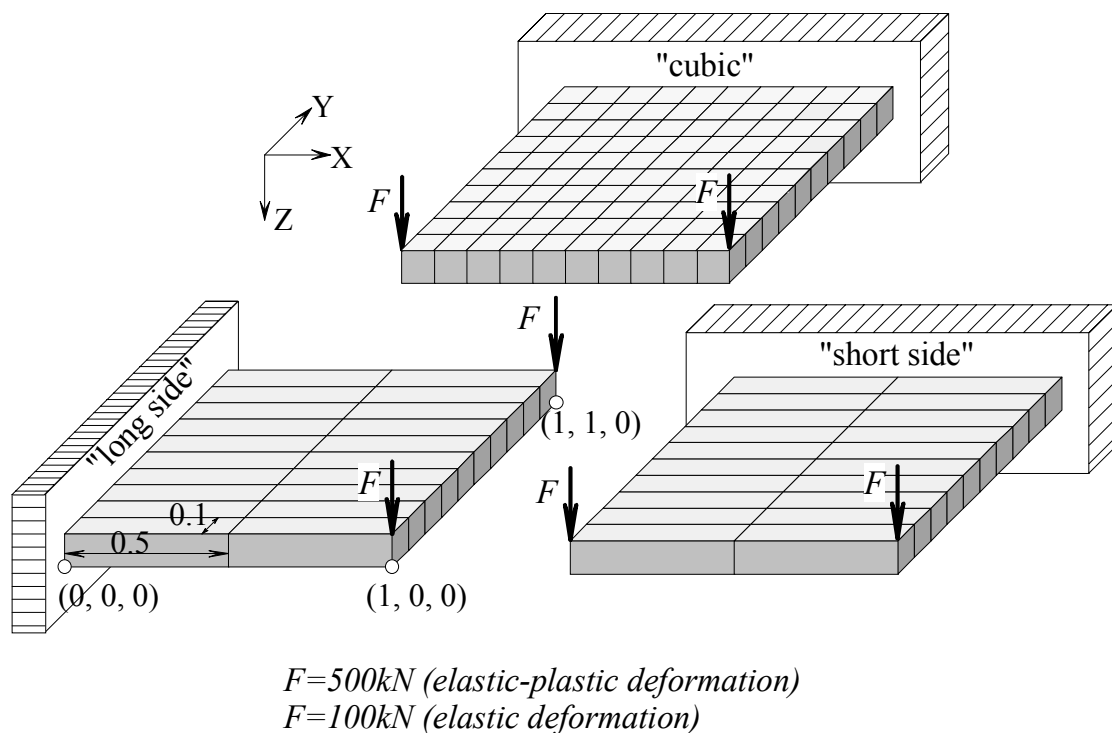


*Fig. F-1. 3D stress analysis model for demonstration of the "locking phenomenon".*

In this model one side of the plate is cantilevered. The deformation of the plate is caused by bending forces  $F=100\text{kN}$  and  $500\text{kN}$ , corresponding to purely elastic and elastic-plastic deformation.

*Fig. F-2* shows the value of the out-of-plane deformation along the free edge of the plate. It is clearly visible that, working in the direction of the short edge, elongated elements give quite reasonable results, both for elastic and elastic-plastic deformation. At the same time, working along the long side, the elongated elements demonstrate very poor accuracy, caused by the "locking phenomenon".

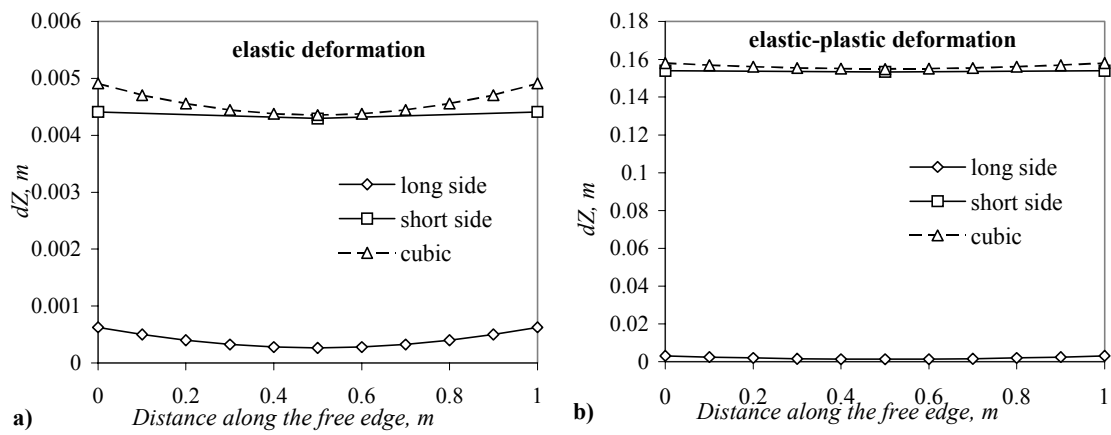


Fig. F-2. Out-of-plane deformation along the free edge of the plate; (a) - for the case of elastic deformation; (b) - for the case of elastic-plastic deformation.

## APPENDIX G

## EFFICIENCY OF THE MODEL DURING ELASTIC LOADING

In order to demonstrate the ability of the 3D FE model to work during the elastic loading, the model was tested by the scheme shown in *Fig. G-1*. One side of the plate is cantilevered. The load in the  $z$ -direction is applied to the corners of the opposite side of the plate. The exact analytical solution is available for such a problem:

$$dZ = -\frac{P \cdot x^2 \cdot (3l - x)}{6EI},$$

where  $dZ$  is the deflection of the plate,  $P$  is the applied force,  $l$  is the length of the plate,  $E$  is elastic modulus,  $I$  is moment of inertia of the plate around the  $y$ -axis.

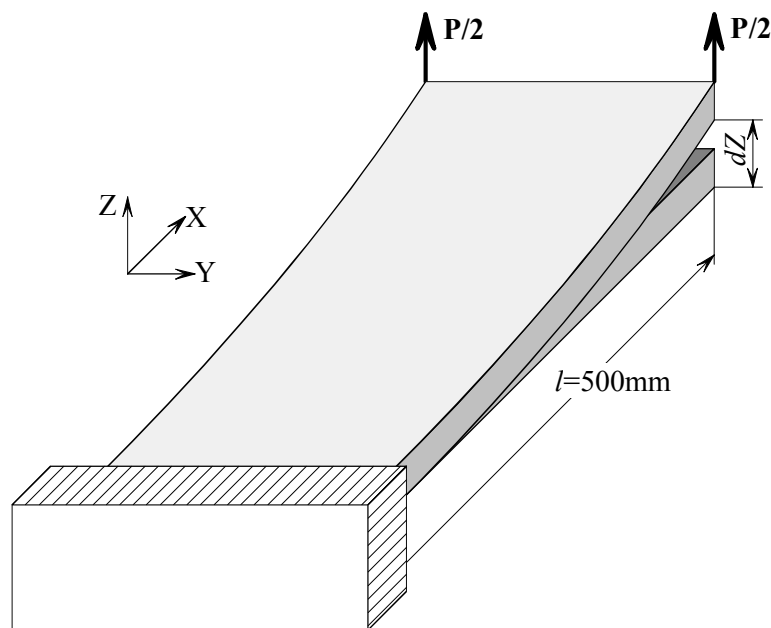


*Fig. G-1. Scheme of the elastic bending.*

In order to correspond to the conditions of the analytical solution, material properties consisted only of Young's modulus  $E=206\text{GPa}$  (Poisson's ratio  $\nu=0$ ).

Results of the analytical and finite-element solutions are compared in *Fig. G-2*. Comparison reveals that the FE model introduces a reasonable error. The error does not exceed 10%.

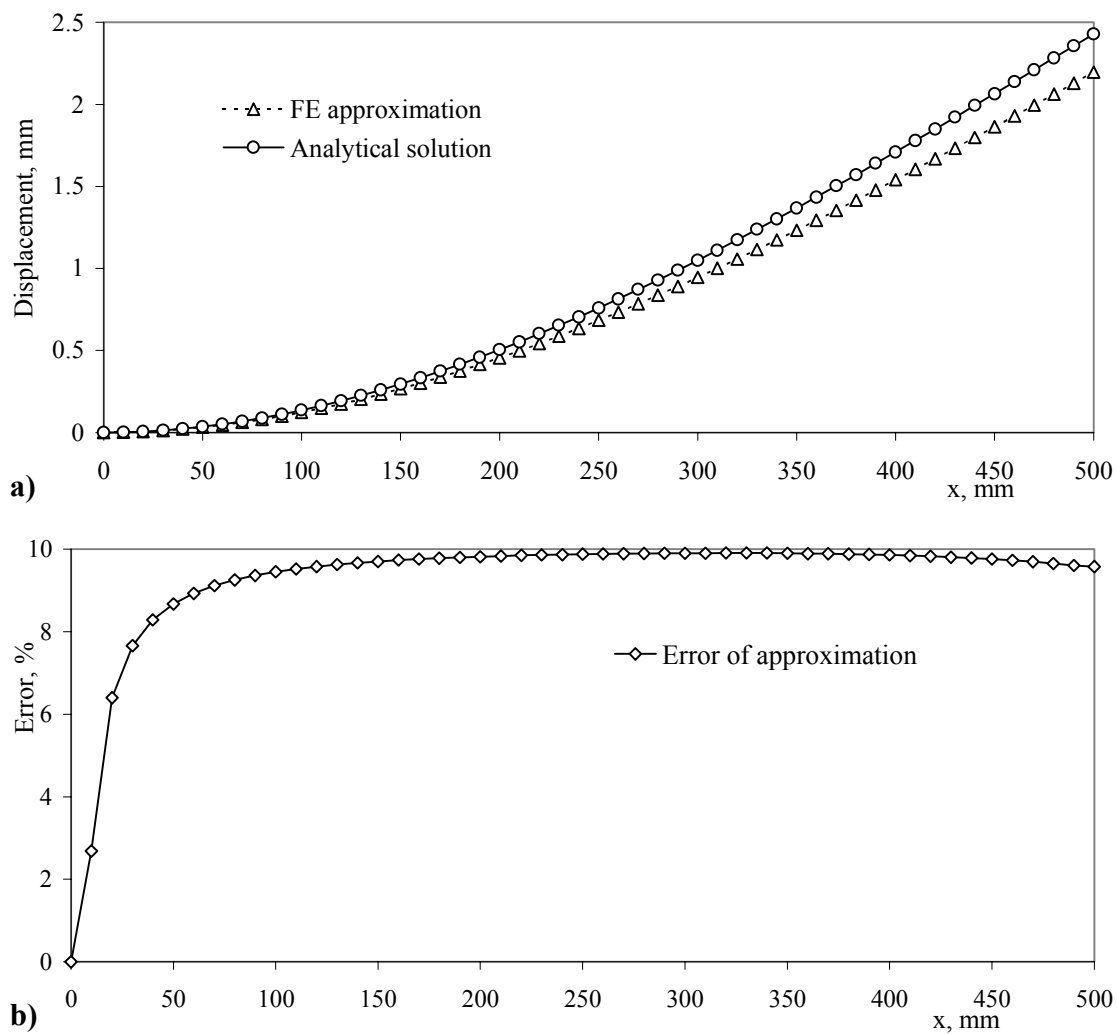


Fig. G-2. Comparison of the analytical and numerical solutions; (a) - displacement in the z-direction; (b) - error caused by the approximation.